Hrvatska akademija znanosti i umjetnosti –
Razred za Tehničke znanosti
Croatian Academy of Sciences and Art –
Department of Technical Sciences

Tehnički fakultet Sveučilišta u Rijeci
Faculty of Engineering, University of Rijeka
Pomorski fakultet Sveučilišta u Rijeci
Faculty of Maritime Studies, University of Rijeka
Fakultet za pomorstvo i promet Sveučilišta u Ljubljani
Faculty of Maritime Studies and Transport
University of Ljubljana
Udruga za proučavanje i razvoj pomorstva
Association for Research and Development
of Maritime Industries

IX. MEĐUNARODNO SAVJETOVANJE
O MORSKOJ TEHNOLOGIJI
in memoriam akademiku
Zlatku Winkleru
11. – 12. studenog 2021.
na Tehničkom fakultetu Sveučilišta u Rijeci
- online -

9th INTERNATIONAL CONFERENCE
ON MARINE TECHNOLOGY
in memoriam of the academician
Zlatko Winkler
November 11 and 12, 2021
at the Faculty of Engineering
University of Rijeka
– online –

Zbornik radova

Conference Proceedings

Rijeka, MMXXII.

TEHNIČKI FAKULTET SVEUČILIŠTA U RIJECI
Faculty of Engineering, University of Rijeka

POMORSKI FAKULTET SVEUČILIŠTA U RIJECI
Faculty of Maritime Studies, University of Rijeka

UDRUGA ZA PROUČAVANJE I RAZVOJ POMORSTVA
Association for Research and Development of Maritime Industries

FAKULTET ZA POMORSTVO I PROMET SVEUČILIŠTA U LJUBLJANI
Faculty of Maritime Studies and Transport University of Ljubljana

Za nakladnika – *For publisher*
Prof. dr. sc. Duško Pavletić
Izv.prof. dr. sc. Siniša Vilke

Grafičko oblikovanje i prijelom – *Lay-out and graphic design*
Dr. sc. Marko Perčić

Tisak – *Print*
Tiskara i grafika Viškovo d.o.o.

Naklada – *Issue*
100 Primjeraka – 100 copies

Organizatori
Host Organisation

Tehnički fakultet Sveučilišta u Rijeci
Faculty of Engineering University of Rijeka
Pomorski fakultet Sveučilišta u Rijeci
Faculty of Maritime Studies University of Rijeka
Fakultet za pomorstvo i promet Sveučilišta u Ljubljani
Faculty of Maritime Studies and Transport University of Ljubljana
Udruga za proučavanje i razvoj pomorstva
Association for Research and Development of Maritime Industries

Pod pokroviteljstvom
Hrvatske akademije znanosti i umjetnosti
Razred za tehničke znanosti
Under auspieces of
The Croatian Academy of Sciences and Arts
The Department of Technical Sciences

Počasni odbor / *Honorary Committee*
Oleg Butković, dipl. ing., Ministar pomorstva, prometa i infrastructure / *Minister of Maritime Affairs, Transport and Infrastructure*
Akademik Ivo Senjanović, predsjednik Znanstvenog vijeća za pomorstvo HAZU / *Chairman of the Scientific Council for Maritime Affairs - Croatian Academy of Sciences and Arts*
Zlatko Komadina, Župan Primorsko-goranske županije / *County President of Primorsko-goranska County*
Mr.sc. Vojko Obersnel, gradonačelnik grada Rijeke / *City of Rijeka Major*
Prof. dr. sc. Snježana Prijić-Samaržija, rektorica Sveučilišta u Rijeci / *Rector, University of Rijeka*
Prof.dr.sc. Heri Bezić, predsjednik Hrvatske gospodarske komore - Županijske komore Rijeka / *President of the Croatian Chamber of Economy - County Chamber Rijeka*
Prof.dr.sc. Peter Vidmar, Dekan Fakulteta za pomorstvo in promet, Univerza v Ljubljani, Slovenija / *Dean, University of Ljubljana, Faculty of Maritime Studies and Transport, Slovenia*
Prof.dr.sc. Alen Jugović, dekan Pomorskog Fakulteta Sveučilišta u Rijeci / *Dean, Faculty of Maritime Studies, University of Rijeka*
Prof.dr.sc. Joško Parunov, prodekan za znanost i suradnju sa gospodarstvom Fakulteta strojarstva i brodogradnje Sveučilaišta u Zagrebu / Vice*dean of Faculty of Mechanical Engineering and Naval Architecture, University of Zagreb*
Prof.dr.sc. Duško Pavletić, dekan Tehničkog fakulteta Sveučilišta u Rijeci / *Dean, Faculty of Engineering, University of Rijeka*
Siniša Ostojić, pomoćnik direktora za komercijalu brodogradilište 3.MAJ Rijeka, Croatia / *Commercial Manager, Shipyard 3.MAJ Rijeka, Croatia*

Izvršni odbor / *Executive Committee*
Prof. dr. sc. Albert Zamarin predsjednik / chairman
Prof. emeritus Julijan Dobrinić,
Prof. dr. sc. Tomislav Mrakovčić,
Izv.prof.dr.sc. Marko Hadjina,
Izv.prof.dr.sc. Tin Matulja,
Doc.dr.sc. Dunja Legović
Dr.sc. Marko Perčić,
Davor Bolf, dipl.ing.

Organizacijski odbor / Organizing Committee
Prof.dr.sc. Albert Zamarin, predsjednik **/**chairman
Prof.dr.sc. Tomislav Mrakovčić,
dopredsjednik / vice chairman
Izv.prof.dr.sc. Marko Hadjina, tajnik / secretary
Prof. emeritus Julijan Dobrinić
Prof.dr.sc. Elen Twrdy
Prof.dr.sc. Špiro Ivošević
Prof.dr.sc. Zoran Vukić
Prof.dr.sc. Jakov Dulčić
Prof.dr.sc. Merica Slišković
Izv.prof.dr.sc. Lidija Runko Luttenberger
Izv.prof.dr.sc. Goran Vukelić
Izv.prof.dr.sc. Tin Matulja
Doc.dr.sc. Siniša Vilke
Dr.sc. Marko Perčić

Međunarodni znanstveni odbor / *International Scientific Comittee*
Prof.dr.sc. Jerolim Andrić, *Fakultet strojarstva i brodogradnje Sveučilišta u Zagrebu / Faculty of Mechanical Eng. and Naval Architecture, Univ. of Zagreb*
Prof. dr. sc. Branko Blagojević, *Fakultet elektrotehnike, strojarstva i brodogradnje Sveučilišta u Splitu / Faculty of Electrical Engineering, Mechanical Engineering and Naval Architecture University of Split*
Prof. dr. sc. Roko Dejhalla, *Tehnički fakultet Sveučilišta u Rijeci / Faculty of Engineering, University of Rijeka*
Prof. emeritus Julijan Dobrinić, *Tehnički fakultet Sveučilišta u Rijeci / Faculty of Engineering, Univ of Rijeka*
Prof. dr. sc. Jakov Dulčić, *Institut za oceanografiju i ribarstvo Split / Institute of Oceanography and Fisheries Split*
Prof. dr. sc. Bernard Franković, *Sveučilište u Puli / University of Pula*
Izv. prof. dr. sc. Marko Hadjina, *Tehnički fakultet Sveučilišta u Rijeci / Faculty of Engineering, Univ of Rijeka*
Prof.dr.sc. Andrzej Grządziela, *Faculty of Mechanical and Electrical Engineering University of Gdynia, Poland*
Prof.dr.sc. Špiro Ivošević, *Pomorski fakultet Kotor, Crna Gora / Maritime Faculty Kotor, Montenegro*
Asist. Prof. dr.sc. Jasmin Jelovica, *University of British Columbia Faculty of Applied Science, Vancouver, Canada*
Izv.prof.dr.sc. Lidija Runko Luttenberger, *Politehnika Svučilište u Rijeci / Polytechics University of Rijeka*
Izv.prof.dr.sc. Boris Ljubenkov, *Fakultet elektrotehnike, strojarstva i brodogradnje Sveučilišta u Splitu / Faculty of Electrical Engineering, Mechanical Engineering and Naval Architecture University of Split*
Izv.prof. dr. sc. Tin Matulja, *Tehnički fakultet Sveučilišta u Rijeci / Faculty of Engineering, Univ of Rijeka*
Prof. dr. sc. Tomislav Mrakovčić, *Tehnički fakultet Sveučilišta u Rijeci / Faculty of Engineering, Univ of Rijeka*
Dr.sc. Zoran Mravak, *Marine and Offshore Division, Offshore Oper. & Services, Bureau Veritas, Paris, France*
Prof. D.Sc. António M. Pascoal, *Instituto Superior Técnico (IST), Lisbon, Portugal*
Izv.prof. dr. sc. Smiljko Rudan, *Fakultet strojarstva i brodogradnje Sveučilišta u Zagrebu / Faculty of Mechanical Eng. and Naval Architecture, Univ. of Zagreb*
Prof. dr. sc. Merica Slišković, Pomorski fakultet Sveučilišta u Splitu / *Faculty of Maritime Studies, University of Split, Cro*
Prof.dr.sc. Elen Twrdy, *Univerza v Ljubljani, Fakulteta za pomorstvo in promet / University of Ljubljana, Faculty of Maritime Studies and Transport, Slovenia*
Izv.prof.dr.sc. Siniša Vilke, *Pomorski Fakulteti Sveučilišta u Rijeci / Faculty of Maritime Studies, University of Rijeka*
Izv.prof.dr.sc. Goran Vukelić, *Pomorski Fakulteti Sveučilišta u Rijeci / Faculty of Maritime Studies, University of Rijeka*
Prof. dr. sc. Zoran Vukić, *Fakultet elektrotehnike i računarstva Sveučilišta u Zagrebu / Faculty of Electrical Engineering and Computing*
Prof. dr. sc. Albert Zamarin, *Tehnički fakultet Sveučilišta u Rijeci / Faculty of Engineering, Univ of Rijeka*
Prof. dr. sc. Nikola Mišković, *Fakultet elektrotehnike i računarstva Sveučilišta u Zagrebu* */ Faculty of Electrical Engineering and Computing*
Doc. dr. sc. Aleksandar Cuculić, Pomorski fakultet Sveučilišta u Rijeci */ Faculty of Maritime Studies, University of Rijeka, Croatia*

Sponzori
Sponsors

Savjetovanje su podržali /
This Conference is supported by:

Jadrolinija Rijeka / Jadrolinija Rijeka, Croatia

MARITIME CENTAR OF EXCELLENCE /
MEMBER OF LÜRSSEN GROUP

IHC engineering Croatia /
Member of Royal IHC Group

MACK d.o.o. za industrijske projekte / MACK d.o.o. Project Engineering Group

AITAC d.o.o. Kastav / AITAC

Pomorski zbornik / Journal of Maritime & Transportation Sciences

Brodogradilište Viktor Lenac d.d. / Shipyard Viktor Lenac

Brodogradilište 3.MAJ
Shipyard 3.MAJ

Hrvatska gospodarska komora, Županijska komora Rijeka /Croatian Chamber of Economy – County Chamber Rijeka

Primorsko-goranska županija / Primorsko-goranska County

UDK 338.47:656.61:504.054(05) **ISSN 0554-6397**

IZDAVAČ:

UDRUGA ZA PROUČAVANJE I RAZVOJ POMORSTVA

PUBLISHER:

ASSOCIATION FOR RESEARCH AND DEVELOPMENT OF MARITIME INDUSTRIES

POMORSKI ZBORNIK	Posebno izdanje	STR. 349
JOURNAL OF MARITIME & TRANSPORTATION SCIENCES	Special edition	PAGES 349

RIJEKA, 2022.

The Journal of Maritime & Transportation Sciences is issued twice a year. Current edition is 100 paperback copies.

Electronic typeface and print: Tiskara i grafika Viškovo d.o.o.

Printed in April 2022.

REVIEWERS
(in alphabetical order):

Saša Aksentijević, Ph. D., Aksentijevic Forensics and Consulting, Ltd., Croatia
Romina Alkier, Ph. D., University of Rijeka, Faculty of Tourism and Hospitality Management Opatija, Croatia
Nikolai Atanasov Velikov, Ph. D., N. Y. Vaptsarov Naval Academy, Faculty of Navigation, Bulgaria
Lidija Bagarić, Ph. D., University of Rijeka, Faculty of Tourism and Hospitality Management Opatija, Croatia
Mate Barić, Ph. D., University of Zadar, Maritime Department, Croatia
Hrvoje Baričević, Ph. D., University of Rijeka, Faculty of Maritime Studies, Croatia
Željko Bartulović, Ph. D., University of Rijeka, Faculty of Law, Croatia
Dean Bernečić, Ph. D., University of Rijeka, Faculty of Maritime Studies, Croatia
Toni Bielić, Ph. D., University of Zadar, Maritime Department, Croatia
Jasna Blašković Zavada, Ph. D., University of Zagreb, Faculty of Transport and Traffic Sciences, Croatia
Dragan Bolanča, Ph. D., University of Zagreb, Faculty of Law, Croatia
Mirjana Borucinsky, Ph. D., University of Rijeka, Faculty of Maritime Studies, Croatia
David Brčić, Ph. D., University of Rijeka, Faculty of Maritime Studies, Croatia
Aleksandar Cuculić, Ph. D., University of Rijeka, Faculty of Maritime Studies, Croatia
Jasmin Ćelić, Ph. D., University of Rijeka, Faculty of Maritime Studies, Croatia
Borna Debelić, Ph. D., University of Rijeka, Faculty of Maritime Studies, Croatia
Roko Dejhalla, Ph. D., University of Rijeka, Faculty of Engineering, Croatia
Aleksandra Deluka-Tibljaš, Ph. D., University of Rijeka, Faculty of Civil Engineering, Croatia
Julijan Dobrinić, Ph. D., University of Rijeka, Faculty of Engineering, Croatia
Davor Dujak, Ph. D., University of Osijek, Faculty of Economics, Croatia
Nastia Degiuli, Ph. D., University of Zagreb, Faculty of Mechanical Engineering and Naval Architecture, Croatia
Nikša Fafanđel, Ph. D., University of Rijeka, Faculty of Engineering, Croatia
Vlado Frančić, Ph. D., University of Rijeka, Faculty of Maritime Studies, Croatia
Daniela Gračan, Ph. D., University of Rijeka, Faculty of Tourism and Hospitality Management Opatija, Croatia
Neven Grubišić, Ph. D., University of Rijeka, Faculty of Maritime Studies, Croatia
Draško Holcer, Ph. D., Croatian Natural History Museum, Croatia
Iva Horvat, Ph. D., Port Authority Vukovar, Croatia
Alen Jugović, Ph. D., University of Rijeka, Faculty of Maritime Studies, Croatia
Marko Hadjina, Ph. D., University of Rijeka, Faculty of Engineering, Croatia
Svjetlana Hess, Ph. D., University of Rijeka, Faculty of Maritime Studies, Croatia
Bojan Hlača, Ph. D., University of Rijeka, Faculty of Maritime Studies, Croatia
Jakov Karmelić, Ph. D., CMA-CGM Croatia
Natalija Kavran, Ph. D., University of Zagreb, Faculty of Transport and Traffic Sciences, Croatia
Goran Kniewald, Ph. D., Ruđer Bošković Institute, Croatia
Ines Kolanović, Ph. D., University of Rijeka, Faculty of Maritime Studies, Croatia
Rob Konings, Ph. D., Delft University of Technology, OTB Research Institute Delft, Netherlands
Vesna Kovač, Ph. D., University of Rijeka, Faculty of Humanities and Social Sciences, Croatia
Božidar Kovačić, Ph. D., University of Rijeka, Department of Informatics, Croatia
Mirjana Kovačić, Ph. D., Regional Development Agency of the Primorje-Gorski Kotar County, Croatia
Maja Krčum, Ph. D., University of Split, Faculty of Maritime Studies, Croatia
Ivan Kristek, Ph. D., University of Osijek, Faculty of Economics, Croatia
Marinela Krstinić Nižić, Ph. D., University of Rijeka, Faculty of Tourism and Hospitality Management Opatija, Croatia

pomorski zbornik

Journal of Maritime & Transportation Sciences

POSEBNO IZDANJE

RIJEKA, 2022.

PUBLISHERS:

ASSOCIATION FOR RESEARCH AND DEVELOPMENT OF MARITIME INDUSTRIES
Address: Studentska 2, 51000 Rijeka, Croatia
Phone: +385 (0)91 443 4475
E-mail: udruga.pomorstvo@gmail.com

PRINTING FROM THE MARITIM PROCEEDINGS WAS CO -FINANCED BY PRIMORSKO-GORANSKA COUNTY

Radovi objavljeni u Pomorskom zborniku uvrštavaju se u sljedeće baze podataka:
Papers published in the Journal of Maritime & Transportation Sciences are indexed in the following databases:

ASFA (CSA) Aquatic Sciences and Fisheries Abstracts
TRID – the TRIS and ITRD database
EBSCO Academic Search Complete
PROQUEST - Natural Science Collection, SciTech Collection, Technology Collection Ulrich's Intl Periodicals Directory
News of New Electronic Journals
ZDB - Zeitschriftendatenbank
PROQUEST-ZDB – Zeitschriftendatenbank
Worldcat Libraries
HRČAK

Klasifikaciju UDK obavila Sveučilišna knjižnica Sveučilišta u Rijeci
UDC is performed by University Library Rijeka.

UDK 338.47:656.61:504.054 (05) ISSN 0554-6397

POMORSKI ZBORNIK

Special edition No. 4 Pages 1-349 Rijeka, 2022.

Conference Proceedings of the 9th INTERNATIONAL CONFERENCE ON MARINE TECHNOLOGY in memoriam of the academician Zlatko Winkler

CONTENTS

Uvodna riječ Glavnog urednika / Foreword Chief Editor

Poštovani Čitatelji,

i ove je godine, u pandemijskom okruženju, specijalni broj Pomorskog zbornika kojeg držite u ruci, rezultat suradnje Udruge za proučavanje i razvoj pomorstva i Organizacijskog odbora Međunarodnog Savjetovanja o morskoj tehnologiji – in memoriam akademiku Zlatku Winkleru, tj. Tehničkog fakulteta Sveučilišta u Rijeci kao glavnog organizatora Savjetovanja. Također i ovaj put, radovi prikazani u ovom broju su probrani i recenzirani radovi koji su bili prezentirani na IX. Međunarodnom Savjetovanju o Morskoj tehnologiji, a koje je održano 11.-12. studenog 2021. godine, kao i dosadašnja, na Tehničkom fakultetu Sveučilišta u Rijeci, ali ovaj put u online okruženju. Odluka Organizacijskog odbora u ožujku 2021. godine da se ide na internetsko online izdanje Savjetovanja se pokazala kao promišljena, obzirom na vjerojatnost jesenskog vala epidemije, a koji se eto, nažalost, sada se to može reći, pokazao i kao najteži do sada.

Ove je godine uz organizatora, Tehnički fakultet Sveučilišta u Rijeci i stalnih suorganizatora, Pomorski fakultet Sveučilišta u Rijeci i Udruge za proučavanje i razvoj pomorstva, u organizaciji ponovo sudjelovala i međunarodna institucija Fakultet za pomorstvo i promet Sveučilišta u Ljubljani. Uz međunarodni znanstveni odbor i određen broj radova stranih autora, savjetovanje je zadržalo međunarodni karakter. Pokrovitelj je već tradicionalno

Dear Readers,

this year again, in the pandemic surroundings, the special issue of the Journal of Maritime & Transportation Sciences held in your hand is the result of a collaboration between the Association for Research and Development of Maritime Industries and the Organizing Committee of the International Conference on Marine Technology - in memoriam academician Zlatko Winkler, i.e. the Faculty of Engineering, University of Rijeka, as the main organizer of the Conference. Once again, the papers presented in this issue are selected and reviewed papers presented at 9th International Conference on Marine Technology which was held on 11-12. November 2021 at the Faculty of Engineering in Rijeka, Croatia, this time as online edition. The decision of the Organizing Committee from March 2021 to go to the online edition of the Conference proved to be thoughtfully, given the likelihood of an autumn wave of epidemics, which, unfortunately, can now be said to be the most difficult so far.

This year, in addition to the organizer, the Faculty of Engineering of the University of Rijeka and co-organizers, the Faculty of Maritime Studies of the University of Rijeka and the Association for Research and Development of Maritime Industries, the international high education institution Faculty of Maritime Studies and Transport of the University of Ljubljana participated in the organization again. With an interna-

bila Hrvatska akademija znanosti i umjetnosti – Razred za tehničke znanosti. Organizacijski odbor Savjetovanja bio je u sastavu: prof. dr. sc. Albert Zamarin, predsjednik, prof. dr. sc. Tomislav Mrakovčić, dopredsjednik, izv. prof. dr. sc. Marko Hadjina, tajnik, prof. emeritus Julijan Dobrinić, prof. dr. sc. Zoran Vukić, prof. dr. sc. Jakov Dulčić, prof. dr. sc. Elen Twrdy (Fakultet za pomorstvo i promet Sveučilište u Ljubljani), prof.dr.sc Špiro Ivošević (Pomorski fakultet Kotor, Crna Gora), prof.dr.sc. Merica Slišković, izv. prof. dr. sc. Tin Matulja, izv. prof. dr. sc. Lidija Runko Luttenberger, izv.prof. dr. sc. Siniša Vilke, izv.prof. dr. sc. Goran Vukelić, i dr.sc. Marko Perčić.

Od prijavljenih 30 sažetka pristiglo je 28 kompletnih radova, sa 85 autora i koautora.

Dodatno je održano i pet plenarnih predavanja i to iz vrlo aktualnih područja i od priznatih međunarodnih firmi i institucija. Teme su bile: Zelena tranzicija i digitalna transformacija pomorskog sektora (Lürsen Design Center Kvarner & Maritime center of Excellence), Koncept broda za zbrinjavanje otpada sa hrvatskih otoka (IHC Engineering Croatia) i jedna uža tehnička tema, Automatska provjera izvijanja ukrepljenih panela (IHC Engineering Croatia), pregled projekta METRO, te prikaz aktivnosti i mogućnosti novog Centra za morsku tehnologiju Rijeka.

Priopćenja su prezentirana kroz 6 sekcija, iz područja tehničkih znanosti iz različitih polja i grana, i to: Zaštita okoliša (5), Pomorska biologija, Biotehnologija, Ribarstvo i Akvakultura (4), Konstrukcija i projektiranje u brodogradnji, Mali plovni ob-

tional scientific committee and a considerable number of papers by foreign authors, the conference retained international character. The patron is traditionally the Croatian Academy of Sciences and Arts - The Department of Technical Sciences.

The Conference Organizing Committee was composed of: prof. Albert Zamarin, president, prof. Tomislav Mrakovčić, vice-president, prof. Marko Hadjina, secretary, prof. emeritus Julijan Dobrinić, prof. Zoran Vukic, prof. Jakov Dulčić, prof. Tin Matulja, assist. prof. Lidia Runko Luttenberger, prof. Siniša Vilke, prof. Goran Vukelic, prof. Elen Twrdy (Faculty of Maritime Studies and Transport, University of Ljubljana), prof. dr.sc Špiro Ivošević (Maritime Faculty Kotor, Montenegro), prof.dr.sc. Merica Slišković, and dr.sc. Marko Perčić.

Out of the 30 abstracts submitted, 28 complete papers were submitted, with 85 authors and co-authors. Additionally, five plenary lectures were held within very actual fields and from respectable international companies and institutions: Green transition and digital transformation of the maritime sector (Lürsen Design Center Kvarner & Maritime center of Excellence), Utility vessel concept for the Croatian Adriatic and automation of buckling check of stiffened panels by using commercial finite element analysis software (IHC Engineering Croatia), Maritime Environment-friendly TRanspOrt systems - METRO Project review and presentation of the capacity of center for marine technology– CMT Rijeka from Faculty of Maritime Studies University of Rijeka.

jekti (6), Pomorski transport, Tehnologija brodogradnje i Brodogradilišta (5), Primjena kompjuterskih aplikacija u projektiranju, proizvodnji i održavanju postrojenja morske tehnologije (5), Brodostrojarstvo, Automatizacija i kontrola (3).

Plenarna predavanja, priopćenja i diskusija su održani na engleskom jeziku, dok je ceremonija otvaranja održana paralelno na hrvatskom i engleskom jeziku. Savjetovanju je, tijekom dva dana prisustvovalo više od 100 sudionika, autora, koautora, organizatora, suorganizatora, sponzora, profesora, studenata, gostiju. Recenzirani sažetci priopćenih radova se nalaze na mrežnim stranicama Savjetovanja i u obliku knjige sažetaka, a kompletni radovi se, nakon drugog kruga recenzije, evo nalaze u Vašim rukama kroz ovaj specijalni broj Pomorskog zbornika.

Srdačan pozdrav

Glavni urednik
Prof. dr. sc. Albert Zamarin

Papers were presented through 6 sections, in the area of technical sciences from different fields: Marine Environmental Protection (5), Marine Biology, Biotechnology, Fisheries and Aquaculture (4), Construction and Design in Shipbuilding, Small Craft (6), Maritime Transport, Shipbuilding Technology and Shipyards (5), Computer applications in the design, manufacture and operation of marine technology facilities (5), Marine Engineering, Automation and Control (3).

Plenary lectures, announcements and discussions were held in English, while the opening ceremony was held in parallel in Croatian and English. The conference was attended by more than 100 participants, authors, co-authors, organizers, co-organizers, sponsors, professors, students, businessmen and guests. Reviewed abstracts are available on the Conference website as well in the form of a Book of abstracts, while the complete papers, after the second round of review, are in your hands through this Journal special issue.

Kind regards

Editor-in-chief
Prof. dr. sc. Albert Zamarin

ISSN 0554-6397
Izvorni znanstveni članak
(*Original scientific paper*)

Claudia Kruschel
E-mail: ckrusche@unizd.hr
Department of Ecology, Agronomy and Aquaculture, University of Zadar, Trg Kneza Viseslava 9, 2300 Zadar, Croatia
Tobias Seidl
E-mail: tobias.seidl@w-hs.de
Westphalian Institute for Biomimetics, Westphalian University of Applied Sciences, Bocholt, Germany

Overcoming Obstacles - Biomimetic Lessons from the Swarming Behavior of Artemia Franciscana

Abstract

We investigated the formation of *Artemia franciscana* swarms of freshly hatched instar I nauplii larvae. Nauplii were released into light gradients but then interrupted by light-direction changes, small obstacles, or long barriers. All experiments were carried out horizontally. Each experiment used independent replicates. Freshly produced *Artemia* broods were harvested from independent incubators thus providing true replicate cohorts of *Artemia* subjected as replicates to the experimental treatments. We discovered that *Artemia* nauplii swarms can: 1. repeatedly react to non-obstructed light gradients that undergo repeated direction-changes and do so in a consistent way, 2. find their way to a light source within maze-like arrangements made from small transparent obstacles, 3. move as a swarm around extended transparent barriers, following a light gradient. This paper focuses on the recognition of whole-swarm behaviors, the description thereof and the recognition of differences in whole-swarm movements comparing non-obstructed swarming with swarms encountering obstacles. Investigations of the within-swarm behaviors of individual *Artemia* nauplii and their interactions with neighboring nauplii are in progress, e.g. in order to discover the underlying swarming algorithms and differences thereof comparing non-obstructed vs. obstructed pathways.

Keywords: Artemia production, swarming in light gradients, mazes and obstacles, high speed videography, adaptations to natural environments

1. Introduction

Vertical swarming in *Artemia* species (Crustacea, Anostraca) can be observed in the lab and is expected to constitute adaptive and useful behavior in their natural aquatic environment. Swarming is suggested to be primarily motivated by the feeding status of the *Artemia* and in response to gradients of salinity, oxygen, and light [1]. In the lab,

swarming of *Artemia* has been shown to vary with population density and age [2]. Positive swarming within point-source light-gradients is most intensive in freshly hatched nauplii and diminishes gradually towards adulthood. *Artemia* are known to readily respond to light with group motion, while they seem not influenced by electro-magnetic fields, DC voltage or thermal gradients [3]. Nauplii will not swarm towards a light source unless a critical group-density is reached [2]. Non-directional light that is uniformly distributed does not result in swarming [4]. *Artemia* nauplii encounter two major challenges when moving as a swarm towards a light source: they need to avoid collision with each other, which is a kind of overcoming obstacles within the swarm, and they need to orient themselves towards the light. Each individual may seek the most direct way towards the most intense light, moving parallel to neighbors avoiding collision [4]. Collisions are predicted to be more likely with decreasing distance from the light, the density of the swarm increases with decreasing distance from the light source.

An understudied question is if *Artemia* nauplii, can navigate in light gradients featuring obstacles and barriers on their path. We set up point-source light gradients with and without obstacles and barriers, testing the null hypothesis of non-random responses with replicated and independently grown experimental swarms, expecting to reject the null hypothesis of randomness.

In natural waters, radiation gradients during the day, are primarily oriented in the vertical, however, natural light in water bodies is never equivalent to a point source. Natural swarms have been described to have two alternative geometries: several vertical bands of swarming *Artemia* that are interconnected into larger structures or alternatively, horizontal strings that hover right beneath the surface. Both swarm-architectures originate near the surface, where light is most intense [5].

In nature, Artemia is expected to show tendencies of moving towards and staying close to the surface - the site of food production. *Artemia* nauplii non-selectively ingest any small particles in their path, mainly planktonic bacteria and small unicellular eukaryotes [5]. There is incentive to seek the surface and stay there. However, the necessity to reside at the surface eventually leads to crowding and competition. Crowd-avoidance behaviors are likely. Aside from finding food, Artemia needs to maintain an oxygenated environment. It is known that crowding leads to low oxygen concentrations within swarms which may limit swarm density [5], so expansion and dilution of the swarms are expected at the surface. In contrast, negative conditions, like exposure to dangerous radiation, like UV-B, may maintain dense swarms for the benefit of shading.

Artemia is the most salinity-tolerant multicellular animal, a recent study disclosed details on the genetic basis of the amazing capacity for osmoregulation from freshwater to 50% salinity in *Artemia franciscana* [6]. *Artemia* is the sole macro-planktonic inhabitant of salty lakes [7]. *Artemia* are globally distributed only across aquatic environments that reach the necessary extremely high salinities. Here *Artemia* are the main predator of plankton and are released from competition and higher order predators that do not tolerate the osmotic extremes.

In contrast to the situation in nature, Artemia raised in hatcheries as food for

juvenile fish and applied to transfer supplemental nutrition, a method called bio-encapsulation [8]. In captivity Artemia do encounter predators. In fact, *Artemia* are guided by light gradients to force horizontal swarming to the location of consumption. At the feeding site, consumption is less efficient because swarming eventually hinders efficient predation. Research into proper management is needed [9] [10]. A wide spectrum of organisms, including most wild zooplankton populations [11], but also fish and bacteria have been shown to swarm as a predation escape. While the concept of swarming as a predation escape is established overall it is not expected to be relevant in wild *Artemia*.

Six sexual species of *Artemia* are now recognized, together with a heterogeneous group of parthenogenetic populations, under the binomen *Artemia parthenogenetica* [12]. Globally, Artemia are only known from biotopes with extreme salinities, other variables (temperature, light intensity and primary food production may have an influence on the sizes of the *Artemia* population, or even cause a temporary absence. Artemia are found in hundreds of lakes and salterns scattered across the globe in tropical, subtropical, and temperate climates. The salt environments are varied in ionic composition, including chloride, sulphate or carbonate. *Artemia* are present at all altitudes, from sealevel to 4500m (Tibet).

Little consensus exists on the adaptive value of swarming in Artemia nauplii in their natural habitat. Some extreme swarming is related to viral and bacterial infections when *Artemia* are manipulated to form dense swarms to enhance the transfer to the final hosts, primarily water birds that feed on zooplankton, e.g. Flamingos. In seafood farms, many such transfers have been reported. Farmed fish often get infected by feeding on wild-harvested and/or cultured *Artemia* that carry parasites, a serious economic hardship awaiting preventive solutions.

One possible benefit of vertical swarming in natural *Artemia* populations may be that the internal swarm-motion transports food or continuously replenishes oxygen in *Artemia* groups. Vertical *Artemia* swarms have been described to cause a kind of convection cell that maintains continuous water flow, like a conveyer belt, through the swarm (CK own observations).

Little is known about horizontal swarming. A potential trigger for natural horizontal swarming could be an uneven distribution of planktonic food and the need to move horizontally between patches. Such movements are easier done in a group than as individuals. Individuals within moving swarms generally benefit from the reduced energetic costs often also accompanied by improved oxygen consumption rates [13], [14], [15].

This paper investigates the swarm-behavior of Artemia instar-nauplii under laboratory conditions within directional, point-source light-gradients with and without obstracles. Overall we predicted non-random responses at the whole-swarm level. We chose light to generate swarms based on previous observations and recommendation, *Artemia* nauplii are unlikely to swarm under non-directional light conditions or in the dark [1].

In all experiments we filmed *A. franciscana* nauplii with high speed cameras for the opportunity to analyze on two spatial levels, the entire swarm and the movements of individual *Artemia* nauplii. Nauplii are anatomical different from adult Artemias.

We predict that nauplii show strong affinity to light and are able to move around obstacles in their path. Obstacles are assumed to be common in nature and strategies to navigate them should have evolved in *Artemia*. The here presented results report exclusively on the experiments featuring horizontal swarms of instar I nauplii.

2. Material and methods

2.1. *Artemia* production

The setup to produce *Artemia* nauplii consisted of 12 two-liter plastic bottles (Soda bottles, SPRITE). From six bottles the lower third had been cut off and from the remaining six the upper third was removed. This resulted in the assemblage of six units each made of two partial bottles: one bottomless head-down placed within one head-less. The growing medium per each unit consisted of 1 liter of distilled water with 25 g table salt (not iodized) added. In addition, 7 grams of baking soda were added to approximate normal seawater hardness and pH. Each unit was supplied with a plastic pipe (25 mm inner diameter) attached to tubing to allow air to be pumped into the medium by one 200 L serving 3 setups. Hereby it is important to place the pipe into the bottle-cap of the inner bottle in order to have stable aeration. The *Artemia* cyst-eggs were purchased online and wre imported from saltern facilities in the San Francisko bay arae, thus the species was *Artemia franciscana*. All cysts came from the same container to assure identical origin of the swarming nauplii used in all experiments. Each cultivation bottle received 1 g of egg-cysts. The vigorous bubble-generation at the bottom of the head-down bottle provided water circulation for constant distribution of the eggs throughout the entire medium. Incubation time varied between 46 and 50 hours, temperature was 23 – 25 degrees Celsius. All six units were placed into a plastic box and two Terra-Grow UV tube-lights were placed over each row of 3 incubator units, at a distance of 15 cm from the top of the open end of the inner incubator bottle.

2.2. *Artemia* development testing

Before the harvest, each incubator was sampled to evaluate the developmental state of the *Artemia* nauplii by taking a sample directly from the well mixed incubator bottles. Upon that four broods were selected based on high similarity and high proportions of Instar I nauplii compared to other developmental stages (unhatched eggs, umbrella-stage hatching nauplii, or nauplii that already miss their yolk sack) Instar I nauplii do not take up food as their digestive system is not functional yet. They are supported completely by yolk reserves. We always had four valid and sufficiently similar broods for all experiments reported here.

2.3. *Artemia* harvest, storage, and preparation for experiments

The harvest of the nauplii was as follows: the selected broods where left for 10 minutes without circulation so that the negatively buoyant nauplii sink to the bottom while unhatched eggs and egg shells float to the surface. Nauplii accumulate in the bottle neck of the brood container and were carefully drained by unscrewing the cap, and releasing the nauplii into plastic dishes, kept in a place without non-directional or artificial light. Immediately before use in any experiments, a strong white-light source illuminated one corner of the currently used brood-specific container which resulted in a quick gathering of active, healthy and swarming nauplii within that corner. Provided that we harvested about the same amount of nauplii from each bottle, we assumed that the same number of drops of nauplii culture from a standardized glass-pipette would assure similar densities of nauplii used in each experimental trial.

2.4. Experimental conditions and sample hierarchy

Incubation, holding-tank and experimental-tank conditions were monitored for consistent temperature and water chemistry, including nitrite, nitrate, pH, salinity, and water hardness. After *Artemia* nauplii had been used in an experiment they were immediately and humanely killed by exposing them to water of extremely high salinity which in the wild is also their most likely death cause aside from starving. No individual nauplii was ever used in two experiments. For each of the experiments the hierarchical replication structure was as follows: four independent broods (incubation containers) were sampled once for 4 independent replicated experiments per treatment (1-3) and control (4), each featuring independently raised populations. In each experiment the three unique nauplii samples were either used in a single procedure or in a series of repeated procedures depending on the experiment-type. Multiple repeated treatments were conducted in non-obstructed channel experiments but only one treatment in experiments with the channel-maze, and barrier designs. The details for each of the three experiments are described below.

2.5. Experimental setups

2.5.1. Unobstracted channel experiments

This type of experiment is designed to reject the null hypothesis that *Artemia* nauplii move randomly within light gradients and do not show swarm formation, do not change swimming direction upon changes in light direction, and that *Artemia* exhibit random passing rates in response to repeated identical light of all treatments.

Our working hypothesis was that *Artemia* nauplii form swarms that move coordinated and non-random and that they maintain passing rates across equal treatments (see figure 1).

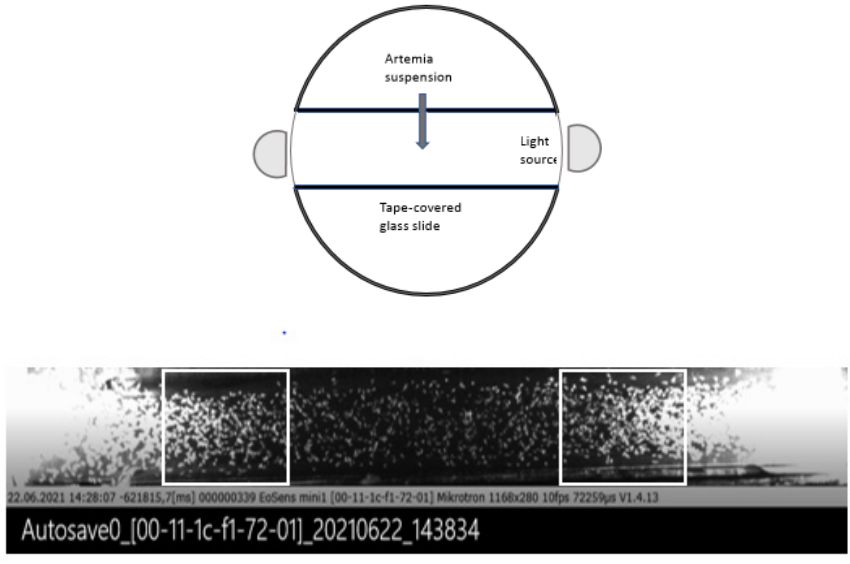

Figure 1: *A. salina* nauplii swarms in unobstracted channel experiments. *Left*: *Artemia* are added to the channel as a defined volume of concentrated *Artemia* brood to the center of the channel, using a pipette to transfer equal amounts of drops of *Artemia* nauplii brood (total of 3 unique samples per experiment) *Right*: *Artemia* organise into two swarms, one swarming to the left light source, one to the right light source. Also indicated are two counting boxes, each at an equal distance from the alternative light sources. *Artemia* entering each of the two boxes from the left and from the right are counted within standardized time periods under three different light conditions: light coming from the 1. left and right simultaneously, 2. from the left only or 3. from the right only.

Hardware

The unobstracted channel was built from a petri dish bottom, two microscope slides and some black electrical tape. The two slides are covered in black tape and positioned in parallel with a 1.5 cm gap in between. The resulting channel spans the length of the petri dish. The petri dish is entirely covered in black tape except for two clear areas at the two ends of the channel. Here the two identical strong white lights (stereo microscope lighting set) provide equal light conditions coming from each side of the channel (see Figure 1, left image). Instead of switching these lights on and off, opaque black plastic blocks have been moved in front of or removed from the light-source, this avoided inconsistencies in the spatial relation between light and channel across repeated experiments.

Procedure and statistical analysis

Ten drops of concentrated *Artemia* naupili (standardized procedure, see above) were placed in the center of the channel and were allowed to spread under equal light input applied from the left and the right ends of the channel. The expectation is that the *Artemia* added will divide into two sub-swarms moving either to the right or the left light source (see Figure 1). Rates of passing towards/away from each light source through the two boxes (see Figure 1) are estimated as the actual number of *Artemia* entering the box (from the left or from the right) within a standardized time period (total of 60 sec, counted within six separate 10 second periods, each played at 0.16 of the original video speed, using the video format MP4 in AVI (Figure 1, right image). All together, we performed three experiments using the unobstructed channel design. Each experiment was done from three independent broods. Statistical analysis has been performed on mean values, calculated from the six independent *Artemia* counts. Counts were applied in the statistical analysis without any transformation, Student t-tests were used upon assurance of equal variances (F-test).

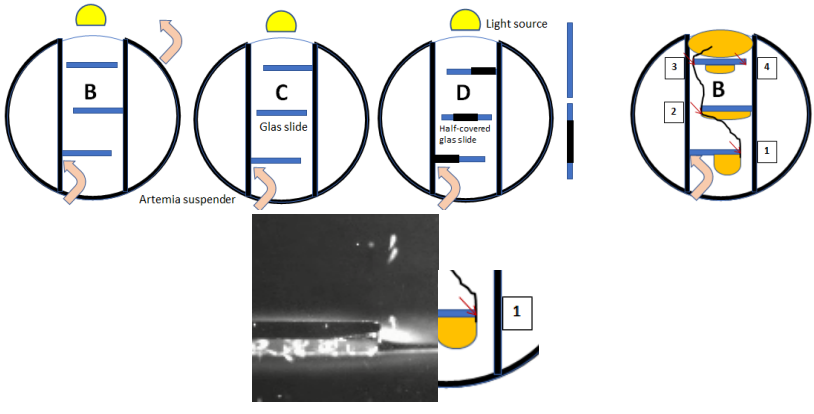

Figure 2: Three images on the left: two mazes with transparent obstacles and one with opaque obstacles. On the two far right images: the predicted movement of *Artemia* nauplii through maze B, indicates the locations at which *nauplii* are counted (red arrows) and a photo demonstrates the actual counting location, featuring nauplii in action.

2.5.2. *Obstracted channel experiment – the maze*

The following experiments were designed to reject the null hypothesis that *Artemia* due to its assumed random movement, will not navigate as a group through a transparent maze offered within the channel (see 2.5.1.) in which a strong light gradient has been set up (Figure 2, a deviant experimental setup from the unobstructed channel design, Fig. 1).

Our working hypothesis was that *Artemia* nauplii can follow the light gradient and thus navigate around obstacles through which a steady beam of unidirectional light is penetrating assuming that small differences in light intensity can be sensed by the *Artemia* nauplii. An additional expectation was that nauplii swarms should be sensitive enough to follow the most distance-efficient pathway when encountering the one obstacle that offers two alternative pathways (closest to the light in B, center in C and D, see Figure 2).

Hardware

The channel-mazes are basically an advanced channel design, now with added obstacles. The obstacles are either transparent coverslips made from thin transparent plastic or alternatively the same coverslips that partially covered with black electrical tape. As a result, the light intensity is suppressed and the light penetrates through two separate pathways (see Figure 2).

Procedure and statistical analysis

The same standardized density of *Artemia* nauplii again was placed at the bottom of the first barrier which was always positioned at base of the first obstacle in all treatments (Figure 2). The other two obstacles are varied in position creating alternative maze varients by placing them in the two possible places second or third one obstacle that offers two alternative gaps pass it, either in position 2 or in position 3 (see Figure 2). Therefore, *Artemia* are offered two alternative pathways in the transparent maze treatment. The maze with the partially opaque obstacles was only offered in one of the two alternative arrangements (see Figure 2).

At each location that offers an opportunity to pass a barrier through a gap, *Artemia* have been counted in ten replicated counting periods for a total standardized accumulated period of 60 seconds. The counting was strictly done at the edges of the barriers. Thus counts truly represent one-way movements with no chance to count the same individual twice at a given obstacle. The various counts have been used to analyze if 1. the swarm actually finds a path to the light, 2. if this path is also the most distance efficient path, and 3. If the *Artemia* find their way to the light source through a partially opaque maze. All together, we performed 9 maze experiments, using three types of mazes in three independent-brood replicates from three independently cultured broods. Aside from evaluating if *Artemia* actuall swarmed and reached the light source, we used mean values of passing *Artemia* at each barrier to get an idea about the flow through, and we compared mean numbers of *Artemia* passing at the obstacle offering two pathways, to test (student T-test, after F-test) if Artemia takes the most efficient path (see table 3).

2.5.2. *Light gradients along an elongated barrier*

The experimental set up consisted of a plastic petri dish entirely covered in black electrical tape except for openings on the left side which in this experiment were only used for illumination at three of five possible equivalent clock positions: 09:00, 10:00, and 11.00 (Figure 3). Attached to the center of the bottom-rim and to the flat-bottom of the petri dish a glass microscope-slide divides the petri dish into identical halves. This barrier reaches from the 06:00 position towards the 12:00 position, however, the slide is shorter than the diameter of the dish so that a small gap is left between the upper rim of the barrier and the top of the petri dish (Fig. 3).

Procedure

Two alternative treatments where performed. One treatment involves all alternative light positions, 09:00. 10:00, and 11:00. The other treatment involves only positions 9:00 and 10:00. In treatment 1 the light source is consecutively placed from 09:00 to 10.00 and from 10:00 to 11:00 with 5 minutes in between switches (Figure 3 short upper arrow). The result is that the lighted area expands towards the gap, because the angle at 10:00 illuminates the barrier at a larger angle than from position 9:00 and at 11:00 light illuminates the barrier at a larger angle than at positions 9:00 and 10:00.

In treatment 2, the light is moved from 9:00 to 10:00 after five minutes, but then not moved to position 11:00, it remains at the 10:00 position.

No light is offered in the lower half of the barrier. At the start, *Artemia* are placed right at the bottom of the barrier (see Figure 3, pink arrow). The only pathway around the barrier is located at the top of the barrier, a gap between the upper edge of the slide and the upper rim of the petri dish. Once *Artemia* pass over the edge of the slide and through the gap, they have a barrier-free path towards the actual light source at position 11:00 in treatment 1 (Figure 3 short upper arrow) and at position 10:00 in treatment 2 (Figure 3 long bottom arrow). We estimated the amount of barrier illuminated from the three alternative light position as follows: positions 60% of the barrier from position 09:00, which is less than 75% from 10:00, and 87% from 11:00. Thus, moving the light source in treatment 1 resulted in a stepwise extension of the illuminated light gradient nearer towards the gap than in treatment 2.

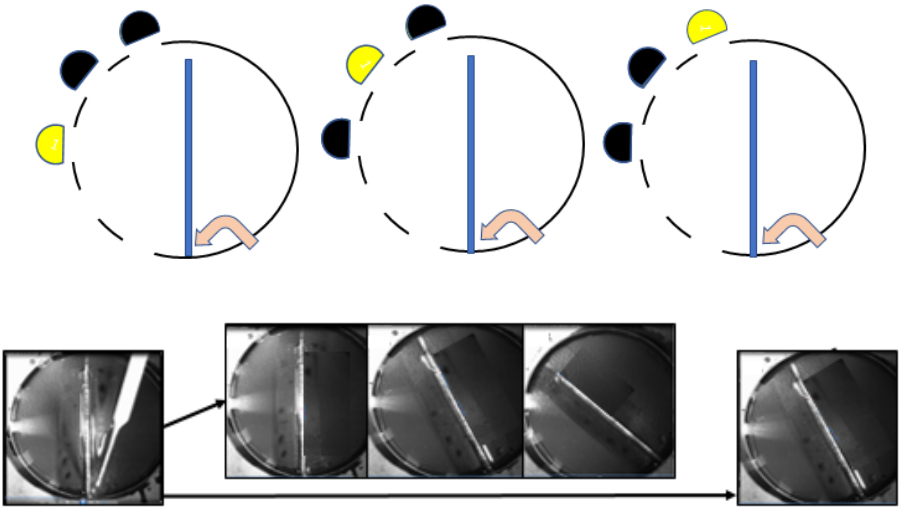

Figure 3: Standardized amounts of *A. franciscana* nauplii are placed at the bottom of the barrier (pink arrow) and the light (stereo microscope light) is focused through the gap at the 9:00 position onto the barrier which constitutes a position just above the midpoint of the barrier. Other light positions are established by rotating the dish to permit the light through the alternative openings (see bottom images). We performed three experiments (see shorter arrow) using three independent broods. Alternatively, a forth brood had been used to rotate the petri dish only from position 9:00 to 10:00 but then in remained at position 10:00 and no move to 11:00 was performed, a procedure that we call „control" (see Figure 3, the lower longer arrow).

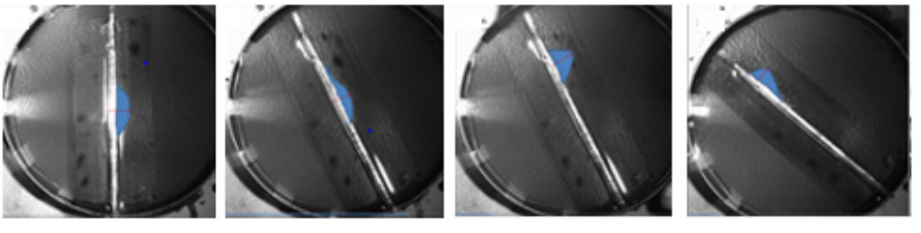

Figure 4: Visual examples to illustrate how the movement of the swarm (blue) was quantified in distance moved per minute (speed). The red line through the swarm is the swarm-axis line (from the highest point of the swarm to the intercept with the barrier line at a right angle).

Tracking the swarm

In order to quantify the movement of the *Artemia* nauplii from the entry point to the gap, movements were measured in centimeters along the barrier. To measure this distance, at each light position (9:00, 10:00. 11:00), the swarm's highest peak was located and an intercept of a line from the from the peak perpendicular to the barrier (Figure 4). The distance the swarm had moved was the distance from the bottom of the barrier to the intercept line. This way we were able to account for the changes in distance per time for each swarm in all treatments. The maximum time it took the swarm to reach the gap varied between 14 and 17 minutes, the time when the swarm completely dissolved and all swarming individuals had passed the barrier's upper edge and accumulated at the 11:00 light source (Figure 4).

Figure 5: Three types of obstacle channel designs. The the obstacle maze "B" and "C" feature unobstracted clear obstacles. Obstacle maze "D" has obstacles that are partially opaque.

3. Results

Three experiments have been carried out to investigate the swarming behavior of *Artemia franciscana* nauplii within horizontal shallow environments which were set up with strong light gradients.

First experiment: the most basic experiment investigated if horizontal unidirectional light-gradients and two-directional light gradients (point light from opposite sites) trigger similar responses, group formation, and motile behavior in *Artemia* nauplii. Repeated one-directional light-gradients and repeated reversals thereof are expected to result in repeated stable (non-significantly different) group patterns (Tables 1 and 2, Figures 1).

Second experiment: experiments investigate the behaviour of *Artemia nauplii* swarms within unidirectional light-gradients within horizontal pathways that offer transparent and also opaque obstacles. We used three obstacles within each maze but varied the arrangements within the same basic horizontal channel (Figures 3, 4, and 5).

Third experiment: a circular dish offering one elongated transparent barrier placed in the center dividing it into two halves leaving one small throu-way at the top only. *Artemia* entry point and throu-way were equally distant from a single light source located perpendicular to the barrier which was moved to two alternative positions at agreed times, resulting in light illuminating the barrier from different angles, setting up a progressing gradient of light over time (Figures 4, 6, nand 8).

Unobstructed channel – first experiment

We observed that repeated direction changes of single-light gradients do result in stable repeated re-organization of *A. franciscana* nauplii into organized swarms that move with the light gradient direction in similar ways and across consecutive trials. During repeated light direction reversals nauplii aggregations promptly reversed swarming direction maintaining similar passing rates at defined loctions (Fig. 1). The passing rates were significantly different comparing moves towards vs. away from the light source, and no significantly differences have been found across trials with the same light intensities offered from the same directions (left or right). When identical lights were used from opposite sites, the passing rates were also consistent across repeated trials but the passing rates towards the light and away from the light were not significantly different. This was true across multiple moves of the same swarms, across three independent repeated swarms from three independent broods (Table 1 and 2, Figure 1).

Table 1: F-/T-tests on nauplii counts in two-light treatments (2LT see Fig. 1).

brood 1	2LT	F-Test			t-Test: Two-Sample			
LEFT	LEFT							
to LT	**away LT**		*to LT*	*away LT*			*to LT*	*away LT*
4.1	9.2	Mean	6.83333	9.6667	Mean		6.83333	9.66667
10.4	12.7	Variance	10.4433	8.0033	Variance		10.4433	8.00333
6	7.1	Observations	3	3	Observations		3	3
		df	2	2	Pooled Variance		9.22333	
					Hypothesized	Mean		
		F	1.30487		Difference		0	
		p-value	**0.43386**		df		4	
							-	
		F Critical	19		t Stat		1.14261	
					p-value		**0.31695**	
					t Crit 2-tail		2.77645	
brood 2	2LT							
LEFT	LEFT							
to LT	**away LT**		*to LT*	*away LT*			*to LT*	*away LT*
4	7.8	Mean	6.7	9.3	Mean		6.7	9.3
10.7	13.3	Variance	12.49	12.25	Variance		12.49	12.25
5.4	6.8	Observations	3	3	Observations			3
		df	2	2	Pooled Variance		12.37	
					Hypothesized	Mean		
		F	1.01959		Difference		0	
		p value	**0.49515**		df		4	
							-	
		F Critical	19		t Stat		0.90539	
					p-value		**0.41646**	
					t Crit 2-tail		2.77645	
brood 2	2LT							
LEFT	LEFT							
to LT	**away LT**		*to LT*	*away LT*			*to LT*	*away LT*
6	7.2	Mean	8.5	6.4	Mean		8.5	6.4
13.3	7.6	Variance	17.29	3.04	Variance		17.29	3.04
6.2	4.4	Observations	3	3	Observations		3	3
		df	2	2	Pooled Variance		10.165	
					Hypothesized	Mean		
		F	5.6875		Difference		0	
		p value	**0.14953**		df		4	
		F Critical	19		t Stat		0.8067	
					p-value		**0.46507**	
					t Crit 2-tail		2.77645	

Table 2: Summary of the above t-test results from the unobstruted channel experiment. Brood (BR) 1,2,3 with 4 (single light, 1LT) or 3 (two lights, 2LTS) repeated treatments (REP) per brood. Bold numbers indicate that the mean number of *Artemia* moving towards the light was higher, regular numbers indicate that the mean number of nauplii moving away from light was higher, grey-background indicates non-significant differences between numbers of *Artemia* moving in opposite directions.

BR	REP	2 LTS Left to LT	2 LTS Left away LT	2 LTS Right to LT	2 LTS Right away LT	1 LT Left to LT	1 LT Left away LT	1 LT Right to LT	1 LT Right away LT
1	1	4.1	9.2	6.3	9.2	**14.1**	**9.7**	**16**	**12.3**
1	2	10.4	12.7	**15**	**10.6**	**18**	**13.1**	**16.4**	**11.7**
1	3	6	7.1	7.4	9.1	**16**	**8.3**	**17.6**	**11.9**
1	4	NA	NA	NA	NA	**22.3**	**10.3**	**20.3**	**7.5**
2	1	4	7.8	6.7	10	**14.4**	**9.7**	**12.2**	**6.6**
2	2	10.7	13.3	**14.7**	**10.3**	**12.4**	**6.6**	**15.8**	**10.6**
2	3	5.4	6.8	6.4	8	**16.3**	**8.6**	**16.3**	**11.8**
2	4	NA	NA	NA	NA	**16.3**	**8.6**	**16.3**	**11.8**
3	1	6	7.2	8.7	10	**12.6**	**9.7**	**15.6**	**12.1**
3	2	13.3	7.6	15.1	10.7	**13.9**	**9.4**	**1.1**	**6.2**
3	3	**6.2**	**4.4**	9.9	7.1	**15.1**	**10.7**	**18.6**	**12.9**
3	4	NA	NA	NA	NA	**16.2**	**12.7**	**17.4**	**10.1**

Obstacle channel experiment – second experiment

In the various maze designs using transparent obstacles in the channels, *A. franciscana* nauplii swarms found their way from the starting point to the light source, however the paths taken were not length-optimized: *Artemia* did not chose the shortest (most economic) overall pathway (Tables 3, Figure 5). In channels with partially opaque obstacles, the swarm basically disintegrated after passing the second barrier. The opaque parts of each barrier seem to obstruct the light gradient in a way that the nauplii act individually, some make it all the way to the light source.

No organized swarm or any kind of non-random movement was observed without any light gradient, neither in the straight channel nor in the circular dish design.

Table 3: Number of *Artemia* nauplii passing the edges of three obstacle (OBS) (see Figures 2 and 5)

Obstacle maze „B“ clear	**Brood 1**	**Brood 2**	**Brood 3**
OBS1 TOP	114	196	221
OBS2BOTTOM	107	134	124
OBS3BOTTOM	**57**	**59**	**58**
OBS3 TOP	**95**	**56**	**36**
		Two-path obstacle (OBS3)	
		bottom	top
		57	95
		59	56
		58	36
Obstacle maze „C“ clear	**Brood 1**	**Brood 2**	**Brood 3**
OBS1 TOP	119	177	200
OBS2 BOTTOM	**111**	**169**	**112**
OBS2 TOP	**101**	**80**	**60**
OBS3 BOTTOM	73	61	38
		Two-path obstacle (OBS2)	
		bottom	top
		111	101
		169	80
		112	60
Obstacle maze „D“ cover	**Brood 1**	**Brood 2**	**Brood 3**
OBS1 TOP	80	69	91
OBS2 BOTTOM	**0**	**0**	**2**
OBS2 TOP	**31**	**25**	**43**
OBS3 BOTTOM	0	0	1
		Two-path obstacle (OBS2)	
		bottom	top
		0	31
		0	25
		2	43

Long barriers within continuous light gradients – experiment 3

Upon adding *Artemia* at the bottom of the barrier (Figure 6, top, see arrows) the nauplii immediately moved within the most direct light impact positioned at 09:00 forming a well-defined swarm (Figure 6 bottom) within a minute. When the light was moved to position 10:00 the swarm moved quickly to the equivalent location at the barrier, and did so again following the move of the light source to position 11:00 (Figure 6 bottom) and further to the edge of the barrier. From there *Artemia* quickly passed the edge of the barrier and accumulated as very dense swarm at the actual 11:00 light source location.

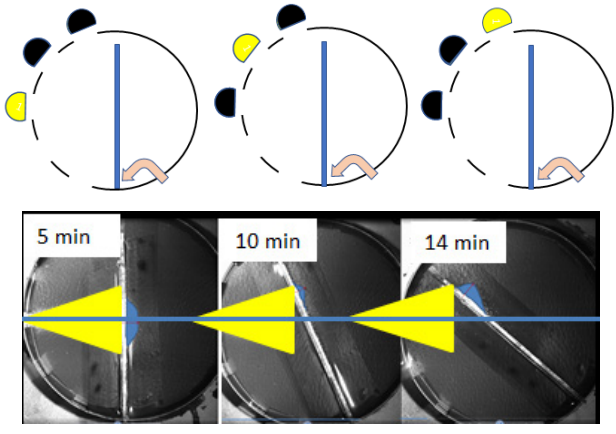

Figure 6: Change in illumination as the light is moved from position 9:00 to 10:00 to 11:00. *Artemia* nauplii follow a stepwise-maintained gradient of light.

In the maze (experiment 2), *Artemia* formed an organized swarm at the first obstacle but gradually became less organized at the 2nd and 3rd obstacle. In contrast, the swarm in experiment 3 started as a very tightly organized swarm and continued to move as that following the entire length of the barrier. Nevertheless, some individual *Artemia* did leave the swarm, however, they continued to move along the barrier The overwhelming majority of *Artemia* stayed within the swarm context. Only at position 11:00 at the barrier did the swarm quickly dissolve and individuals moved around the barrier's edge an on towards the actual light source (Table 4).

Table 4: Distances and total time *A. franciscana* nauplii moved as a well-defined swarm along the central barrier (see Figure 6 and 7)

time (min)	brood 1 1st, 2nd, 3rd light	brood 2 1st, 2nd, 3rd light	brood 3 1st, 2nd, 3rd light	control only 1st, 2nd light
1	6	6.4	6.1	6.1
2	6.4	6.5	6.6	6.9
3	7.2	7	6.9	6.9
6	7.2	6.9	7.6	7.2
7	8.5	8	9	9.4
8	10	9.9	10.2	10.4
9	9.9	10	10.4	10.1
10	10.3	10.1	10.5	10.3
13	12	10.6	12.6	10.4
14	13	12	12.7	10.6

During the move of the swarm we recognized phases of fast movement immediately following the placement of the light source at the next position, which was followed by swarm stagnation at the current light position until another move of the light source was executed (Table1, Figure 7). No *Artemia* moved into any other direction but along the barrier, thus all Artemia, those swarm-bound and those individually moving stayed within the continuous light gradient.

In summary, we observed obvious differences in *Artemia* swarm-organization within a maze vs. along a continuous barrier. In the maze it is difficult to predict the light gradient. *Artemia* were not able to distinguish between pathways and dead-ends and were not able to choose the more efficient path at obstacles with two alternative pathways. Within a maze consisting of separate and spatially independent barriers swarms tend to disintegrate into smaller groups. In contrast, the swarm moving along a single barrier and within a continuous and highly predictable light gradient stayed intact.

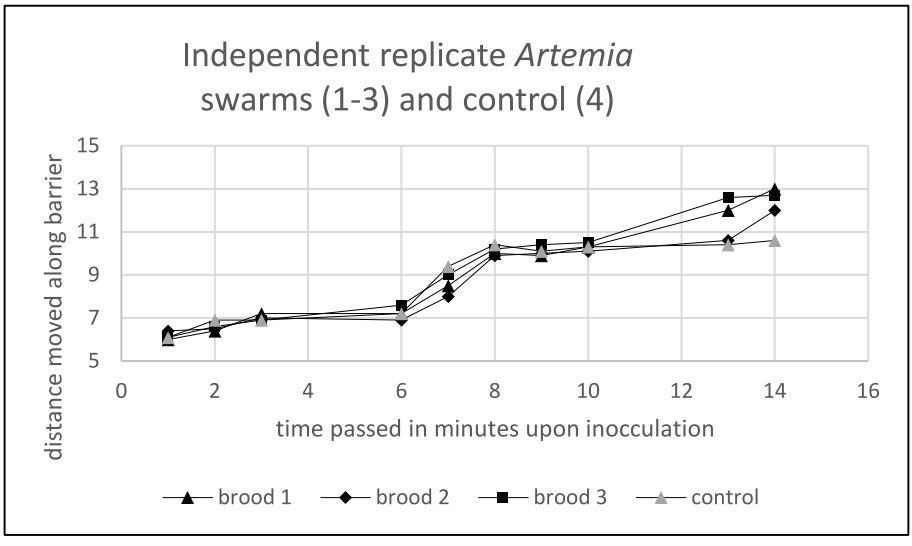

Figure 7: Movement of *A. franciscana* nauplii swarms in response to light switches from 1st to 2nd to 3rd light position

Even though when the swarm ("control 4") in experiment 3 was arrested at position 10:00, individual *Artemia* continued to move along the barrier and towards the edge of the barrier (Figure 7).

Discussion

Experiment 1: In response to switching the directional light conditions from the left to the right and vice versa, *Artemia* nauplii showed *non-random movement, significantly more nauplii moved towards the light than away from the light*. In contrast, we observed non-signifcant differences in the passing-rates of *Artemia* nauplii at each of the two simultaneous lights at opposite sides, left vs. right. *We must assume random movements.* The first experiment confirms that directional light results in directional swarming while non directional light causes random movement. This is in line with other studies that also applied directional vs. uniform light in a vertical set-up [16]

The nauplii swarm quickly responding to changes in light conditions, when unidirectional light is switched from the left to the right and vice versa they move with comparable speed into the new direction, and reverse direction immediately. Likewise a switch from the unidirectional light to a two-directional light arrangement quickly becomes random

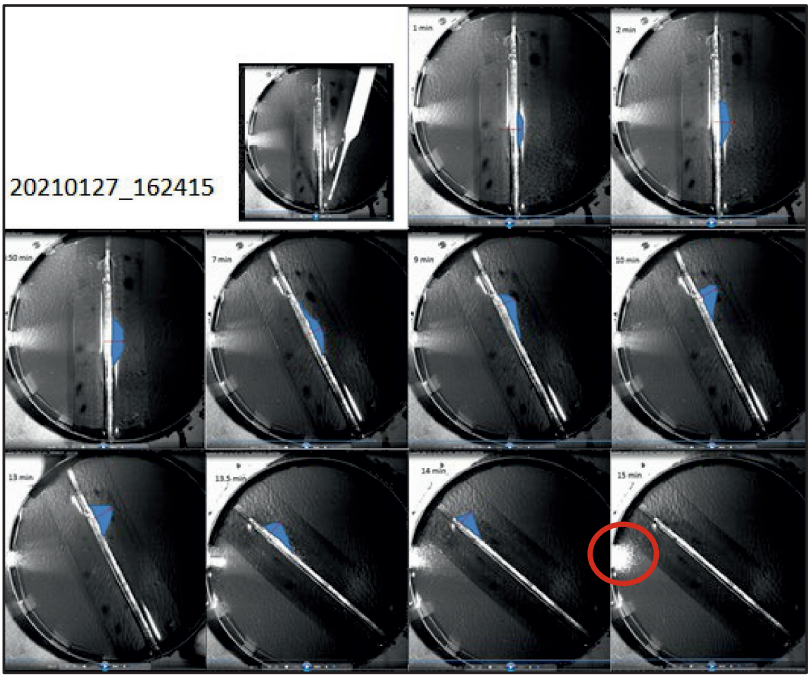

Figure 8: Petridish with three entry points of a standardized light source. *Artemia nauplii* are placed at the bottom right of the barrier, and the swarm forms and moves with the light gradient along the glass barrier to the light in position 9:00 (phase 1, 0-5 min), followed by phase 2 (5 -10:00 min) upon a move of the light source to position 10:00 and further to position 3 (11:00). The swarm moves with the changing light position along the barrier until all individuals within the swarm moved all the way to the far end of the barrier, spilling over the edge, and accumulate at the actual light source. After a total of 14-15 minutes, all *Artemia* form a tight swarm around the actual light source (see red circle around a bright glowing swarm). The swarm itself seems to „slow down“at every light position and „pauses in place“ until the light source is moved to the next position. In the “control” experiment, we did not move the light source from position 10:00 to position 11:00, the swarm remained at the 10 min light source position, but individual *Artemia* nauplii did move along the barrier and around the barrier however, a few more minutes passed before all *Artemia* had gathered again as a swarm at the light at position 10:00, approximately after the 17th minute.

around each of the two local light, yet light maintained an associated local swarm with a steam of Artemia moving between the swarms. This pattern supports observations in nature when large swarms form vertically or horizontally aggregates which are composed of several denser aggregations thinly connected with each other by thin

bands of commuting individuals [1].

The fact that Instar I nauplii at that developmental stage are supported by yolk food may support the extremely enduring activity level observed. When nauplii hatch from a metabolically inactive cyst-eggs, they have dormant rested in dried-up mud, or salt-crystal crusts, or in sand mixed with rocks, etc... all dried up for lack of precipitation. When precipitation returns, and water accumulates, hatching is the response

The cysts hydrates and the arrested embryo resumes to metabolize. Two days later, the cyst's membrane breaks open and an embryo appears which needs a few hours more to develop into the instar I nauplius. It will immediately be capable of free swimming. It is equipped with a red nauplius eye in the head region and it has three pairs of appendages (sensory antennae and locomotive antenna) but the instar I nauplii do not immediately take up food, the digestive system is not functional yet. It lives off its yolk reserves. While its appendages further develop into soon-needed plankton-filters and food-ingestion tools the most important step to survive is to seek the surface, where plankton resides. With the yolk sack still there the young *Artemia* is negatively buoyant and will have to actively swim there. If upon hatching they encounter a homogeneous water body they will sense the direction to the surface easily, their single eye guides them and they are good swimmers. If there are other nauplii around, it is beneficial to join into groups as movement is energetically more efficient in a group, especially for small animals. Aside from following the light they will align with others, looking out to avoid collisions. A vertical swarm forms.

Once they reach the surface they should maintain this position and start being preoccupied with sensing particles at the surface, possibly something they can see with their eyes, maybe by recognizing promising spectra as a proxy. Horizontal movement could be important now to move between food rich patches and once there, resume vertical swarming.

Vertical swarming potentially supports efficient feeding. From my casual observations of the patterns within the swarms, I noticed that within swarms some kind of convections cells form. Some nauplii move to the light thus surface and others volunteer to move away from the light and thus downwards. The whole pattern resembles a close loop conveyer-belt. Food particles could be collected that way and passed through the swarm but also be moved from the outside of the swarm into the swarm. A great benefit would also be the circulation of water from the outside into the swarm to replenish oxygen.

Experiment 2: The second experiment showed that *Artemia* nauplii are capable of following obstructed light gradients within a straight channel if the obstacles are transparent but not when the obstacles are opaque, thus blocking the light and creating patterns of shade. We also showed in experiments 2 that nauplii have no sense for very small differences in light. Nevertheless, all *Artemia* that, in experiment 2, passed the first obstacle in the transparent maze arrived eventually at the light source. The question

again is how does a within-a-maze behavior in the lab reflect genetically based behavior of nauplii in their natural environment? Is there a maze-challenge at the edge of dry ponds or lakes in the process of filling up with water? There is.

When a Salt Lake or a commercial salt pond dries up, the surface is a tangle of salt crystals, mud, small rocks. The cysts that develop into a hatching Instar I nauplius reside in a maze of structures, now increasingly covered with rain water or flood water. What are the environmental cues to guide the hatching nauplii? Again there is a light gradient to follow, but not a very uniform one. First the nauplii need to navigate through the debris and the salt crystals. As experiment 2 has shown, this navigation is not a simple swarm path. Instead groups of nauplii may move along each obstacle but each individual must make local decision to maintain an overall path to the light, to the water's surface. Within this obstacle maze they join and leave various smaller aggregations. Eventually most of them will find their way out and reach the open water. This natural maze is a place of scattering, reflection, shading and darkness, so we would not expect dense uniformly moving swarms to follow it. It has been shown that individual nauplii can be attracted to each other part-time and at random, joining and leaving groups [17].

Experiment 3 has shown that nauplii will master a barrier within a coherent swarm as long as there is a clear light gradient that is maintained. The resulting movement is very efficient, the swarm moves as a unit and fast. However, we have also seen that the loss of the light gradient does not mean that nauplii just move totally randomly in all direction. While individuals do move out of the swarm, they eventually find the way in the correct direction. In experiment 3 they all found the gap followed by a very direct swift swim to the light source. All *Artemia* ended up at the light source it just took a bit longer to get there.

In their natural environment feeding at the surface *Artemia* can be exposed to dangerously high levels of radiation. As scattered as natural *Artemia* populations are across the planet, their preferred lakes and ponds are in areas with intense solar radiation. Deadly UV-B must be avoided. Joining dense horizontal swarms may be beneficial again. Light can be an attraction and repulsion. UV-B are not directly sensed, but UVA levels are proportional to the intensity of UV-B. Measuring UVA is a proxy for truly damaging radiation that has been discovered in many terrestrial and marine organisms from phototrophic bacteria [18] to eukaryotic algae [19] and planktonic larger animals [20].

4. Conclusions

Much more work could be invested in understanding *Artemia* behaviour in their natural environments or in artificial salt ponds. Studying the indoor models will instruct us about the potential and the variety in swarming, grouping, and individual behaviors. Likewise studying them in the lab will help us to improve *Artemia* production for a

sustainable aquaculture with a circular feed-production of Artemia and for enhancing bio-incapsulating methods used to transfer medications and supplements directly into the target species body rather than distributing these substances in the surrounding water from where they easily may move into natural habitats, potentially doing harm. *Artemia* are definitely worth more research in both: basic ecology and evolution studies and in applied research alike.

We are planning to further analyze our data collected in the three experiments described here. The follow up analysis is to look at individual's movement within the experimental treatments. What are the algorithm behind the movements and behaviors? What are the rules for swarming, for random grouping or for individual actions in Artemia?

5. Acknowledgements

The authors, Claudia Kruschel and Tobias Seidl, want to thank the DAAD, German Academic Exchange Service, for the opportunity to work together on our first biomimetic research project.

Many follow up questions remain and new questions have emerged, a good reasons to continue. We are happy to be able to, again, rely on the support and collaboration with colleagues at the Technical University in Fulda (Jonas Jaeger and team) which for years have suppported Kruschel and Schultz at the UniZD with fish tracking, habitat recognition, species identification and other vision-based IT and co-authored papers for this conference.

6. References

1. Van Stappen, G. (1996) Introduction, biology and ecology of Artemia, in *Manual on the production and use of live food for aquaculture*, vol. 361, P. Lavens and P. Sorgeloos, Eds. Rome, Italy: FAO, 1996, pp. 79–106. 1996
2. Gulbrandsen, I. (2001) Artemia Swarming--Mechanisms and Suggested Reasons". Journal of Plankton Research 23(7):659-669
3. Turky, R.M., Frasca, M., Ali, A.A., Ali, R.S., Fortuna, L., Xibilia, M.G., (2012) Artemia swarm dynamics and path tracking, Nonlinear Dynamics", Springer, 68, 4, 555-563
4. Turky, R.M., Frasca, M., Ali, A.A., Ali, R.S., Fortuna, L., Xibilia, M.G., (2012), Nonlinear model identification for Artemia population motion, Nonlinear Dynamics, Springer, 69, 2237–2243
5. Andrew, S., Brierley, M., Cox, J. (2010) Shapes of Krill Swarms and Fish Schools Emerge as Aggregation Members Avoid Predators and Access Oxygen". Current Biology, 20 (19), 1758-1762
6. Lee, J. M., Park, J.S. (2020) Tolerance at the genetic level of the brine shrimp *Artemia salina* to a wide range of salinity, Research Square. DOI: https://doi.org/10.21203/rs.3.rs-91049/v1
7. Gajardo, G., Beardmore, J. (2012) The Brine Shrimp Artemia: Adapted to Critical Life Conditions Frontiers in Physiology. 3, p.185, URL=https://www.frontiersin.org/article/10.3389/fphys.2012.00185
8. Varó, I., Taylor, A.C., Amat, F. (1993) Comparative study of the effects of temperature, salinity and oxygen tension on the rates of oxygen consumption of nauplii of different strains of *Artemia§" Marine Biology* 117**,** 623–628, 1993. https://doi.org/10.1007/BF00349774
9. Léger, P., Bengtson, D.A., Simpson, K.L., Sorgeloos, P. (1986) The use and nutritional value of

Artemia as a food source". In: Barnes M. (Ed.), Marine Biology and Oceanography: An Annual Review, Vol. 24. Aberdeen Univ. Press: 521-623.
10. Van Stappen G. (2002) Zoogeography. In: Abatzopoulos T.J., Beardmore, J.A., Clegg J.S., Sorgeloos P. (eds) Artemia: Basic and Applied Biology. "Biology of Aquatic Organisms", Vol. 1. Springer, Dordrecht. https://doi.org/10.1007/978-94-017-0791-6_4
11. Milinski.,M. (1984) A predator's costs of overcoming the confusion-effect of swarming prey" Animal Behaviour, 32 (4) 1157-1162. https://doi.org/10.1016/S0003-3472(84)80232-8.
12. Abatzopoulos, T., Kappas, I., Bossier, P., Sorgeloos, P., Beardmore, J.A. (2002) Genetic characterization of Artemia tibetiana (Crustacea: Anostraca)". Biological Journal of the Linnean Society. 75 (3), 333-344
13. Marras, S., Killen, S.S., Lindström, J. (2015) Fish swimming in schools save energy regardless of their spatial position". *Behav Ecol Sociobiol* 69, 219–226, https://doi.org/10.1007/s00265-014-1834
14. Ritz, D., Foster, E., Swadling, K. (2001) Benefits of swarming: Mysids in larger swarms save energy". *Journal of the Marine Biological Association of the UK, 81*(3), 543-544. doi:10.1017/S0025315401004210
15. Andrew, S., Brierley, M., Cox, J. (2010) Shapes of Krill Swarms and Fish Schools Emerge as Aggregation Members Avoid Predators and Access Oxygen, Current Biology, 20 (19), 1758-1762
16. Ali, A.A., Fortuna, L., Frasca, M., Rashid, M.T., Xibilia, M.G. (2011) Complexity in a population of Artemia" Chaos, Solitons & Fractals.44 (4–5) 306-316
17. Hinz, R.C., Gonzalo G. de Polavieja (2017) Ontogeny of collective behavior reveals a simple attraction rule" PNAS 114 (9) 2295-2300, https://doi.org/10.1073/pnas.1616926114
18. Kruschel, C. Castenholz, R. W. (1998) The effect of solar UV and visible irradiance on the vertical movements of cyanobacteria in microbial mats of hypersaline waters" FEMS *microbiology, ecology,* 27 (1), 53-72, doi:10.1111/j.1574-6941.1998.tb00525.x
19. Sinha, R.P., Klisch, M., Gröniger, A., Häder, D.P. (1998) Ultraviolet-absorbing/screening substances in cyanobacteria, phytoplankton and macroalgae, Journal of photochemistry and photobiology B: biology 47, 83–94
20. Leech, D.M., Padeletti, A., Craig E. Williamson, (2005) Zooplankton behavioral responses to solar UV radiation vary within and among lakes" *Journal of Plankton Research*, 27 (5), 461–471, https://doi.org/10.1093/plankt/fbi020

ISSN 0554-6397
Pregledni članak
(*Review article*)

Lidija Runko Luttenberger
E-mail: lidija.luttenberger@uniri.hr
School of Polytechnics of the University of Rijeka, Sveučilišna avenija 4, 51000 Rijeka
Merica Slišković
E-mail: merica@pfst.hr
Faculty of Maritime Studies of the University of Split, Ruđera Boškovića 37, 21000 Split
Ivica Ančić
E-mail: ivica.ancic@uniri.hr
School of Polytechnics of the University of Rijeka, Sveučilišna avenija 4, 51000 Rijeka
Helena Ukić Boljat
E-mail: hukic@pfst.hr
Faculty of Maritime Studies of the University of Split, Ruđera Boškovića 37, 21000 Split

Environmental Impact of Underwater Noise

Abstract

The description of sound as a form of energetic pollutant is very complex as is also its impact on aquatic life. Human activities causing continuous and implosive underwater noise, such as marine traffic, maintenance of ships, coastal tourism, marine research, military, offshore energy platforms, generation of ocean energies and construction operations are expected to increase. The paper analyses current approach to minimise the impact of underwater noise and limit its emissions, examines regulatory approach and discusses the possibilities to control this type of pollution in order to ensure the preservation of natural underwater soundscape. The timely implementation and further development of the European Marine Strategy Framework Directive and its provisions related to underwater noise is of exceptional importance for the Adriatic Sea, which is facing increasing pressure from various industries generating underwater noise.

Keywords: underwater noise, anthropogenic activities, soundscape, Marine Strategy Framework Directive

1. Introduction

Modern research into underwater acoustics began in the 19th century, when the speed of sound was calculated to be 1435 m/s, which is only 3 meters below today's accepted values. The experiment showed that a small amount of energy can travel great distances without dissipating significantly [1]. Because the release of noise

into the marine environment is a non-material discharge, it is unfortunately less comprehensively and systematically regulated in international and national law than "classical" impacts such as fishing, shipping, or physical-chemical pollution. The major obstacle is the current knowledge gap. Underwater noise generated by various activities could as well be considered as inefficiency or wasted energy [2].

One of the most significant international events in which noise pollution of the marine environment from underwater or anthropogenic noise received increased attention was the stranding of whales on the Greek coast in 1996. It also pointed to the regulatory challenges posed by the presence of a transboundary pollutant in the international arena, given that the sonar, the source, was owned by the U.S. government, the vessel was owned by 16 nations of NATO and was German flagged, while the experiment was conducted in Greek waters. Public perception of low-frequency sonars was also affected by demise of the Cold War [1].

The article introduces the physical characteristics of underwater noise, analyses the ocean soundscape and its effects, examines the regulatory approach as well as various measures to control underwater noise, and discusses the limits and possibilities to control this type of pollution and ensure the preservation of natural underwater soundscape.

2. Definitions and physical characteristics of underwater sound

Sound as defined by International Standardization Organization constitutes the alteration in pressure, stress or material displacement propagated via the action of elastic stresses in an elastic medium and that involves local compression and expansion of the medium, or the superposition of such propagated alterations. The scientific meaning of sound therefore has no judgemental connotation and is strictly confined its physical meaning. The acoustic environment represents the sound at the receiver from all sound sources as modified by the environment. In marine acoustics it is currently used synonymously with the term soundscape which, however, in terrestrial acoustics represents a subjective perception, i.e. the acoustic environment as perceived by the listener [3]. Ambient sound is the sound that would be present in the absence of a specified activity. Ambient sound includes ambient noise [4].

Sound is thus a vibration that travels as a wave by causing pressure changes in a fluid. While light and chemical cues are effective at small spatial scales only, sounds travel fast through water and are capable of conveying significant information over considerable distances. Given that sound transmission in seawater is almost five times that in the air and the generally limited transparency of marine waters, marine species use sounds for numerous different functional processes. The sounds in marine habitats are thus fundamental for the life cycle of marine animals [5].

The lower the frequency of sound, the further it can travel in the ocean. Low frequency sound (below 1000 Hz) can travel thousands of kilometres and interfere

with the communication and navigation of many marine mammals. In addition, seawater has a frequency-dependent absorption coefficient, so low-frequency sounds remain perceptible at great distances from the source compared to the overall acoustic environment. Underwater sound is also affected by the properties of the interface such as depth, structure, and composition of the seabed [3].

The unit decibel (dB) does not represent a physical metric, but simply indicates that the preceding number is proportional to the decimal logarithm of the ratio between the property and the reference value. The standard reference pressure for ocean sounds is 1 micro-Pascal (1μPa), while the standard reference pressure for air sounds is 20 micro-Pascals (20 μPa). Therefore, the loudness of an underwater sonar cannot be directly compared to that of a jumbo jet. The perception of sound by different species of animals must also be considered. In addition, there is no clear correlation between the sound level in the air that is harmful to a human and that which is harmful to an animal in the water. In addition, the nature of noise in water is a multi-source [1].

3. Soundscapes

Soundscape is the characterization of the ambient sound in terms of its spatial, temporal, and frequency attributes, and the types of sources contributing to the sound field [4]. It represents the sum of sounds in particular area. Soundscapes are changing rapidly as the number of sound-producing animals decreases, human-induced noise increases, and the contributions of geophysical sources such as sea ice and storms change due to climate change. As a result, the sound of the Anthropocene ocean is fundamentally different from that of the pre-industrial era, with anthropogenic noise having a negative impact on marine life. Indeed, marine animals have evolved a variety of receptors to perceive sound, which have been well studied for marine mammals but only recently described for invertebrates such as jellyfish [6]. Unfortunately, the acoustic behaviour of most fish species remains unknown. On the other hand, sounds produced by snapping shrimp have been shown to cause bottlenose dolphins to change the frequency of their echolocation clicks to be outside the band of snapping shrimp. Marine mammals produce sounds to communicate, navigate, and detect underwater objects. They are known to communicate the presence of food, danger, or other animals, as well as information about their identity, location, or reproductive status. Echolocation allows animals to see underwater, hunt and characterise prey, locate and avoid obstacles, and move easily through ocean terrain [1].

Shipping contributes to background noise in the ocean. The frequency content of ship noise overlaps significantly with the hearing ranges of marine fauna. Although the propagation of ship noise is lower in shallow coastal waters, the higher concentration of ships often increases noise levels in coastal regions significantly above ambient noise levels [6].

Man-made ocean sounds include seismic surveys, which produce high-energy,

low-frequency sounds of short duration to detect oil and gas deposits on the seafloor, and multibeam echosounders and side-scan sonars, which generally produce high-frequency sounds to map the seafloor and detect organisms and particles in the water column.Scientific surveying uses similar instruments to map the seabed and identify geological features. Fishermen use fish finders for fishing, while the navies use active sonars over a range of frequencies to detect submarines and other targets. In addition, there are the by-products of different human acttivities regarding coastal development and resource extraction, traffic on bridges and aircraft flying at low altitudes over the sea, pile driving during the construction of offshore wind farms, operating noise from turbines, dynamic positioning systems used to maintain the position of offshore structures, dredging of the seafloor, mineral extraction, trawling, dynamite fishing still practised in some parts of the world, controlled detonation of bombs, explosion of mines, missiles and bombs during naval warfare or military exercises, and fireworks, which also constitute a source of destructive sound [6,7].

In addition, various construction activities on land, such as dock building, can cause marine noise, although their effects depend on how well the land and sea media are coupled, which has not yet been adequately researched [1].

Areal drones and coastal recreational activities contribute anthrophony to marine soundscapes, see also [8]. Recreational vessels contribute the most to a shallow water soundscape as corroborated by a study of noise pollution from recreational boats compared to other vessels [9]. The authors showed that in shallow coastal areas, noise in the one-third octave bands at 0.125, 2, and 16 kHz is mainly caused by motorised recreational boats, without AIS. Additional source of noise from recreational boating are jet skis, small motorised watercraft propelled by water jets, which are usually present near shore. This can be a problem because these areas are often heavily inhabited by organisms [1]. Nautical tourism in the Mediterranean as a tourist hotspot remains a growing concern [10]. During the summer season, a significant increase in noise levels can be observed in the Adriatic Sea. The measuring site, which is quiet and peaceful outside the tourist season, is polluted by the large number of recreational boats, which peaks in the period of July-August [11].

In addition to fish finders and echo sounders, the fishing and aquaculture industry also uses acoustic deterrent devices that generate noise to keep marine mammals away from fishing gear and aquaculture cages [1].

To monitor changes in ocean temperature, low-frequency sonars, i.e., acoustic thermometry, are used [1]. One of the most important effects of climate change is the increase in ocean temperature and, consequently, sound, which travels faster in a warmer ocean. Ocean acidification, i.e., lowering pH, also alters sound propagation by reducing sound absorption for frequencies below 10 kHz [6].

High number of noise-producing human activities is located in the Adriatic [12]. Besides shipping, tourism and other noise-generating sectors and despite the climate change targets agreed in Paris Agreement, there is still a large industrial demand for energy from fossil fuels. In the last decade, the extent of seismic investigations has

increased, especially in the Adriatic Sea area [10].

Covid-19 control strategies have also led to an unusual expansion of marine mammal and shark movements in formerly busy and noisy waters such as harbours and urban coastal areas where they are not regularly seen. On the other hand, there is an increasing focus on ocean-based economy which includes industries that may be major sources of underwater noise. However, the High Level Panel for a Sustainable Ocean Economy has not considered anthropogenic noise in addressing the actions required to achieve Sustainable Development Goal (SDG) 14: Life Below Water [6].

There are no long-term (more than 10 years), systematically collected ocean acoustic data for any frequency band. In addition, there are very few data outside the Northern Hemisphere, no data have been collected in biologically sensitive areas for specific species, and there are few data for frequencies above several kilohertz [1].

4. Effects

Duarte et al [6] synthesised the negative effects of noise pollution on marine animals in the literature. Anthropogenic underwater noise can have detrimental effects on marine biodiversity. Effects include physical damage to auditory organs, injury to other body tissues, death of individual specimens, behavioural changes, chronic/cumulative effects, and stress [3,10,13]. Recent research revealed negative effects of seismic surveys on zooplankton, which, along with phytoplankton, form the basis of the marine food web on which fish and other marine animals depend [10]. The contribution of individual species to the overall health of the ecosystem is fundamental to the concept of the marine food chain. If noise affects the reproduction or viability of one prey species, all species above it in the food chain may be affected, so noise can have a negative impact on the entire ecosystem. Noise could be a source of overall habitat degradation [1]. The full extent of seismic impacts on populations is largely unknown, in part due to the lack of baseline knowledge of species abundance and distribution. Potentially the most serious effect of low-level sound is sound masking (covering up one sound by another).

The health risks that underwater sound poses to marine mammals are similar for divers and swimmers. These effects can range from nonexistent to life-threatening, including temporary and permanent changes in hearing sensitivity (threshold shifts), resonance in air-filled cavities (including lungs, sinuses, and airways), disorientation, and acoustic annoyance [1].

5. Regulation

Although there is no international legal instrument that specifically and exclusively addresses underwater noise, the precautionary principle undoubtedly provides legislators with a framework for action. Regulatory frameworks for underwater noise have mostly

been developed in the form of soft law standards, meaning that they are not legally binding and are therefore difficult to enforce. Guidelines and best practices, on the other hand, are easily modifiable and can be adapted to new developments. Updating is often left to the relevant expert bodies rather than international conferences or national legislators, which means it is quicker and less complicated [2].

In the United Nations Convention Convention on the Law of the Sea (UNCLOS), Article 1(1)(4) states that "Pollution of the marine environment means the introduction by man, directly or indirectly, of any substance or energy into the marine environment..." Article 206 contains a provision requiring an assessment of the potential impact of activities that may cause significant pollution. It requires an assessment of planned activities before they begin. It contributes to a comprehensive environmental management system. Article 65 relates directly to marine mammals and requires States to cooperate. All these provisions provide a framework for the development of international regulation of underwater sound.

The IMO has issued the Guidelines for the Reduction of Underwater Noise from commercial shipping to address the negative impacts on marine life [14]. The 2018 submission on IMO's work on anthropogenic underwater noise states that the issue of underwater noise and its impact on marine life is also addressed through the Particularly Sensitive Sea Areas (PSSAs) adopted by IMO. It also notes that the issue of noise has been discussed in the context of the work of the London Convention and the Protocol on the Protection of the Marine Environment from Pollution by Dumping of Wastes and Other Matter, noting that dredging, which is the main source of waste discharged into the sea under these treaties, is also a source of anthropogenic noise [15].

Two other conventions could also serve as forums where protection from underwater noise arises from their general obligations, namely the Convention on Migratory Species (CMS) and the Convention on Biological Diversity (CBD).

The EU has made a unique effort to protect against underwater noise with the publication of Marine Strategy Framework Directive (MSFD), which develops a common approach among Member States to address underwater noise pollution, see also [16]. To determine good environmental status, 11 qualitative descriptors were defined, with descriptor 11 focusing on energy discharges, including underwater noise. Underwater noise has been formally defined as a pollutant in Article 3(8) of the Directive. Member States are required to cooperate at European and regional level to ensure coherent implementation of the Directive. The criteria and methodological standards were set out in the subsequent Commission Decisions of 2010 and 2017. In the Commission Decision of 2017, two criteria are defined for descriptor 11: The first criterion (D11C1) concerns anthropogenic impulsive sound in water, which is described as follows: The spatial distribution, temporal extent, and levels of anthropogenic impulsive sound sources do not exceed levels that adversely affect population of marine animals; the second criterion (D11C2) concerns anthropogenic low-frequency continuous sound in water, which is described as follows: The spatial distribution, temporal extent and levels of anthropogenic continuous low-frequency sound sources

do not exceed levels that adversely affect the population of marine animals [17].

Several projects and initiatives are addressing the implementation of descriptor 11, and one of the ongoing initiatives entitled Soundscapes in the North Adriatic Sea is funded by EU-INTERREG V-A, Italy-Croatia with lead organization being the Institute of Oceanography and Fisheries, to be completed in 2021. In the Baltic Sea and North-East Atlantic Ocean regions, there is now a joint register for impulsive sound. Efforts are also underway in the Mediterranean Sea and Black Seas to establish a register for impulsive sounds.

In addition to the MSFD, the Habitats Directive, the EIA Directive and the SEA Directive are the main parts of the EU acquis communaitaire dealing with nature conservation and anthropogenic underwater noise. A Maritime Spatial Planning (MSP) Directive also aims at a balanced use of already competitive marine areas.

6. Measures

Compared to other stressors that persist in the environment, anthropogenic noise is typically a point pollutant whose effects diminish rapidly once the sources are removed. When considering ocean noise, all sources of noise must be considered, both random and continuous.

Since shipping is a major contributor to anthropogenic noise pollution of the acoustic environment, priority should be given to finding regulations and technical solutions for this industry. Currently, most ships lack equipment to monitor their acoustic condition. At comparatively low cost, such systems could be integrated into the hull of new ships when they are built, allowing crews to monitor and control their acoustic state [3]. Technological improvements, such as the use of diesel-electric systems, have had a major impact on reducing noise from ships. Also, larger ships have a greater draft, so there is less cavitation from the propellers [1]. A recent study compared sound level measurements of container ships before and after modifications to improve energy efficiency. The modifications included replacing the bulbous bow, lowering the main engines for slow steaming and installing new propellers with boss caps fins to reduce cavitation. The estimated underwater source sound pressure levels of the five vessels were lower by a median of 6 dB in the 8-100 Hz frequency band and a median of 8 dB in the 10-1000 Hz frequency band for the retrofitted vessels [18]. Four-stroke engines have resulted in significantly quieter vessels. Regarding recreational boating, if we compare newer engines with those which are built in a past few years, newer engines for leisure boats are reportedly nearly 70 percent quieter. Noise reduction could be achieved by using new noise suppressing materials, redesigning the intake/exhaust system, and isolation of the engine drive train. In fact, it is not yet known how much underwater noise is actually reduced since some of the noise reduction is achieved by moving the exhaust system from above the waterline to below the waterline. In addition, noise reduction technology for vessels registered

under flags of convenience is costly and may be difficult to implement. Additional cost of reducing noise emissions would hit flag states with large merchant fleets, such as Panama or Liberia, hard. To date, the shipping industry has generally paid little attention to the problem of noise pollution at sea [1].

Other applicable measures include regulating speeds and routes, targeting 15% of ships that generate half of the total noise emitted by the shipping fleet, noise-dampening technology for ship structures, and alternative technologies for seismic air guns (vibroseis) [6].

A promising approach to prevent noise pollution is the determination of environmental capacity. In addition, an important ex-ante tool is environmental impact assessment [19], which provides a basis for decision-making, offers a comprehensive information and opinion platform, takes into account externalities and alternatives to proposed projects when properly conducted, and involves the public.

In matters of underwater noise, it is important to apply the best available technology (BAT), at least the best practicable technology (BPT), which takes into account technology costs, or preferably the best practicable environmental option (BPEO), which implies that among equally effective techniques, the one that causes the least environmental damage should be used [1].

If spatial components of threats can be defined, marine protected areas (MPAs) are a useful conservation measure. However, their designation is in itself no guarantee that their objectives will be achieved, the world being littered with paper parks, see also [20]. The successful implementation of an MPA depends on biological, ecological, economic, and social factors. Due to conflicts of use, the establishment of protected areas will be increasingly contentious, difficult, and dependent on compromise. For example, regulating tourism and fisheries within MPAs has proven difficult. There is also the problem of protecting a moving target. Buffer zones around MPAs should provide an additional level of security [1].

Zoning is an important component of MPA management plans. In the context of acoustic habitat description and marine spatial planning [21], increasing attention is being paid to mapping soundscapes at national and regional levels. It is important to consider acoustic habitats when determining the sustainable level of industrial use in any area [22].

The framework for risk assessment of problems related to the impact of anthropogenic sound on underwater fauna should be developed in several steps: Hazard identification, dose-response assessment, exposure assessment, risk characterization, and finally risk management, which depends on whether the risk of harm exceeds thresholds set by legislation, societal views, or the biological significance of the impact [7].

7. Conclusion

Underwater noise as a form of pollution is beginning to receive adequate public attention, but still not in the form of globally binding legislation. Addressing underwater noise should focus on habitats rather than on the effects of individual sound sources on individual species. Such an approach requires overcoming sectoral divisions and approaches, i.e. integration and interdisciplinary work, as well as the involvement of various stakeholders such as the fishing industry, oil companies, the military, environmentalists and scientists.

The potential of the blue economy in the seas and oceans poses a particular challenge to marine soundscapes. The timely implementation and further development of the European MSFD and its provisions related to underwater noise is of exceptional importance for the Adriatic Sea, which is facing increasing pressure from various industries generating underwater noise.

8. References

1. McCarthy, E. (2004)*„International Regulation of Underwater Sound: Establishing Rules and Standards to Address Ocean Noise Pollution*, Springer Science and Business Media Inc.
2. Markus, T., Silva Sanchés, P.P.(2018) Managing and Regulating Underwater Noise Pollution. In: Salomon, M. & Markus T. (eds.) *Handbook on Marine Environment Protection*, Springer, pp. 971-996.
3. Boebel, O., Burkhardt, E., Van Opzeeland, I. (2018) Input of Energy/Underwater Sound. In: Salomon, M. & Markus T. (eds.) *Handbook on Marine Environment Protection*, Springer, pp. 463-486
4. International Organization for Standardization (2017) ISO 18405: 2017: *Underwater acoustics – Terminology.*
5. Pieretti, N., Lo Martier, M., Danovaro, R. (2017) Marine soundscape as an additional biodiversity monitoring tool: A case study from the Adriatic Sea (Mediterranean Sea), *Ecological Indicators*. Vol. 83, 13-20. Available from: https://doi.org/10.1016/j.ecolind.2017.07.011 [Accessed 8th August 2021].
6. Duarte, C. et al. (2021) The soundscape of the Anthropocene ocean. *Science.* 371, 6529. Available from: https://www.science.org/doi/10.1126/science.aba4658 [Accessed 5th September 2021].
7. European Science Foundation (2008) *Position Paper 13 – The effects of anthropogenic sound on marine mammals.*
8. United Nations (2018) *Contribution from the Secretariat of the International Whaling Commission to Part 1 of the Report of the United Nations Secretary General on Oceans and Law of the Sea Anthropogenic Underwater Noise*, Available from: https://www.un.org/Depts/los/consultative_process/contributions_19cp/IWC.pdf, accessed 10.08.2021 [Accessed 15th September 2021].
9. Hermannsen, L., Mikkelsen, L., Tougaard, J. et al. (2019) Recreational vessels without Automatic Identification System (AIS) dominate anthropogenic noise contributions to a shallow water soundscape. *Scientific Reports* 9, 15477. Available from: https://doi.org/10.1038/s41598-019-51222-9 [Accessed 8th September 2021].
10. Štrbenac, A. (2017) *Overiew of underwater anthropogenic noise, impats on marine biodiversity and mitigation measures in the south-eastern European part of the Mediterranean, focusing on seismic surveys"*. A report commissioned by OceanCare, Croatia and Switzerland.
11. *Vukadin, P. (2016) Underwater noise monitoring experiences in Croatia, Proceedings of Meetings on Acoustics*, Volume 27, Acoustical Society of America. Available from: https://asa.scitation.org/doi/abs/10.1121/2.0000263 [Accessed 12th September 2021].
12. Maglio, A. et al. (2016) *Overview of the Noise Hotsposts in the ACCOBAMS Area, part I*

– *Mediterranean Sea.* Technical Report, ACCOBAMS. doi: 10.13140/RG.2.1.2574.8560/1 [Accessed 10th September 2021].
13. Gedamke, J. (2016) *Ocean Noise Strategy Roadmap*. NOAA.
14. International Maritime Organization (2014) *Gudielines for the reduction of underwater noise from commercial shipping to address adverse impadts of marine life.* MEPC.1/CIRC.833.
15. International Maritime Organization (2018) *IMO and anthropogenic underwater noise.* Submission on IMO's work on anthropogenic underwater noise to the 2018 nineteenth meeting of the United Nations Open-Ended Informal Consultative Process on Oceans and the Law of the Sea, on „Anthropogenic underwater noise".
16. Runko Luttenberger, L., Slišković, M. (2020) Implementation Challenges for Marine Strategy Framework Directive in the Republic of Croatia. *Pomorski zbornik.* **Special edition No. 3**, 89-102.
17. MSFD Common Implementation Strategy Technical Group on Underwater Noise (TG-NOISE) (2019) *Management and monitoring of underwater noise in European Seas – Overview of main European-funded projects and other releant inititaties".* 2nd Communication Report.
18. Internationbal Maritime Organization (2018) *Further information related to impacts of underwater noise on marine life submitted by International Whaling Commission.* MEPC 72/INF.9.
19. Runko Luttenberger, L., Matić, J., Mihelić, D., Mandić, N. (2020) Environmental impact assessment procedures for projects in marine environment – evaluation analysis*. Pomorstvo: scientific journal of maritime research.* **34** (1), 65-73. Available at: https://doi.org/10.31217/p.34.1.8 [Accessed 5th September 2021].
20. Runko Luttenberger, L., Ančić, I., Luttenberger, A. (2021) The challenges for Croatian fisheries within current regulatory environment*. Pomorstvo : scientific journal of maritime research.* **35** (1), 170-178. Available at: https://doi.org/10.31217/p.35.1.18 [Accessed 18th September 2021].
21. Runko Luttenberger, L., Luttenberger, A. (2014) Challenges of Marine Spatial Planning in Eastern Adriatic. In: Vidan, P. Twrdy, E., Leder, N. & Mulić, R. (eds.) *Book of Proceedings 6th International Maritime Scientific Conference,* Split: Faculty of Maritime Studies Split. pp. 33-40.
22. Haver, S. et al. (2018) Monitoring long-term soudscape trends in U.S. Waters: the NOAA/NPS Ocean Noise Reference Station Network*. Marine Policy.* 90 (2018) 6-13, Available at: https://doi.org/10.1016/j.marpol.2018.01.023 [Accessed 6th September 2021].

ISSN 0554-6397
Prethodno priopćenje
(*Preliminary communication*)

Goran Vizentin
E-mail: vizentin@pfri.hr
Goran Vukelić
E-mail: gvukelic@pfri.hr
University of Rijeka, Faculty of Maritime Studies, Marine Engineering Department, Studentska 2, Rijeka, Croatia

Prolonged Real Marine Environment Exposure of Composite Marine Structures

Abstract

As fiber reinforced polymer (FRP) composites become ever more established construction materials in the marine industry sector the influence of the harsh environmental operational conditions and its consequence on failure prediction of such structures is an imperative. Coupons of epoxy/glass and polyester/glass with various fiber layout configurations have been submerged under the sea for prolonged periods (6 and 12 months) in order to assess the impact on mechanical behavior of the material exposed to real marine environment as opposed to the more commonly adopted artificially produced laboratory sea environment and accelerated testing. Changes in mass, marine microbiology growth, tensile strength and morphological structures were analyzed after submersion and compared with samples exposed to room environment. All coupons have shown mass increase due to seawater absorption and microorganism growth in the organic resins matrices. The dynamic and level of change in tensile strength proved to be dependent on the fiber layout configuration. Optical and scanning electron microscopical investigation performed showed significant matrix morphological changes primarily due to salt crystal formation and the impact of sea microorganisms embedding in the resin. The collected experimental data will be used to develop a more realistic environmental input parameters for structural modeling of marine structures.

Keywords: FRP composites, marine environment, marine structures durability

1. Introduction

Fiber reinforced polymer (FRP) composites are used in the engineering constructions, whether as an exclusive option for construction [1] or as a combination with traditional materials, such as steel concrete [2] or rock [3]. In the last couple of decades, significant effort was made to combine the experimental and scientific

knowledge obtained so far in these field of research to enable prediction models that can be safely used to achieve sustainable and safe design of engineering structures [4–7].

Mechanical properties of composite materials can be customized accordingly to specific applications demands by defining layup sequences, number of plies, and fiber orientation in the load direction [8,9], which makes them appealing for design of marine structures with complex shapes. As the application field for marine composites widens, the request for mechanical and environmental resilience rises. Adequate knowledge of limit stress states, durability and life span, failure modes, fracture toughness, fire resistance, and environment influence parameters is crucial for an efficient and sustainable design process for structures in this demanding industry sector [10,11].

The micromechanical aspect of composite materials design is often considered too complex and time-consuming for marine structural designers to deal with. The scientific research in this field of study should be aimed at simplifying the complex micromechanical level analysis and transform it into simple-to-use and time-saving engineering tools. The current practice for obtaining data for composites failure is based on experiments. As experiments can be relatively expensive and microscale data are usually unavailable to shipbuilders, they often turn to data and models prescribed by rules and procedures, thus leading to empirical based design process of marine structures. All of this yields rules that are very conservative in formulating design requests, which in turn hinders optimal design of marine structures concerning failure mechanisms.

One of the most important parameters influencing the mechanical properties of composite materials in marine applications is the absorption of seawater [12]. Previous research on this matter is based on immersing test samples, called coupons, in laboratory conditions using accelerated procedures [13] to simulate 20+ years of expected lifespan of typical marine structures [14,15]. The ageing of composites is usually carried out in climatic chambers in laboratory conditions to reduce the time of the test [16–19].

In addition, water absorption tests are often done with tap water, demineralized water, or artificial seawater [20,21]. This approach yields a lack of long-term data pertaining to degradation of mechanical properties exposed to the marine environment. Furthermore, the effects of the moving seawater (waves, sea level variations due to tides) and radically variant environmental effects that a typical marine vessel or structure are exposed to during their life cycle [22] are not considered in accelerated ageing laboratory methods.

The absorption process of moisture and water of a composite exhibits complex behavior and dependence on various factors [23], such as resin type and curing characteristics, void content, resin/fiber volume fractions [24], the manufacturing technique, etc., [25–27].

All this served as motivation to concentrate the research presented here on the influence of absorbed water on marine composites in real-life conditions, not laboratory, by submerging the coupons in the sea for prolonged periods of 6 and 12 months.

The dominant choice of composite materials in the civil sector of the marine

vessels industries is glass fiber reinforced plastics (GRP), both for commercial and leisure vessels hulls [28], resulting in a more cost-effective product. Classification societies can be somewhat restrictive when it comes to allowing composites as structural material. The choice of fibers is restricted to E-glass or carbon fibers, whilst resins are limited to epoxy, polyester, or vinyl-ester.

2. Materials and methods

2.1. Materials

The ISO 527 standard series prescribe the testing procedures for the determination of tensile properties of fiber-reinforced plastic composites. In this research, standardized tensile testing coupons were produced as various combinations of continuous glass fibers layout with epoxy (Sicomin SR 8200 and SD 720 series hardener) and polyester resin (Reichhold POLYLITE 507-574) used as matrices. The resins mechanical properties are shown in Table 1, as provided by the manufacturers of each component.

Table 1. Resin systems properties.

Property	**Epoxy**	**Polyester**
Tensile strength [MPa]	47	42
Elasticity modulus [MPa]	3,240	2,700
Glass transition temperature [°C]	50	55

UD stitched E-glass fiber matt fabric (Sicomin UDV600), with 594 g/m^2 ply specific area weight, was used. Four different layup configurations were chosen for both matrix/fiber combinations to evaluate mechanical properties deterioration in the marine environment. The layup schematics are unidirectional with longitudinal fiber orientation (UD0) and two multidirectional (0/90 and 0/45/90 symmetrical), all according to standard notation for composite layup [29].

Rectangular plates (300×450 mm) with the mentioned different layup schemes were produced for each of the material combinations using 8 plies of the UD fabric per plate. The epoxy/glass plates were produced by vacuum assisted infusion process, resulting in 3 + 0.2 mm thick plates. The infusion process proved problematic for the polyester resin as it was resulting in dry fibers on the tool surfaces, so the polyester/glass plates were finally produced by hand layup process, resulting in 5±0.5 mm thick plates.

2.2. Coupons and exposure to marine environment

Coupons measuring 250 mm in length and 25 mm in width [30] were then cut out of the plates on a waterjet cutting machine (OMAX Maxiem series). The cutting

pressure was between 1,400 and 3,400 bar, with the average cutting speed of 1,187 mm/min.

Waterjet cutting takes advantage of the brittleness of composite materials as localized damage points on the locations of first contact of the cutting high-pressure waterjet with the material can be introduced precisely. The intent here is to introduce a point on the coupon in order to simulate real damage on marine structures. This damage point theoretically represents a facilitated entry point of seawater in a real marine structure on eventual damage spots that would occur during exploitation. Composite marine vessels and structures are usually protected by a final layer of gel coat that protects them from water penetration. When this protective layer is damaged during application, a more significant sea water intake rate in the structure material is expected.

All the coupons were weighed dry and measured with a ±0.1 mm accuracy. The coupons were divided in groups of 5 pieces according fiber-matrix combinations (epoxy/glass, polyester/glass) and subdivided into 3 groups according the time of exposure to real marine environment (dry, 6 months, 12 months).The "dry" groups were control ones, while the other two subgroups were exposed to real-life sea environment, i.e., submerged into the sea on a depth of 10 m, at northern Adriatic in front of the city of Rijeka in Croatia for a duration of 6 and 12 months, respectively. The sea temperature at the location of experiment varies between 10–14 °C annually, salinity changes between 37.8–38.3 PPT, while the pH value is between 8.22–8.29 [31]. The coupons were mounted on special stainless-steel frames (AISI 316L).

2.3. Testing procedures

Each coupon was weighed with the same digital scale (200 g measuring range and 0.01 g resolution) as dry and after the submerging time-period to determine the mass gain of the absorbed seawater. Wet coupons were taken out of the sea, cleaned from sea organisms accumulated during submersion with a soft brush, still submerged in seawater. Special care was taken not to damage the coupon. After cleaning, the coupons were left to drain, dried superficially with a cloth, and weighed all in a period under one minute to assure maximal possible measuring of the absorbed water amount.

The coupon ends were reinforced using end tabs before the tensile test to minimize the influence of the grips pressure on the test results [32]. The size of the tabs was chosen based on ISO 527-4 recommendations.

Uniaxial tensile tests used for the determination of the material properties were performed on a Zwick 400 kN universal testing machine. A macro extensometer was used to measure the specimens' elongation. The displacement rate of the testing machine crosshead during testing was 2 mm/min.

Tensile testing was conducted in accordance with ISO 527 series standards recommendations.

Microscopical investigation was performed on all fractured coupons. Surface and

cross-sectional images were taken of all coupons, with special attention given to the grips areas and locations with observed damage after the tensile test

Optical microscopy systems (Olympus SZX10 stereo optical microscope and Olympus BX51 SM optical microscope analysis system, both produced by Olympus corporation, Japan) and scanning electron microscope (SEM, FEI QUANTA 250 FEG, FEI Company, USA) with the OXFORD INSTRUMENTS PENTAFET, UK, Energy Dispersive Spectroscopy (EDS) analysis module were used to investigate the state of the coupon's surfaces exposed to real sea environment and to identify changes in surface morphology caused by the exposure to seawater. Photographs were taken before and after the tensile tests.

3. Results

The results of the experimental investigation of epoxy/glass and polyester/glass coupons exposed to marine environment are presented in the form of diagrams, images, and tables. Experimental testing results shown here are comprised of coupon weight change (seawater absorption, algae growth) analysis, tensile strength determination, and surface morphology changes observations.

3.1. Mass gain - algae and marine organisms' growth and water intake

The average aggregate mass gain due to the coupled algae/marine organisms' growth and water absorption and only water absorption for the two matrix resins is given in Figure 1, where the denotations E and PE stand for epoxy and polyester resin respectively, while the numbers 6 and 12 indicate the period of submersion in months.

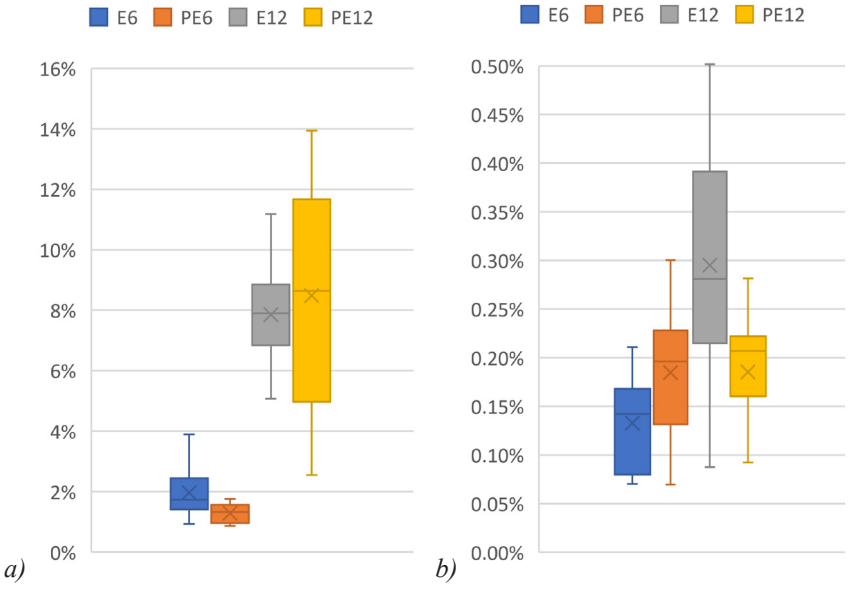

Figure 1: Mass gain due (a) bio growth and water absorption; (b) only water absorption.

3.2. Tensile test results

Engineering stress-strain diagrams were obtained from performed uniaxial tensile strength on dry coupons and wet coupons that were submerged in the sea for 6 and 12 months. The change in tensile strength due to the prolonged submersion in seawater is shown in Figures 2 and 3.

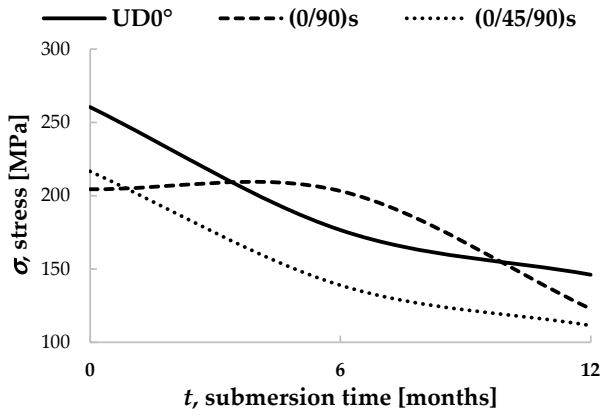

Figure 2: Average tensile strength degradation of epoxy resin coupons

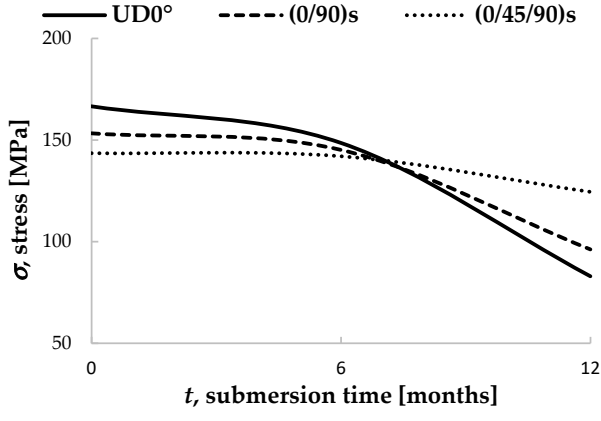

Figure 3: Average tensile strength degradation of polyester resin coupons.

3.3 Microscopical investigation

Surface and cross-sectional images obtained by optical microscopy are not presented here but are available in a publicly accessible repository to save paper space and keep the readers focus on the more detailed and more illustrative SEM results.

The images obtained by SEM investigation are presented in Figures 4 to 6. Only some representative images were chosen as a portrayal of the performed research to limit the length of the paper, whilst the complete set of all obtained images is posted on an online repository as supplementary material to this article.

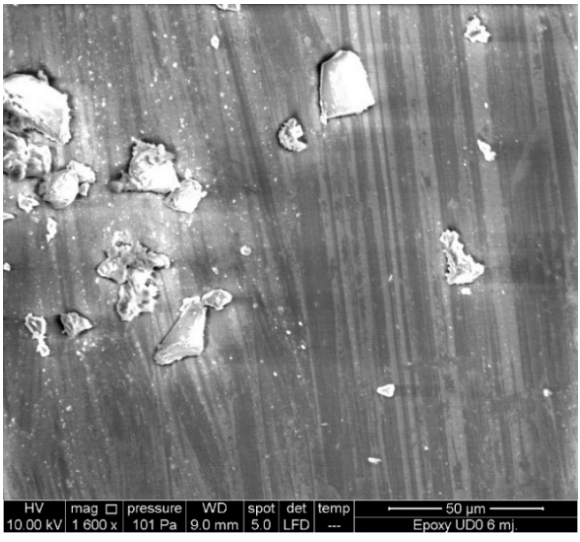

Figure 4: Epoxy coupons, salt crystals

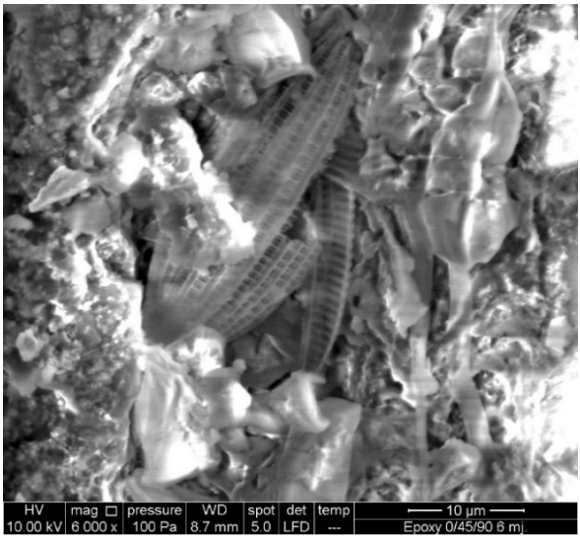

Figure 5: Epoxy coupons embeded microbes.

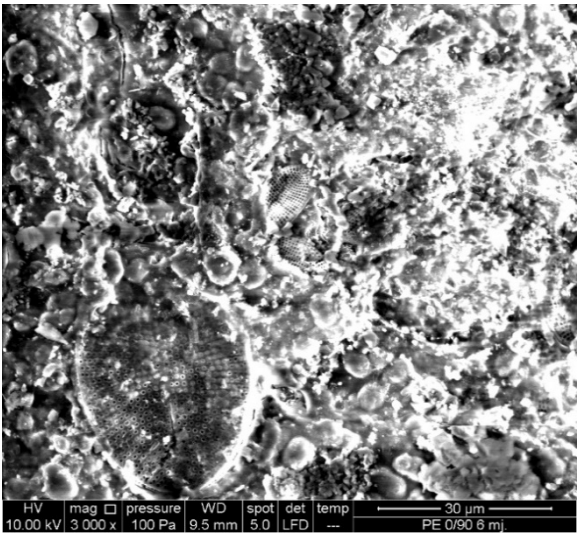

Figure 6: Polyester coupons - embeded microbes

4. Conclusions

The real sea environment has considerable effects on composite materials in the form of reduced mechanical strength for the tested coupons submerged in the sea. The submerged UD0, 0/90, and 0/45/90 epoxy/glass coupons exhibited tensile strength reduction of 32%, 14%, and 36% after 6 months of submersion (with the exception of one inadequately manufactured 0/90 coupon), whilst 44%, 40%, and 49% after 12 months of submersion, respectively. The polyester/glass UD0, 0/90, and 0/45/90 coupons have lost 11%, 5%, and 1% after 6 months of submersion, and 50%, 37%, and 13% after 12 months in the sea. The 0/45/90 layout configuration for the polyester/glass combination showed the greatest resilience to the marine environment. The research indicated that further study is needed here because the polyester coupons were made by hand-layup process, which can significantly affect mechanical characteristics of the composite. This issue will be examined more in detail during future research.

The growth of microorganisms embedded in the resin and invertebrate (Nematoda) organism attached to the surface of the coupons effectively created voids in the matrix resin and produced a direct effect on mechanical properties. The mechanism of this effects needs deeper analysis and research. The findings of the research indicate the importance of biofouling in environmental degradation of mechanical properties of composite materials in the marine environment. The main goal of this research remains the development of a reliable predictive numerical model of the mechanical behavior of composite materials exposed to real sea environment, which would represent a basic

tool to assess the durability of composite marine structures during their exploitation. Research findings can be useful in design process of composite marine structures or in use of composite for repair of already damaged structures [33,34]. In order to fully understand the effect of exposure effect on the composites, additional coupons are already submerged in the sea and data should be presented in the continuation of this paper. This additional set of data will help in building a predictive numerical model that could successfully replace the time and resource consuming experiments which is a next step of this research However, the stochastic nature of the environmental loading must be incorporated in that model [35]. For that reason, placing coupons in different types of marine environment (regarding the temperature, salinity, pH value, etc.) would bring even better accuracy of the numerical model.

5. References

1. Andreazza, I. et al. (2020) 'Flexural fatigue behaviour of an asymmetric sandwich composite made of limestone and cork agglomerate', International Journal of Fatigue, 130, p. 105264. doi: 10.1016/j.ijfatigue.2019.105264.
2. Belingardi, G., Paolino, D. S. and Koricho, E. G. (2011) 'Investigation of influence of tab types on tensile strength of E-glass/epoxy fiber einforced composite materials', Procedia Engineering, 10, pp. 3279–3284. doi: 10.1016/j.proeng.2011.04.541.
3. Bian, L. et al. (2012) 'Effects of seawater immersion on water absorption and mechanical properties of GFRP composites', Journal of Composite Materials, 46(25), pp. 3151–3162. doi: 10.1177/0021998312436992.
4. Bond, D. A. (2005) 'Moisture diffusion in a fiber-reinforced composite: Part I - Non-Fickian transport and the effect of fiber spatial distribution', Journal of Composite Materials, 39(23), pp. 2113–2142. doi: 10.1177/0021998305052030.
5. Brčić, M., Kršćanski, S. and Brnić, J. (2021) 'Rotating Bending Fatigue Analysis of Printed Specimens from Assorted Polymer Materials', Polymers, 13(7), p. 1020. doi: 10.3390/polym13071020.
6. Cejuela, E., Negro, V. and del Campo, J. M. (2020) 'Evaluation and optimization of the life cycle in maritime works', Sustainability (Switzerland), 12(11). doi: 10.3390/su12114524.
7. Cysne Barbosa, A. P. et al. (2017) 'Accelerated aging effects on carbon fiber/epoxy composites', Composites Part B: Engineering, 110, pp. 298–306. doi: 10.1016/j.compositesb.2016.11.004.
8. Davies, P. (2020) 'Towards More Representative Accelerated Aging of Marine Composites', in Advances in Thick Section Composite and Sandwich Structures. Cham: Springer International Publishing, pp. 507–527. doi: 10.1007/978-3-030-31065-3_17.
9. Davies, P. and Rajapakse, Y. D. S. (eds) (2014) Durability of Composites in a Marine Environment. Dordrecht: Springer Netherlands (Solid Mechanics and Its Applications). doi: 10.1007/978-94-007-7417-9.
10. Davies, P. and Rajapakse, Y. D. S. (eds) (2018) Durability of Composites in a Marine Environment 2. Cham: Springer International Publishing (Solid Mechanics and Its Applications). doi: 10.1007/978-3-319-65145-3.
11. Eftekhari, M. and Fatemi, A. (2016) 'Tensile behavior of thermoplastic composites including temperature, moisture, and hygrothermal effects', Polymer Testing, 51, pp. 151–164. doi: 10.1016/j.polymertesting.2016.03.011.
12. Fan, Y. et al. (2019) 'Diffusion of water in glass fiber reinforced polymer composites at different temperatures', Journal of Composite Materials, 53(8), pp. 1097–1110. doi: 10.1177/0021998318796155.
13. Gellert, E. P. and Turley, D. M. (1999) 'Seawater immersion ageing of glass-fibre reinforced polymer laminates for marine applications', Composites Part A: Applied Science and Manufacturing, 30(11), pp. 1259–1265. doi: 10.1016/S1359-835X(99)00037-8.

14. Gljušćić, M. et al. (2021) 'Digital image correlation of additively manufactured CFRTP composite systems in static tensile testing', Procedia Structural Integrity, 31, pp. 116–121. doi: 10.1016/j.prostr.2021.03.019.
15. Helbling, C. S. and Karbhari, V. M. (2008) 'Investigation of the Sorption and Tensile Response of Pultruded E-Glass/Vinylester Composites Subjected to Hygrothermal Exposure and Sustained Strain', Journal of Reinforced Plastics and Composites, 27(6), pp. 613–638. doi: 10.1177/0731684407081769.
16. Institute of Oceanography and Fisheries (2012) Početna procjena stanja i opterećenja morskog okoliša hrvatskog dijela Jadrana. Split, Croatia.
17. INTERNATIONAL STANDARD (2020) ISO 527 Plastics - Determination of tensile properties.
18. Joliff, Y., Belec, L. and Chailan, J. F. (2013) 'Modified water diffusion kinetics in an unidirectional glass/fibre composite due to the interphase area: Experimental, analytical and numerical approach', Composite Structures, 97, pp. 296–303. doi: 10.1016/j.compstruct.2012.09.044.
19. Kastratović, G. et al. (2021) 'Composite material selection for aircraft structures based on experimental and numerical evaluation of mechanical properties', Procedia Structural Integrity, 31, pp. 127–133. doi: 10.1016/j.prostr.2021.03.021.
20. Kožar, I. et al. (2019) 'Bond-slip parameter estimation in fiber reinforced concrete at failure using inverse stochastic model', Engineering Failure Analysis, 104, pp. 84–95. doi: 10.1016/j.engfailanal.2019.05.019.
21. Kožar, I. et al. (2020) 'Stochastic properties of bond-slip parameters at fibre pull-out', Engineering Failure Analysis, 111, p. 104478. doi: 10.1016/j.engfailanal.2020.104478.
22. Martin, R. (2008) Ageing of composites, Ageing of Composites. Cambridge England: Woodhead Publishing Limited. doi: 10.1533/9781845694937.
23. Mayya, H. B. et al. (2021) 'Effect of Marine Environmental Conditions on Physical and Mechanical Properties of Fiber-Reinforced Composites—A Review', Journal of The Institution of Engineers (India): Series C, 102(3), pp. 843–849. doi: 10.1007/s40032-021-00676-w.
24. Milenkovic, S. et al. (2021) 'Effect of the raster orientation on strength of the continuous fiber reinforced PVDF/PLA composites, fabricated by hand-layup and fused deposition modeling', Composite Structures, 270, p. 114063. doi: 10.1016/j.compstruct.2021.114063.
25. Morla, P. et al. (2021) 'Corrosion evaluation of geopolymer concrete made with fly ash and bottom ash', Sustainability (Switzerland), 13(1), pp. 1–16. doi: 10.3390/su13010398.
26. Panaitescu, I., Koch, T. and Archodoulaki, V.-M. (2019) 'Accelerated aging of a glass fiber/polyurethane composite for automotive applications', Polymer Testing, 74, pp. 245–256. doi: 10.1016/j.polymertesting.2019.01.008.
27. Rubino, F. et al. (2020) 'Marine Application of Fiber Reinforced Composites: A Review', Journal of Marine Science and Engineering, 8(1), p. 26. doi: 10.3390/jmse8010026.
28. Sousa, J. et al. (2020) 'Mechanical characterization of sandwich composites with embedded sensors', Engineering Failure Analysis, 117, p. 104765. doi: 10.1016/j.engfailanal.2020.104765.
29. de Souza Rios, A. et al. (2016) 'Effects of accelerated aging on mechanical, thermal and morphological behavior of polyurethane/epoxy/fiberglass composites', Polymer Testing, 50, pp. 152–163. doi: 10.1016/j.polymertesting.2016.01.010.
30. Takacs, L., Kovacs, L. and Olajos, T. (2020) 'Numerical tool with mean-stress correction for fatigue life estimation of composite plates', Engineering Failure Analysis, 111, p. 104456. doi: 10.1016/j.engfailanal.2020.104456.
31. Vailati, M.; Mercuri, M.; Angiolilli, M.; Gregori, A. (2021) 'Natural-Fibrous Lime-Based Mortar for the Rapid Retrofitting of Masonry Heritage', Preprints. doi: doi: 10.20944/preprints202107.0431.v1.
32. Vizentin, G. et al. (2020) 'Marine Propulsion System Failures—A Review', Journal of Marine Science and Engineering, 8(9), p. 662. doi: 10.3390/jmse8090662.
33. Vizentin, G. and Vukelic, G. (2019) 'Degradation and damage of composite materials in marine environment', Medziagotyra. doi: 10.5755/j01.ms.26.3.22950.
34. Vukelic, G. et al. (2021) 'Failure analysis of a ruptured compressor pressure vessel', Procedia Structural Integrity, 31, pp. 28–32. doi: 10.1016/j.prostr.2021.03.006.
35. Vukelic, G., Vizentin, G. and Bakhtiari, R. (2021) 'Failure analysis of a steel pressure vessel with a composite wrap repair proposal', International Journal of Pressure Vessels and Piping, 193, p. 104476. doi: 10.1016/j.ijpvp.2021.104476

ISSN 0554-6397
Izvorni znanstveni rad
(*Original scientific paper*)

Gordan Janeš
E-mail: gjanes@uniri.hr
Ante Sikirica
E-mail: ante.sikirica@uniri.hr
Center for Advanced Computing and Modelling, University of Rijeka,
Radmile Matejčić 2, 51000 Rijeka
Luka Grbčić
E-mail: lgrbcic@riteh.hr
Lado Kranjčević
E-mail: lado.kranjcevic@riteh.hr
Faculty of Engineering, University of Rijeka, Vukovarska 58, 51000 Rijeka

MPI Associated Scalability of Open-Source CFD Codes for Oil Spill Assessment

Abstract

General-purpose CFD codes have recently become an increasingly discussed alternative to standardized, simplified and usually empirically calibrated specialized tools for pollution analyses. Commonly, CFD codes tend to provide physically more sensible results and can indicate the underlying cause for a given problem. Use for ecological problems, however, has usually been avoided due to the sizes of computational domains and inherent complexity of the calculations that need to be conducted. Adoption in recent years is mostly driven by significant improvements in computational capabilities and advancements related to code and communication optimizations. Unfortunately, due to substantial branching of codes and accompanying indispensable communication routines, especially in open-source community, performance and consequently applicability of codes, can vary significantly. This article aims to outline key limitations and quantify performance gains which can be obtained in a high-performance computing environment through the use of different communication protocols, when evaluating typical pollution problems such as oil spills. Obtained results indicate that savings of up to 40% in computational time can be achieved, depending on the code and message passing interface implementation for a problem in question, thus demonstrating the importance of communication protocols.

Keywords: MPI, CFD, oil spill

1. Introduction

Assessing oil spills and predicting their spread and extents on a larger scale is a complex problem, both numerically and in terms of physics/modelling. From an ecological standpoint, this topic is of great significance, especially in closed or semiclosed littoral regions, since the disturbance of the innate ecosystem can have long-lasting side-effects. This is the case of the Kvarner Bay, which is observed in this study.

In their study, Lončar et al. [1] modelled oil spills in the Kvarner Bay with MIKE 3 using Regional Ocean Modelling System (ROMS) data for the region in question. Wind influence on the overall circulation in the bay was also considered. Results are interesting, however, there are some obvious discrepancies between modelled and expected flow fields. Results presented in Ivić et al. [2] tackle a similar problem. Velocity field is obtained from MIKE 3 and subsequently advective-diffusive transport of a passive scalar (i.e. pollutant) was considered. It was shown that presented approach has merit. Spread of pollutants in the Bay was discussed in [3]. Similarly, MIKE 3 was used.

If we disregard the complexity of the interactions governing the spread of the oil spill, computational requirements are typically still great, especially for finite volume based CFD codes. However, due to generational improvements in code efficiency as well as increase in computational capabilities, CFD codes can be tuned in a manner which allows faster execution and hence enables their use for immensely large domains and complex problems. OpenFOAM has therefore been chosen for modelling of oil spills in Kvarner Bay, as it can be massively parallelised in high-performance computing (HPC) environment.

Scalability of OpenFOAM has been investigated by Culpo [4]. Results show acceptable speedups when using up to 1000 MPI processes for a given problem. The author has suggested further code improvements which could improve performance in HPC environments. In their study, Axtman and Rist [5] affirm that OpenFOAM can achieve ideal scaling when using up to 1000 processes. However, it is important to note that the underlying hardware plays a significant role. Observations presented in [6] suggest that OpenMPI offers performance improvements over Intel MPI.

In this study, data obtained from the Regional Ocean Modelling System [7] is used to establish a velocity field in the Kvarner Bay, which subsequently governs the spread of a randomly defined oil spill modelled as a passive scalar transport problem. Scalability of the presented problem is assessed on an HPC system with the goal of determining the optimal methodology for conducting similar simulations. Different variants of the OpenFOAM code as well as MPI libraries have been analyzed. By optimizing the use of computational resources for a given software package, data of interest can be generated in an acceptable time frame.

2. Methodology

2.1. Numerical model

Computational domain is a full-scale model of the Kvarner Bay, roughly 25044 × 22705 m in size, with a maximum depth of 77 m and an average of 60 m. The domain is modeled based on available geographical data and bathymetry measurements. Initially, three sets of grids, namely coarse, medium and fine, were generated through HEXPRESS. Numerical grids are fully hexahedral, generated by a successive increase in cell sizing with a factor of 1.4, and consist of $3.1 \cdot 10^6$, $3.8 \cdot 10^6$ and $7.1 \cdot 10^6$ cells respectively. Generated grids have an average y^+ value of 134.6.

Simulations are conducted in OpenFOAM. Variants maintained by the OpenFOAM Foundation Inc. [8] and OpenCFD Ltd. [9] have been considered. Identical (where applicable) case setups were defined for each distribution. An incompressible transient solver, pimpleFoam, has been used for flow modelling, whereas oil spill has been modelled as a simple scalar transport problem governed by the

$$\frac{\partial s}{\partial t} + \mathbf{u}\nabla s - D\nabla^2 s = 0 \tag{1}$$

where s is the scalar, $\mathbf{u}$ velocity field, t time and D diffusion coefficient. Diffusion coefficient can be calculated according to

$$D = \alpha_1 \nu + \alpha_2 \nu_t \tag{1}$$

where α_1 and α_2 are constants and are equal to 10^{-9} and 0.714 respectively. ν_t represents turbulent viscosity. Kinematic viscosity ν is set to 10^{-6} m^2/s. Expression noted in (1) is implemented as an additional equation in the pimpleFoam solver to be calculated based on resolved (updated) velocity field. The k − ω SST model [10] is employed for turbulence modelling.

The problem in question is defined so that only the bottom of the bay is a fixed wall. Remaining patches, which correspond to atmosphere, passage Vela vrata and regions north of Srednja vrata and west of Mala vrata, are prescribed initial values or defined as outlets. ROMS [7] data is used as an input for boundaries in question. In total, 3721 data points can be extracted to model the region. These data points are interpolated and adapted to fit the observed domain.

For all tests, first order time discretization scheme is used. All divergence terms are prescribed second order schemes; linearUpwind, vanLeer and limitedLinear schemes are used for velocity, scalar and all remaining terms, respectively. Courant number is kept below 0.8 whilst residuals are set to 10^{-6} for pressure and velocity and 10^{-8} for the rest. Oil spill is defined as an arbitrary-shaped zone in the domain (on surface and extends 1 m below) with an area of roughly 2.23 km^2. An overview of the computational

domain, position and shape of the spill and boundary conditions, is given in Figure 1. Additionally, numerical grid is also shown.

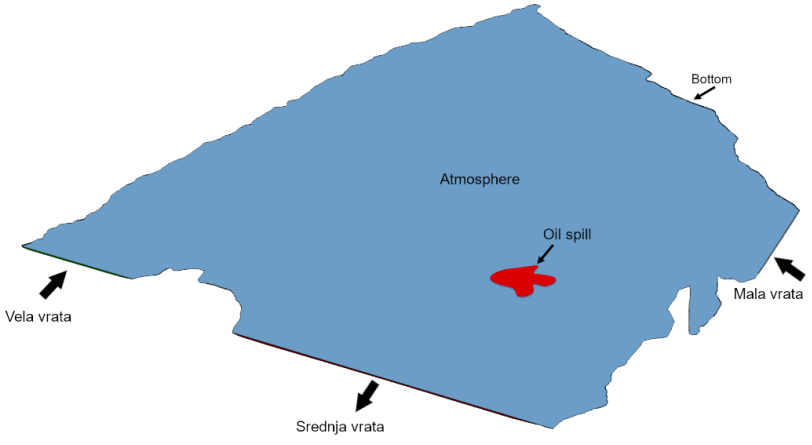

(a)

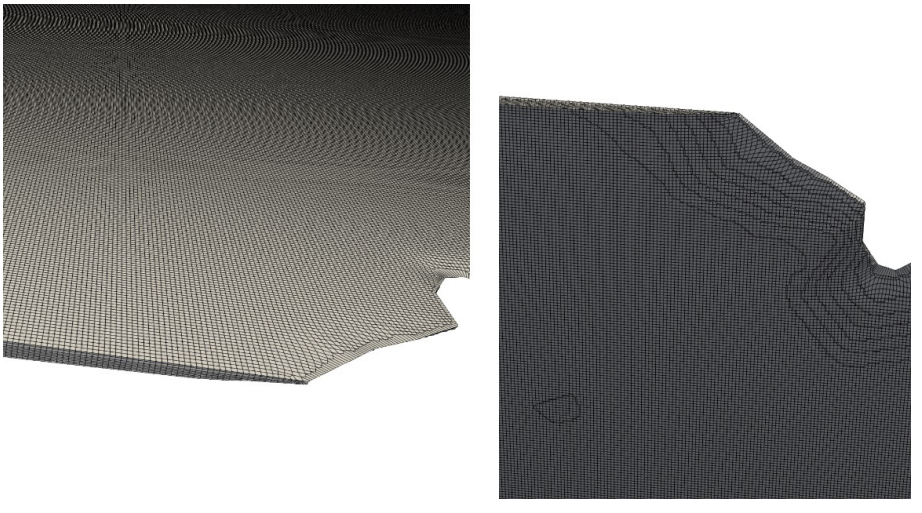

(b)

Figure 1: Computational domain, spill and boundary conditions (a); details of the numerical grid when observed from top (left) and bottom (right) (b).

2.2. Testing environment

Evaluation matrix considers two OpenFOAM versions: OpenFOAM 8 (OpenFOAM Foundation) and OpenFOAM v2012 (OpenCFD). OpenFOAM 8 has been built with several MPI versions available. OpenMPI version 4.1.1 is used as the reference, with Intel MPI version 5.1.2 and version 2019 Update 8 additionally evaluated. Comparison with the OpenFOAM v2012 has been performed for the OpenMPI 4.1.1 implementation.

Evaluation is conducted on an Intel Xeon E5-2690v3 based cluster. Each node has 24 physical cores and 64 GB of RAM. Hyperthreading has been disabled in all scenarios and only 16 cores per node were used. Communication between nodes is achieved through the Infiniband FDR with a throughput of approximately 51 Gb/s. Use of the infiniband interconnect has been enforced throughout.

The overall impact of the MPI and general scalability have been assessed for 8 different core/node configurations; cases were evaluated when using 32, 64, 96, 128, 256, 512, 768 and 1024 cores.

3. Results and discussion

3.1. Grid convergence and numerical results

As noted, three grids have been considered for the simulations. Since one of the goals is to contrast the accuracy and performance i.e. achieve the optimal performance with acceptable accuracy, grid chosen for performance evaluation must exhibit balance between those aspects.

Accuracy has been determined based on consistency of results between several reference points in the domain. However, the most significance has been attributed to the overall congruency of the oil spill extents. These have been compared for concentration value $s = 0.01$ and, based on results, medium grid has been deemed appropriate for further analyses. This choice is appropriate since when using OpenFOAM 8 and Intel MPI 2019, whilst running on 48 cores, execution times for coarse, medium and fine grid are 52509 s, 35188 s, 110356 s, respectively. A comparison of spill's extents after 72 hours is shown in Figure 2.

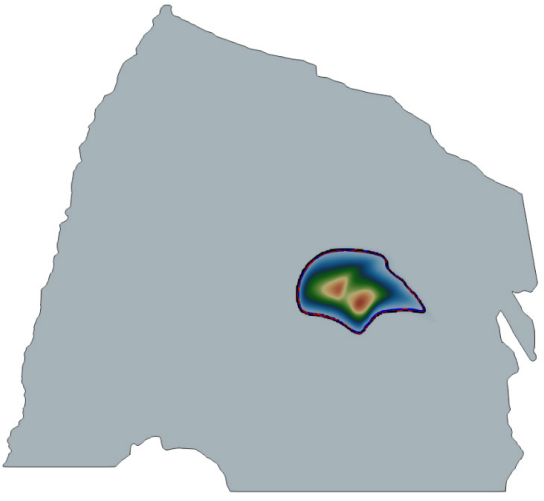

Figure 2: Extents of the oil spill after 72 hours visualized for s = 0.01; coarse grid (black), medium grid (red) and fine grid (blue).

Spill extents after 7 days of simulation time are shown in Figure 3.b. Additionally, velocity field is given after 7 days (Figure 3.a). The evolution of the flow field governs the spill's movement. The overall approach with ROMS data nested in the OpenFOAM problem case produces convincing results.

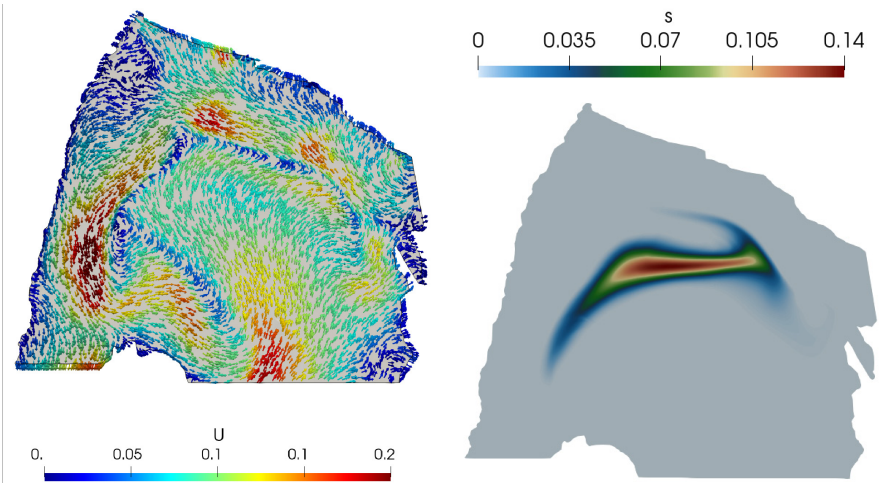

Figure 3: Results of the numerical simulations after 168 hours: velocity field after 168 hours (a); spill extents (scalar concentration) after 168 hours (b).

3.2. Performance and speedup

All performance assessment tests have been conducted three times. Averaged results are hence reported. Noted computational times correspond to simulations covering a 72-hour period. Results for a single-core-run are omitted from following tables (i.e. not considered), but will be included in the speedup calculations. Observations for different OpenFOAM distributions and MPI versions are given in Tables 1-4. Results include clock time, memory use and average time spent by the solver for the evaluation of each time step (TS).

Table 1: Scaling in OpenFOAM 8 when using Intel MPI version 2019 Update 8.

Cores	**32**	**64**	**96**	**128**	**256**	**512**	**768**	**1024**
Clock time [s]	60957	28222	18638	14232	8165	6452	6749	6841
Avg. time per TS [s]	1.097	0.512	0.338	0.269	0.155	0.114	0.117	0.123
RAM usage [GB]	7.839	11.391	15.468	19.431	37.801	45.105	68.370	90.839

Table 2: Scaling in OpenFOAM 8 when using Intel MPI version 5.1.2.

Cores	**32**	**64**	**96**	**128**	**256**	**512**	**768**	**1024**
Clock time [s]	61320	28183	18797	14478	8859	7478	8329	8501
Avg. time per TS [s]	1.105	0.511	0.341	0.270	0.164	0.130	0.147	0.146
RAM usage [GB]	5.584	6.909	8.141	9.656	15.780	24.957	36.865	52.760

Results attained for different Intel MPI versions (Tables 1-2) suggest a notable generational improvement. When comparing clock times, a reduction by up to 20% can be noted for Intel MPI version 2019. These savings, however, are accompanied by a significant increase in average memory – increase in RAM usage of up to 250% is observed when using Intel MPI version 2019.

Table 3: Scaling in OpenFOAM 8 when using OpenMPI version 4.1.1.

Cores	**32**	**64**	**96**	**128**	**256**	**512**	**768**	**1024**
Clock time [s]	63629	30001	19986	15857	9110	7056	7106	6989
Avg. time per TS [s]	1.150	0.545	0.366	0.299	0.170	0.126	0.124	0.120
RAM usage [GB]	7.123	9.471	11.849	14.208	23.823	45.321	68.624	94.411

OpenFOAM 8 with OpenMPI version 4.1.1 behaves similarly to the variant with Intel MPI version 2019 (Table 2). Although on average slightly slower in terms of overall computational time, as evidenced by the results presented in Table 3, this implementation is still adequate and viable option.

Table 4: Scaling in OpenFOAM v2012 when using OpenMPI version 4.1.1.

Cores	**32**	**64**	**96**	**128**	**256**	**512**	**768**	**1024**
Clock time [s]	57608	27312	17984	13490	7702	5289	5268	5251
Avg. time per TS [s]	0.999	0.490	0.328	0.247	0.148	0.092	0.092	0.091
RAM usage [GB]	7.321	9.866	12.411	14.998	25.592	48.057	71.138	96.805

Despite using the same OpenMPI version, OpenFOAM v2012 scales better than OpenFOAM 8 and provides reduction of up to 25% in computational time (clock time) when comparing equivalent test scenarios, as shown in Tables 3 and 4.

If we analyze the overall speedup, it is evident that the OpenFOAM v2012 with OpenMPI version 4.1.1 achieves the best results. Additionally, unlike in other test cases, there is no degradation in performance, although the efficiency is reduced and we are at the point of diminishing returns. Clearly, for a problem in question, 512 cores are the optimal choice, which suggest that approximately 7500 grid cells per core is a maximum for a given system and configuration. These results are in line with observations noted in [5]. With the subsequent increase in core count, the interconnect becomes a bottleneck. Speedup for conducted tests is given in Figure 4.

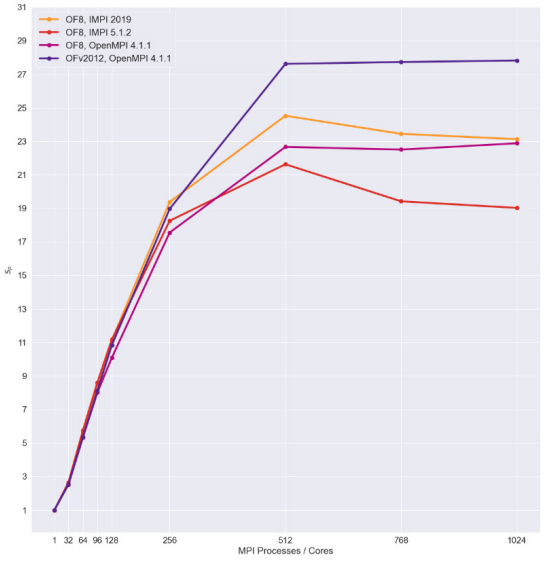

Figure 4: Speedup for different cases.

It is important to note that obtained results are influenced by hardware/software installed. Similar system configurations should achieve the same levels of scaling and speedup, particularly for a given problem type (incompressible, transient problem).

4. Conclusion

The main focus of this article is MPI associated computational speedup that can be achieved for a given problem. The problem in question, oil spill and its propagation as influenced by the sea currents, is an ecological problem that relies on appropriate response in a timely manner. For that purpose, data from the Regional Ocean Modelling System is utilised to simulate real-world conditions in Kvarner Bay and estimate the extents of the oil spill after a given period. Oil spill propagation is simulated as a simple scalar transport problem.

For the problem in question, computational efficiency is quintessential as it enables prompt propagation estimates and consequently quick response. With that in mind, two variants of the open-source CFD code OpenFOAM have been assessed with regards to MPI libraries at their disposal. This allows users to assess, and based on needs and hardware capabilities, tune their distributions in order to achieve optimal performance. We have clearly shown that there is a significant difference between OpenFOAM variants themselves as well as between the MPI libraries for a given option. Depending on the configuration, adoption of a proper MPI library can lead to a 25% reduction in computational time while generational advancements can additionally provide up to 25%.

5. References

1. *(scientific article, printed)* Lončar, G., Beg Paklar, G. & Janeković, I. (2012) Numerical modelling of oil spills in the area of Kvarner and Rijeka bay (The northern Adriatic Sea). *Journal of Applied Mathematics.* 2012 (497936), 1-20.
2. *(scientific article, printed)* Ivić, S., Mrša Haber, I. & Legović, T. (2017) Lagrangian coherent structures in the Rijeka bay current field. *Acta Adriatica.* 58 (3), 373-390.
3. *(scientific article, printed)* Mrša Haber, I., Legović, T., Kranjčević, L. & Cukrov, M. (2020) Simulation of pollutants spreading from a sewage outfall in the Rijeka bay. *Mediterranean Marine Science.* 21 (1), 116-128.
4. *(report)* Culpo, M. (2011) Current bottlenecks in the scalability of OpenFOAM on massively parallel clusters. *PRACE.* PRACE white paper 2011.
5. *(book chapter)* Axtmann, G. & Rist, U. (2016) Scalability of OpenFOAM with large eddy simulations and DNS on high-performance systems. In: Nagel, W. E., Kröner, D. H. & Resch, M. M. (eds) *High Performance Computing in Science and Engineering '16: Transactions of the High Performance Computing Center, Stuttgart (HLRS) 2016.* Cham, Springer, pp. 413-424.
6. *(report)* Keough, S. (2014) Optimising the parallelisation of OpenFOAM simulations. *Defence Science and Technology Organisation.* Report Number: DSTO-TR-2987.
7. *(scientific article, printed)* Shchepetkin, A. F. & McWilliams, J. C. (2005) The regional oceanic modeling system (ROMS): a split-explicit, free-surface, topography-following-coordinate oceanic model. *Ocean modelling.* 9 (4), 347-404.
8. *(software)* OpenFOAM 8. (2020) London. Weller, H.
9. *(software)* OpenFOAM v2012. (2020) Bracknell. OpenCFD Ltd.
10. *(scientific article, printed)* Menter, F.R. (1994) Two-equation eddy-viscosity turbulence models for engineering applications. *AIAA journal.* 32 (8), 1598-1605.

ISSN 0554-6397
Izvorni znanstveni rad
(*Original scientific paper*)

Marta Alvir
E-mail: marta.alvir@riteh.hr
Luka Grbčić
E-mail: luka.grbcic@riteh.hr
Faculty of Engineering, University of Rijeka, Vukovarska 58, 51000 Rijeka, Croatia
Ante Sikirica
E-mail: ante.sikirica@uniri.hr
Center for Advanced Computing and Modelling, University of Rijeka, Radmile Matejčić 2, 51000 Rijeka, Croatia
Lado Kranjčević
E-mail: lado.kranjcevic@riteh.hr
Faculty of Engineering, University of Rijeka, Vukovarska 58, 51000 Rijeka, Croatia

Numerical Modeling of Inclined Buoyant Jets for Different Flow Conditions

Abstract

The processes of discharge of higher density effluent into the recipient of lower density occur during the release of wastewater into the sea from desalination process, which is increasingly common today due to the shortage of drinking water. During such discharges, the goal is to achieve the best possible mixing, so that the impact of water with a high salt concentration on the environment is as small as possible. Since the jet returns to the bottom because of the influence of gravity, the use of nozzles at an angle increases the zone in which mixing occurs. In this paper, a numerical model of effluent discharge was made and buoyancy jets inclined at 45° were observed for different flow regimes. The influence of density and velocity on jet characteristics is shown. The numerical model was developed in OpenFOAM, and a comparison with experimental data from previous research is presented.

Keywords: Desalination, Inclined buoyant jets, OpenFOAM, Mixing, Wastewater

1. Introduction

As shortages of portable and freshwater have become a common occurrence, mainly due to the increased demand for drinking water linked to the population growth, desalination processes are of increasing importance. This is especially a problem on islands due to an increase in the population during the summer. Nowadays, ships,

submarines and platforms are more frequently applying the desalination process to get drinkable water and reduce the size of the water tanks.

In the desalination process, seawater or brackish water is used to produce potable water by eliminating the suspended matter and the dissolved minerals, mostly salt. A by-product from the process, desalination brine, is discharged using submerged outfalls back to the sea. Since this type of wastewater has a higher concentration of salt than the ambient water, it can potentially have negative effects on marine ecosystems. Increased salinity results in cell dehydration and possibly the death of these organisms [1]. To minimize harmful effects, it is a prerequisite to properly design diffusers and to predict the mixing behaviour of dense jets and assess their environmental impact. Inclined dense jets have many other applications. They also appear during the discharge of cooling water from liquefied natural gas plants, industrial discharges and wastes from mining and dredging operations, so they have been investigated by several researchers.

The earliest experimental study on inclined dense jets was conducted by [2] on discharges for inclinations 30°, 45°, 60° and 90°. The research has shown that the longest trajectory and highest dilution is achieved at an angle of 60°. Later studies [3] have shown the substantial effect of the water surface on dilution rate and mixing for larger discharge angles, so it was proposed to use dense jets inclined at smaller angles such as 45° for shallow coastal waters, where desalination plants are mostly located. Cipollina et al. [4] made an experimental investigation for the inclined dense jet at angles 30°, 45° and 60° for various ranges of Froude and Reynolds numbers, indicating that fluid viscosity has no significant effect on the flow. Shao et al. [5] used a combination of Planar Laser Induced Fluorescence (PLIF) and Particle Image Velocimetry (PIV) to experimentally investigate boundary effects. Vafeiadou et al. [6] applied computational fluid dynamics (CFD) to simulate the behaviour of inclined dense jets using commercial software CFX. Zhang et al. [7] used large eddy simulation (LES) to simulate 45° inclined dense jets with OpenFOAM and compared results with experimental data. Gildeh et al. [8] investigated various RANS turbulence models to study the behaviour of 30° and 45° inclined dense jets and found that both the LRR and realizable k-ε model produce the most accurate results.

In this study, the open-source CFD toolbox OpenFOAM was used to investigate characteristics of the inclined jet for different flow conditions. The results of the numerical model were compared with the experimental results from previous research [7]. Most previous works and experiments focused on ambient freshwater, but in most cases, the desalination effluent is discharged into seawater, where density can vary considerably, especially in the winter-summer seasons. Additionally, the effluent may have a different density, depending on the method used and the setting of the desalination process. As velocity, the density of effluent and brine have a strong impact on dilution rate and mixing, their behaviour has been investigated. Characteristic geometrical features of the dense jet for each case, including return point, centerline peak location and terminal rise height, were observed.

2. Material and methods

2.1. Dimensional Analysis

The main flow characteristics of an inclined dense jet in a stationary environment are shown in Figure 1. The jet is discharged through a round nozzle of diameter d with initial velocity U_0 inclined at the angle θ to the horizontal plane. During the initial vertical momentum flux, the jet is moving upward until it reaches peak height, which can be described with horizontal and vertical locations of the centerline peak x_m and z_m and terminal rise height z_t. Since the brine density ρ_b is bigger than ambient density ρ_a, after reaching maximum height, buoyant forces become dominant and the jet falls over and impacts the seabed. The dashed curved line presents the centerline of the jet, which is defined as the location of time-averaged local maximum concentration or velocity for the various cross-sections. Return point location x_r is defined as a location where the centerline intersects with the initial jet elevation. After reaching the bottom, the plume will continue spreading horizontally as density current at the horizontal direction with smaller speed and dilution.

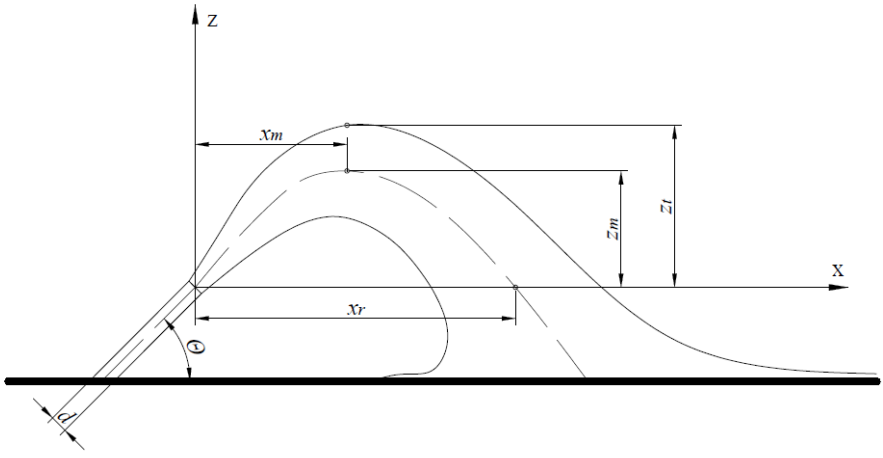

Figure 1: Schematic diagram of an inclined dense jet.

Variables of turbulent jets φ depend on the discharge angle θ, momentum M, buoyancy B, jet kinematic fluxes of volume Q and acceleration due to gravity g. They can be defined as follows:

$$\varphi = f(Q, M, B, \theta) \tag{1}$$

$$Q = \frac{\pi}{4} d^2 U_0 \qquad M = U_0 Q \qquad B = g_0' Q \tag{2}$$

$$g'_0 = \frac{g\left|(\rho_b - \rho_a)\right|}{\rho_a} \tag{3}$$

Previous studies have shown that dilution and jet geometry features mainly depend on densimetric Froude number Fr which is the ratio of inertial and buoyant forces and can be expressed as:

$$Fr = \frac{U_0}{\sqrt{g_0' D}} \tag{4}$$

Momentum-buoyancy length scale L_M is the measure of the distance in which momentum is more significant than buoyancy on the behaviour of the jet:

$$L_M = \frac{M^{3/4}}{B^{1/2}} = \left(\frac{\pi}{4}\right)^{1/4} d\, Fr_d \tag{5}$$

Another relevant dimensionless parameter is Reynolds number Re, which represents the ratio of inertial to the viscous forces is given as:

$$Re = \frac{\rho_b U_0 l}{\mu} = \frac{U_0 l}{\nu} \tag{6}$$

where l is characteristic length scale, ν is kinematic viscosity and μ is dynamic viscosity.

2.2. Numerical setup

In this study, the partial differential equations of fluid flow were calculated utilizing the open-source CFD package OpenFOAM, which is based on the finite volume method. Domain has been shown in Figure 2. with all dimensions in millimetres. The size of the geometry is similar to the experiment in [7]. The origin of the coordinate system was set to the centre of the discharge port.

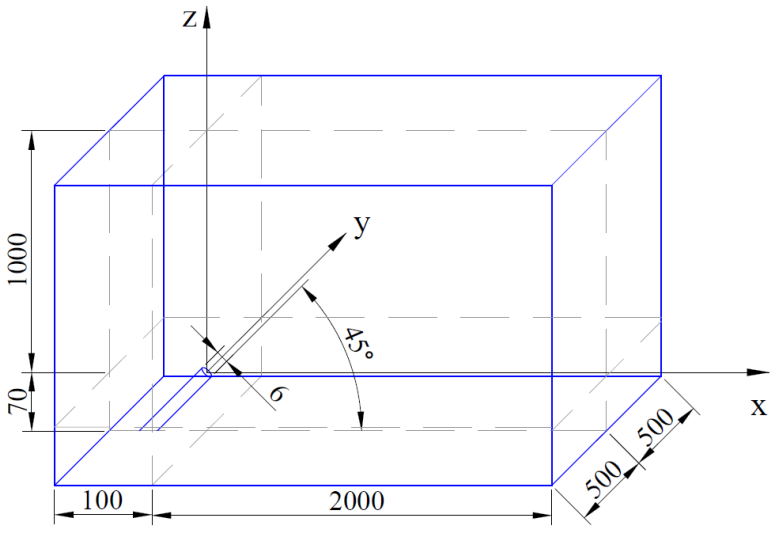

Figure 2: Computational domain

CF-MESH+ software was used to create the mesh. It contains 1962909 elements with refinement in zones near the nozzle. A transient OpenFOAM solver for mixing two incompressible fluids, twoLiquidMixingFoam was used. As suggested by the results from previous studies [8], realizable k − ε turbulence model was selected. The viscosity of both fluids was set to 10^{-6} m^2/s, while diffusivity and turbulent Schmidt number were 10^{-9} m^2/s and 0.7, respectively. The time step was adaptively varied so as to satisfy the condition that the Courant number is less than 1. The simulation time is 120 seconds.

Boundary conditions were chosen to match the experiment used for validation. Back, front, right and left boundaries were set to be zero gradient open boundaries. The top surface was set to free slip boundary condition. On the bottom side and pipe, standard turbulence wall functions and no slip condition was used. At the inlet of the pipe, uniform discharge velocity U_0 was set at turbulence intensity of 10%.

In Table 1. flow configurations for different cases are shown. Sixteen different cases have been simulated. Brine with density ρ_b and initial velocity U_0 was discharged in homogeneous stationary ambient fluid with density ρ_a. Conditions in case V0 were identical to the experimental study [7]. In experimental cases U1-U5, inlet velocity was changed in A1-A5 ambient density was changed and in B1-B5, brine density was changed.

Table 1: Numerical setup parameters for different cases.

Case	Initial velocity U_0, m/s	Brine density ρ_b, kg/m^3	Ambient density ρ_a, kg/^{m}3	Froude number *Fr*	Reynolds number *Re*
V0	0.515	1034	997	11.21	2987
A1	0.515	1034	1020	18.43	2987
A2	0.515	1034	1022.5	20.36	2987
A3	0.515	1034	1025	23.04	2987
A4	0.515	1034	1027.5	27.15	2987
A5	0.515	1034	1030	34.65	2987
B1	0.515	1030	1025	30.91	2987
B2	0.515	1035	1025	21.86	2987
B3	0.515	1040	1025	17.85	2987
B4	0.515	1045	1025	15.46	2987
B5	0.515	1050	1025	13.82	2987
U1	0.250	1034	1025	11.18	1450
U2	0.750	1034	1025	33.55	4350
U3	1.000	1034	1025	44.74	5800
U4	1.250	1034	1025	55.92	7250
U5	1.500	1034	1025	67.11	8700

Since the brine is usually discharged with salinity less than 5% higher than the density of receiving water, in this study, cases for different densities of seawater and brine were observed. Simulation is also obtained for larger velocity and Reynolds number to show their relations. All simulations were performed on the Bura supercomputer at the Center for Advanced Computing and Modelling at the University of Rijeka.

3. Results and discussion

Previously described problems are transient in nature, hence all results are shown as time-averaged from 50 to 120 seconds when the simulation has no considerable variations. The results from case V0, experimental and LES results from [7] which were used to validate the model are shown in Figure 3.. Length on the axis is divided with the momentum-buoyancy length scale from Eq. (5) to get the dimensionless length since the diameter from an experimental pipe and LES domain are slightly different. While RANS model slightly under-predicts the trajectory from experimental results, LES model gets over-prediction. Results show especially good agreement in the jet-like

region where momentum flux is dominant. In Figure 4., contours of the concentration and velocity magnitude for the cross-section of the flow are shown from case V0.

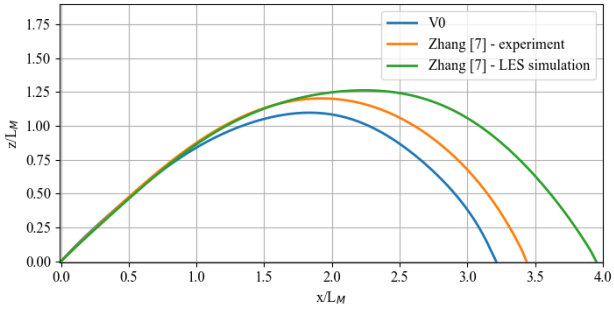

Figure 3: Comparison with experimental data.

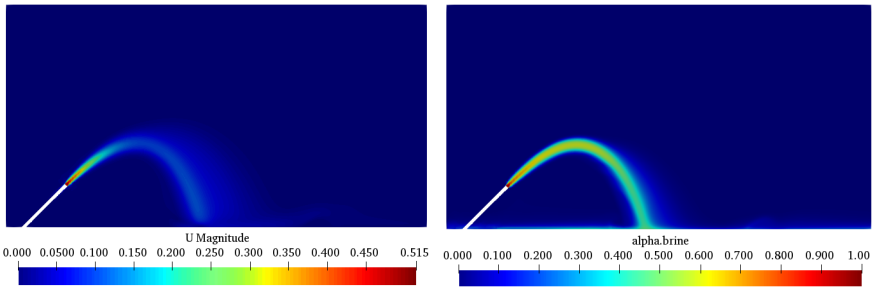

Figure 4: Time averaged velocity (left) and concentration (right) contours at the centre plane for case V0.

The jet centerline or jet trajectory is the main characteristic of the general jet flow. It shows coordinates of the centerline peak and returns point location, which is crucial to understand the characteristic of the flow. The jet centerline is defined from maximum concentration location at different cross-sections. The centre of the coordinate system is in the middle of the nozzle. Figure 5. shows the centerline for starting case and cases A1-A5 for different ambient densities. Case V0 represents freshwater, while other densities represent seawater of different properties. It can be observed that by increasing the density of the ambient water, the centerline will increase and better mixing will occur. In Figure 6. the centerline for different effluent densities are shown. Brine density has the opposite effect. The smaller it is, the centerline is higher and longer. Figure 7. shows the centerline for cases U1-U5 for different initial velocities. It is shown that, that in stationary ambient, larger velocity results in higher momentum flux and better mixing characteristics.

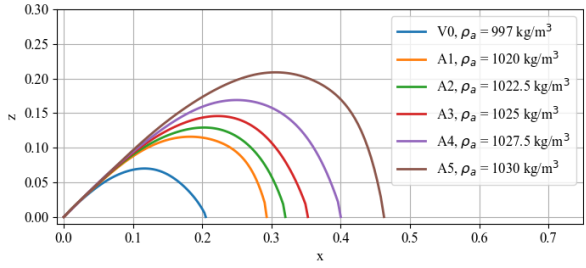

Figure 5: The jet centerline for different ambient densities.

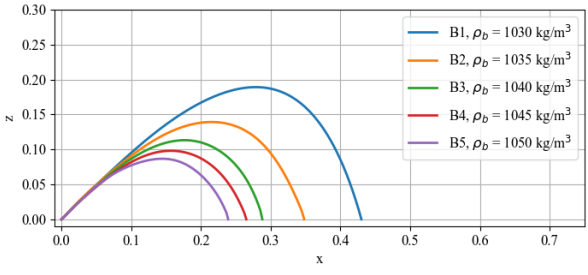

Figure 6: The jet centerline for different brine densities.

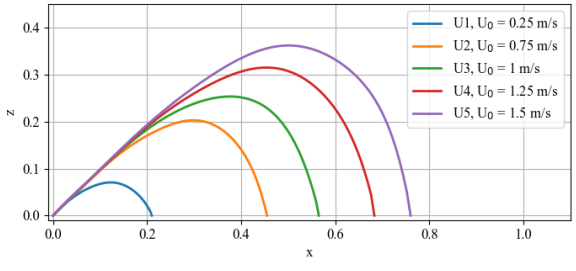

Figure 7: The jet centerline for different velocities.

The geometrical specifications of a buoyant jet, the horizontal and vertical locations of jet centerline peak with coordinates x_m and z_m, the jet terminal rise height z_t and the horizontal location of the jet return point x_r for each case are shown in Tables 2. and 3.. V0 has good agreement with experimental data which can be attributed to the fact

they have the same setup. Characteristics from other cases depend on the settings and parameters that have changed.

Table 2: Geometrical specifications for experiment and numerical case V0.

Case	x_m	z_m	z_t	x_r
V0	0.1225	0.07	0.0825	0.205
Experiment [7]	0.119	0.074	0.11	0.212

Table 3: Geometrical specifications for different cases with changed flow parameters.

Case	x_m	z_m	$_z$t	x_r
A1	0.19	0.116	0.15	0.293
A2	0.21	0.129	0.165	0.32
A3	0.23	0.146	0.1925	0.353
A4	0.25	0.17	0.2175	0.4
A5	0.305	0.21	0.2575	0.463
B1	0.288	0.19	0.2525	0.43
B2	0.22	0.139	0.18	0.348
B3	0.183	0.113	0.148	0.288
B4	0.16	0.098	0.123	0.265
B5	0.153	0.086	0.105	0.239
U1	0.125	0.071	0.078	0.21
U2	0.298	0.203	0.263	0.455
U3	0.378	0.253	0.335	0.565
U4	0.466	0.315	0.375	0.683
U5	0.505	0.362	0.435	0.76

4. Conclusions

The aim of this work was to analyze flow characteristics of the inclined buoyant jets for different cases when the density of effluent is larger than the density of ambient water and the effect of buoyant forces are significantly increased. These comparisons focused on the main characteristic of the flow and centerline of the jet for the design of brine discharge and assess effects on marine ecosystems, as well as the environmental impact for regulatory purposes.

The focus of this paper was on diffusers inclined at 45^o in stationary ambient. Flow and mixing were assessed in OpenFOAM. Results indicate that OpenFOAM can be successfully applied for predicting jet characteristics. These observations have been validated with previous experimental results. Sixteen numerical cases with different flow regimes have been made and their results have been shown.

The main characteristic of jets is shown with the jet centerline. For a design of desalination systems, it is important to determine the geometrical characteristics of the brine plume, including the horizontal and vertical locations of jet centerline peak, terminal rise height, the horizontal position of the return point.

Numerous cases of jet Froude and Reynolds numbers were observed in this work. Jet centerline and other jet characteristics strongly depend on those numbers, especially the Froude number. Results show as the Froude number increases, the range of the jet also increase.

5. References

1. Missimer, T. M., & Maliva, R. G. (2018). Environmental issues in seawater reverse osmosis desalination: Intakes and outfalls. *Desalination*, 434, 198-215.
2. Zeitoun, M. A., & McIlhenny, W. F. (1971) Conceptual designs of outfall systems for desalination plants. *In Offshore Technology Conference*. April, Houston, Texas
3. Abessi, O., & Roberts, P. J. (2016). Dense jet discharges in shallow water. *Journal of Hydraulic Engineering*, 142(1), 04015033.
4. Cipollina, A., Brucato, A., Grisafi, F., & Nicosia, S. (2005). Bench-scale investigation of inclined dense jets. *Journal of Hydraulic Engineering*, 131(11), 1017-1022.
5. Shao, D., & Law, A. W. K. (2010). Mixing and boundary interactions of 30^o and 45^o inclined dense jets. *Environmental fluid mechanics*, 10(5), 521-553.
6. Vafeiadou, P., Papakonstantis, I., & Christodoulou, G. (2005) Numerical simulation of inclined negatively buoyant jets. *In The 9th international conference on environmental science and technology*, September, Rhodes Island, Greece, pp. 1-3.
7. Zhang, S., Jiang, B., Law, A. W. K., & Zhao, B. (2016). Large eddy simulations of 45^o inclined dense jets. *Environmental Fluid Mechanics*, 16(1), 101-121.
8. Kheirkhah Gildeh, H., Mohammadian, A., Nistor, I., & Qiblawey, H. (2015). Numerical modeling of 30^o and 45^o inclined dense turbulent jets in stationary ambient. *Environmental Fluid Mechanics*, 15(3), 537-562.

ISSN 0554-6397
Izvorni znanstveni rad
(*Original scientific paper*)

Špiro Ivošević
E-mail: spiroi@ucg.ac.me
University of Montenegro, Maritime Faculty Kotor, Put I Bokeljske brigade 44, Kotor, Montenegro
Nataša Kovač
E-mail: natasa.kovac@udg.edu.me
University of Donja Gorica, Faculty of Applied Sciences, Oktoih 1, DonjaGorica, Podgorica, Montenegro
Gyöngyi Vastag
E-mail: djendji.vastag@dh.uns.ac.rs
University Novi Sad, Faculty of Sciences, Trg Dositeja Obradovića 3, 21 000 Novi Sad, Serbia
Peter Majerič
E-mail: peter.majerič@um.si
Rebeka Rudolf
E-mail: rebeka.rudolf@um.si
University of Maribor, Faculty of Mechanical Engineering, Smetanova ulica 17, 2000 Maribor, Slovenia

The Analyses of the Rate of Pitting Corrosion of a NiTi Rod in a Natural Marine Environment

Abstract

The analysis of the behaviour of new materials in the natural environment is important for their application and commercial use. In order to explore the application of Shape Memory Alloys in the Maritime industry, this research focuses on the corrosive behaviour of the NiTi rod that was produced by means of a continuous casting process. The experiment included three samples of NiTi rods that were exposed to the marine environment for 6, 12 and 18 months at a depth of 3 metres below the surface. The morphological and chemical changes were analysed separately during the experiment. Ultrasonic thickness equipment and the Scanning Electron Microscope (SEM) technique were used for the tests that determined the corrosion rates and detected pitting. The changes in the chemical composition of the NiTi rod were investigated by means of an Energy Dispersive X-ray (EDX) analysis, in order to define the pitting behaviour of the rod`s surfaces during its exposure to seawater. The obtained research results prove that the rate of pitting corrosion follows a progressive curve – the minimum value of corrosion rate equalled 0.04 mm/month, while the maximum value was 0.12 mm/month.

Key words: NiTi rod, seawater, pitting corrosion, chemical composition, SEM, EDX

1. Introduction

Shape memory materials are now applied in various industries, such as the Automotive, Railway, Aircraft and Maritime industries, as well as in Medicine and Robotics [1]. The behaviour and various applications of these materials are researched in laboratories and natural settings. Although laboratory tests are necessary for the research on the basic physical and mechanical characteristics and chemical composition of materials, the practical application of materials requires research in natural environmental conditions over a longer period of exposure. The behaviour of materials and their susceptibility in different exploitation conditions can only be determined in natural settings.

Shape memory materials were discovered in 1932, and recognised for their thermo-mechanical properties, such as superelasticity, shape memory effect, high damping capacity and double shape memory effect [2]. The key thermo-mechanical properties were discovered on the basis of Ag, Au, Al, Cu, Fe, etc. However, the most significant applications are based on Cu, Al and Ni [3]. Binary, trinary and quaternary systems of alloys ensure good mechanical and chemical characteristics, as well as biocompatibility and corrosion resistance.

In addition to chemical composition, the process of alloy production is also very significant for the provision of their good performance. The main problem with the production is the possibility of further plastic deformation, especially cold drawing, that is caused by large grain size. New processing techniques, such as continuous casting and rapid solidification, can be used to prevent the formation of coarse grains on Shape Memory Alloys (SMAs).

NiTi alloys shaped like discs, wires and rods are applied frequently in different industries as a result of various production processes. Among the different production processes, including the melting process and the standard techniques for hot and cold working [4], casting processes are used most frequently for the production of NiTi alloys [5]. Continuous casting has recently emerged as a new production process of SMAs [6]. SMAs are characterised primarily by their capacity to restore their original dimensional integrity (pre-deformed shape and size) after undergoing substantial deformation when heated to a certain temperature [4]. This temperature induced strain recovery and other elasticity variants exhibited by SMAs make these materials suitable for use in various industrial applications.

The application of SMAs in the Maritime industry depends on the different conditions of their exploitation and characteristics. Corrosion is considered a dominant degradation process in seawater. More precisely, the corrosion of metal structures in seawater is an electrochemical process that occurs through the interaction between the metal surface, the seawater and the conductivity of the seawater.

There are different types of physical corrosion, e.g. intergranular, galvanic, crevice [7], stress, cavitation corrosion, corrosion fatigue, etc. However, the most frequent types in the Maritime industry are uniform and pitting corrosion [8]. For this reason, a number

of studies calculated the corrosion potential of SMAs prior to their application. SMAs are based on two-phase changes, in which the corrosion rate of the austenitic phase is higher than the rate of the martensitic phase. Almost all SMAs are more resistant to corrosion than traditional alloys. This is the result of the hyperelastic behaviour of the polycrystalline structure [9]. Due to their pseudoelasticity, NiTi alloys show excellent resistance to cavitation erosion [10]. The appearance of different physical forms of corrosion requires research on the causes of corrosion, and determination of the extent and rate of the corrosion. Numerous corrosion models have been developed so far, and are based mainly on linear and nonlinear models [11].

Experimental research in a real marine environment can best describe which forms of corrosion can occur and how intense the corrosion rate is. This paper indicates the intensity of pitting corrosion and chemical changes in the pitting itself, on its edge and in the hole of the pit for the case of NiTi alloys in the form of rods. In fact, it is a continuation of research work shown in the previous articles, where the behaviour of SMAs was presented in the marine environment [6, 11, 12]. In this study, the motivation was to determine the degree of pitting corrosion in seawater on a NiTi rod fabricated by a continuous casting process. After the introductory considerations and a description of the characteristics and corrosion of the NiTi rod, the second chapter analyses the NiTi rod and the research methodology. The third chapter presents the research results of the pitting corrosion rate, while the fourth chapter exhibits the concluding remarks.

2. Materials and Methods

2.1. The Characteristics of the NiTi rods

This paper analyses a NiTi rod whose diameter was d = 11,9 mm and a length of 50 mm (Figure 1a). The rods were produced by means of the vertical continuous casting process with a previous vacuum remelting. The production of the rod was based on the use of pure metal components - Ni and Ti - with a high degree of purity (99.99 %). All NiTi rod samples were ground after electro-erosion, so that they were cut longitudinally into two halves, thus obtaining a sample of a rod with a half cross-section (Fig. 1a). A notch was incised on this half-bar so that the samples could be dropped with a plastic wire to the desired test site at sea. Analyses of three rods samples in a natural marine environment were performed in this research. The initial analysis of the initial rod was based on the macro observation, and, in the second part, the microstructure was examined (Figure 1b) obtained by light microscopy (Nikon Epiphot 200, Japan), showing characteristic dendritic growth.

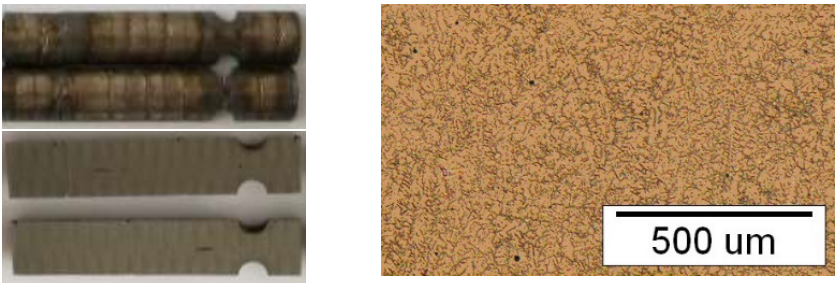

a) b)

Figure 1. NiTi rod test samples: a) Both sides of the test samples of the NiTi rod (diameter of 11.9 mm), b) Dendritic microstructure [6]

In order to determine the chemical composition of the NiTi rod in seawater before testing, the samples were measured by Inductively Coupled Plasma-Mass Spectrometry (ICP-MS) and X-Ray Fluorescence (XRF). The analysis of chemical composition of the NiTi rods detected a range of metals, as shown in Table 1 [6]. The difference in the desired chemical composition was due to the manufacturing process itself - remelting, where sufficient mixing of the melt was not provided. The induction melting furnace does not have the possibility of switching from medium to low frequency (1500 Hz), so a distinctly inhomogeneous NiTi rod was formed.

Table 1. The percentage composition of the NiTi rod analysed

Rod	% Ni		% Ti		% Fe	
	ICP	XRF	ICP	XRF	ICP	XRF
NiTi	62.6	62.5-62.6	35.9	35.9	1.4	1.4

2.2 Proposed Problem and Corresponding Methodology

However, this research focuses on the progress of pitting corrosion on the NiTi rod that was exposed to the influence of seawater. Namely, 3 samples of a NiTi rod were exposed to the marine environment for 6, 12 and 18 months. The samples were immersed into the sea near the coast, at a depth of three metres, over the maximum period of 18 months.

During the research between August, 2018 and March, 2020, the parameters of the seawater (temperature and salinity) were measured by the Institute of Biology at the University of Montenegro. Table 2 shows the relevant data on the minimum and maximum sea temperatures and salinity on the sea`s surface, which were measured during 2019 and 2020 in January and December. The previously published data [13] show a very small difference between the temperatures on the sea`s surface and at the

depth of 5 m, while a more significant difference was noted in salinity on the surface and in shallow water, mostly during the rainy season.

Table 2. The values of marine parameters during 2019 and 2020 [14].

Year	**Temperature ^{0}C**	**Temperature ^{0}C**	**Max. Temp. ^{0}C**	**Min. Temp. ^{0}C**
2019	13.4 - January	12.88-December	25.42-September	11.7-February
2020	13.61 - January	15.41-December	25.90-August	13.0-March
Year	**Salinity** (‰)	**Salinity** (‰)	**Max. Salinity** (‰)	**Min. Salinity** (‰)
2019	32.8 - January	14.00-December	39.00-September	14.00-December
2020	38.20 - January	34.90-December	28.30-August	20.0-March

In Figure 2 can be see the conceptual model of the conducted research. In total three NiTi rods were exposed to seawater at a depth of three metres below the surface, close to the shore. After 6, 12 and 18 months of exposure the rod samples were tested by visual inspection, in order to identify surface corrosion. After visual inspection, the rod samples after 18 months of exposure were observed by a Scanning Electron Microscope (SEM), and chemical composition analysis was also performed on them using Energy Dispersive X-Ray (EDX) analyses. The first SEM inspections were used to calculate the corrosion rate, while the second EDX analyses enabled calculation of the chemical composition of the hole and the edge of the pitting.

Figure 2 shows the conceptual model of the research.

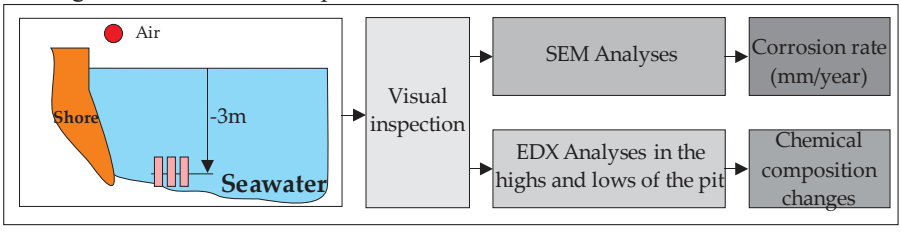

Figure 2. The scheme of the conceptual model of the research (location of the rod samples and type of characterisation)

2.2.1. The SEM Dimensional Analysis

The pitting corrosion depth was measured with a SEM microscope, Quanta 200 3D (FEI, USA). Figure 3 shows the measuring scheme of the pitting corrosion depth for the NiTi rods based on the SEM microscopy. Due to the irregular shape of the corroded sample, the corrosion depth was calculated based on the difference between

the high and low focus areas on the corrosion features of the sample. The distance Z determines the distance from the SEM aperture to the focused feature. When the focus area is centred on an area above the corrosion pit, the SEM shows a smaller Z value than when the focus area is centred inside the corrosion pit. The focusing values are shown in this paper as Z high and Z low, as shown in Figures 3 and 5 and Table 2. The pitting depth was calculated as the distance between the low Z focus area minus the high Z focus area:

$$d_{pit} = Z_L - Z_H \tag{1}$$

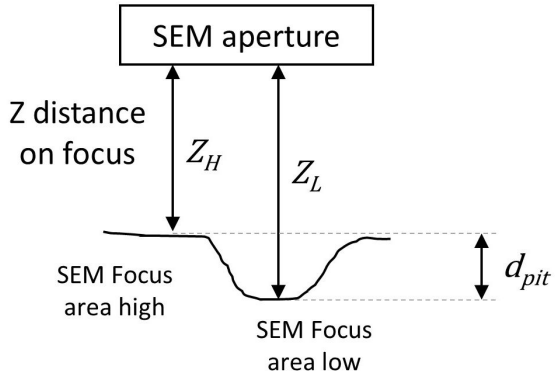

Figure 3. The scheme of focus measuring of the NiTi rods by the SEM microscope

The obtained values of pitting corrosion depth of the NiTi rods were subjected to statistical analysis in order to determine the beginning of the corrosive processes. The scientific literature investigated different corrosion models [15-20]. In this paper, statistical analysis was performed by fitting the usual corrosion linear models [21] to the data presented in Table 2. Accordingly, the linear corrosion model can be expressed as:

$$d(t) = c_1(t - T_{cl})^{c_2} \tag{2}$$

whereby the unknown coefficient (c_2) usually has the value of 1 or 1/3 [21]. This study examined the pitting corrosion depth as a linear model with the coefficient $c_2 = 1$. The statistical approach thus resulted in three different linear models, whose form was:

$$d(t) = c_1(t - T_{cl}) \tag{3}$$

whereby c_1 is the corrosion rate expressed in mm/month, $d(t)$ is the pitting corrosion depth measured in mm, T_{cl} is the time when the corrosion started expressed in the number of months, while t is the time of exposure to the environment expressed in the

number of months. The fitted models were based on the assumption that corrosion starts immediately after the exposure of the samples to the environmental influences (T_{cl} = 0), or that corrosion starts after 6 or 12 months (i.e. T_{cl} = 6, and T_{cl} = 12) of exposure to the environment.

2.2.2. The EDX Analysis of the NiTi rod

All rod samples exposed to the influence of seawater at a depth of 3 metres were afterwards inspected visually. Fouling and surface corrosion were observed on the rod samples that were exposed to seawater for 6 and 12 months (Figures 4a and 4b). Pitting was observed on the rod sample that was exposed to seawater for 18 months (Figure 5b).

The chemical composition of the selected NiTi rod samples was determined by means of a high-resolution, field-emission SEM Sirion 400 NC (FEI, USA), which was equipped with an EDX detector - INCA 350 (Oxford instruments, UK), that enables extremely high magnifications (up to a million times) in high resolution (1 nm). The EDX semi-quantitative analysis determined the chemical composition of the NiTi rod after exposure to the marine environment, as well as the content of the elements on the pit edge and in the pit. The analysis included a total of 10 spectrums - five spectrums from the pit and five from the edge (Figure 5b).

a) b)

Figure 4. NiTi rods: (a) After 6 months of exposure, (b) After 12 months of exposure

3. Results

3.1. The Value of the Pitting Corrosion Rate

An illustration of the execution of the measurement by placing the sample in the SEM chamber of the microscope is shown in Figure 5a, while the corresponding values (Z high and Z low) and the calculated pit depth expressed in mm are shown in Table 3. Five pit depths were calculated by the measurement of the difference between the high and low SEM focus. Figure 5b shows the locations of the ten values (five on the pit edge and five in the pit) that were obtained by means of the SEM. The SEM views of sample edges and pits are presented in Figures 5c and 5d.

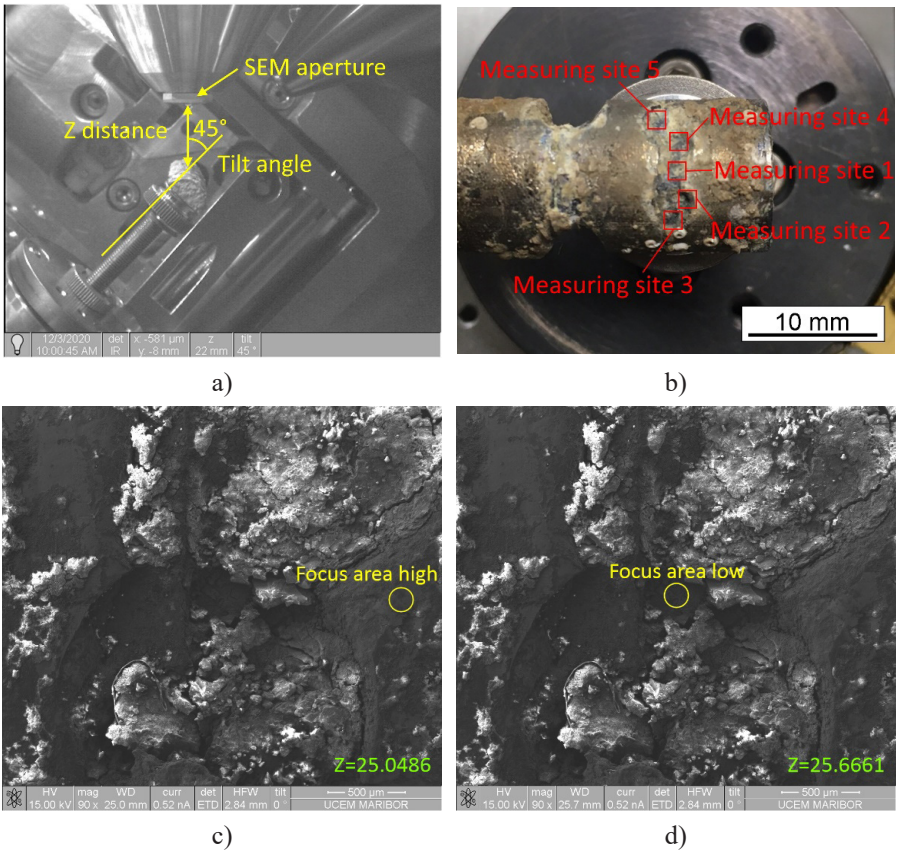

Figure 5. The NiTi rod after 18 months of exposure a) Measuring equipment b) The position of the measured pit c) High focus measuring - area 1 d) Low focus measuring - area 1

Table 3. Pit depth calculated by the SEM

	Z high Z_H	Z low Z_L	Pitting depth d_{pit}	
Measurement 1	25.0486	25.6661	0.6175	mm
Measurement 2	26.1029	26.5829	0.4800	mm
Measurement 3	30.0068	30.7716	0.7648	mm
Measurement 4	26.2902	26.5852	0.2950	mm
Measurement 5	30.6398	31.7052	1.0654	mm

Based on the fits of the linear models to the data shown in Table 3, the monthly corrosion rates equal 0.0414176 mm/month, 0.0621264 mm/month, and 0.124253 mm/month, assuming that corrosion starts immediately, or after six and twelve months of exposure (, , and months). More precisely, the depth of pitting corrosion in the three cases can be represented by the following linear corrosion models:

$$d(t) = 0.0414176t \tag{4}$$

$$d(t) = 0.0621264(t-6) \tag{5}$$

$$d(t) = 0.124253(t-12) \tag{6}$$

The three models can also be interpreted in terms of corrosion rates. Namely, expression (4) corresponds to the model whose monthly pitting corrosion rate was the lowest, expression (5) corresponds to the model with a moderate monthly corrosion rate, while expression (6) describes the model with the highest monthly corrosion rate.

The fitted linear models (4-6) are presented graphically in Figure 6, and show a functional dependence of pitting corrosion depth on the time of exposure.

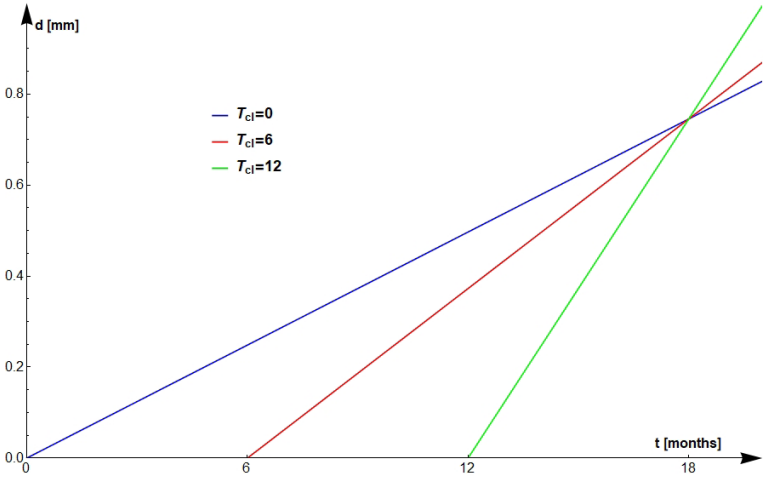

Figure 6. Fitted linear models

Figure 7 shows the residual plot of the models described by expressions (4) - (6). The graph shows if the residuals follow the normal distribution well. According to Figure 7, the fitting characteristics of models (4) and (5) are not good enough, as there are significant deviations from the straight line. On the contrary, in the case of model

(6) the probability plot is normal, and the points generally follow a straight line. There is no evidence of non-normality, outliers, or unidentified variables. This confirms that model (6) fits the data from Table 2 in the best way.

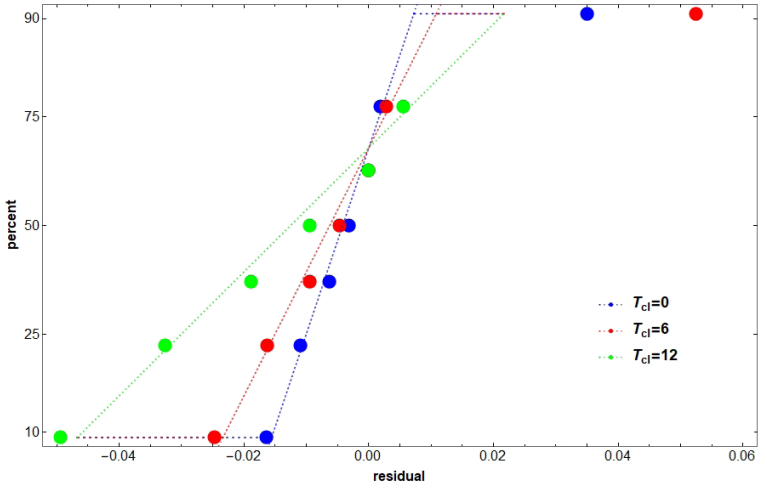

Figure 7. Normal residual plot of the fitted linear models

For the fitted model (6) in the case of , the variance around the fitted values is 0.0899699. More precisely, the calculated mean squared error is 0.0899699, which results in a low Standard Deviation value of the distance between the data values and the fitted values. The corresponding Standard Deviation equals 0.299950. The R squared (R^2) value of the model (6) is R^2=0.860677, which means that the variation of 86.07% in can be explained by a fitted model. In that sense, it can be concluded that the model represented by expression (6) describes the pitting corrosion values very well.

3.2. NiTi rod pitting chemical composition

The EDX analysis determined the chemical composition of the pit and the pit edge at 5 points on the NiTi rod. There were 6 spectra for each point scanned. Figure 8 shows the average chemical composition obtained by means of the EDX analysis for the pit and the pit edge.

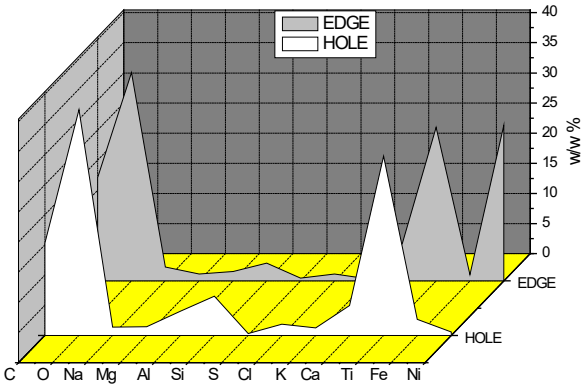

Figure 8. The average chemical composition of the pit edge and the pit based on the EDX analysis

As shown in Figure 8, the chemical compositions of the pit and the pit edge differ slightly in terms of the majority of the elements detected through the EDX analysis. A small increase in the oxygen content indicates slightly more intensive corrosion in the pit than on the edge, which was expected, considering that the corrosion flows with the formation of pitting.

Interestingly, according to Figure 8, there is another difference between the chemical compositions of the edge and pit - the pit has a rather increased content of aluminium and silicon compared to the edge, which can be attributed to the deposition of silicate (sand) in the pit.

The notable differences in the corrosive behaviour of the analysed NiTi rods at different pitting points can be attributed to the content of nickel. Namely, a slightly lower content of titanium on the edge compared to the pit, along with a significant difference in the average content of nickel on the edge (~ 26%) and in the (pit ~ 4.5%), indicate an excessive degradation or corrosion of the nickel during pitting. The presence of nickel could not be detected at most of the points measured.

4. Conclusion

This article investigated the behaviour of a NiTi rod in seawater at a depth of 3 m below the sea surface. The research relied on a linear corrosion model, and confirmed that the minimum corrosion rate was 0.04 mm/month, while the maximum corrosion rate was 0.12 mm/month. The presence of Si was observed in the pit, which accelerated the degradation of the pit. The whole process of corrosion of a NiTi rod in the sea is based on the fact that the degradation of Ni is more affected by pitting corrosion than the degradation of Ti.

Based on the statistical analysis, it was proven that the model with a moderate monthly corrosion rate, whose monthly corrosion rate was the highest, is also the most suitable for describing pitting corrosion depth on similar alloys. Statistical analysis shows that a NiTi rod in a seawater environment shows the tendency of a delayed onset of pitting corrosion i.e., corrosion occurs after 12 months of exposure to environmental influences. In that sense, rapid corrosive processes with intensive pitting start on the metal structures of a NiTi rod after 12 months of exposure.

Acknowledgement:

This paper is the result of the research on the different influences of seawater on the production and application of smart materials of Shape Memory Alloys in the Maritime industry. Project PROCHA-SMA is a part of the EUREKA Project, which is realised jointly by the Faculty of Stomatology in Belgrade, Zlatarna Celje d.o.o. Belgrade, Serbia and the Faculty of Maritime Studies Kotor, University of Montenegro.

Funding: The research was funded by the EUREKA PROGRAM PROCHA-SMA E!13080, the Ministry of Science, the Republic of Montenegro and bilateral projects: Slovenia – Montenegro and Serbia – Montenegro (BI-ME/18-20-024).

References:

1. J. Mohd Jani, M. Leary, A. Subic, and M. A. Gibson, "A review of shape memory alloy research, applications and opportunities," *Mater. Des.*, vol. 56, pp. 1078–1113, 2014, doi: 10.1016/j.matdes.2013.11.084.
2. A. Ölander, "An electrochemical investigation of solid cadmium-gold alloys," *J. Am. Chem. Soc.*, vol. 54, no. 10, pp. 3819–3833, Oct. 1932, doi: 10.1021/ja01349a004.
3. Weimin Huang, Shape Memory Alloys and their Application Disertation, University of Cambridge Department of Engineering, to Actuators for Deployable Structures, 1998.
4. D. Hodgson and S. Russel, "Nitinol melting, manufacture and fabrication," *Min lnvas Ther & Allied Technol,* vol. 9, no. 2, pp. 62-63, 2000.
5. Mwangia, J. W., L. T. Nguyena, V. D. Bui, T. Berger, H. Zeidler and A. Schuberta, "Nitinol manufacturing and micromachining: A review of processes and their suitability in processing medical-grade nitinol," *Journal of manufacturing processes,* vol. 38, pp. 357-358, 2019.
6. Ivošević, R.; Majerić, Š.; Vukićević, P.; Rudolf, M. A Study of the Possible Use of Materials With Shape Memory Effect in Shipbuilding. J. Marit. Transp. Sci., 2020, 3, 265–277.
7. Merola, C., H. W. Cheng, K. Schwenzfeier, Y. H. Chen, H. A. Dobbs, J. N. Israelachvili and M. Valtiner, "In situ nano- to microscopic imaging and growth mechanism of electrochemical dissolution (e.g., corrosion) of a confined metal surface," *PNAS,* vol. 36, no. 114, pp. 9541-9546, 2017.
8. J. B. William, E. W. Frederick, „A summary of recent research on the nitinol alloys and their potential application in ocean engineering", Ocean engineering, t.1, pp. 114-116, 119, 1968.
9. S. Sathish, U. S. Mallik, T. N. Raju, Corrosion Behavior of Cu-Zn-Ni Shape Memory Alloys, Journal of Minerals and Materials Characterization and Engineering, pp.49-54, Vol.1, No.2, 2013, http://dx.doi.org/10.4236/jmmce.2013.12010
10. D. Y. Li, "A new type of wear-resistant material: pseudo-elastic Ni-Ti alloy," *Wear,* vol. 221, pp. 116-121, 1998.
11. Ivošević, Š., Kovač, N., Vastag, G., Majerič, P., Rudolf, R.: A Probabilistic Method for Estimating

the Influence of Corrosion on the CuAlNi Shape Memory Alloy in Different Marine Environments, Crystals 2021, 11, 274. https://doi.org/10.3390/cryst11030274
12. Ivošević Š., Vastag G., Majerič P., Kovač D., Rudolf R. (2020) Analysis of the Corrosion Resistance of Different Metal Materials Exposed to Varied Conditions of the Environment in the Bay of Kotor. In: . The Handbook of Environmental Chemistry. Springer, Berlin, Heidelberg. https://doi.org/10.1007/698_2020_644
13. Ivošević, Š., Rudolf, R., Kovač, D., "The overview of the varied influences of the seawater and atmosphere to corrosive processes", 1st International Conference of Maritime Science & Technology, NAŠE MORE, Dubrovnik, 17 - 18 October, 2019, Croatia. pp.182-193
14. „Coastal Sea Ecosystem Monitoring Program of Montenegro during 2019. and 2020., Institute of Marine Biology, University of Montenegro.
15. J. Paik, S. Kim, S. L.-O. Engineering, and undefined 1998, "Probabilistic corrosion rate estimation model for longitudinal strength members of bulk carriers," Ocean Engineering, Volume 25, Issue 10, November 1998, Pages 837-860
16. Wang, G., Spencer, J., Elsayed, T.: "Estimation of corrosion rates of oil tankers", 22nd International Conference on Offshore Mechanics and Arctic Engineering, Cancun (Mexico), 8–13th June, 2003, pp. 253–258
17. Soares, C.G., Garbatov, Y.: "Reliability of maintained, corrosion protected plates subjected to non–linear corrosion and compressive loads", Marine Structures, Vol. 12, No.6, 1999, pp. 425–445
18. Š. Ivošević, R. Meštrović, N. Kovac: "An Approach to the Probabilistic Corrosion Rate Estimation Model for Inner Bottom Plates of Bulk Carrier", Shipbuilding: Theory and Practice of Naval Arhitecture,Vol.68 No.4, December 2017., p. 57-70, 2017., doi:10.21278/brod68404
19. Ivošević, Š., Meštrović, R., Kovač, N. (2018), Probabilistic estimates of corrosion rate of fuel tank structures of aging bulk carriers, International Journal of Naval Architecture and Ocean Engineering, 13 pages, https://doi.org/10.1016/j.ijnaoe.2018.03.003; ISSN: 2092-6782.
20. Špiro Ivošević, Romeo Meštrović, Nataša Kovač, „A Probabilistic Method for Estimating the Percentage of Corrosion Depth on the Inner Bottom Plates of Aging Bulk Carriers", Journal of Marine Science and Engineering 8(6):442, 2020. DOI: 10.3390/jmse8060442
21. Paik, J.K., Thayamballi, A.K.: "Ultimate strength of ageing ships" Journal of Engineering for the Maritime Environment, Vol. 216, No. M1, 2002, pp. 57–77

ISSN 0554-6397
Prethodno priopćenje
(*Preliminary communication*)

Davor Bolf
E-mail: dbolf@riteh.hr
Marko Hadjina
E-mail: hadjina@riteh.hr
Albert Zamarin
E-mail: zamarin@riteh.hr
Mario Iveković
E-mail: mivekovic@riteh.hr
University of Rijeka – Faculty of Engineering; Vukovarska 58, 51000 Rijeka, Croatia

Definition of Deformations and Stresses of Large Ship Blocks within Transportation and Manipulation

Abstract

Deformations and stresses during the transport and manipulation of large ship blocks within ship assembly and erection stages are a common and significant issue, particularly in the construction of complex ships and variable production mix, as is the case in many European shipyards. The appearance of deformations and stresses requires adequate addressing with the aim of their early determination and reduction with a goal to reduce a significant number of working hours spent for the large ship blocks transport preparation, for the transport and manipulation itself, and for the reworks. The appearance of residual stress in blocks that are not adequately addressed can be an issue in the exploitation, reducing the quality and ship service life. In this paper, the authors present the procedure of determining deformations and stresses in the large ship block. The procedure is based on computer modelling and numerical analysis of the selected ship block. Various scenarios of the foundations' arrangement and the arrangement of the transport hooks were analysed, and the optimal solutions were proposed. The procedure allows determining deformations and stresses at an early stage of ship technology design to define the adequate preparation for ship block foundations layout, transportation and manipulation before production starts. In doing so, it is expected to reduce deformations and stresses itself, necessary working hours for block accommodation, transportation and manipulation and to reduce repair works. Such procedure application is expected to raise the efficiency of the overall ship production process and the quality of the final product. Finally, further research is proposed regarding various scenarios of technological procedures, ship blocks structures or used materials.

Keywords: shipbuilding, deformations, stresses, transport of large ship blocks, 3D Experience model, numerical analysis, efficiency

1. Introduction

Assembly is the process of joining and manipulating several steel parts and joining them in one larger structure, called blocks, [1]. The production of the block is usually situated as an extension of the shipyard's panel line, creating a more fluent flow of material from the panel line to the block assembly area, [2]. The blocks are transported to a dry dock or the slipway upon assembly. Therefore, the transportation of the building materials is an essential part of the shipbuilding assembly process. It summarises procedures that involve horizontal, vertical or/and complex movements of materials and finished products, thus securing the continuity of workflow and finalisation of the final product, [3]. It is essential to predefine, predict and develop proper transformation procedures, as deformations and stresses can occur during the transport and manipulation of large ship sections. These deformations can negatively impact overall process duration, cost, and quality, due to corrective actions needed for correcting them. Therefore, the article's goal is to describe and elaborate on the process of early detection of deformations and stresses. The described procedure is based on the selected ship block computer-aided modelling and finite element analysis. Several scenarios were tested in terms of the block foundations number and their spacing and the number of transport mounting points and their position on the given ship block. The established procedure determines deformations and stresses at an early stage of designing shipbuilding technology. It also supports decision-making within defining technological procedures, particularly the block position on foundations and its adequate preparation for transport and handling. Furthermore, it is expected to reduce deformations and stresses in the ship block, reduce the required working hours for adequate section preparation for accommodation and transport, and reduce subsequent repair work. At the same time, the application of this procedure is expected to increase the efficiency of the production process and the quality of the final product.

2. Ship block modelling

A chemical tanker ship's double bottom block, [4], (block dimensions 22.50 m x 32.20 m x 5.00 m, with a total mass of 467.34 t) was modelled using software 3D Experience within its Structure Functional Design app. The model was detailed to the level needed for targeted FEM analysis and scenarios in question. Using the methodology described in [5, 6], all primary elements were modelled, alongside secondary stiffeners, creating the model from available documentation. The final model of the double bottom block can be seen in Figure 1.

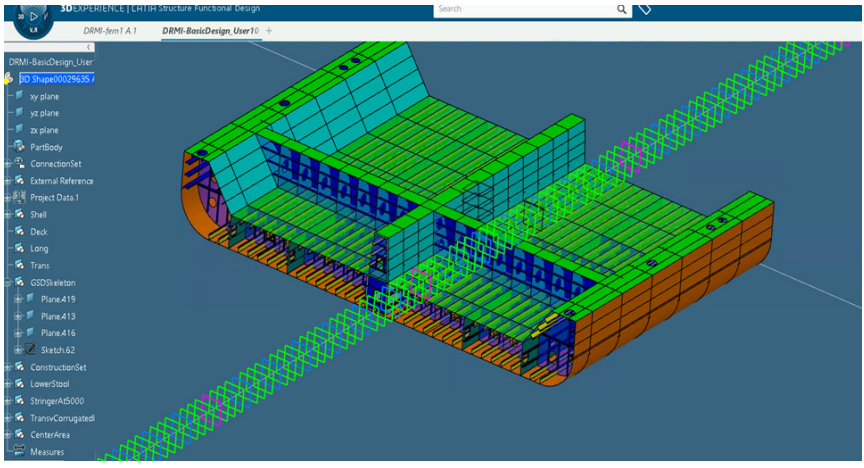

Figure 1: Model of ship double bottom block [7].

The modelling of the structural details was up to the level of stiffeners and large openings. The brackets, penetrations smaller than 600x400 mm were not taken into consideration. The slots and profile end-cuts were not defined. Possible piping and outfitting elements that may be installed in the actual section during the phase of block assembly were not modelled. Some adjustments on the placement of the stiffening elements were taken to minimise the time needed to repair the mesh, keeping in mind that the mesh will be automatically generated from the Structural Functional Design model (SFD model). The detailed modelling can be seen in Figure 2.

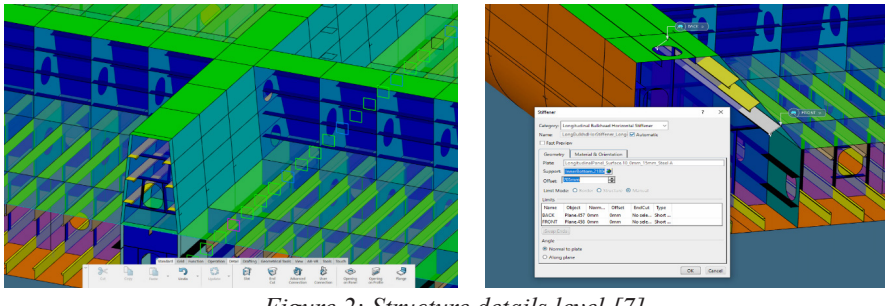

Figure 2: Structure details level [7].

3. Finite elements model creation

The SFD model was meshed automatically using the automatic meshing process available in 3D Experience platform. The FEM and proxy geometry models needed to be created prior to activation of the automated meshing, as shown in Figure 3. The

mesh size for 1D and 2D elements was set to 200 mm, resulting in a total of 1253670 elements. The stiffeners were meshed as 1D beam elements, while the plating was meshed using the 2D triangular and quadrilateral mesh elements. The properties of the stiffeners and plating elements were taken directly from the SFD model. Thus, no additional input was needed for defining the beam and shell elements. The automatic meshing menu and mesh model can be seen in Figure 3.

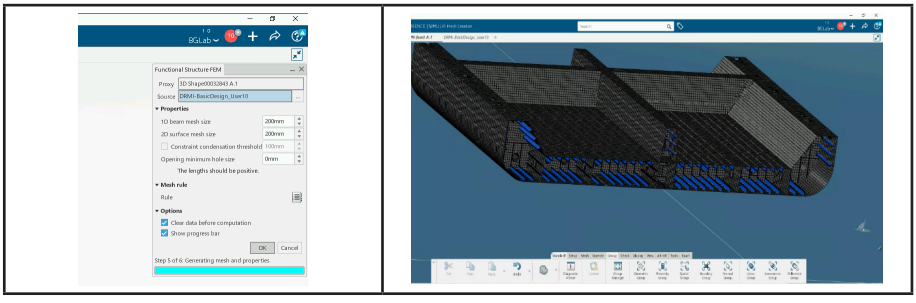

Figure 3: Automatic meshing menue and model mesh [7]

Though the meshing in 3D Experience is an automated process, some areas need to be repaired manually, especially around the openings. The mesh quality was checked alongside mesh connectivity and free edges, and the mesh was repaired and prepared for scenario definition.

4. Scenario definition

Following the finite elements model creation, scenario cases were defined and analysed to improve solutions regarding block foundations number on the ground and hooks number in transport, in correlation with identified structure deformation and stress. A total of five cases of foundations layout and five hook layouts were analysed, varying foundations and hook positions and numbers, thus creating 10 different scenarios.

Scenarios were defined and analysed within 3D Experience Structural Scenario Creation module in the SIMULIA application. The linear elastic material was defined as shipbuilding grade A steel with properties shown in Table 1. The factor of safety of 1.5 for the linear FEA model was considered, and therefore, the allowed von Mises stress in the structure should be under 180 MPa (with dynamic factor for lifting included in the factor of safety and may allowable stress).

Table 1: Material properties – shipbuilding steel grade A.

Density [kg/m^3]	7850
Young's Modulus E [GPa]	210
Yield Strength [MPa]	235
Tensile Strength [MPa]	400-520
Poisson's ratio	0.3

The load was applied as gravity load in the z-direction of the model, as seen in Figure 4. The gravity load was calculated and increased to 10.33 m/s^2 to compensate for missing weights not modelled in SFD model. The gravity load was used for both foundation and hook scenarios. The foundations were modelled using simplification on the safe side and constraining the translation and rotation. The same constraints were applied to the hooks in the model analysing hook positions.

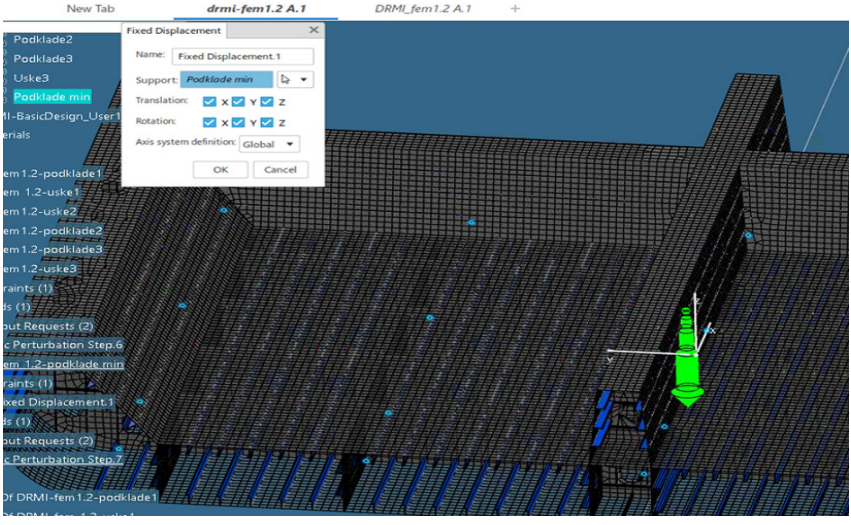

Figure 4: Mesh model representing boundary and loading condition [7].

5. Scenario simulation and analysis

The foundations are usually placed under the stiffened parts of the structure. Therefore, their arrangement will depend on the topology of the section and the placement of the primary structure in the section. A total of 5 different placements for foundation elements were analysed, differing their position and number used in the model. The foundation arrangement for each case can be seen in Figure 5. The foundations are presented with red dots.

Case 1
58
foundations

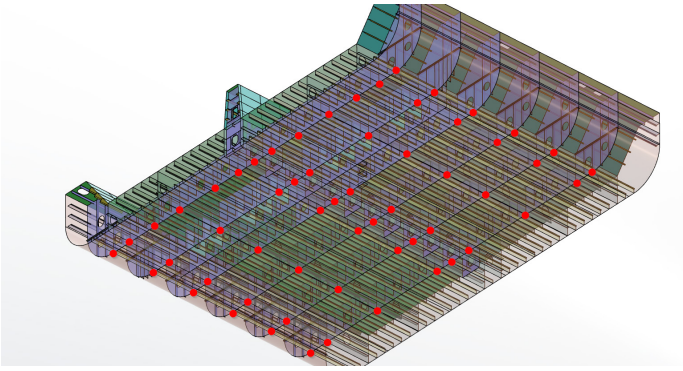

Case 2
38
foundations

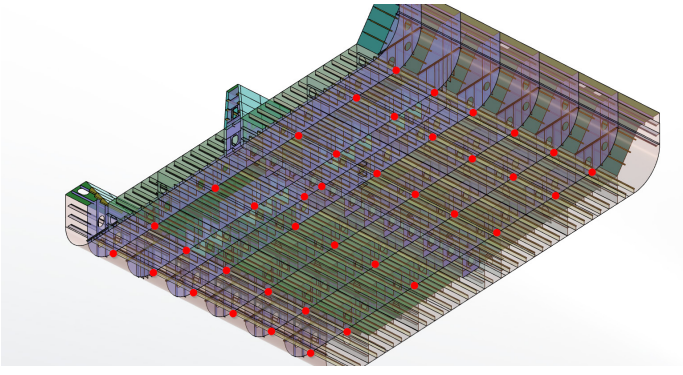

Case 3
31
foundations

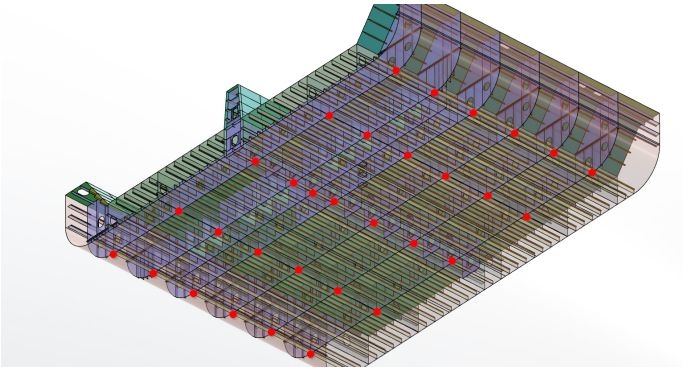

Case 4
20
foundations

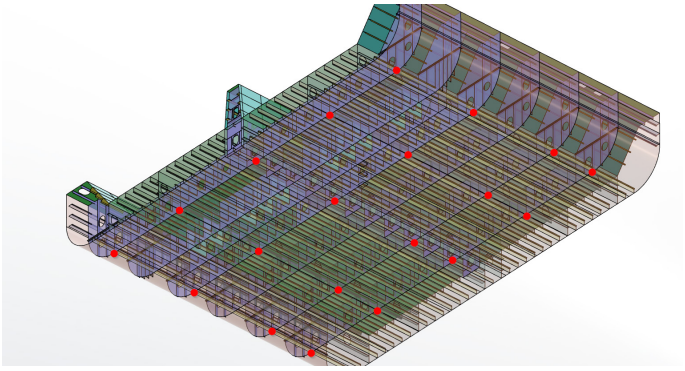

Case 5
15
foundations

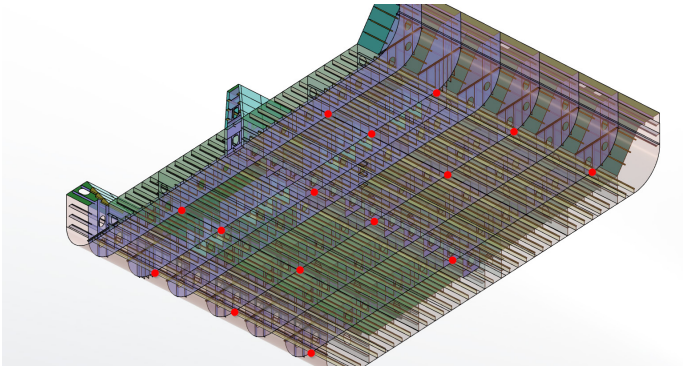

Figure 5: Foundation position for five cases.

For Case 1, a total of 58 foundations were modelled. The maximum stress of 35.5 MPa will occur in the foundations near the bilge plating, while a maximum resulting displacement of 1.86 mm occurs near the edges of the section on unsupported plating. In Case 2, the number of foundations is reduced, which resulted in a slight increase of stress to 58.5 MPa, with a resulting maximum resulting displacement of 2 mm, still positioned near the free edge of the section. Foundations arrangement for Case 3 yields slightly higher stresses. The maximum stress for this case is 82.4 MPa, with a resulting displacement of 1.91 mm occurring at the free edge of the section. Case 4 was calculated for a total of 20 foundations. The resulting displacement of the structure is 1.91 mm, and the maximum stress is 110 MPa. The arrangement with 15 foundations, designated as Case 5, yielded stresses of 171 MPa, which was close to the limit of allowable stress. Still, the resulting displacement of the section was 2.19 mm, occurring on the free edge of the section. However, the resulting displacement of the structure in any other part of the structure is under 1 mm. The comparative results for the stresses and displacements are presented in Table 2.

Table 2: Comparative results for stress and displacement for five different cases.

Scenario case	No. of foundations	Stress [MPa]	Displacement [mm]
Case 1	58	35.5	1.86
Case 2	38	58.5	2.00
Case 3	31	82.4	1.91
Case 4	20	110	1.91
Case 5	15	172	2.19

Stresses for cases 1,2,3 and 5 can be seen in Figure 6, occurring in the structure just above the foundations (Case 4, being similar to Case 3, was omitted from representation). However, the maximum displacement is visible on the edges of the section, and it is uninfluenced by the support number and arrangement, as seen in Figure 7.

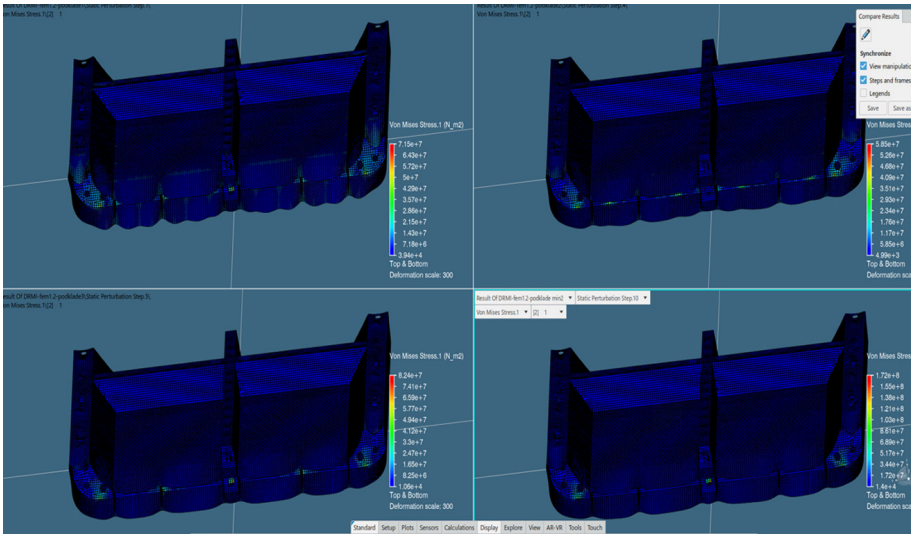

Figure 6: Stress on section for cases 1,2,3 and 5 [7].

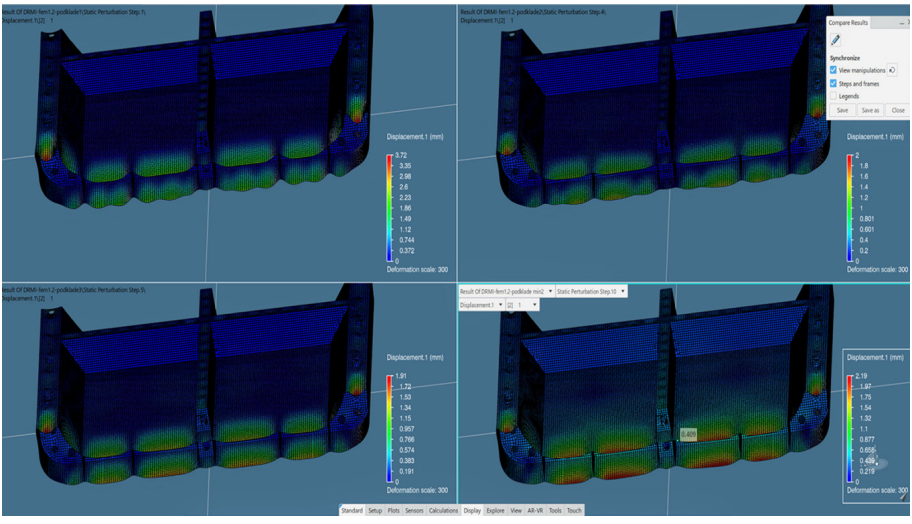

Figure 7: Displacement on section for cases 1,2,3 and 5 [7].

Simulation for different lifting arrangements was made for five cases in total. Cases are numbered from Case 6 to Case 10, respectively. Case 6 and Case 7 have the same number of hooks, but the attachment in Case 7 was placed on the unsupported plate without any primary stiffening member beneath the attachment point. Case 8 attachment points were placed closer to the centre of gravity of the section. Two hooks were attached near the stool section on each side of the centreline, and four hooks were placed on the tank bottom plating above the floor element in the double bottom structure. The placement was symmetrical to the centre line. The attachment points for Case 9 were the same as in Case8. The number of hooks attached to the stool remained the same, while the number of hooks in the tank bottom plating was four on each side. In Case 10, the hooks were attached to the longitudinal double bottom girder. The attachment points are marked with red circles, while hook arrangements are presented with red dots, see Figure 8.

Case 6
4 attachment points
4 hooks

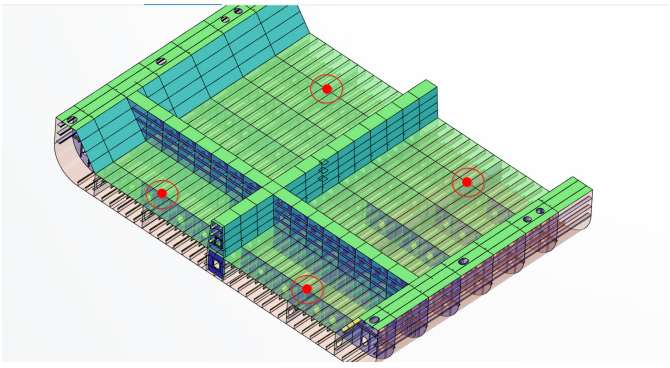

Case 7
4 attachment points
4 hooks

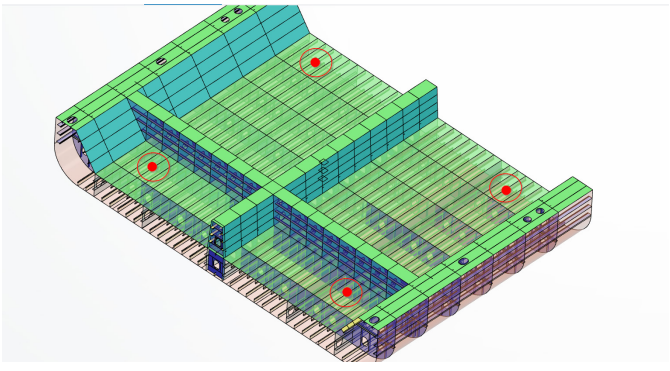

Case 8
4 attachment points
8 hooks

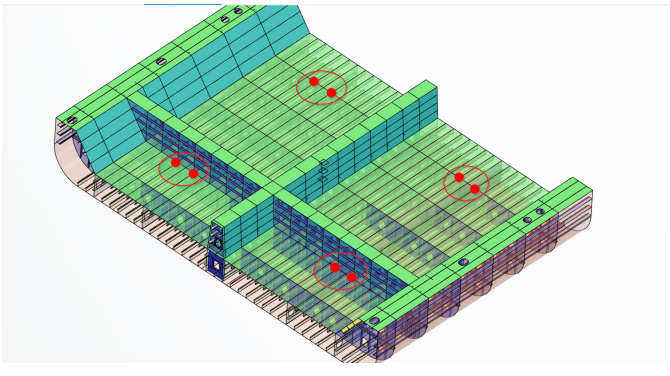

Case 9
4 attachment points
12 hooks

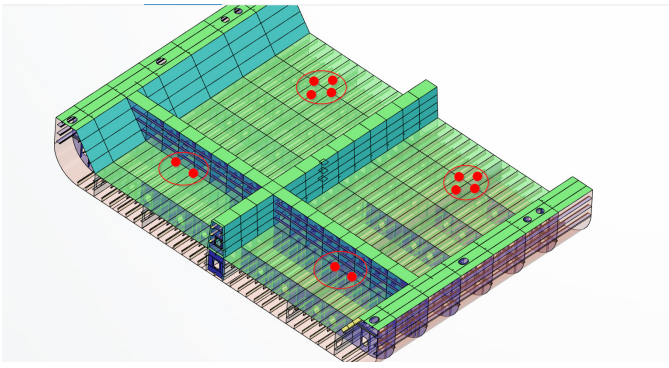

Case 10
4 attachment points
10 hooks

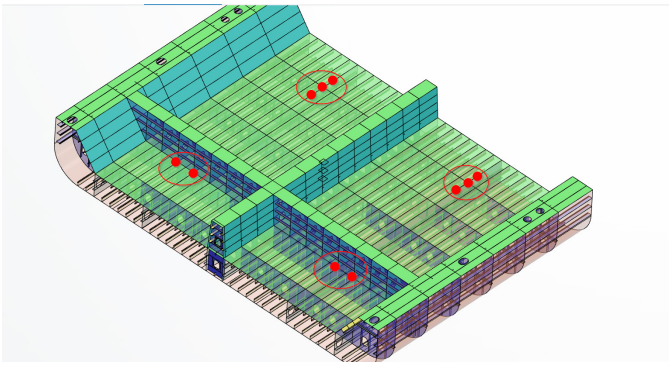

Figure 8: Hook position for five cases.

The resulting stress and displacement values are presented in Table 3. The stress on the structure for cases 6 and 8 was above the 180 MPa, and Case 7 arrangement yielded maximal stress of 458 MPa, which is close to the breaking strength of the steel plating. Case 7 also exhibits the highest deformation. However, this is usually not a real case scenario, as the hooks are not placed on any supporting structure; thus, higher loads and higher displacements are calculated. Stress for Case 9 and Case 10 is below the limit. The arrangement with 12 hooks in Case 9 is marginally better than in Case 10. However, considering that Case 10 can be done with fewer attachment points, thus reducing the welding cost and time. The author must stress out the fact that these cases, Case 9 and Case 10, have unusual hook arrangements to cover the different variations of lifting to test different lifting arrangements (theoretical and real-life case scenarios). The results for stress and displacement can be seen in Figure 9 and Figure 10, respectively.

Table 3: Comparative results for stress and displacement for five different hooking arrangements.

Scenario case	Number of hooks	Stress [MPa]	Displacement [mm]
Case 6	4	247	4.83
Case 7	4	458	14.2
Case 8	8	254	4.87
Case 9	12	139	4.40
Case 10	10	142	4.55

Similarly to foundation calculation, the displacement is maximal in the edge area of the section. The position and number of hooks do not significantly influence the maximal displacement, as it occurs due to the section's unsupported and unstiffened edge. The exception is Case 7. However, Case 7 can be excluded, as it is not a real case scenario, while Case 9 was very similar to Case 10 and was omitred from the presentation.

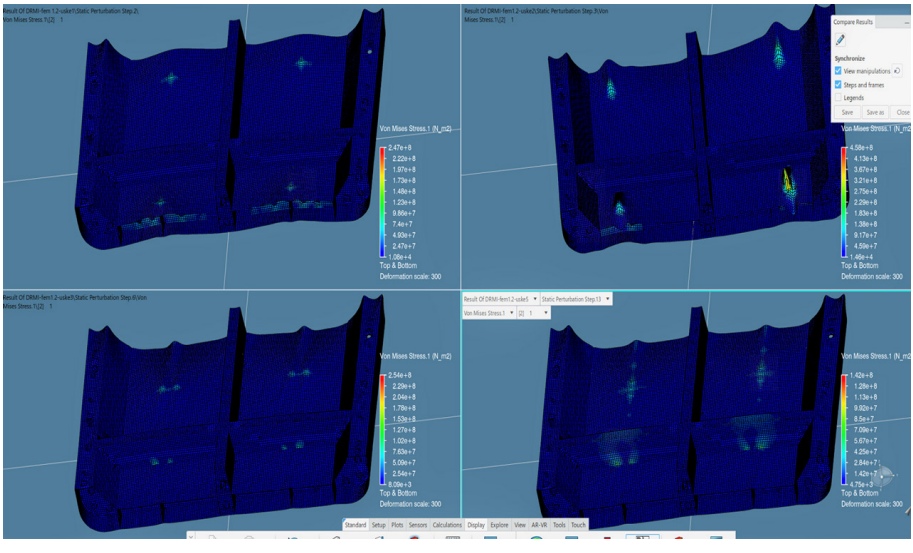

Figure 9: Stress on section for cases 6,7,8 and 10 [6].

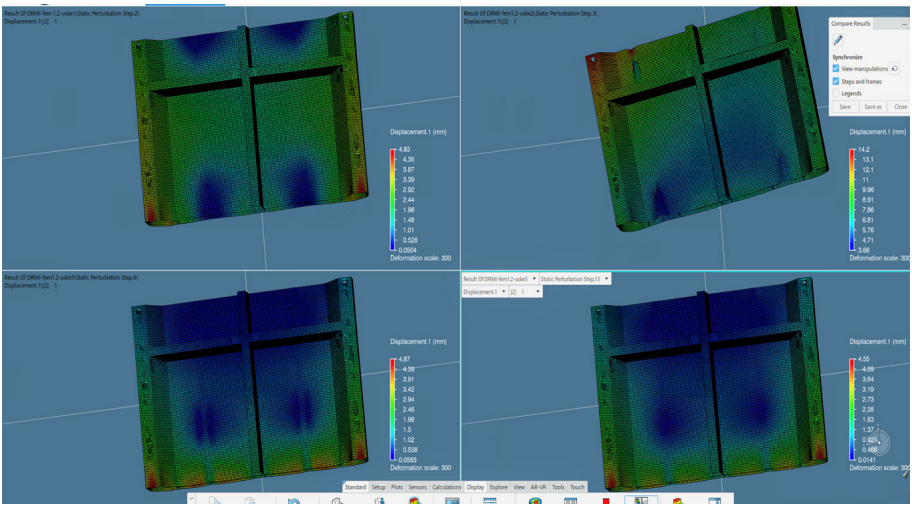

Figure 10: Displacement on section for cases 6,7,8 and 10 [7].

6. Conclusion

The presented procedure enables the definition of stress and deformation in ship blocks in the early phase of planning the layout and number of foundations and the layout and number of hooks for transport, which primarily enables:

- Reducing the number of foundations and related works
- Early prediction of stress and deformation in blocks during production and transport
- Early prediction of adequate positions of transport hooks, especially for complex outfitted structures
- Predicting adequate positions for temporary structural supports
- Reducing working hours and resources while increasing the overall efficiency and quality

The case study was made using the shipyards documentation for transportation and placement of the different sections. Cases were calculated based on the experience and workflow in a well-known shipyard. However, more cases could be analysed in future work using the optimisation tools, and optimal solutions could than be presented.

Acknowledgements

This research is supported by funds from the support research at the University of Rijeka for the project “Development of Methodology for Ship Design and Production towards Industry 4.0. Concept”

References

1. Eyres, D. J., Bruce, G. J. (2012) *Ship Construction.* Elsevier Ltd.
2. Lamb, T. (2003) *Ship Design and Construction, Volume I*. New Jersey, SNAME.
3. Storch, R.L. et al. (1995) *Ship Production*. New Jersey, SNAME.
4. Shipyard "3.MAJ ". *Projektna dokumentacija*. Rijeka.
5. Bolf, D., Hadjina, M., Zamarin, A., Matulja, T. (2020) Methodology of Integrated Design of the Ship Structure and Production Using the 3DExperience platform. In: Matulja, T. at. all. (eds) *Book of Proceedings of 24th Symposium on the Theory and Practice of Shipbuilding (in memoriam prof. Leopold Sorta)*, SORTA 2020, 15-16 October 2020, Rijeka, Croatia, Rijeka: University of Rijeka, Faculty of Engineering, pp. 235-242.
6. Bolf, D., Hadjina, M., Matulja, T. i Knapić, I. (2020) Implementation of Advanced Collaborative Platform for Project Based Learning in Naval Architecture Studies. *Pomorski zbornik*. Special edition (3),
7. Iveković, M. (2021) *Analiza naprezanja I deformacija pri manipulaciji sekcijama u proizvodnom procesu gradnje broda*, *Croatia,* Master's thesis, University of Rijeka, Faculty of engineering.

ISSN 0554-6397
Stručni članak
(*Professional paper*)

Darin Majnarić
E-mail: dmajnaric@riteh.hr
Davor Bolf
E-mail: dbolf@riteh.hr
Albert Zamarin
E-mail: zamarin@riteh.hr
Faculty of Engineering University of Rijeka, Vukovarska 58, Rijeka, Croatia

Structural Analysis of Hybrid Ro-Pax Ferry

Abstract

With the aim of improving the environmental sustainability in the field of maritime transport and with special reference to multimodality and 'green' solutions for coastal transport, within the *METRO* project (Maritime Environment-friendly TRanspOrt systems), funded under the Interreg VA CBC Programme Italy-Croatia, a project of a hybrid Ro-Pax medium range ferry for coastal navigation in the Adriatic area is developed. The paper presents a part of the conceptual design for the assessment of the global hull structure strength, which is not common for this phase of the project, and that is the structural analysis of the complete ship. For this purpose, a detailed computer model of the geometry of the whole ship was made, which includes all primary and basic secondary structural elements, with the aim that such a model can serve later as a good basis for classification and workshop documentation production during contract phase. Additionally, a preliminary calculation of the scantlings of the complete ship was performed according to *BV* rules and regulations using the *MARS2000* software package, with regard to bending and buckling. Loads were modeled according to real conditions for two unfavorable loading conditions, and static linear analysis was performed using the *LS-DYNA* software package. The global analysis of bending strength in still water could reveal problematic areas in the structure.

Keywords: preliminary design, Ro-Pax, hull structure, *FEA*

1. Introduction

Within the process of conceptual designs of ships, one of the basic activities is the design of the structure, which should within the first round of the design spiral define the basic structural layout, preliminary dimensions of all structural elements as a basis for estimating mass and cost of materials and hull construction. In the standard commercial procedure, the next step would be the preparation of complete classification documentation, selection of investors/owner followed by signing of the

contract and finally production of the workshop documentation. As this paper is result of a research project, so the investor / shipowner is unknown, the project did not aim to prepare a workshop or complete classification documentation, nor its confirmation by the classification society. Therefore, it was decided to make a structural analysis of the complete ship, and the goal was to check the global strength and confirm the calculation of the dimensions of structural elements against yielding and buckling. The remaining structural design assessment activities, such as fatigue assessment and ultimate strength calculation, have been omitted as they belong to the final, detailed structure assessment. It should be noted that this scope of work, modeling and structural analysis of complete ship, is not common at this stage of the conceptual design, due to the high consumption of human and computer resources, but it is still done because there is a lack of data to assess the load capacity of superstructures. The analysis of the structure is based on the initial calculations of the structure made by *Tehnomont shipyard Pula* and *Flow Ship Design* where the midship section are defined. Based on these data, the remaining parts of the structure were defined and dimensioned by the authors, as well as rest of *FEA* with the aim of verifying the calculated scantlings of the hull and superstructure [1]. Since the project did not envisage the preparation of hull classification documentation, and therefore no drawings such as *Shell expansion*, *Decks plans*, *Watertight and longitudinal bulkheads, Engine room structure*, *Superstructure*, it was necessary to determine the preliminary dimensions of the structure of other parts of the hull and superstructure outside the midship. This problem was solved by using the classification society Bureau Veritas software package MARS2000, which using the rules and regulations of the same classification society provides for class [2], supervision and possible construction, and which are integrated into the software package, all in order to determine the scantlings of the remaining part of the hull structure. This was done in such a way that the minimum required dimensions were determined for additional cross-sections with regard to the requirements such as longitudinal strength, minimum section modulus of cross-sections, minimum structural dimensions, as well as checking of structural elements against buckling. Later on, geometric model could be meshed and the elements could be given specific dimensions in terms of material type, as well as scantlings for plating thickness and dimensions of stiffeners based on their actual section modulus of cross section. After meshing and defining the physical properties of the material, the boundary conditions and loads were determined. The real load modelling approach was used, which included modelling the hydrostatic load according to the actual drought, and the load from the vehicle for the specific loading condition. Hydrodynamic analysis as well as accelerations were not considered. A static analysis was performed in the elastic region using the LS-DYNA software package [3], based on FEM, [4], [5]. Through analysis, the two most unfavourable loading conditions were observed, according to the recommendations of the classification society. Additionally, the possible influence of the superstructure above the main deck on the longitudinal strength was observed, but due to lack of time, detailed analysis was not performed, as well as racking phenomena, [6], although the designer takes into consideration

racking stiffens where front and sides of superstructures and deckhouses is to be extra stiffened wherever necessary by racking bulkheads, [7]. Results of the global strength analysis that taking into account only static load are presented in form of displacements and stresses with aim to spot high stress area as a base for further structural analysis involving wave load and buckling strength criteria.

2. Vessel structural arrangement

The designed vessel presented is a Ro-Ro passenger ship, Figure 1, Table 1, compliant with SOLAS regulations for Short International Voyages (excluding US waters), in accordance with builder's standards and to comply with the listed Rules and Regulations. The Vessel is a twin screw, twin rudder, dual fuel-driven ship of welded steel construction including superstructure and wheelhouse, with one cargo deck and one hostable deck for cars. The hull with bulbous bow, transom stern, twin skegs and lines is so designed to ensure good seaworthiness and maneuverability. The hull under the freeboard deck is divided into sufficient watertight compartments, to satisfy damage stability as well as SRtP requirements according to the SOLAS regulations. The vessel shall have a capacity of abt. 630 lm for trailers or area of abt. 2020 m^2 for cars and transporters on the level of main garage decks. In addition to that, the area of abt. 1865 m^2 for cars on hostable car deck is ensured. Further, it will accommodate abt. 1340 passengers and 75 crew members. The cargo section consists of fully enclosed main cargo hold suitable for storing of trucks and other wheeled cargoes, as well as hostable car deck for stowage of cars only. Loading and unloading of wheeled cargo is performed by two ramps, one stern and other bow with hinged arms. All vehicle decks are designed to carry vehicles with fuel in their own tanks. Hull of the vessel is divided on following main compartments: fore and aft peak, double bottom / side tanks, engine rooms. The double bottom is extended between fore and aft peak bulkheads and subdivided as shown in *GAP*, Figure 1. Double bottom is provided in engine rooms for storage of water, lubricating oil and other service tanks. The vessel including its hull, machinery and equipment is to be constructed in accordance with the Rules of the Classification Society of Bureau Veritas to obtain the following Class notations: I ✠HULL ✠MACH; Ro-Ro Passenger Ship, Unrestricted navigation, SRTP, POWERGEN(DUALFUEL), ✠AUT-UMS, ✠SYS-NEQ, ELECTRIC HYBRID (PM, ZE), MON-SHAFT, INWATERSURVEY. The hull is arranged with transverse watertight subdivision below main deck. Passenger deck and Main deck are supported by transverse frames. Pillars are arranged in the service spaces below the Main deck and in the superstructure in order to minimize steel weight and structure height. The cargo area is arranged without pillars. Structural arrangement is based on longitudinal framing system. Transverse framing system is arranged for superstructure sides. Bilge keels 2 x HP320, having abt. 35% of ship length. Frame spacing is 800 mm. Main transverse frame spacing is 3200 mm. Longitudinal stiffener spacing on decks is generally 600

mm. Material main hull in general is mild steel (MS). Cargo area will have one fixed deck and one hostable deck for Ro-Ro cargo. Cargo hold is made as fully enclosed Ro-Ro space. Bow ramp with suitable bow door and stern ramp will be implemented for facilitated loading/unloading.

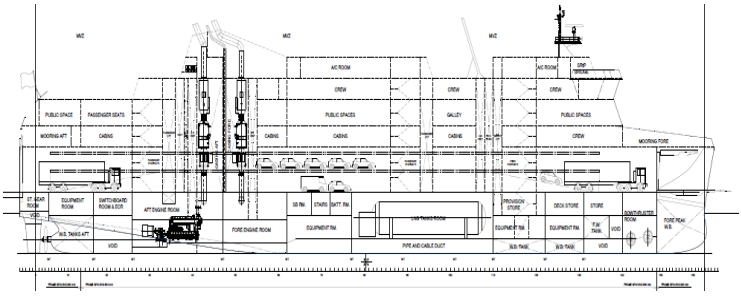

Figure 1: General arrangement plan of Ro-Pax ferry

The front and sides of superstructures and deckhouses is to be extra stiffened wherever necessary by racking bulkheads. The funnel will be made of steel plates and properly stiffened from the inside.

Table 1: Ro-Pax ferry main particulars

Length, overall	129.27	m
Length, between perpendiculars	124.45	m
Breadth, moulded	23.60	m
Hull depth to freeboard deck (midship)	8.00	m
Draught, scantling	5.60	m
Draught, design	5.25	m
Deadweight (at scantlings draught)	abt.2240	t
Deadweight (at design draught)	abt.1400	t
Gross tonnage	15040	GT
Main engines MCR	2x4000	kW @ 750 rpm
Design speed (design draught)	abt.15.5	knots
Maximum trial speed (design draught)	16.1	knots

3. Structural model

Modelling the structure for FEM analysis differ from the standard structural modelling for basic and detail production. In order to prepare graphical and surface model of the ship some necessary simplifications needed to be made and model was adjusted to easily mesh the surfaces and proceed with the structural analysis. Upon completion of the project setup, the hull shape was inserted into the model. Following the methodology presented in [8], and adopted to FEM modelling, first hull plating and decks were created using the available 3D software for modelling of the vessels. Later on, watertight bulkheads and longitudinal bulkheads were modelled. After the bulkheads, all primary structure was modelled (deck girders and beams as well as web frames and floors). Structure was modelled from double bottom to the wheelhouse deck, creating the structure one deck at the time. In order to prepare the model for meshing, all plates needed to be cut at the intersections and prepared for meshing. All major openings were created, but not the manholes, lightning holes in floors and beams and doors in the bulkheads. Hull and deck longitudinals were also modelled, thus creating the structure from first two stages of modelling presented in [8], while structural details were not modelled. Entire geometry of the ship is presented on Figure 2 and Figure 3 through section rings.

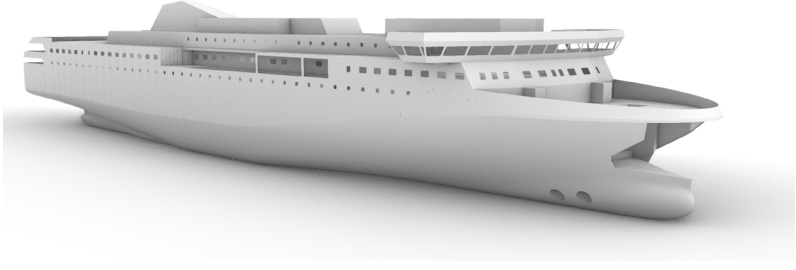

Figure 2: Hull 3D render geometry model of the whole ship

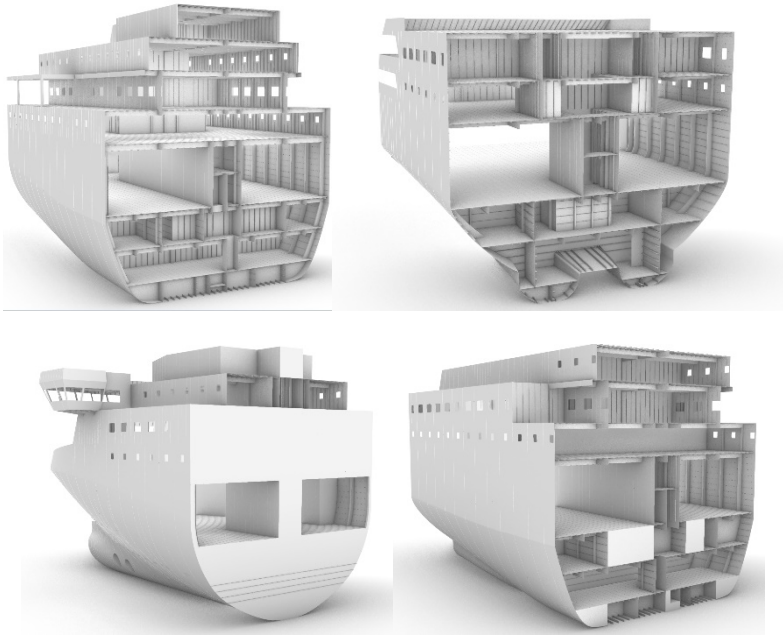

Figure 3: Internal structural geometry, frames FR0-FR30 (top left), FR30-FR70 (top right), Fr70-Fr110 (bottom left) and Fr110-Fr130 (bottom right)

4. Preliminary structural design

In order to model the structure within the *FEA* procedure, it is necessary to determine the dimensions of all structural elements. The standard design procedure would include the production of basic classification drawings of the structure from which all dimensions of the primary and secondary hull elements can be listed, [9], [10]. As this was not provided, the scantlings of the structural elements on the midship section (midship section preliminary draft) were first determined on the basis of the trim and stability book document over the longitudinal strength calculation. Input data for scantlings calculation are still water bending moment obtained from the mentioned calculation/document and wave vertical bending moment determined according to the rules and regulations of BV classification society [2] and are shown in Table 2 (left).

Table 2: Hull girder loads (left) and section modulus and inertia (right)

Vertical Bending Moment

	Hogging (kNm)	Sagging (kNm)
S.W.B.M. Builder's proposal in Basic Ship Data	300 000.	0.
S.W.B.M. Builder's proposal at X = 61.5 m	-	-
S.W.B.M. preliminary value at midship	344 410.	- 256 411.
S.W.B.M. preliminary value at X = 61.5 m	344 410.	- 256 411.
Rule Vertical Wave Bending Moment at X = 61.5 m	345 927.	- 433 927.

The hereabove wave bending moments have been calculated with Cb = 0.6

Design Hull Girder Loads at X = 61.5 m

	Hogging (kNm)	Sagging (kNm)
S.W.B.M.	300 000.	0.
Wave bending moment (Rule)	345 927.	- 433 927.
Horizontal wave bending moment	127 207.	

	Positive (KN)	Negative (KN)
Vertical still water shear force	7 500.	
Vertical wave shear force	6 699.	- 6 699.

Admissible Vertical Shear Forces

Total Admissible Vert. Shear Force	(KN)	34 912.
Positive Admissible Vert. Still Water Shear Force	(KN)	28 213.
Negative Admissible Vert. Still Water Shear Force	(KN)	28 213.

Rule section moduli

	Deck (m^3)	Bottom (m^3)	Top (m^3)
Modulus based on design BM, Hog. (645 927.4 kNm)	3.6910	3.6910	3.6910
Modulus based on design BM, Sag. (- 433 926.5 kNm)	2.4796	2.4796	2.4796
Rule Modulus	3.6910	3.6910	3.6910

Check of section moduli and inertia

		Rule	Actual
Deck	(8.000 m k = 1.00)	3.6910	66.3737
Bottom	(0.000 m k = 1.00)	3.6910	7.7894
Top	(16.800 m k = 1.00)	3.6910	5.7851
Inertia		14.6344	55.7699

Check of Net/Gross Moduli

		Actual Gross	Actual Net	%
Deck	(8.000 m)	66.3737	73.1267	110.2
Bottom	(0.000 m)	7.7894	6.9746	89.5
Top	(16.800 m)	5.7851	5.3639	92.7

Using the remaining data on material type (MS) and yield strength (s_y) and considering of the above rules and regulations, the minimum structural dimensions on the midship section is determined, using the classification society Bureau Veritas software package MARS2000, which in the assumed structural arrangement meet the required minimum section modulus of the midship section and are shown in Table 2 (right) and Figure 4.

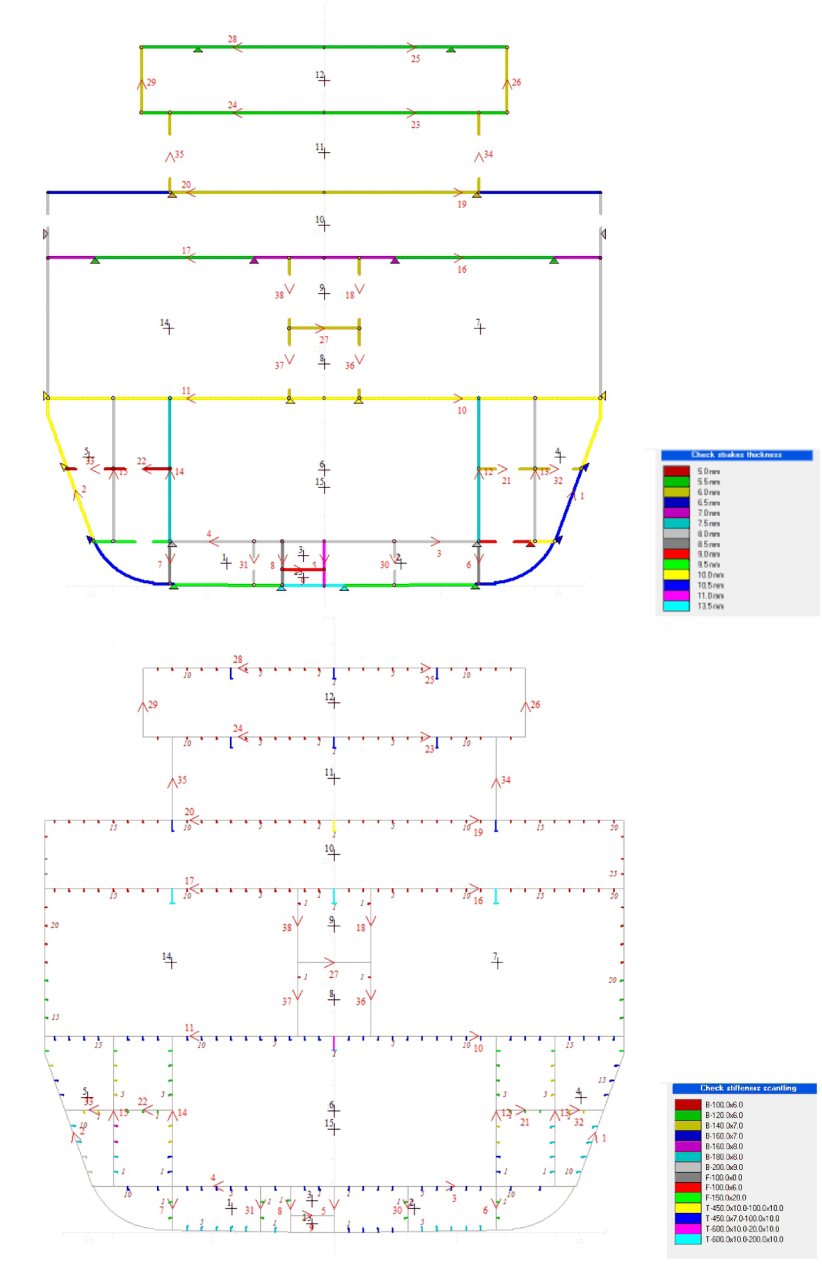

Figure 4: Plating(top) and stiffener (bottom) scantling on Midship section

Within yellow boxes, on Figure 5 and 6, plating thickness in millimetres and, on the left side, the required scantlings of the girders and stiffeners are given.

As the load varies along the length of the ship, it was necessary to repeat this procedure for a number of characteristic cross-sections in order to obtain the dimensions for the structure model and FEA as accurately as possible. The sections considered are: FR20, FR41, FR98, FR119, FR137, only two are presented due to limited space, Figures 7, and 8.

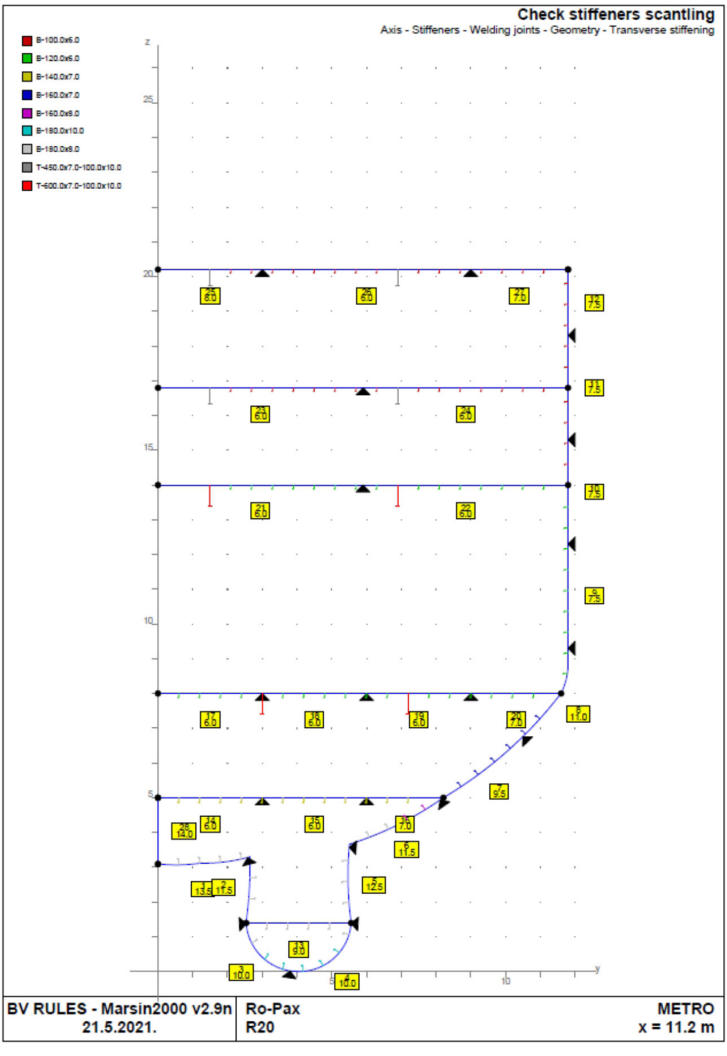

Figure 5: Plating and stiffeners scantlings on FR20

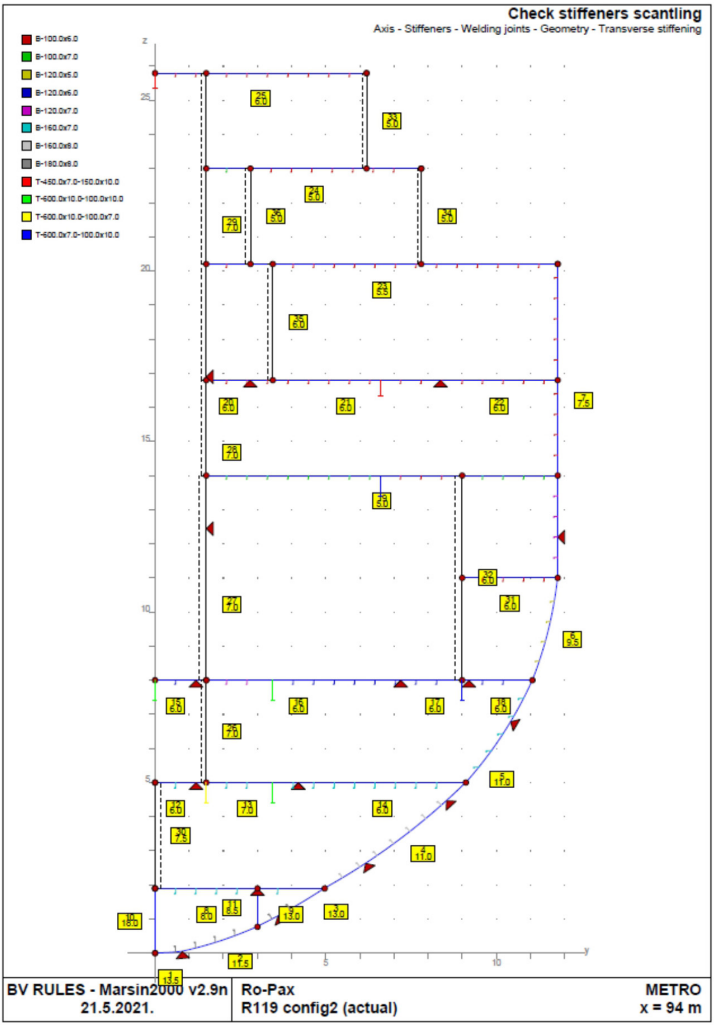

Figure 6: Plating and stiffeners scantlings on FR119

In addition, it should be noted that the dimensions are determined for the middle-low efficiency of the superstructure in longitudinal strength, Figure 7. This could be investigated later in more detail through different models of the hull and part of the superstructure with the aim to point out the possible stronger positive influence of the superstructure on the longitudinal strength, which can be proven only by direct calculation methods (FEM) and presentation to the classification society as a possible basis for optimizing the dimensions of hull structure elements, [11], [12], [13].

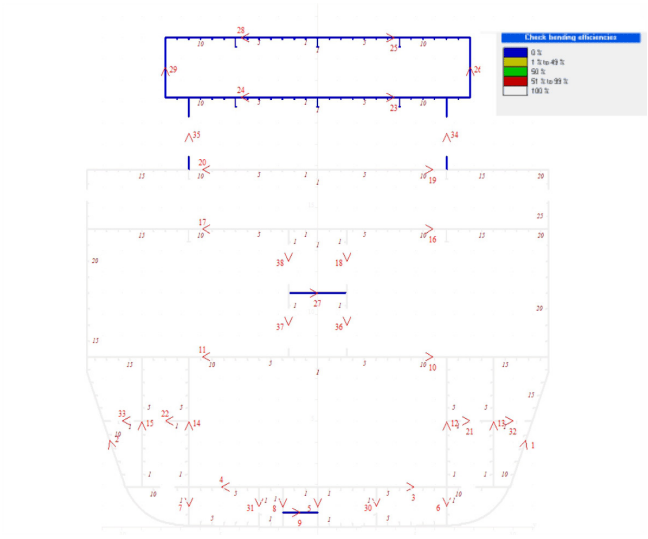

Figure 7: Midship section bending efficiency

The resulting scantlings of the plating and stiffening of transverse structural elements such as the bow watertight bulkheads (FR41 and FR 78) are shown on Figure 8.

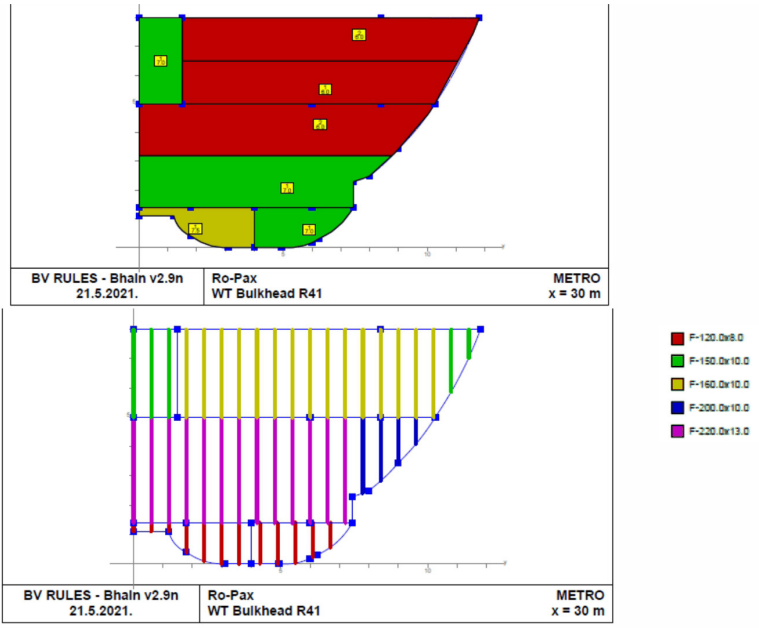

Figure 8: Plating and stiffeners on watertight bulkhead FR41

5. Global FE strength analysis

5.1. Referential Documents and 3D Model Description

A list of the main documents, named Referential Documents, used are:

Technical description:	ROPAX-METRO-Outline-REV2
General Arrangement Plan:	ROPAX-METRO-GAP-REV2
Body Lines:	METRO-RO-PAX-1101301-REV2
Midship section:	METRO-RO-PAX-1200301-REV2-Midship section preliminary
	METRO-Ropax-TRIM & STABILITY BOOK_REV1

Complete structure model (*CSM*) of Ro-Pax ship is created for the simulation purposes, Figure 9, [14]. Model is positioned in the working space (*FEM environment*) according to standard naval architectural practices in which x-axis is oriented aft to the fore in the longitudinal direction, y axis is oriented from starboard to the portside with its origin at the centreline of the vessel and z axis is oriented vertically to the base line of the ship with its positive direction from base to the top part of the ship, Figures 9. Model consists of 395 different FE parts, in which each part represents one structural element or in some cases a group of structural elements with same geometric properties. One type of steel is used, with following properties; Young's modules: $E = 201\ 000$ MPa, Poisson's ratio $\nu = 0.29$ and yield stress $\sigma_Y = 235$ MPa.

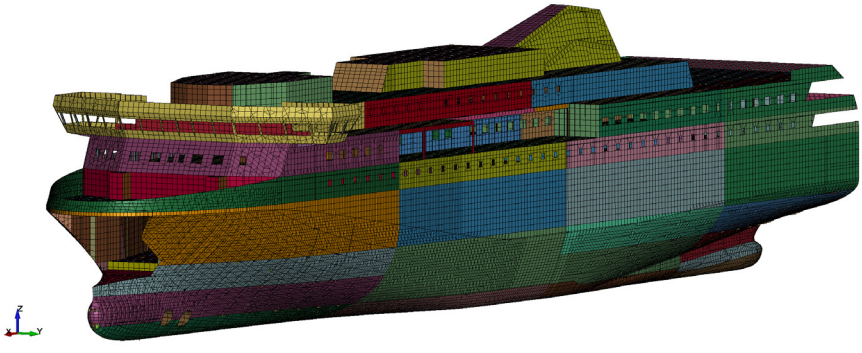

Figure 9: Isometric view on the model with the Coordinate system

5.2. Modelling of Loads

Presented Ro-Pax ferry is Passenger / Ro-Ro types of ship that have such a shape and distribution of their own weight (quite uniform along the ship) that they are always in a hogging condition on calm water, i.e. they have extra buoyancy in the middle and weights at the ends. Due to such static load distribution, they are usually loaded with a

very high bending moment on still water. The combination of the maximum still water bending moment in hogging and the maximum wave bending moment in hogging gives maximum longitudinal stresses. The combination of the minimum hogging bending moment on still water and the maximum wave sagging bending moment gives the possibility of compressive stresses in the upper decks. This is to be avoided at all costs because the compressive stresses in the upper decks of the superstructure, which are mostly made of very thin plates (5-6 mm), can cause buckling problems. The shear force distribution on still water usually follows the theoretical distribution with maximum values in the range of about 0.25 *L* and 0.75 *L* of the stern vertical. Significant values of the shear force are obtained by summing the maximum value of the shear force due to the wave with the maximum value of the shear force on still water. This can cause large shear stresses on the side of the ship in areas of openings where shear stiffness is reduced, which is not the case of presented Ro-Pax ferry. Static load is divided into following groups:

- weight of structure, weight of paint, equipment, welds,
- weight of cargo per deck (usually default pressure per deck),
- cargo weight in cargo / ballast tanks,
- weight of supplies, fuel, lubricants, water,
- hydrostatic pressure due to buoyancy.

This part of analyse is accompanied by a detailed elaboration of Trim and Stability (T&S) book in which load cases of ship loading are defined. The static load of an idealized structure is increased and adjusted to the weight of the light ship according to the T&S book for the considered loading case. The shape of the FE model quite faithfully follows the actual shape of the ship, and differences in displacement of up to 2% are considered acceptable [15]. The hydrostatic pressure distribution is directly defined by the ship's draft and has to be checked also. The load on the decks is explicitly given in the form of pressure. The weight of the cargo in the tanks is derived from the volume of the tank and the density of the liquid. The mass of the main machine and larger equipment is defined at the exact position as concentrated mass. The self-weight of the idealized construction is calculated directly by FEM programs from the structural model and are increased by the weight of the neglected reinforcement, welds, paint, small equipment, inventory, etc. The difference is defined by the magnification factor which increases the density of the steel. In this case, the total weight distribution follows the own weight distribution of the idealized structure. The magnification is obtained in parallel with the adjustment of the weight curve obtained from the FEM program and that from the T&S book.

When modelling the wave load, it should be on mind that is generated with much more uncertainty than the structural model, and therefore was not considered at this stage of the analysis. Direct methods for calculating the wave loads of various authors still give large variations in the results of even the vertical wave moment [16]. For the practical implementation of wave loads on the 3D FE model of the whole ship, the design wave method [15] and [17] is usually used due to the speed and practicality

of the calculation. They use elements of a deterministic and / or statistical approach in determining the equivalent design wave that will load the FE model. Two different loading cases were used in the analyses/simulations. In both simulations hydrostatic pressure is included which is changed depending on the draught. In the second loading case apart from hydrostatic load, load from the trucks on the deck is implemented. Hydrostatic load is set onto the hull surface in seven separated areas. So, each draught that is implemented into the simulation is separated by height into seven areas. For each areas pressure is calculated separately based on Bernoulli's equation. With explained approach hydrostatic load is set as distributed load on the hull surface which changes with the depth. Loads form the truck are imposed based on the inputs [2] (see Ref. Documents), Figure 10.

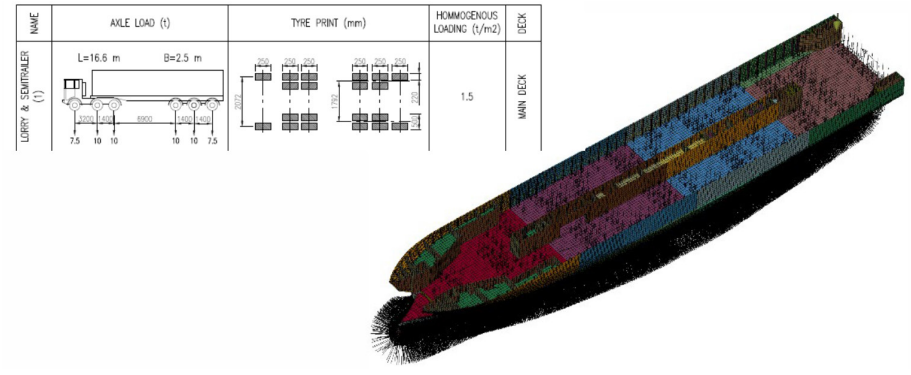

Figure 10: Permissible loadings from the trucks on the deck (left) and representation of hydrostatic and trucks load on the same model, section view

5.3. Loading conditions

Two different static loading conditions, Table 3, are used in the simulations according to T&S book as lightweight ship (LC1) and load case that correspond maximum value of stillwater bending moments (LC2) that reads kNm and shear force of kN. Load case LC1 has got only hydrostatic load, while LC2, has got hydrostatic load and cargo load from trucks on the Main garage deck, Figure 10.

All simulations are performed with the following assumptions; static analysis, small displacement and linear behaviour of materials.

Table 3: Schematic representation of load conditions

Load case		Displacement, t	Draught, m	Cars	Trucks
LC1	**Trim&Stability Book**	7210	4.619	-	-
	FEM*	6741	4.501	-	-
LC2	**Trim&Stability Book**	9246.5	5.536	-	Yes
	FEM*	9187.4	5.51	-	Yes

***Weights, t**	**LC1**	**LC2**
FEM structure + main equipment	4575	4575
Cargo equipment	428	428
Ship equipment	300	300
Crew and Passengers equipment	1000	1000
Ship systems	438	438
Bunkers	-	45.6
Ballast waters	-	290.8
Deadweight	-	2110
Total:	6741	9187.4

5.4. Boundary condition

In order to prevent rigid body motions of the overall model, the constraints specified below are applied, Table 4, Figure 11. The model itself needs to be in quasi-static equilibrium so that the reactions in the nodes in form of displacement and rotation are minimal. A total unbalanced force below 2% of the displacement is considered acceptable according to BV [15], Table 3. The model balancing procedure changes two parameters, ship draft and trim angle, in the case of a symmetrical load case. By varying the above parameters in an iterative procedure (which is usually a preparation for FEM calculation), [18], the conditions of buoyancy and minimum reactions at the ends are met.

Table 4: Boundary conditions imposed on the model

Boundary conditions	**Degree of freedom (DOF)**		
	X	**Y**	**Z**
Fore node in CL, 1	fixed	fixed	fixed
Aft node in CL, 3	free	fixed	free
One node, portside, aft end, 2	free	free	fixed
One node, starboard side, aft end, 4	free	free	fixed

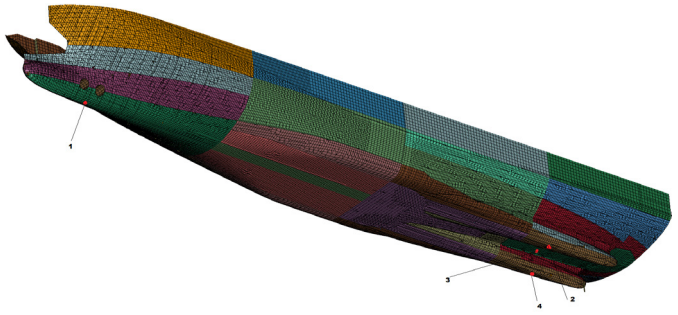

Figure 11: Boundary conditions positions

5.5. FE Modelling Characteristics and Checking Criteria

Mesh was created of the shell elements with the usage of the *Fully integrated shell element* formulation option. In creating mesh two elements types were used which are quadrilateral and triangular element, Table 5. Initial dimension of the mesh element is 600 mm, where that was necessary elements were smaller in order to better define geometry and to sustain mesh quality in problematic areas.

FE model is based on the scantlings with 50% corrosion deductions for primary supporting members analysed through complete ship model, according to the rules, [2] (Pt. B, Ch.4, Sec.2, Table2).

Hull girder bending strength checks within 0,4 L amidship are:

$s_1 = 175/k$, MPa - normal stress, where k=1 is material coefficient of mild steel,

$t_1 = 110/k$, MPa - shear stress, and

$f = l/200$ – deflection, where l is unsupported span.

Table 5: Number of elements for the model and their shape (formulation)

	No. of elements	Quads	Trias
Model	296780	*27430*	*269350*

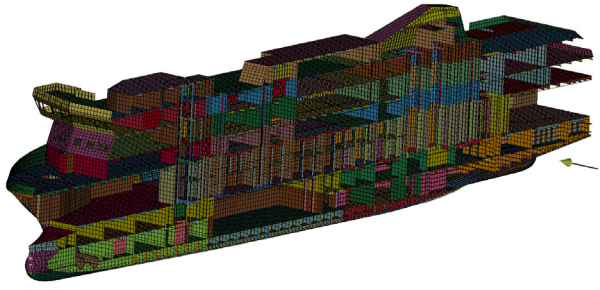

Figure 12: Longitudinal global section views of the mesh

6. Results and discussion

Reviewing and evaluating the results on the global FE model of the whole ship due to the size and complexity of the model is a long and demanding job. Software packages that automatically check the suitability of all structural elements greatly speed up the work on the evaluation of results, but still is not completely automatic process. The analysis of the results is carried out on the prepared model for which two loading conditions are analysed. Results are presented globally for the whole model and both load cases, in case of resultant displacement, Figure 13, 14 and 15, and locally for some parts of the structure in case of effective stress response, Figures 16, 17, 18 and 19. Only those figures showing areas of the structure that are under significant or high stress are selected.

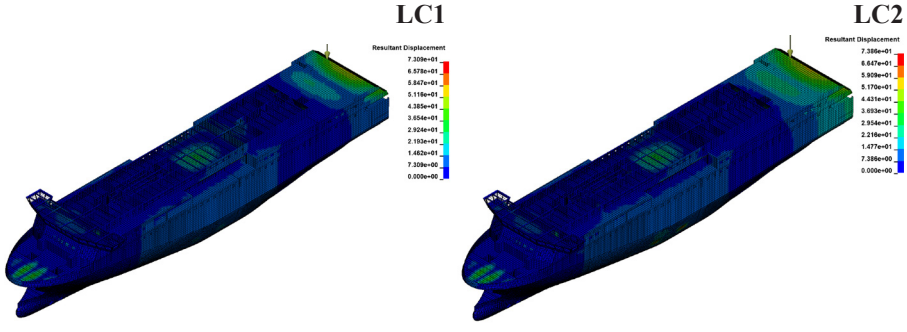

Figure 13: Resultant displacement of the model, Wheelhouse top

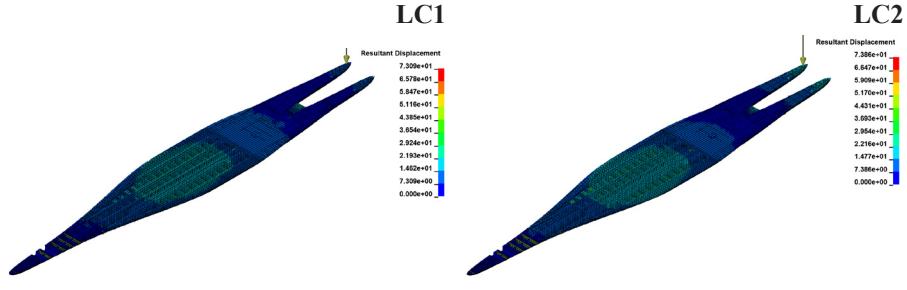

Figure 14: Resultant displacement of the model, Tank top

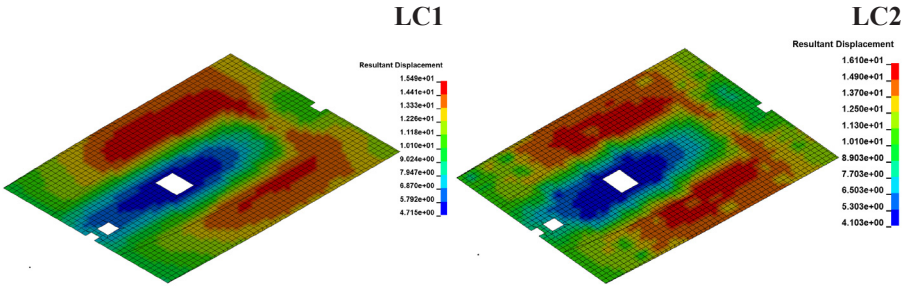

Figure 15: Resultant displacement for Main garage deck

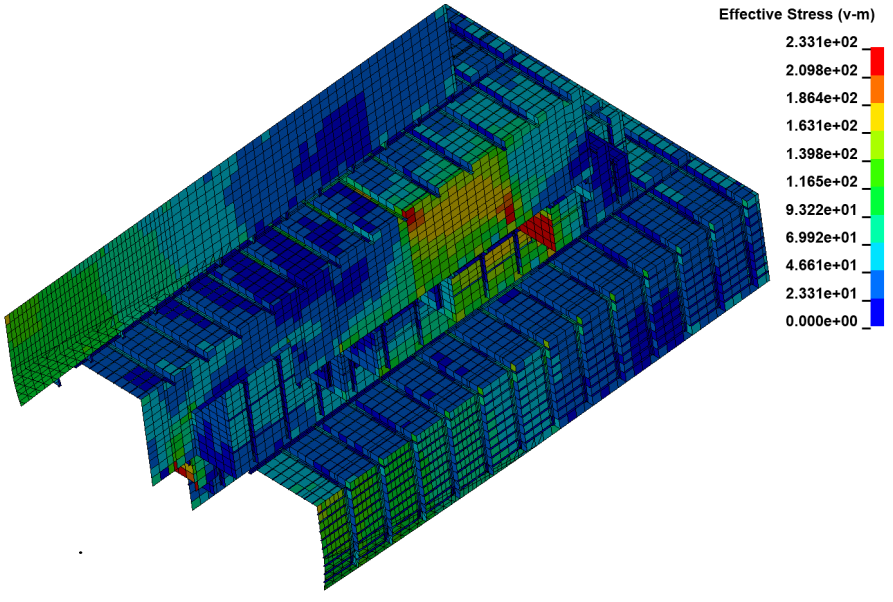

*Figure 16: **LC1** - Von Mises stress for structure between Fr70 -Fr110 and Main garage deck and 1st Accommodation deck*

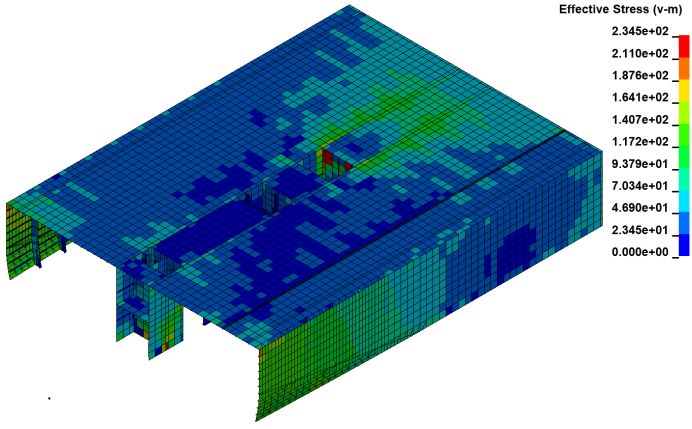

*Figure 17: **LC2** - Von Mises stress for structure between Fr70 -Fr110 and Main garage deck and 1st Accommodation deck*

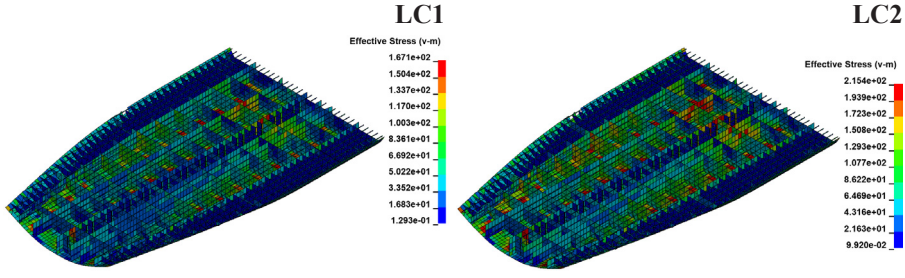

Figure 18: Von Mises stress for structure between Fr70 -Fr110 and from the bottom to the Tank top

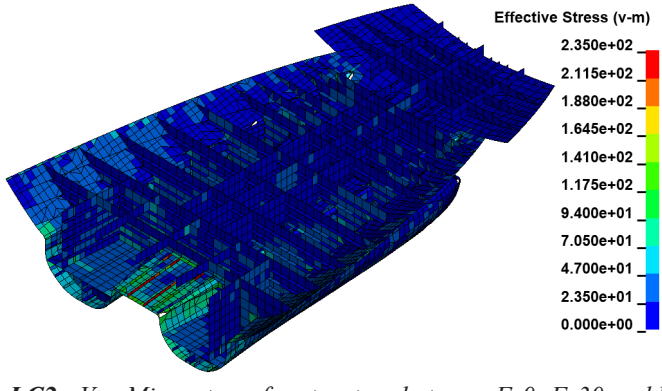

*Figure 19: **LC2** - Von Mises stress for structure between Fr0 -Fr30 and hull bottom under the Main garage deck*

7. Conclusion

In order to check part of the global ship strength related to static load of the Ro-Pax ferry hull structure, complete ship model finite element analysis is performed. Previously, minimal scantlings are determined in accordance to BV prescribed rules, where yielding and local buckling criteria were applied. Within FEA only global checking criteria regarding stillwater bending moment was applied. Two load cases are considered as most unfavourable ones from trim and stability book regard to lightweight ship and maximum vertical bending moment. Results are presented in form of displacement and stresses. Static loads are modelled as much realistic as possible from load cases. It means that distribution of weight is considered and consequently the buoyancy distribution at proper water line. Additional mass of engine, equipment and other groups are considered as well as loads from the car and trucks.

Stresses are presented in the form of equivalent stresses instead in the form of longitudinal (x) ones, which are lower in comparison to equivalent and might be more appropriate for global strength evaluation. Still, bearing in mind that the wave vertical bending moment is not included as load and therefore the stress response should be lower, leaving enough space for stresses due to wave bending moment, up to stress limit. Therefore, structural element showing stress value near to limit of 175 MPa were of interest. In general, the response, both deflection and stress, is small and within the expected range, and only some local structural elements show excessive stresses. After detailed inspection, following elements/positions are extracted from analysis, Table 6, as potential high stress area that would require more detailed analysis as a future work and are likely to be addressed by local reinforcements or local structural rearrangement.

Table 6: High stress structural positions / elements

Load case	Structural part	Position / Frame	Level of stress	Figure
LC1	Main garage deck	0 -30	High	18
	Bottom shell	0 - 30	High	20
	Bottom shell, double bottom	70 - 110	Significant	21
LC2	Main garage deck	70 – 110	High	19
	Hull bottom	0 - 30	High	20

References

1. Žanić, V., Jančijev, T., Cvitanović, G., Pavičević, M., Biskupović, J., Čudina, P., Andrić, J. (2000) Hull Structure Analysis and Optimization of RO-PAX Ship, XIV Simpozij Teorija i praksa brodogradnje, SORTA 2000, Rijeka, Croatia, pp.255-262.
2. Bureau Veritas Rules for the classification of Steel Ships (2021), Part B Hull and Stability, July 2021, France
3. ANSYS/LST, LS-DYNA R11 (2019), User manual Vol I, II, III, Theory manual; https://www.lstc.com/products/ls-dyna
4. Bathe, K. J. (1998) Finite Element Procedures, McGraw – Hill
5. Zienkiewicz, O. C., Taylor, R. L. (2000) The Finite Element Method, Volume 1, The Basis, Fifth edition, Butterworth-Heinemann
6. V. Žanić, V. Jančijev, T., Andrić, J., Frank, D., Bralić, S., Sponza, D., Dundara, Đ. (2001) Racking Analysis of Car-Truck-Carrier, Brodogradnja, Vol. 49, No.3, 181-190
7. Andrić, J. Prebeg, P. Žanić, V. (2019) Multi-level Pareto Supported Design Methodology–Application to RO-PAX Structural Design, Marine Structures, Vol. 67, https://doi.org/10.1016/j.marstruc.2019.102638.
8. Bolf, D. Hadjina, M. Zamarin, A. Matulja, T. (2020) Methodology of Integrated Design of the Ship Structure and Production Using the 3D Experience Platform, Proceedings SORTA, 319-327, ISBN 978-953-8246-20-3, RITEH, Rijeka
9. Hughes, O. F. Paik, J.K. (2010) *S*hip structural Analysis and Design, SNAME, New Jersey
10. Okumoto, Y., Takeda, Y., Mano, M., Okada T. (2009) Design of Ship Hull Structures, Springer
11. Žanić, V. Andrić, J. Frank, D. (2003) Structural Optimization Method for the Concept Design of Ship Structures, International Marine Design Conference-IMDC, Athens, Greece
12. Lee, K. Y. Roth, M. (2001) An Efficient Genetic Algorithm Using Gradient Information for Ship Structural Design Optimization, Ship Technology Research, Vol.48, 161-170
13. Riggo, P. (2001) Module-Oriented Optimization Tool, Practical Design of Ships and Other Floating Structures - PRADS, 51-58,
14. DNV-CSA (2013) - Direct Analysis of Ship Structures CLASSIFICATION NOTES No34.1
15. Bureau Veritas, (2000) 2000 Rules, Analysis Based on Three Dimensional Models, Pt B, Ch 7, App1-3
16. Zamarin, A. Prpic-Orsic, J.. Čorič, V. (2003) *Non-Linear Wave Load of Ship in Head Waves*, BRODOGRADNJA 51 (2), 147-157
17. Payer, H. G. Fricke, W. (1994) Rational Dimensioning and Analysis of Complex Ship Structures, SNAME Transactions, Vol. 102, 395-417
18. Žaja, D., Zamarin, A., Hadjina, M. (2007) Longitudinal strength of a Container Ship, Engineering Review, 27(1) 55-66

ISSN 0554-6397
Konferencijski članak
(*Conference paper*)

Enrique Alejandro Russell Montiel
E-mail: erussellmontiel@gmail.com
Jade University of Applied Sciences, Faculty of Maritime and Logistic Studies, Weserstr. 52, 26931 Elsfleth, Germany; erussellmontiel@gmail.com
Alen Jugović
E-mail: alen.jugovic@pfri.uniri.hr
Dea Aksentijević
E-mail: dea.aksentijevic@pfri.uniri.hr
University of Rijeka, Faculty of Maritime Studies, Studentska 2, Rijeka, Croatia

Impact of the One Belt and One Road Initiative on the European Maritime Field

Abstract

China is nowadays the most influential country in the world market, therefore the Chinese government introduced the One Belt and One Road project in 2013 in an attempt to reinforce its global power, including its major partner (Europe). In this paper the authors analyze the possible advantages and disadvantages that this Chinese initiative brings to the European market and the possible challenges that international policies may bring to the infrastructure created in recent years in the European Union. The authors concentrate on current examples based on China's COSCO Shipping and the influence that this initiative gives to the Chinese government in the world market. The aim of this paper is to present general overview on some of the consequences, positive or negative, of this important project.

Keywords: One Belt and One Road, Maritime field, Logistics, European transport system

1. Introduction

Maritime transportation has a significant social, environmental, political, and economic impact worldwide, as the most important mean of transportation of goods and people [1] participating in 90% of the global exchange [2].

In recent decades China has developed into the European Union's largest trading partner, accounting for $709 billion in 2020, leaving the United States of America behind with $671 billion in 2020 [3]. This creates a great weight of Chinese policies in

international markets and gives China great power worldwide with respect to policies and business. In order to strengthen these attributes and advantages, the Chinese government decided to create a massive project.

Since China unveiled its project *"one Belt and One Road"* in 2013, many experts, countries, societies, partnerships and companies have been asking themselves, how will the "One Belt and One Road" project change the negotiations in the world and what advantages and disadvantages it will cause for local companies with respect to Chinese companies? This is a key point that people are not clear about due to the lack of official information and the magnitude of the project. Today, there is great uncertainty in the European region, as it is not known exactly what the effects of the Chinese project will be, the only thing that is clear is that it will have a great impact, both positive and negative.

"In accordance with Chinese governmental reports and with several papers, BRI has a plurality of goals that are mainly connected to political and economic issues (e.g. opening of developing markets for Chinese companies, economic cooperation)" [4].

The idea of the authors in this research work is to contribute to a better understanding about the possible effects and impacts that this project could have at European level, showing some current examples such as the expansion of the Chinese company COSCO Shipping and the development of the Greek port of Piraeus, the possible consequences of the introduction of invasive foreign policies in the market that give high advantages to Chinese companies and the Chinese government and the role of Europe in the One Belt and one Road initiative.

The authors will also discuss on the changes in the logistics sector in the Mediterranean area due to the connection of the Greek port of Piraeus by rail and sea, giving landlocked countries the opportunity to a better connection to the mark and what could be the consequences in the maritime field and what challenges this could create for logistics companies and shipping companies.

2. One Belt and one Road initiative

The One Belt One Road (OBOR) project is a Chinese economic and diplomatic initiative with two main components, the first component being a land route connecting Asia and Europe, and the second component being a sea route connecting the most important ports between Asia and Europe [5]. The land route "Silk Road Economic Belt" will connect 65 countries and 4.4 billion people between Xi'an in western China, through Central Asia to the Middle East, Russia and Europe [6]. China's vision for the sea route is to connect Asia with Europe, starting the route in Quanzhou passing through Chinese ports before reaching the Strait of Malacca. From Kuala Lumpur the route heads to Kolkata, then through the rest of the Indian Ocean to Nairobi and from there, around the Horn of Africa and into the Mediterranean Sea, through Greece and on to Italy [7]. Figure 1 shows the graphic view of the land and sea route.

The initiative was announced in 2013 by the Chinese government, this is the initiative with the largest economic, social, political and environmental impact in the world [5], involving important aspects that will change the infrastructure of several countries, as this project involves trade policies and interests of countries worldwide [8]. The original plan of this project was to include 65 Eurasian and African countries, covering 62 percent of the global population and 40 percent of the world's surface, giving China great political power in the world. But today the plan has changed, extending the project to Latin American countries [9]. Several countries have shown interest in this project and want to attract China's attention to invest money in infrastructure, technology development, trade policies, routes, etc [10].

Since 2014, the One Belt and Road project has triggered a growth of China's money lending around the world of more than $120 billion for the construction of highways, railroads and power plants, thus stimulating China's business expansion with other countries, accessibility to land bases and shipping facilities [11].

According to the Chinese government, the main goals of this huge initiative are policy coordination, infrastructure connectivity, unimpeded trade, financial integration and closer ties between the countries that are part of this project. The policy coordination between the countries that must be part of this project is important for the guarantee and success of this initiative. Today different countries and important international organizations have incorporated and supported the project established by China, such as the United Nations in November 2016, the G20 in September 2016, APEC and other international and regional organizations. In March 2019, the Chinese government signed 173 cooperation agreements with 125 countries and 29 international organizations. The Chinese government is expanding the project to include not only Asia, Africa and Europe but also Latin America and the South Pacific [12].

The Chinese project has been interpreted in many ways, one of which is the interpretation as a strategy of developed economies using new infrastructure to intensify regional and global trade relations. It has also been interpreted as a way for China to increase its influence in East and Southeast Asia to compete geopolitically with the United States.

The Belt and Road Initiative (BRI) may not be an economic or political project, but what is certain is that it will transform policies with China on multiple scales and simultaneously create possibilities for global cooperation, global trade and conflict [13].

Source: Bruce-Lockhard (2017)

Figure 1: One Belt and One Road [14]

3. Impact of the one Belt one Road on the European transport system

The last few decades have seen the growth of trade between China and the rest of the world grow exponentially. With the growth of China's exports to the rest of the world, China wants to develop this initiative to improve its transport chains, especially with Europe. The development of this project requires investment in new infrastructure, the adjustment of European trade policies, and the agreement of all countries involved in the One Belt One Road initiative [15]. The implementation of this project will bring benefits and consequences for the transport infrastructure and for the European market [16].

The advantages of implementing the Chinese project between China, Asian, African, and European countries are based on increased rail services, reduced transit times, increased frequency, reduction in transportation costs, and spare capacity on some trains. This may offer opportunities for shippers and their logistics providers to shift some or all of their cargo to rail.

One way to reduce the transit time of products coming from China is for example China's investment in the construction of the Kra canal or the Kra Isthmus Canal [17], with this canal is intended to avoid the Malacca straight, making faster the trade route Far East to Europe, reducing the route to 1,200 kilometers less and 72 hours less travel time, and thus also avoiding the potential bottleneck represented by the Malacca straight [4].

Consequences will also arise, particularly if the new traffic induced by BRI investments causes bottlenecks and capacity constraints, and if these cannot be resolved or alleviated at reasonable cost or within reasonable timeframes [18].

This initiative implies major challenges for the transport structure in the European

Union. The implementation of this initiative entails the change of the structure implemented during the last years in Europe and in the European Union, bringing consequences for seaports, airports, transport routes and landlocked states infrastructure [16].

3.1. Effects of the one Belt one Road on the shipping transport

In recent decades, shipping has been the most important means of transport for global trade changes, as it is capable of transporting large volumes of cargo over long distances. With this feature all major operators used to compete independently to attract customers and serve shipowners all over the world. Ocean transport dominates more than 90% of the world's transports and thus contributes to the world's most important means of transport for the exchange of goods between countries.

The European continent is a crucial area in the Chinese project since it is the end of the connection of sea "21st Century Maritime Silk Road" ending in Greece, and land "Silk Road Economic Belt" ending in Germany, routes between the Asian continent and Europe [6]. The countries of Europe will be efficiently connected by land and sea, especially the countries of Eastern Europe that do not have sea connections.

It is evident that the Chinese initiative is a project that invades the foreign and regional policies of the areas involved, and it will cause many competitive disputes and disturbances with the parties involved (e.g. with the European Union, Russia, etc.). The Trans-European network is an example of policies in Europe that will be affected as this is a European regional policy, while the project, promoted by the Chinese government, is a global policy that will change and distort regional policies.

This project will be a great advantage for Chinese trade *"a 10% improvement in connectivity between countries along the "Maritime Silk Road" [i.e., the part of BRI connected to maritime corridors] would deliver a 3% decrease in Chinese trade costs which would, in turn, boost China's imports and exports by around 6% and 9%, respectively"* [4]. The new logistical route will not only affect the Mediterranean logistical industry and ports, but also the entire European transport industry as discussed by Yang [19] and Costa [20]. While many countries have welcomed this initiative as a form of development opportunity, other countries are concerned about the possibility that China will receive many advantages in competition with local economies. The competition between sea and rail in Europe will increase, as better rail connections from Greece to Central and Eastern European countries will decrease transport times to countries that do not have a sea connection [4].

China has tried to influence the European market and other regions through ad-hoc investments, this has allowed them to enter and somehow manage some important aspects of the initiative in an easier way. A notable example was the investment of the Chinese shipping company COSCO in the Greek port during the financial crisis (2012-2016) [21], another important example was the investment in Sri Lanka container hub in (2016-2017) [22].

Many of the projects that are intended to improve the infrastructure for the Chinese project are under construction or are still being negotiated with the different countries. Some of these projects were completed before the major Chinese "One Belt and one Route" project was unveiled in 2013, these actions allow for the control or expansion of existing infrastructure. An example is again the Chinese shipping company's investment in Piraeus, where COSCO decided to invest in the Greek port system before the BRI started. This move facilitated COSCO's entry into the Greek port authorities. Thanks to this negotiation and investment by the Chinese government, COSCO became the main shareholder (currently holding 67% of the capital) making the Greek port an important player in the Mediterranean [4].

The port of Piraeus is not only connected to the Maritime Silk Road, but also to the railroads connecting the port with Central and Eastern Europe, thus using the railroads in a complementary way for a new logistic option in Europe.

Railway transport services are starting to gain an important influence and started to operate before the promotion of the Chinese project. These strategies will affect the logistics industry in a big way, especially the Mediterranean area will be the most affected due to its fundamental role in connecting Europe with the Far East.

3.2. Euro-Asia landbridge corridor

The Euro-Asia landbridge corridor is a rail service that connects all major Chinese industrial cities with strategic cities in Eastern and Central Europe. Most of the services are planned to run on an infrastructure that passes through several Asian countries. This corridor is being created to overcome the Russian rail route (that needs to be updated) and the corridor is intended to serve a wider and stronger Asian network.

This railway project covers all the most economically important countries in Europe, such as Germany, Poland, Baltic countries, Hungary, Czech Republic, among others) in this way allowing the arrival of goods to potential markets, avoiding the (slow) sea routes [4].

Competition between sea routes and rail routes is growing steadily with the development of the China initiative. As described by Li [23], rail services are gaining importance as there are potential goods in need of reliable and fast transport solutions.

The One Belt and One Route project will implement interventions in different ways, mainly through international trade agreements or incorporating currently EuroAsia rail services within other intermodal solutions, and thus improve services and optimize the connectivity of the COSCO network [19].

Cosco started to develop its expansion and connection in the mid 00's, not only growing in the port of Piraeus but also trying to get involved in multiple economic connections. In the European continent, COSCO Shipping is involved in the port of Zeebrugge (Belgium) and also in the ports of Rotterdam (Netherlands) and Antwerp (Belgium) on a minority basis. COSCO plans the port of Piraeus as the main hub. COSCO bought

Noatum Ports, initiating the management of a container terminal in Valencia and Bilbao.

COSCO owns minority shares in the port of Kumport (Turkey) it is a possible end point of the EuroAsia corridor, and in the Suez Canal, this is a key point to enter the Mediterranean market.

Together with COSCO Shipping's strategy, the investments and expansion included in the BRI could soon mark the future of the maritime sector in the Mediterranean basin. The current investments will allow COSCO to handel and operate over main trade routes, concentrating intercontinental traffic in its hub port. The creation, expansion and connectivity of this network will create advantages for China COSCO Shipping with respect to non-allied maritime competitors, and this will also affect the port market given the potential impact on transhipment flows in both sides of the Mediterranean basin.

3.3. The impact of BRI on Mediterranean ports

Today there is a lack of information about what the impact of the BRI project will be on the European transport sector, it is clear that this project will greatly affect the current structure of this sector and also the competences of the maritime sector. As discussed in the previous report, the only major maritime node currently included in the BRI strategy has already secured a pivotal role in the Europe-Asia trade lanes and an important role in other intercontinental routes. The growing power of China's COSCO Shipping in the European shipping market and the shift and development of connectivity from the port of Piraeus to rail and sea connectivity will generate a major competitive advantage for COSCO, with a cascading effect on other competing ports.

As an example of this impact, it is worth noting that the port of Piraeus has increased its connectivity and has grown by 50% in the last 6 years since the beginning of the BRI era, whereas before it was one of the lowest ports in the world in terms of connectivity [24].

Some competing companies in the maritime market are trying to gain ground in order to be included in the Chinese project, but COSCO has the biggest advantages because it is China and has gained the most ground in the European market in recent years, so it can be included in the project in an easier and more natural way. While the Chinese project generates great opportunities for European and Asian regions that are difficult to reach, this project also generates great problems for local (European) companies, as it creates a gap in the market with Chinese companies.

To obtain the best opportunities for Mediterranean port and logistics players, coordinated efforts should be made with the TENT-T projects to avoid overcapacity and possible competitive advantages for only a few market players.

4. Conclusion

This paper analyzed the One Belt One Road initiative unveiled by the Chinese government in 2013. So far there are many research papers focusing on the political implications of this initiative for Europe and Asia, but there are very few research papers focusing on the advantages and disadvantages of this initiative in the area of maritime logistics and European transport infrastructure. This Chinese initiative offers improved connectivity to countries in Central and Western Europe, especially for countries that do not have a water connection.

The introduction of foreign policies, in this case Chinese, can lead to a large gap and disadvantages for local (European) companies, such as current power that COSCO Shipping currently has as the largest shareholder of the Greek port of Piraeus, since it dominates the port and for this reason dominates the market and the entry and movements in this port.

Other challenges can be taken into account with the introduction of the initiative are the possible overcapacity that can easily be created and the potential competitive advantage for some players in the market.

Countries and governments interested in this initiative should try to strike a balance between the advantages and disadvantages of this initiative and try to maintain stability in the region.

References

1. Naletina, D. & Perkov, E. (2017). The economic importance of maritime shipping with special reference on Croatia. Available at: https://www.researchgate.net/publication/324389577_THE_ECONOMIC_IMPORTANCE_OF_MARITIME_SHIPPING_WITH_SPECIAL_REFERENCE_ON_CROATIA. [Accessed: 20-Mar-2020] [accessed: Jun. 9, 2021].
2. Serry, A. (2016.) The automatic identification system (ais): a data source for studying maritime traffic. *Maritime Transports ´16*, Barcelona, Spain Available: https://hal.archives-ouvertes.fr/hal-01724104/document [accessed: Jun. 9, 2021].
3. China overtakes US as EU's biggest trading partner (2021) *BBC News*, 17 Feb. 2021. [Available at: https://www.bbc.com/news/business-56093378] [Accessed: May 11, 2021].
4. Ferrari C & Tei A. (2020) Effects of BRI strategy on Mediterranean shipping transport. *J. shipp. trd.*, vol. 5, no. 1 doi: 10.1186/s41072-020-00067-x.
5. Chatzky A. (2019) China's Massive Belt and Road Initiative. *Council on Foreign Relations*, 21 Feb. 2019. [Available at: https://www.cfr.org/backgrounder/chinas-massive-belt-and-road-initiative] [Accessed: May 11, 2021]
6. Du M. (2016) China's "One Belt, One Road" Initiative: Context, Focus, Institutions, and Implications. *Chin J Global Gov*, vol. 2, no. 1, pp. 30–43 doi: 10.1163/23525207-12340014.
7. Google Books, China's way: the new Silk Road. [Available: https://www.jstor.org/stable/pdf/resrep06773.pdf] [Accessed: May 11, 2021]
8. Council on Foreign Relations. How the U.S. Should Respond to China's Belt and Road. [Available: https://www.cfr.org/report/chinas-belt-and-road-implications-for-the-united-states/] [Accessed: May 12, 2021]
9. Brînză, A. (2018) Redefining the Belt and Road Initiative [Available: https://thediplomat.com/2018/03/redefining-the-belt-and-road-initiative/] [Accessed: May 12, 2021]
10. Rolland N., Arudino, A., Chase, M., Duchâtel, M., Gunness, K., Pantucci, R., Kley D. & Xue, G. (2019) Securing the Belt and Road Initiative: China's Evolving Military Engagement Along

the Silk Roads. *The National bureau of Asian research.* No. 80 [Available: https://www.nbr.org/wp-content/uploads/pdfs/publications/sr80_securing_the_belt_and_road_sep2019.pdf]
11. Steil, B & Della Rocca, B. (2019) Belt and Road Tracker. *Council on Foreign Relations*, 19 Feb. 2019. [Available at: https://www.cfr.org/article/belt-and-road-tracker] [Accessed: May 12, 2021]
12. Permanent mission of People`s Republic of China to the United Nation Office at Geneva and other international organization in Switzerland. *The Belt and Road Initiative.* [Available at: http://www.china-un.ch/eng/zywjyjh/t1675564.htm] [Accessed: May 20, 2021]
13. Flint C., & Zhu, C. (2019) The geopolitics of connectivity, cooperation, and hegemonic competition: The Belt and Road Initiative. *Geoforum*, vol. 99, pp. 95–101 doi: 10.1016/j.geoforum.2018.12.008.
14. Yang F. & Yang M. (2019) Greening the one belt and one road initiative (in En;en) *Mitig Adapt Strateg Glob Change*, vol. 24, no. 5, pp. 735–748 doi: 10.1007/s11027-018-9828-6.
15. Silin, Y., Kapustina, L., Trevisan, I., & Drevalev, A. (2017) China's economic interests in the "One Belt, One Road" initiative. *SHS Web Conf.*, vol. 39, p. 1025 doi: 10.1051/shsconf/20173901025.
16. Dunmore, D., Preti, A. & Routaboul, C. (2019) The "Belt and Road Initiative": impacts on TEN-T and on the European transport system. (in En;en), *J. shipp. trd.*, vol. 4, no. 1, pp. 1–17 doi: 10.1186/s41072-019-0048-3.
17. Abdul Rahman, N.S.F., Mohd Salleh, N.H., Ahmad Najib, A.F. et al. (2016) A descriptive method for analysing the Kra Canal decision on maritime business patterns in Malaysia. *J. shipp. trd*. 1, 13 https://doi.org/10.1186/s41072-016-0016-0
18. Davis Gleave S. (2018) Research for TRAN Committee: The new Silk Route - opportunities and challenges for EU transport [Available: https://www.europarl.europa.eu/RegData/etudes/STUD/2018/585907/IPOL_STU(2018)585907_EN.pdf]
19. Yang, D., Pan, K., & Wang, S. (2018) On service network improvement for shipping lines under the one belt one road initiative of China. *Transportation Research Part E: Logistics and Transportation Review*, vol. 117, pp. 82–95 doi: 10.1016/j.tre.2017.07.003.
20. Costa P., Haralambides H., & Roson R. (2020) From Trans-European (Ten-T) to Trans-Global (Twn-T) Transport Infrastructure Networks. A Conceptual Framework. *A European Public Investment Outlook.* [Available at: https://www.academia.edu/43443490/From_Trans_European_Ten_T_to_Trans_Global_Twn_T_Transport_Infrastructure_Networks_A_Conceptual_Framework_]
21. *Piraeus.indd* [Available at: https://d1wqtxts1xzle7.cloudfront.net/34336394/Piraeus_web.pdf?1406875001=&response-content-disposition=inline%3B+filename%3DChinese_Investment_in_the_Port_of_Piraeu.pdf&Expires=1622195555&Signature=D-TpEJ7vpaX2HD4q40CKm9-4d30do0OcCnCzOO4DmAqCifxSKWBNDpd8D8-OFZG~fVd2wU9HccdAOc91ug4pyKU2-BxN3JeS7ri2I8Nzv-KsoVSgdXGBq2p5lSyrumC~FAcDTbhMy7cBsTZviZUsgLgxIpdIGiq0LPzHks1feiLtIrivLQV02J89CfIausKXbJiRpd6i3rE3B8LQQlJk0jJVcSQbgWJg2ssIVT-sG05K-o4WxEkXzo5qt67tQYhZVBDaTVNzi9oha6TGVln81yP8so5nl1pQ~Z1I5KqdIEFuoh8dxwQEsLLKxbwwRaRpm9xUDmi7oe2rb1NKg3kh6Q__&Key-Pair-Id=APKAJLOHF5GGSLRBV4ZA]
22. Chen D., & Yang Z. (2019) Investment in container ports along the Maritime Silk Road in the context of international industry transfer: the case of the port of Colombo," (in En;en), *Marit Econ Logist*, vol. 21, no. 2, pp. 241–257 doi: 10.1057/s41278-017-0067-7.
23. Li, Y., Bolton, K. Westphal & T. (2018) The effect of the New Silk Road railways on aggregate trade volumes between China and Europe *Journal of Chinese Economic and Business Studies*, vol. 16, no. 3, pp. 275–292 doi: 10.1080/14765284.2018.1453720.
24. Unctad, *UNCTADstat.* [Available: https://unctadstat.unctad.org/EN/] [Accessed: Jun. 9, 2021].

ISSN 0554-6397
Stručni članak
(*Professional paper*)

Aleksandar Cuculić
E-mail: aleksandar.cuculic@pfri.uniri.hr
Ivan Panić
E-mail: ivan.panic@pfri.uniri.hr
Jasmin Ćelić
E-mail: jasmin.celic@pfri.uniri.hr
Antonio Škrobonja
E-mail: antonio.skrobonja@pfri.uniri.hr
University of Rijeka, Faculty of Maritime Studies, Studentska 2, Rijeka, Croatia

Implementation of Charging Stations for Hybrid and Electrical Ferries in Croatian Ports

Abstract

An important aspect of introducing hybrid or all-electric ferries on coastlines is to analyze the supporting land-based energy infrastructure to determine if it is possible to implement charging systems that such vessels rely on. The battery energy storage systems on such vessels will need to be rapidly recharged as passengers and vehicles disembark, which means that the flow of electricity through the distribution grid will be much higher and may lead to power quality issues on the local grid. Once implemented, shore connection and battery charging systems must be safe for both people and connected equipment. The issue of implementing shore connections needs to be analyzed from a technical, economic, and legal perspective. This paper presents the challenges and problems of implementing charging stations for ferries in Croatian ports as a result of the research conducted within the project METRO - Maritime Environment-Friendly Transport Systems.

Keywords: hybrid and electric ferry, battery charging stations, shore connections, battery energy storage, ferry ports

1. Introduction

The introduction of hybrid and electric ferries on coastlines is impossible if the necessary supporting infrastructure is not in place in ports [1]. For such vessels to make sense at all, and to enable the reduction or complete elimination of harmful emissions, it is necessary for all or most of the energy for propulsion to come from clean sources, primarily batteries [2].

As the available storage space for battery storage modules is usually limited, the total capacity of batteries that can be installed on a ferry is often only slightly higher than the minimum required to safely maintain an existing line. This means that the batteries need to be recharged every time (or every few trips on shorter routes) while the vessel is in port. As the time spent in port is short (especially on the routes between the coast and the islands during the tourist season), the charging system is expected to be able to recharge the batteries quickly, which means very high charging currents and therefore a high load on the local distribution network.

The electricity distribution networks on the islands and smaller towns along the Croatian coast are mostly designed to meet the needs of the local infrastructure. As there are no important industrial plants in the tourist centers, they are usually simple radial networks without bidirectional power supply and with limited capacity. A sudden load increase caused by high charging currents, as well as possible harmonic distortions caused by power electronic devices in battery charging systems, can significantly affect the quality of power supply in such networks.

Therefore, when designing a charging system, it is necessary to have a good knowledge of the vessel's operating profile and to anticipate the peak loads that may occur during battery charging. If the available resources of the distribution network cannot meet the ship's requirements, additional energy storage (ES) must be installed or some of the available renewable energy sources must be used. In addition, the battery charging system must be safe for people and port infrastructure, as well as comply with regulatory requirements and technical standards for distribution networks and shore connection systems [3][4].

The aim of this article is to shed more light on the topic of implementing charging stations for ferries in the Republic of Croatia, based on the research results of the project METRO - Maritime environmentally friendly transport systems

2. Basic features of hybrid and electrical ferries

The power requirements and configuration of the shore connection and charging system for electric and hybrid ferries depend largely on the topology of the marine power plant and the requirements of the particular line. Propulsion drives with battery ES on a ferry can be implemented in four basic ways:

- hybrid electric propulsion with diesel generators (DG) and battery ES with AC distribution,
- hybrid electric propulsion with DG and battery ES with DC distribution,
- hybrid electric drive with power take-off (PTO)/power take-off (PTI) combining mechanical and electric drive in one kinematic driveline,
- all-electric battery drive.

All-electric propulsion depends entirely on the shore-based charging system, while the other three configurations offer much greater flexibility in adapting to the

capabilities and performance of the port's electrical infrastructure. Therefore, when planning the introduction of a battery-powered ferry on a particular route, it is necessary to consider multiple propulsion options and determine the peak loads and required battery charging times while the ferry is in port according to the vessel's planned operational profile.

Analysis of battery-powered ferries currently in operation shows that installed battery capacity varies between 500 kWh and 5000 kWh, with required charging powers of up to 10 MW. Fully electric ferries are small in size and capacity due to the limitations imposed by the weight of the size of the battery storage, and are suitable for maintaining shorter routes where the focus is mainly on passenger transport. It is for these very reasons that most ferries on commercial lines where there is the possibility of carrying a larger number of passengers and vehicles use hybrid propulsion or a combination of batteries and internal combustion engines[5].

Analyzing the required capacities of vessels on existing ferry lines in the Republic of Croatia, as well as the state of the distribution network (especially in smaller areas where most ferry ports are located), it can be assumed that hybrid vessels would be a more reasonable choice compared to all-electric solutions. The use of hybrid propulsion also allows for greater flexibility in the choice of battery storage size, i.e. it is easier to adjust the required power of the charging stations to the capabilities of the distribution network in a given area.

3. Battery charging solutions

Battery charging systems for electric and hybrid ferries can basically be implemented in the following ways:

- direct charging from the grid of LV,
- direct charging from the MV or HV grid,
- combined charging from the ship's own DG and the shore-side grid,
- combined charging from the shore-side grid, ES and renewable sources.

A low-voltage shore connection (LVSC) is a shore connection system that uses either 400-, 440-, or 690-V cable to connect shore and ship. It is designed to handle up to 1.5 MW.

LVSCs typically allow the integration of the charging system into the port infrastructure with relatively minor interventions in the distribution network, usually involving the upgrade or installation of a new MV / LV distribution transformer [6].

If they can meet the charging power requirements, such connections are a very good option for smaller ferry ports on shorter routes (e.g. Brestova-Porozina, Prizna-Žigljen, Valbiska-Merag and the like). Due to the relatively low investment costs and small space requirements, the filling station can be easily installed in both ports, which allows much greater flexibility in maintaining the line.

High voltage shore connections (HVSC) can deliver currents in excess of 1 MW and allow rapid charging of batteries at high current. Such systems are now widely used in container ships and cruise ships, except that there they are not used to charge the batteries but to power the ship's electrical system while in port. The integration of such systems in small ferry ports usually faces some obstacles, the most common of which are: limited capacity of the distribution system and supply lines in the port, the availability of space for the installation of HVSC-specific cables, sockets, switchboards, converters and transformers, the need to upgrade the ship's own power management system (PMS) in order to operate the ship in parallel with the shore grid and avoid power outages [7]. To overcome these obstacles, significant modifications are often required, resulting in high implementation costs.

Such systems are more suitable for larger ports that serve as hubs for multiple ferry lines to nearby islands, such as Split and Zadar, because the better developed power distribution network and higher capacity of supply lines make such connections easier to implement.

Due to the technical challenges and high implementation costs mentioned above, it is not realistic to expect that installing this type of connection for both ports on a single ferry line will be cost effective. This may somewhat limit the flexibility in terms of overnight charging of the battery storage if the ferry has to spend the night in a port where the HVSC connection is not installed. This problem can be solved to some extent by installing an LVSC in another port that is used exclusively for slow battery charging during the night.

For ports where it proves impossible or unprofitable to expand the capacity of the supply network, and where one wants to reduce emissions as much as possible, one of the solutions is combined charging via the ship's own DG and the shore-side network. In this approach, the marine battery energy storage system is charged directly from the ship's electrical grid, which is powered by diesel generators, and the battery power is then used for maneuvering in port. This approach not only reduces the number of generator operating hours, but also allows the charging current to be regulated to keep the load on the diesel generators in the optimum mode where specific fuel consumption, and therefore harmful gas emissions, are lowest. During the ferry's night stay in port, the batteries can be recharged to the extent allowed by the LVSC capabilities.

Although it is technically the most complex and requires the installation of power electronic converters, combined charging from the shore power grid and the system installed in the port area ES is probably the best solution for ferry ports, as shown by experience in the Nordic countries where such solutions have been used for some time. In the areas where this is possible, and this certainly includes the Croatian coast, part of the electrical energy for charging the batteries can be obtained from renewable sources, mainly sun and wind, which promotes the use of green electrical energy and improves environmental friendliness.

4. Distribution grid capacity analysis

Future electric charging stations must be connected to the national electricity distribution grid. The first step in introducing battery-powered vessels is to assess the condition and capabilities of the distribution network in the port in question.

The distribution network is the final stage of the electricity transmission system and is used to distribute electrical energy to end users. Typical consumers connected to the distribution network are households, industry, ports, urban infrastructures, etc. The distribution network in Croatia is divided into two parts: the medium voltage network (MV) with nominal voltages of 10/20/35kV and the low voltage network (LV) with a nominal voltage of 0.4kV [8]. The maximum connected load that the customer can reach via the medium-voltage grid is in the range between 10MW and 20 MW, of course only if the existing cable infrastructure at the desired connection point allows this [9].

Once the power demand has been determined, when it comes to connecting their equipment to the distribution network, the user does not have too much influence on the realization of the LV or MV connection point. These aspects fall within the scope of the national distribution system operator (Hrvatska Elektroprivreda - HEP in Croatia). While the user (electricity buyer) is responsible for all equipment from the connection point, the DSO has to ensure the quality, reliability and continuity of electricity supply according to the existing regulations.

For certain consumers, such as charging stations for ferries, a continuous power supply is crucial, as a power failure would prevent the charging of batteries while the vessel is in port. Power supply indicators (which are publicly available for the distribution network in the Republic of Croatia) are calculated based on data from electronic records, i.e. using the DISPO (Distribution Reliability) application, which has been in use on HEP since 2006. The application allows statistical processing of manually entered planned and unplanned outages of network components with a duration of more than three minutes.

To represent the state of power reliability, the most important indicators are: average number of long power outages per network user (SAIFI), average duration of long power outages per network user (SAIDI), and average duration of long power outages per network user (CAIDI).

As most public MV /LV substations are designed to meet the needs of households and civil infrastructure in the area where the ferry port is located, it is unrealistic to expect them to have sufficient power reserve to meet the demands of future shore connections/charging systems. It is expected that in ports with limited electricity reserves, shore-based energy storage systems or renewable energy sources (if available and economically viable) will play an important role in supporting the local grid.

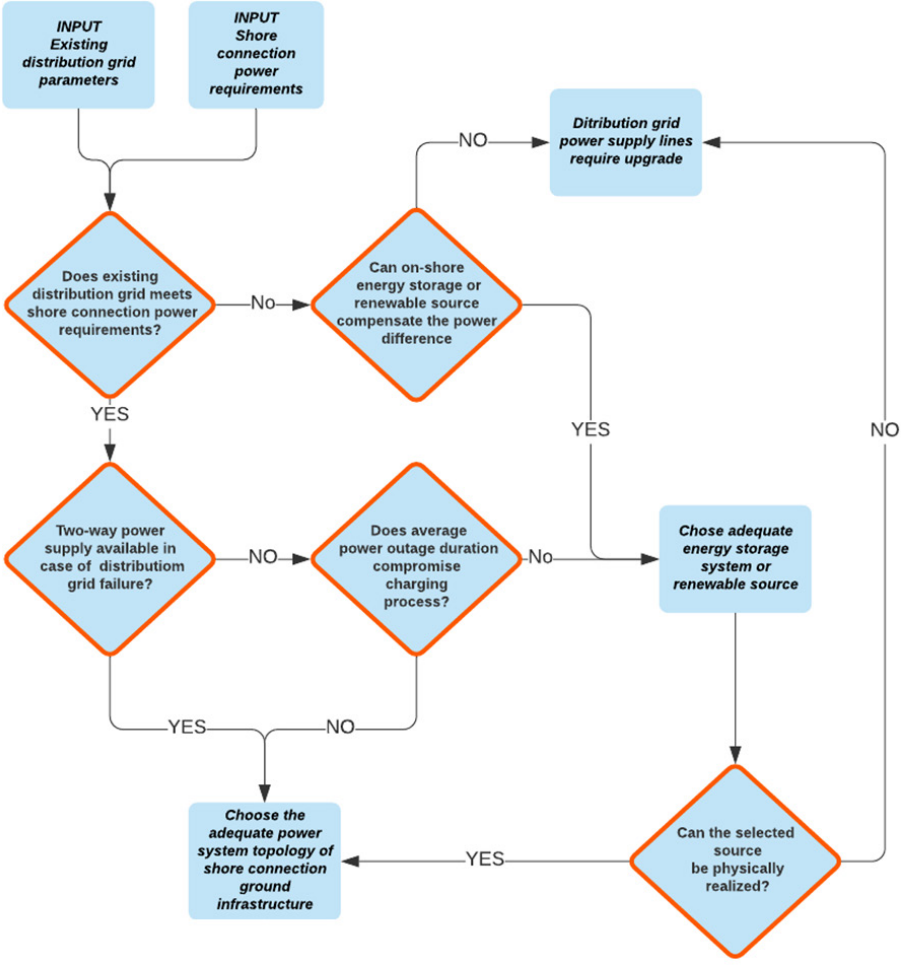

Figure 1: Suggested methodology for choosing adequate shore connection and charging system topology according to distribution grid characteristics

In this first step, it is necessary for the investor who implements the charging system, whether it is the port authority or the ferry line operator, to determine the real possibilities of the distribution network in the area covered by the ferry port of interest in cooperation with HEP. Wrong assessment of actual possibilities and load on the distribution grid by months (especially in the summer season) can jeopardize the continuity of line maintenance or its economic viability due to possible subsequent upgrade needs.

Suggested methodology for choosing adequate shore connection and charging system topology according to distribution grid characteristics is shown in Figure 1.

5. Optimizing shore side power system

Once the parameters and constraints of the distribution network are defined, which determine the possible technical solutions of the charging system in a given area, it is necessary to choose the most favorable solution from the technical and economic point of view. Due to the large number of interdependent parameters and the fact that each ferry line is specific in itself, simulations will play an important role in the evaluation of the system behavior. Although simulations cannot replace realistic measurements and tests, with well chosen and calculated electrical network parameters they can still provide satisfactory results for proper evaluation of future solutions.

In this paper, the process of optimization of shore connection and charging station components is described for the ports of Brestova and Porozina, but the same methodology can be applied to any ferry port.

The software HOMER Pro microgrid was chosen as the simulation tool. It simulates the operation of a system by performing energy balance calculations at each time step (interval) of the year. For each time step, HOMER compares the electrical and thermal demand at that time step to the energy that the system can supply at that time step, and calculates the energy flow to and from each component of the system. For systems that contain batteries or fuel-powered generators, HOMER decides at each time step how to operate the generators and whether to charge or discharge the batteries.

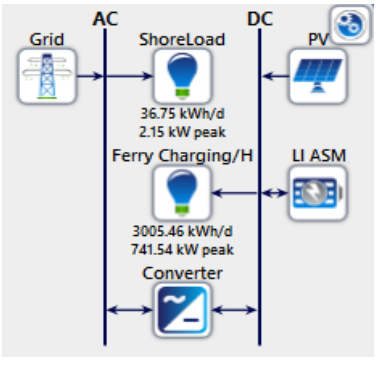

Figure 2: Ferry charging station model realized in HOMER Pro® microgrid software

It performs these energy balance calculations for each system configuration you are considering, and then determines whether a configuration is feasible (i.e., whether it can meet the power demand under the conditions you specify) and estimates the cost

of installing and operating the system over the life of the project. HOMER Pro has two optimization algorithms; the original grid search algorithm simulates all feasible system configurations and HOMER Optimizer uses a proprietary, derivative-free algorithm to find the lowest cost system.

The configuration of the proposed loading station model for the ports of Brestova and Porozina, implemented in the HOMER Pro® Microgrid software, is shown in Figure 2.

The following initial parameters are used:

1. Grid parameters;
   ◊ Grid sale capacity: 1000 kW.
   ◊ Stand by charge (annual fee for connecting consumers to HEP's network-calculated from HEP's site for industrial consumers): $ 100 per year.
   ◊ The purchasing price of electricity (including the price of labour and reactive power because industrial consumers pay both): $ 0.17 per kW
   ◊ The selling price of electricity: $ 0.016 per kW

2. Grid reliability:
   ◊ Number of power outages: 5 per year
   ◊ Mean time to repair: 120 minutes

3. Power converter:
   ◊ Installation costs: $ 400 per kW
   ◊ Replacement costs: $ 300 per kW
   ◊ Annual maintenance costs: $100 per year
   ◊ Estimated life cycle: 15 years

4. On shore battery ES (Corvus Orca Energy is used in model):
   ◊ Capacity of one battery bank: 125 kWh
   ◊ DC voltage (min/rated/max): 800V/980V/1100V
   ◊ Initial state of charge (SOC): 100%
   ◊ Minimal allowed SOC: 20%
   ◊ Degradation limit: 30% of full capacity (the influence of temperature on battery aging was taken into account)

5. Photovoltaics (PV):
   ◊ A generic flat panel without curvature or active sun tracking was modelled
   ◊ Price: $2500 per kW
   ◊ Global horizontal irradiance (GHI) data for Brestova-Porozina area is taken from NASA database (part of HOMER software)

6. Shore side load:
   ◊ According to data from HEP, a generalized model was developed. The port infrastructure consumed power, both in Brestova and Porozina are extremely small to have an impact on the Ferry load.

7. Ferry charging and hotel load:
   ◊ Estimated power of the ferry hotel load is 250 kW and charging power is 500 kW. The schedule of arrivals and departures of the ferry was taken from the Jadrolinija and based on it a generalized charging schedule was made.

Simulation results based on previously defined parameters show two possible solutions for charging stations in Brestova and Porozina which are briefly summarized in Table 1.

Table 1: Summary of two possible solutions for ferry charging stations in Brestova and Porozina

	Solution 1	**Solution 2**
PV power	9.36 kW	No PV installed
Battery ES power	3 x 125 kW	3 x 125 kW
Required converter power	207 kW	338 kW
Autonomy on battery ES only	2,08 hours	2,08 hours
Estimated initial costs	$ 220000	$ 250000

The first solution includes PV panels, but the battery is almost depleted to the end and is constantly at the lower SOC limit. In this configuration, the downsizing of the converter is supported because the batteries are partially charged by the solar panels. This reduces the cost of the system, but also the reliability.

The second solution is much better in terms of reliability. The converter is larger, so it keeps the status of the battery SOC above the minimum level. Also, it is possible to install 5 to 10 kW of PV, but according to Homer, this is suboptimal from a financial point of view.

The choice of solution ultimately depends on the investor, but since reliability is paramount in such systems, option number 2 is considered the best solution. Also, if needed, it is very easy to add additional PV modules once the price and efficiency are more favorable.

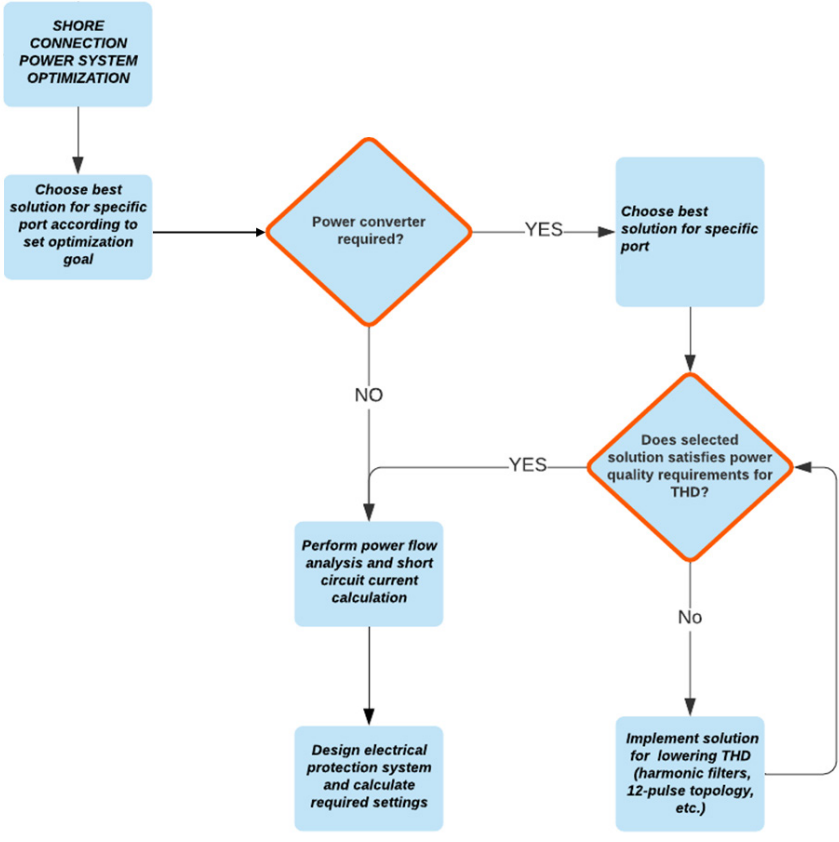

Figure 3: Suggested methodology for shore connection power system optimization

After selecting the appropriate topology for the charging station, the power flow analysis should be performed and the appropriate electrical protection system should be designed. It is also necessary to consider the impact of the converter on the power quality of the utility grid through field measurements or simulations to ensure that the proposed solution meets the requirements specified in the standard EN 50160 for the maximum allowable harmonic distortion of voltage THDv in public distribution systems.

The proposed methodology for optimizing the shore power network is shown in Figure 3.

6. Rules and regulations

When introducing hybrid and electric ferries on a large scale, it is important to focus on the regulatory context, both in terms of regulations and standardization. This chapter provides an overview of the regulations, guidelines and standards currently in place for the use of batteries and shore connections in shipping.

The design concept for these systems is included in the current LVSC draft standard, International Electrotechnical Commission (IEC)/ IEEE 80005-3. Although this application has not yet been standardized at the international level, it is usually partially covered by national standards. The general rules for the construction of LV shore connections in the Republic of Croatia are established in accordance with the European standard that defines the technical requirements for inland vessels (ES - TRIN). For currents up to 125 A, they comply with the requirements of the European Standards EN 15869-1: 2019 and EN 15869-3: 2019 and for currents above 250 A, they comply with the requirements of the European StandardsEN16840: 2017.

The stringent requirements and complexity of the issues associated with shore-side power supply to ships at berth have led to the development (in collaboration with the IMO) of the European pre-standard IEC/PAS 60092-510:2009 Electrical installations in ships - Special features - High Voltage Shore Connection (HVSC) Systems, which describes the general requirements for S2SP systems. On this basis, the International Electrotechnical Commission has issued the standard HVSC Systems - General Requirements (IEC/ISO/ IEEE Std 80005-1).

Regulation of the use of batteries in ships does not yet appear to be on the agenda of the International Maritime Organization (IMO). To date, most of the development work has been done by certain flag States and classification societies. The current relevant standards for specific maritime battery applications or battery technologies are summarized in Table 2.

Table 2: Current relevant standards for specific maritime battery applications or battery technologies [10]

Standards / Rule	Year of publication	Short description
EN 50110 Edition 2.N (2013-06-01)	2013	Operation of electrical installations -- Part 1: General requirements - Supporting documentation for batteries and electrical testing
IEC 61508 Edition: 1.0 (2005-01-20)	2005	Functional safety of electrical/electronic/ programmable electronic safety-related systems – Supporting documentation for batteries and electrical testing

IEC 61511 Edition: 1.0 (2003-12-19)	2003	Functional safety - Safety instrumented systems for the process industry sector - Supporting documentation for batteries and electrical testing
ISO 26262 Edition: 1 (2011-11-14)	2001	Road vehicles -- Functional safety - Supporting documentation for batteries and electrical testing
IEEE 45-2002	2002	Recommended Practice for Electrical Installations on Shipboard

Guidelines on battery and shore connection utilization given by the four major Class Societies member of IACS are shown in table 3.

Table 3: Guidelines on battery and shore connection utilization given by the four major Class Societies member of IACS

Class Society	Date	Type	Title
ABS	2020	Guideline	**Hybrid electric power systems for marine and Offshore applications** - Dedicated to the application of hybrid electric power systems
	2020	Guideline	**Use of lithium batteries in the marine and Offshore industries** - Provides class requirements and reference standards to facilitate effective installation and operation of lithium battery systems.
	2011	Guideline	**High Voltage Shore Connection**
BV	2020	Rules	**Rules for Classification of Ships:** Pt F, Ch 11, Sec 21 – Battery system Pt F, Ch 11, Sec 22 – Electric Hybrid Pt F, Ch 11, Sec 29 – Electric Hybrid Prepared
	2010	Rule Notes	**RN557** - High-Voltage Shore Connection System
DNV GL	2020	Rules	**Rules and Standards for classification: Ships (RU-SHIP)** Pt. 6 Ch.2 Sec.1 - Electrical Energy Storage
	2020	Rules	**Rules and Standards for classification: Ships (RU-SHIP)** Pt.6 Ch. 7 Sec. 5 - Electrical shore connections - Shore power

LR	2020	Rules	**Rules and Regulations for the Classification of Ships** Pt 6, Ch 2, 12 - Batteries
	2020	Rules	**Rules and Regulations for the Classification of Ships** Pt 7, Ch 13 – On-shore Power Supplies
	2016	Guideline	**Battery installations** - Key hazards to consider and Lloyd's Register's approach to approval

While the aforementioned standards for shore connections define the requirements and protection of standard connectors needed for cold ironing, there are no official standards yet for battery chargers and their integration. Future electric and hybrid vessels will require new solutions and topologies for shore connections characterized by the increased use of power electronics devices, the integration of energy storage and environmentally friendly renewable sources, and the use of DC distribution systems. Accordingly, there is a need to extend existing standards or develop new ones that incorporate these solutions, with the aim of facilitating an easier transition to greener solutions for ferry and RO - RO transport.

7. Conclusions

With existing and future regulations aimed at reducing maritime emissions, shipping companies are forced to look for alternative environmentally friendly propulsion solutions. One such solution, which is particularly suitable for coastal ferries in the Republic of Croatia, is the use of battery energy for propulsion, either in the form of all-electric or hybrid propulsion.

The introduction of such vessels is impossible without adequate shore-side electrical infrastructure, especially the battery charging system. The design and analysis of the shore connection and charging system should include the vessel design, shore connection technology and port electrical infrastructure in order to have the right amount of information to choose the best solution for the application. It is very important to accurately determine the electrical power requirements of the ferry port in question so that the distribution system operator can assess whether the existing infrastructure meets the requirements or whether an upgrade is needed, which will ultimately determine the choice of shore connection topology. Such infrastructure projects involve several stakeholders, primarily the port authority, the ferry operator and the distribution system operator. It is expected that the legal and administrative work and the obtaining of the necessary permits will take a long time, so that such projects need to be planned several years in advance.

This paper proposes the methodology for planning shore connections and charging

systems for ferries using the ports of Brestova and Porozina as examples, but the proposed methodology can be used for any port.

While the existing draft standard IEEE /IEC 80005-3 defines the requirements and protective measures for standard connectors needed for cold ironing, the standards for battery chargers and their integration do not officially exist yet. There is a need to extend existing standards or develop new ones that incorporate these solutions, with the ultimate aim of enabling an easier transition to more environmentally friendly solutions for ferry transport.

8. Acknowledgements

The research was funded by European Regional Development Fund (ERDF), through the 2014–2020 Interreg V-A, Italy—Croatia CBC Programme, by means of the 2017 Standard call research project "METRO—Maritime Environment-friendly TRanspOrt systems" (Project ID: 10044221), Priority Axis: Maritime transport.

9. References

1. Nguyen, H. P., Hoang, A. T., Nizetic, S., Nguyen, X. P., Le, A. T., Luong, C. N., ... & Pham, V. V. (2021) The electric propulsion system as a green solution for management strategy of CO2 emission in ocean shipping: A comprehensive review. International Transactions on electrical energy systems. 31(11), e12580.
2. Gagatsi, E., Estrup, T., & Halatsis, A. (2016) Exploring the potentials of electrical waterborne transport in Europe: the E-ferry concept. Transportation Research Procedia. 14, 1571-1580.
3. Kumar, J., Parthasarathy, C., Västi, M., Laaksonen, H., Shafie-Khah, M., & Kauhaniemi, K. (2020) Sizing and allocation of battery energy storage systems in Åland islands for large-scale integration of renewables and electric ferry charging stations. Energies. 13(2), 317.
4. Kumar, J., Memon, A. A., Kumpulainen, L., Kauhaniemi, K., & Palizban, O. (2019) Design and Analysis of New Harbour Grid Models to Facilitate Multiple Scenarios of Battery Charging and Onshore Supply for Modern Vessels. Energies. 12(12), 2354.
5. Anwar, S., Zia, M. Y. I., Rashid, M., Rubens, G. Z. D., & Enevoldsen, P. (2020) Towards ferry electrification in the maritime sector. Energies. 13(24), 6506.
6. IEC/IEEE (2019) DIS 80005-3 Utility connections in port - Part 3: Low Voltage Shore Connection (LVSC) Systems - General requirements.
7. IEC/IEEE (2016) 80005-2:2016 Utility connections in port - Part 2: High and low voltage shore connection systems - Data communication for monitoring and control.
8. Goić, R., Jakus, D., Penović, I. (2008) Electrical power distribution. Faculty of Electrical Engineering, Mechanical Engineering and Naval Architecture. University of Split.
9. HEP - Croatian Distribution System Operator (2017) Ten-year (2018-2027) plan for development HEP distribution network with detailed elaboration for the initial three-year and a one-year period.
10. DNV-GL (2020) Study on electrical energy storage for ships for EMSA Report No. 2019-0217, Rev. 04.

ISSN 0554-6397
Konferencijski članak
(*Conference paper*)

Alen Marijančević
E-mail: alen.marijancevic@riteh.hr
Sanjin Braut
E-mail: sbraut@riteh.hr
Roberto Žigulić
E-mail: zigulic@riteh.hr
Faculty of Engineering University of Rijeka, Vukovarska 58, Rijeka, Croatia

Analysis of Ship Propulsion Shafting Vibration Using Coupled Torsional-Bending Model

Abstract

The paper describes a coupled torsional-bending model of ship propulsion system vibrations. The developed model is based on the modified model of the Jeffcott rotor. In order to test the model and determine the coupled torsional-bending vibrations, several cases were analyzed. First, a reference case corresponding to a fully axisymmetric ship propulsion system is set up. Then, the influence of the constant radial force in the vertical direction at the position of the stern bearing was analyzed, such as the conditions of navigation of the ship at calm sea under partial or fully loaded hull. Finally, the case of sailing on rough sea is analyzed, when the propeller racing occurs due to the stern lifting out of the sea. For simplicity, the harmonic law of amplitude changing of the vertical radial force on the stern tube bearing as well as of the propeller load was adopted. Based on the results of numerical analysis, it was found that the proposed model well describes the case of coupling of torsional and bending vibrations of the propulsion system.

Keywords: ship propulsion system, coupled torsional-bending vibration model, numerical analysis, propeller racing

1. Introduction

The ship's propulsion system suffers various complex loads during operation. The shaft line is usually loaded externally due to combination of radial forces that represent reactions in the bearings and the torque variations caused by the torsional vibration applicable for continuous operation, basically due to engine firing pulses [1, 2].

A proper consideration of the single and coupled vibration modes of the propeller shaft, including torsional, longitudinal, and transverse vibrations is important to ensure safe ship propulsion and navigation at sea, [3, 4].

The weather conditions under which the ship sails can also have a impact on the shaft line loadings since the rough sea can cause periodical emerging and immersion from the sea, causing a propeller racing phenomenon, [5, 6].

Due to mentioned loads the torsional and transverse vibrations of a shaft line are expected, having the influence on fatigue [7-9] as well as fractural [10,11] behavior of shaft line system.

Additionally, due to always present shaft unbalance and bow [12], the conditions for appearance of coupled torsional – transverse vibrations, are met.

This paper presents a contribution in terms of explaining the coupling between torsional and bending vibrations of the shaft line when the ship is navigating on calm and rough seas.

2. Mathematical and numerical model for coupled torsional-bending vibrations of ship propulsion shafting

In this paper mathematical model based on the modified model of the Jeffcott rotor is used, Figure 1. The propulsion shaft, subjected to both torsional as well as bending vibrations is modelled as rigid disc characterized with inertial parameters such as mass *m* and mass moment of inertia *J*. Propulsion shaft is also subjected to cross – section eccentricity due to unbalance *e*. The equations of motion for the disc due to planar motion are

$$x = x(t),\ \ y = y(t),\ \ \varphi = \varphi(t) = \theta(t) + \omega t \tag{1}$$

In the previous equation, the total rotational angle φ of disc is a sum of rotational angle due to shaft rotation with constant rotational speed ω and torsional vibrations angle θ. The unknown displacement vector, as function of time *t*, consists of two translational displacements and one rotational angular displacement:

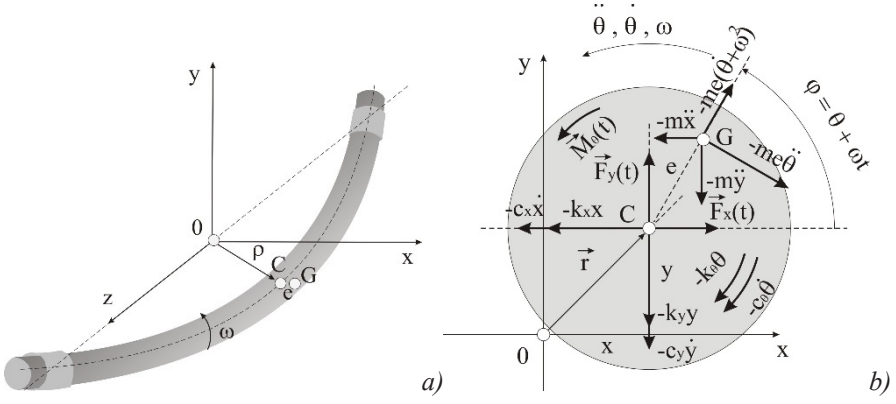

Figure 1. Shaft with the eccentricity of cross section

$$\{u(t)\} = \{x(t), y(t), \theta(t)\}^T \tag{2}$$

Having in mind the elastic and dissipative forces acting in shaft geometrical centre C in both vibrating directions x and y, as well as inertial forces in this directions and inertial forces due to centripetal and tangential rotational accelerations, acting on center of mass G, the equations of motion obtained due D'Alambert principle take the following form (Figure 1b):

$$\begin{gathered} m\ddot{x} = \sum F_x \rightarrow m\ddot{x} - me\ddot{\theta}\sin(\omega t + \theta) + c_x\dot{x} + k_x x == me\left(\omega + \dot{\theta}\right)^2 \cos(\omega t + \theta) \\ m\ddot{y} = \sum F_y \rightarrow m\ddot{y} + me\ddot{\theta}\cos(\omega t + \theta) + c_y\dot{y} + k_y y == me\left(\omega + \dot{\theta}\right)^2 \sin(\omega t + \theta) \\ J\ddot{\theta} = \sum M_\theta \rightarrow \left(J + me^2\right)\ddot{\theta} - me\ddot{x}\sin(\omega t + \theta) + + me\ddot{y}\cos(\omega t + \theta) + c_\theta\dot{\theta} + k_\theta\theta = 0 \end{gathered} \tag{3}$$

The nonlinear equations of motion (3) are coupled through the presence of torsional angle θ and its time derivations in bending equations as well through the presence of horizontal and vertical accelerations in the equation for motion in torsional direction. Equations (3) can be further rearranged by means of angles addition theorem as well as torsional angle approximation as small quantities ($\sin\theta \approx \theta$, $\cos\theta \approx 1$):

$$\begin{gathered} m\ddot{x} - me\ddot{\theta}sin(\omega t)\sin(\omega t) + c_x\dot{x} + k_x x - 2me\omega\dot{\theta}\cos(\omega t) + me\omega^2\theta\sin(\omega t) = \\ = me\omega^2\cos(\omega t) + F_x(t) m\ddot{y} + me\ddot{\theta}\cos(\omega t) + c_y\dot{y} + k_y y - \\ -2me\omega\ddot{\theta}\sin(\omega t) - me\omega^2\theta\cos(\omega t) = me\omega^2\sin(\omega t) + F_y(t)\left(J + me^2\right)\ddot{\theta} - \\ - me\ddot{x}\sin(\omega t) + me\ddot{y}\cos(\omega t) + c_\theta\dot{\theta} + k_\theta\theta = M_\theta(t) \end{gathered} \tag{4}$$

Finally, equations (4) should be written in the matrix form as follows:

$$[M]\{\ddot{u}\} + [C]\left\{\dot{u}\right\} + [K]\{u\} = \{F_c\} + \{F_{ext}\} \tag{5}$$

where inertia matrix $[M]$, matrix of dissipative forces $[C]$, stiffness matrix $[K]$ and vectors of time dependent centrifugal $\{F_c\}$ and external forces $\{F_{ext}\}$, are defined as:

$$[M]=\begin{bmatrix} m & 0 & -me\sin(\omega t) \\ 0 & m & me\cos(\omega t) \\ -me\sin(\omega t) & me\cos(\omega t) & J+me^2 \end{bmatrix},$$

$$[C]=\begin{bmatrix} c_x & 0 & -2me\omega\cos(\omega t) \\ 0 & c_y & -2me\omega\sin(\omega t) \\ 0 & 0 & c_\theta \end{bmatrix},$$

$$[K]=\begin{bmatrix} k_x & 0 & me\omega^2\sin(\omega t) \\ 0 & k_y & -me\omega^2\cos(\omega t) \\ 0 & 0 & k_\theta \end{bmatrix}, \quad (6)$$

$$\{F_c\}=\begin{Bmatrix} me\omega^2\cos(\omega t) \\ me\omega^2\sin(\omega t) \\ 0 \end{Bmatrix}, \{F_{ext}\}=\begin{Bmatrix} F_x(t) \\ F_y(t) \\ M_\theta(t) \end{Bmatrix}$$

In the matrix equation (6) parameters c_x, c_y, c_θ, k_x, k_y and k_θ represent dampings and stiffnesses of the system in directions of coordinate axis x and y while c_θ and k_θ are torsional damping and stiffness.

In terms of getting results of simulation i.e. vector $\{u\}$, system (6) is solved by using of Newmark's time stepping method. Between it's parameters, the combination containing $\gamma = ½$ and $\beta = ¼$ (average acceleration method) is selected [14].

2.1. External forces and torsional torque

External loadings on the shaft line can be simply defined as a combination of radial forces that represent reactions in the bearings and the torque caused by the propulsion torque load. Two cases are considered in the paper. The first case represents the shaft line response to loads when the ship is navigating on calm seas and the other one represents the shaft line response to loads when the ship is navigating on rough seas.

In the first case, different hull structure deflections and their impact on propulsion shaft line are assumed regarding different ship service load conditions, Figure 2. It is assumed that ship hull structure has constant deflections when navigating at the same service load condition. Therefore, three subcases are considered, $F_x = 0$; 0; 0, $F_y = 0$; 300; 600 N and $M_\theta = M_{\theta 0}\sin(\omega_s t)$, where F_x and F_y are external radial forces, M_θ is external torque on propulsion shaft and $\omega_s = 2\pi/T$ ($f_s = 1/T$) is shaft rotational frequency.

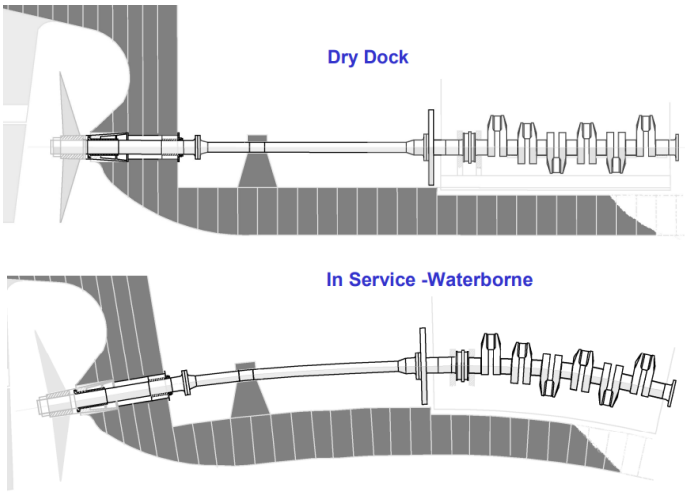

Figure 2. Hull structure deflections and their impact on propulsion shaft line, [13]

In the second case it is assumed that rough sea causes a propeller racing, Figure 3. This phenomenon happens when a ship pitches and heaves heavily. Due to these motions, the stern lifts out of the sea periodically exposing part of the propeller and causing instant increase of propeller speed as well as instant drop of propeller load, Figure 4. It is assumed that wave period T which causes propeller racing is equal to 6 s. To simulate rough sea beside the parameters used for calm sea the following conditions are additionally set: $F_x = 0$, $F_{yr} = F_{yr0}$ $(0.5 + 0.5\sin(\omega_r t))$ and $M_{\theta r} = M_{\theta r0}$ $(0.6 + 0.4\sin(\omega_r t))$, where $\omega_r = 2\pi/T$ ($f_r = 1/T$) is wave rotational frequency and $M_{\theta r0}$ is torque amplitude due to static propeller torque drop caused by propeller racing. Table 1 presents torque and transverse force loads used in numerical analysis.

Table 1. Torque and transverse force loads used in numerical analysis

Case No.	f_s, Hz	F_y , N	$M_{\theta 0}$, Nm	f_r, Hz	F_{yr0} , N	$M_{\theta r0}$, Nm
1	1.67	0	0.06	0	0	0
2	1.67	300	0.06	0	0	0
3	1.67	600	0.06	0	0	0
4	1.67	0	0.06	0.167	600	1

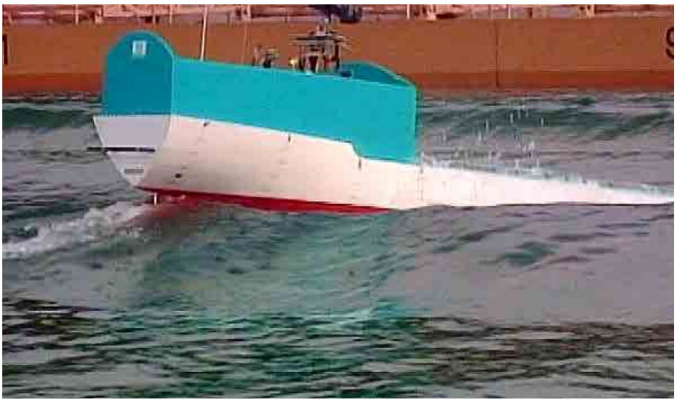

Figure 3. Propeller racing [6]

Figure 4. The emergence of the stern at the rough sea [2]

3. Numerical simulation

To investigate the coupling effect between torsional and bending vibration, propulsion shaft with following parameters was used: shaft density $\rho = 7800$ kg/m^3, Poisson's ratio $\nu = 0.3$, Young's modulus, $E = 206$ GPa, shear modulus, $G = 77$ GPa, shaft length, $L = 2.665$ m, shaft diameter, $D = 0.086$ m, rotational speed $n = 100$ rpm, stiffness of system $k_x = k_y = 7\times10^5$ N/m, $k_y = 1.7\times10^5$ N·m/rad, damping of system, $k_x = k_y = 7\times10^5$ N·s/m and $k_y = 1.7\times10^5$ N·m·s/rad.

Equation (6) was solved by using of Newmark's time stepping method. Time step in each simulation case was 1×10^{-3} s whereas the initial conditions of displacements x_0, y_0, θ_0 were set to zero.

The first three cases of simulation, according to Table 1, correspond to the conditions of navigation on calm seas while the fourth simulation corresponds to the conditions of navigation on rough seas. The total simulation time was equal to 30 s. Results are presented as displacements in time domain, frequency domain as well as in the form of Short time Fourier transform – STFT spectrograms. Figure 5 presents the response of the propulsion shaft displacements in horizontal, vertical direction and torsional angles for case 1 in time and frequency domain. Likewise, Figures 6 and 7 show the frequency responses of shaft displacements in horizontal, vertical direction and torsional angles for cases 2, 3 and 4. In order to gain a more detailed insight

into what happens to the vibrations of the shaft line when navigating rough seas, the spectrograms for case 4 are additionally presented in Fig. 8.

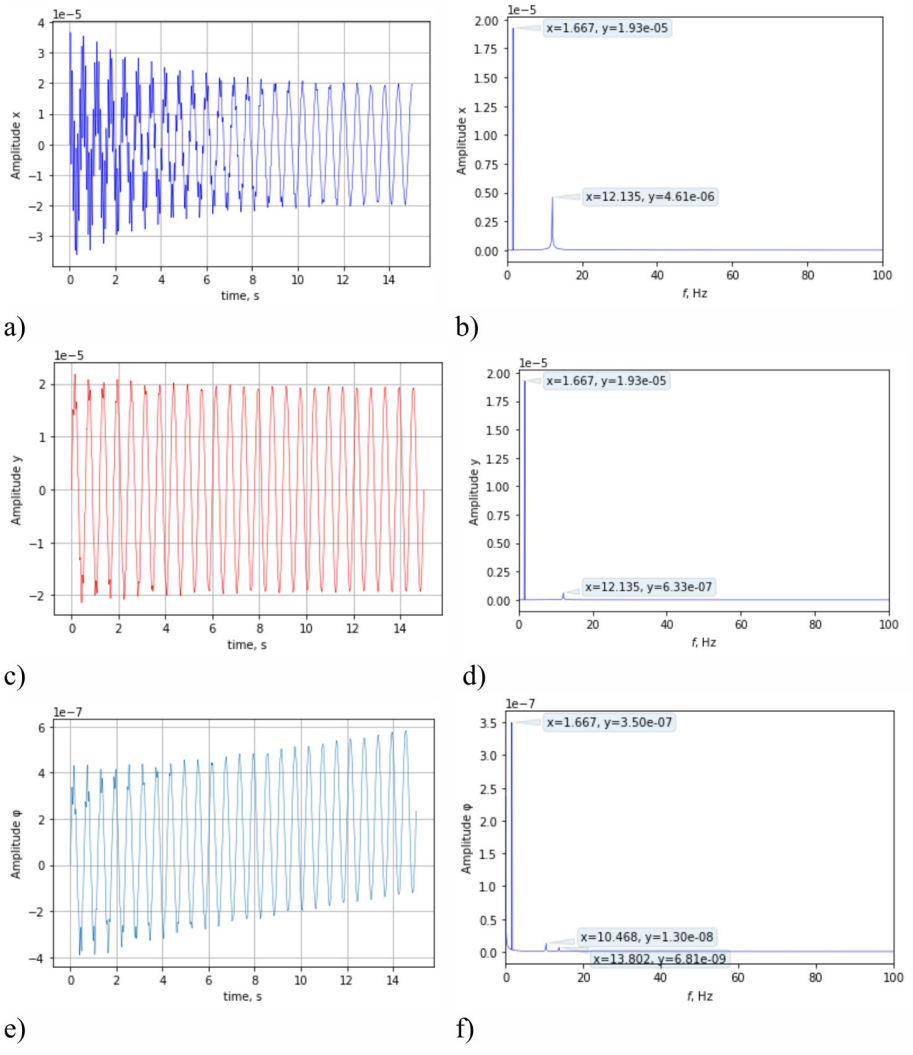

Figure 5. Response of the propulsion shaft displacements in horizontal, vertical and torsional angles for case 1, a) $x(t)$, b) frequency spectrum of $x(t)$, c) $y(t)$, d) frequency spectrum of $y(t)$, e) $\theta(t)$, f) frequency spectrum of $\theta(t)$

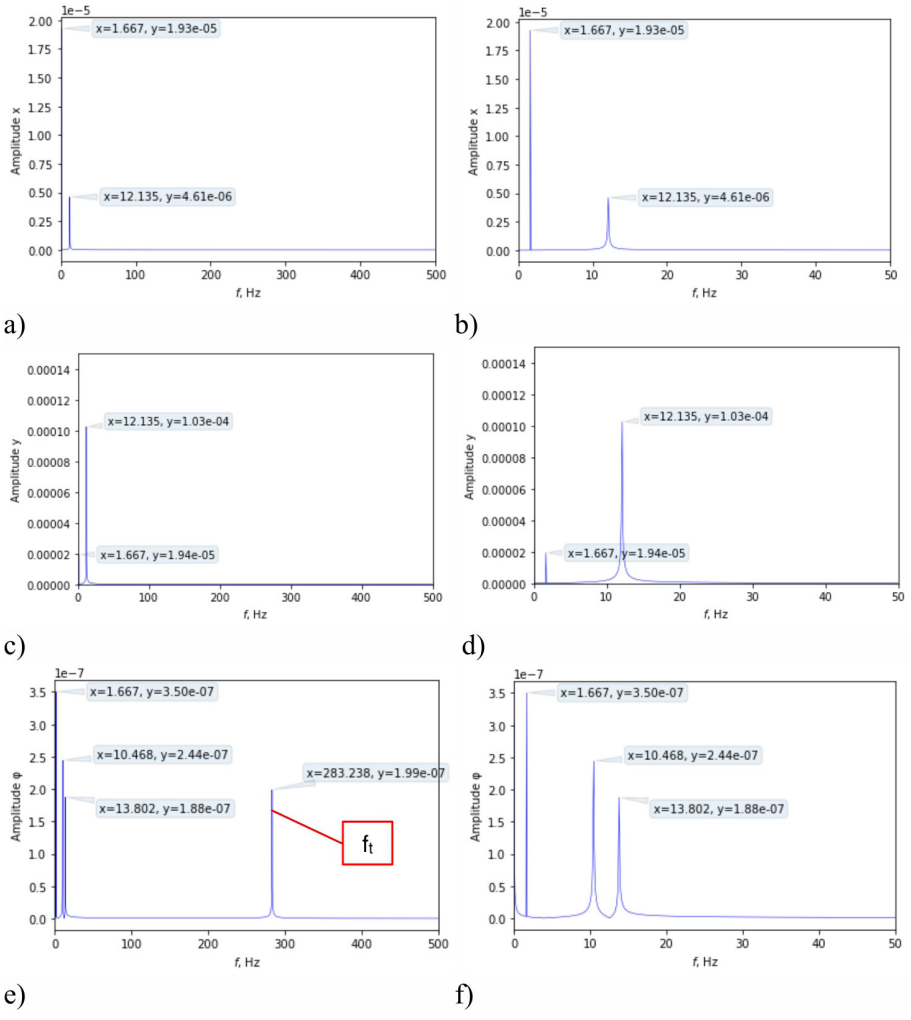

Figure 6. Response of the propulsion shaft displacements in horizontal, vertical and torsional angles for case 2, a) FFT of $x(t)$, b) FFT of $x(t)$ 0-50 Hz, c) FFT of $y(t)$, d) FFT of $y(t)$ 0-50 Hz, e) FFT of $\theta(t)$, f) FFT of $\theta(t)$ 0-50 Hz

Figure 6e shows the frequency responses of the torsional angles of shaft in frequency range 0-500 Hz for case 2. It is important to note that 1 natural torsional frequency has a value of $f_t = 283.2$ Hz, i.e. the frequency components that are visible on the zoom display (Figure 6f) do not actually have anything to do with the torsional free vibrations of the propulsion shaft.

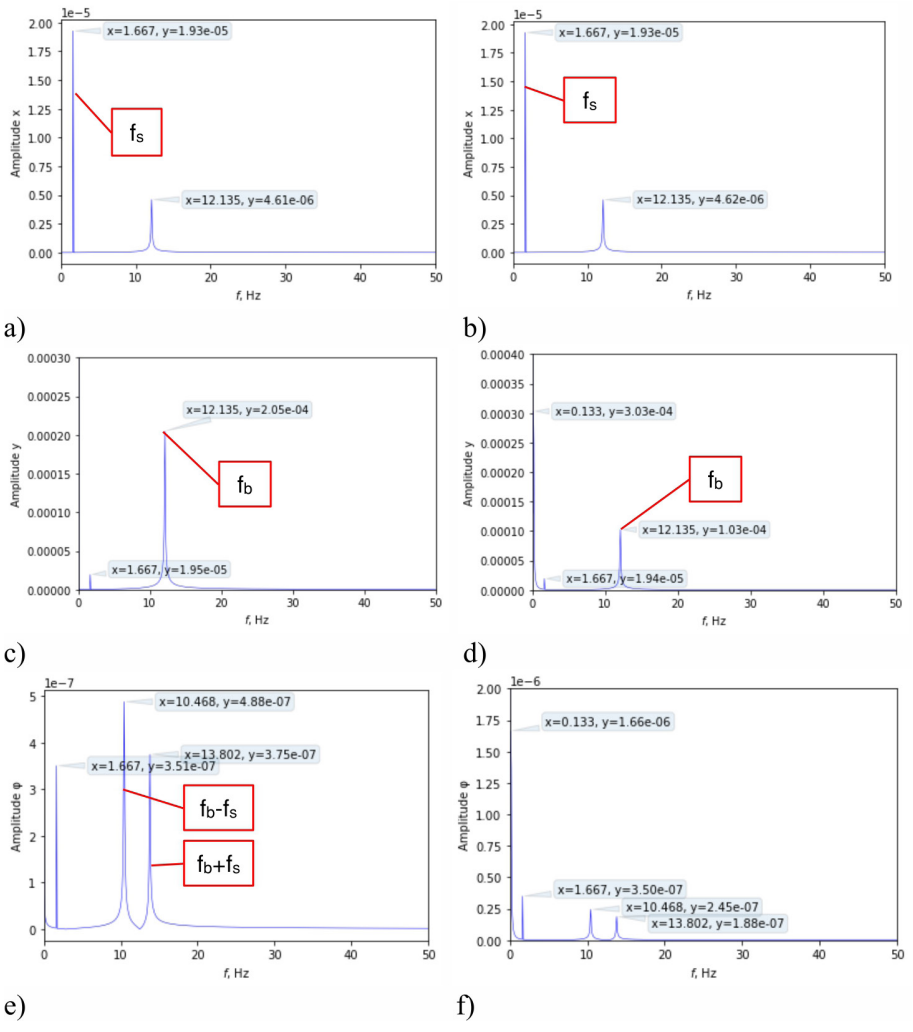

Figure 7. Response of the propulsion shaft displacements in horizontal, vertical and torsional angles for cases 3 and 4, a) c3 FFT of $x(t)$, b) c4 FFT of $x(t)$, c) c3 FFT of $y(t)$, d) c4 FFT of $y(t)$, e) c3 FFT of $\theta(t)$, f) c4 FFT of $\theta(t)$

As the first natural bending frequency of the shaft is at $f_b = 12.1$ Hz, the frequency components, visible in Figures 6f, 7e, 7f and 8c, actually represent the modulated frequencies $f_b \pm f_s = 10.5$; 13.8 Hz and thus prove the coupling between the bending and torsional vibrations of the propulsion shaft.

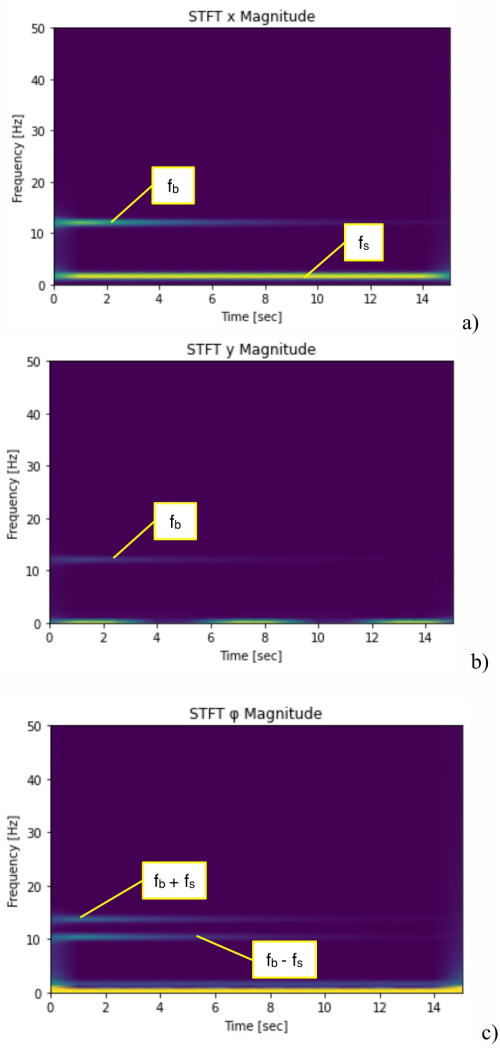

Figure 8. Response of the propulsion shaft displacements in horizontal, vertical and torsional angles for case 4, a) STFT of $x(t)$, b) STFT of $y(t)$, c) STFT of $\theta(t)$,

5. Conclusion

A coupled torsional-bending vibration model of ship propulsion system is considered in this paper. This model is based on the modified Jeffcott rotor model. Two cases are considered. First, when the ship is navigating on calm seas and second,

when navigating on rough seas. Coupling between bending and torsional vibration was observed in each of analyzed cases. It is manifested in the appearance of modulated frequency components ($f_b \pm f_s$) in the torsional domain even though modulation occurs around a central frequency which is actually first bending natural frequency.

Coupling is minimal in the first case when the lateral force is equal to zero but it increases with increasing amplitude of the lateral force. In the STFT spectrogram of the 4th case the wave beating in vertical direction at 0.1333 Hz is more intense than speed frequency harmonic at 1.667 Hz.

Acknowledgements

This study has been fully supported by the Croatian Science Foundation under the project IP-2020-02-8568.

References

1. DNVGL-CG-0038, CLASS GUIDELINE: Calculation of shafts in marine applications, 2015.
2. Radan, D. (2004) *Uvod u hidrodinamiku broda,* Sveučilište u Dubrovniku,
3. Huang, Q., Yan, X., Wang, Y., Zhang, C., Wang, Z. (2017) *Numerical modeling and experimental analysis on coupled torsional-longitudinal vibrations of a ship's propeller shaft*, Ocean Engineering, ELSEVIER.
4. Halilbeşe, A.N., Zhang, C., Özsoysal, O.A. (2021) Effect of Coupled Torsional and Transverse Vibrations of the Marine Propulsion Shaft System, Journal of Marine Science and Application, Springer
5. Journée, J.M.J., Massie, W.W. (2001) Offshore Hydromechanics, Delft University of Technology
6. JAPAN P&I CLUB (2019) *Marine Weather Ship Handling in Rough Sea*, The Japan Ship Owners' Mutual Protection & Indemnity Association Loss Prevention and Ship Inspection Department
7. Cazin D., Braut, S., Božić, Ž., Žigulić, R. (2020) Low cycle fatigue life prediction of the demining tiller tool, Engineering failure analysis, 111 (2020), 104457, 14 doi:10.1016/j.engfailanal.2020.104457
8. Braut, S., Sikanen, E., Sopanen, N., Jussi, J., Božić, Ž. (2021) Fatigue life prediction of Electric RaceAbout (ERA) traction motor rotor, Procedia structural integrity 31, 45-50
9. Braut, S., Tevčić, M., Butković, M., Božić, Ž., Žigulić, R. (2021) Application of modified Locati method in fatigue strength testing of a turbo compressor blade, Procedia Structural Integrity 31, 33-37
10. Pantazopoulos, G., Papaefthymiou, S., (2015) Failure and Fracture Analysis of Austenitic Stainless Steel Marine Propeller Shaft, J Fail. Anal. and Preven. 15:762–767, DOI 10.1007/s11668-015-0024-7
11. Sitthiponga, S., Towatanaa, P., Sitticharoenchai, A. (2017) Failure analysis of metal alloy propeller shafts, Materials Today: Proceedings, 6491–6494
12. Braut, S., Žigulić, R., Butković, M. (2008) Numerical and experimental analysis of a shaft bow influence on a rotor to stator contact dynamics, Strojniški vestnik, 54, 10; 693-706
13. Leontopoulos, C. (2011) *Shaft Alignment and Powertrain Vibration*, ABS
14. Rajasekaran, S. (2009) Free and forced vibration of a continuous system in relation to structural dynamics during earthquakes, Structural Dynamics of Earthquake Engineering; Theory and Application Using Mathematica and Matlab, Woodhead Publishing

ISSN 0554-6397
Stručni članak
(*Professional paper*)

Emir Bešić
E-mail: besic.emir1994@gmail.com
Tin Matulja
E-mail: tin.matulja@riteh.hr
Marko Hadjina
E-mail: hadjina@riteh.hr
Marin Smilović
E-mail: msmilovic@riteh.hr
Faculty of Engineering University of Rijeka, Vukovarska 58, Rijeka, Croatia

Development of Technical Documentation of Small Vessels

Abstract

The development of technical documentation of vessels provides that the design, construction and conformity assessment is clearly understood and meets the competent requirements. This paper presents the development process of technical documentation for a small vessel, i.e. a motorboat of project category B (navigation on the high seas), whose hull length is within the range from 2.5 m to 24 m, according to the given norms. For example, the paper will present a boat intended as a polyvalent workboat in service on the Adriatic Sea, whose documentation has been prepared according to standards, i.e. the requirements of the Croatian Register of Shipping (HRN EN ISO Standards) [1].

Keywords: Technical documentation, Small vessel, Croatian Register of Shipping

1. Introduction

Every year, we witness a growing small vessels market and the need for polyvalent workboats. The Adriatic Sea is a well-known tourist destination, and nautical tourism is one of the most growing branches. Due to climate, most of the income is made during summer; therefore, the idea of a polyvalent workboat is that it's capable of fishing and can be used as passenger transport during summer. This paper's short overview includes structural members assessment, stability calculation, weight management, and essential systems evaluation.

Figure 1. Polyvalent boat render

2. General

The material used for the construction of polyvalent vessel hull plating is glass fibre reinforced polyester resin. Bulkheads are made of water-resistant plywood, while all internals are made of wooden core lined with fibreglass laminate which complies with relevant ISO rules [2]. Since the hull is made of glass fibre, there is a need to design and construct a mould for the vessel hull. Mould for hull manufacturing can be used from previous builds of a similar vessel when no significant changes are needed for the new build. Standard equipment for the hull, machinery, firefighting and safety equipment etc., comply with national rules "Ordinance on amendments to the Ordinance on Boats and Yachts" [3]. For additional customer requests for the outfit, manufacturers must comply with the national rule "Ordinance on Boats and Yachts", Annex 6, Technical Documentation [4]. All rules for which a vessel must comply are defined in Annex 1 of the mentioned national rules.

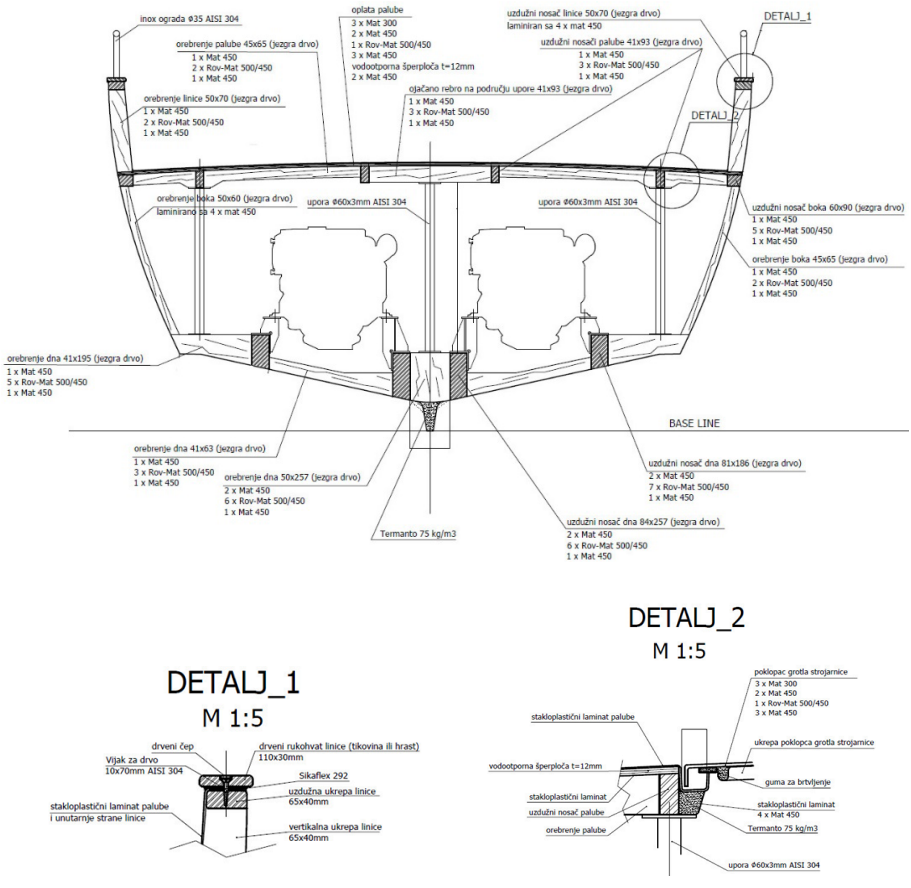

Figure 2. Midship section

3. Stability assessment

Calculations have to be made for the worst-case scenario during their exploitation for polyvalent vessel stability. Because of construction and size, small vessels are more exposed to the effects of large waves, strong winds and more intense sea conditions. Vessel will be used to transport crew, fishing equipment, and fish itself. The stability calculation case with full fish tanks is used as the worst-case scenario. Downflooding opening requirement seeks to establish that there is no non-watertight opening in the hull or superstructure that may be submerged during navigation and which is a potential hazard for flooding the vessel's interior. The requirement applies to all openings except those that are watertight, openings in the hull that are permanently closed, openings in the side of the superstructure, which must be closed during navigation and marked

with a special mark and specified in the user manual and engine exhaust parts that are watertight. All elements have to comply with HRN EN ISO 12216 [5]. The stability calculation must comply with HRN EN ISO 12217-1 rules for design category B [6]. During calculation, special consideration must be taken for resistance to waves and wind and minimum opening area for deck drainage.

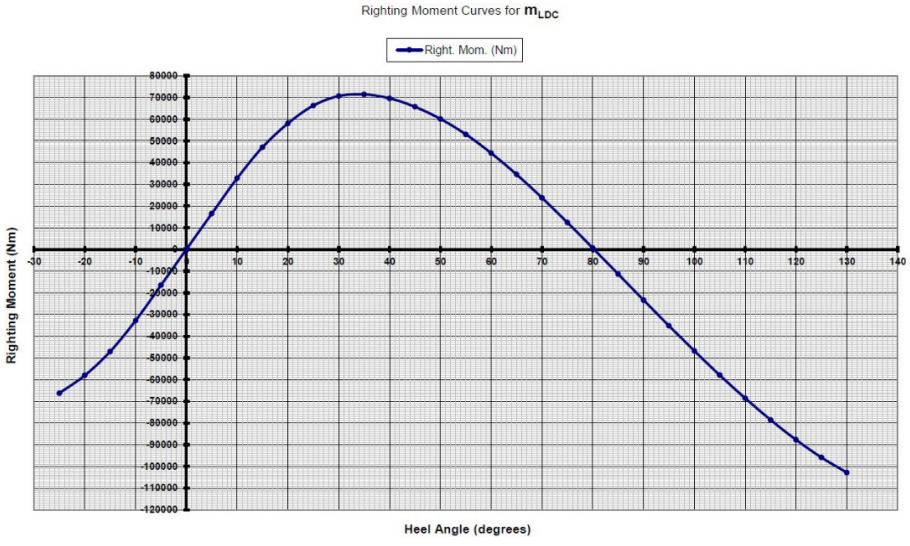

Figure 3. Righting moment curve

4. Systems

Term "systems" for a vessel is defined as all needed systems necessary for the vessel to operate. All systems have to comply with ISO rules and regulations. Systems needed for one polyvalent vessel are fuel, exhaust, cooling, bilge, black and grey, and fresh water systems.

For fuel system, fuel tanks, and testing relevant standard used is ISO 10088 [7]. Fuel tanks are made of stainless steel, and they have to be grounded so that the connection is made to the vessel hull with a maximum resistance of 10 Ω. Foundations for fuel tanks have to be made so that they need to be separated from the surface, which can cause sparking.

The exhaust system is designed so that the exhaust position is located 150mm above the waterline.

The engine cooling system is open type design with a seacock positioned aft of the engine.

The Bilge system is designed with three immersed bilge pumps in compliance with ISO 8849 [8] rules with hull valve per ISO 9093-1 [9]. After installation, a complete bilge system must be tested for pressure 1.5 times higher than operating pressure.

The Black and grey system is designed according to ISO 8099 [10], with one black/gray tank and macerator pump that fits the vessel's need. The black/grey water tank has a vent connection so that it is connected from the pipe to the filter and the hull. A vent is used to prevent unpleasant odours in the boat cabins. Since the tank needs to be emptied, it contains a direct discharge through the opening on the deck.

The freshwater system complies with ISO 9093-1 [9], the freshwater tank is located aft, and the system is equipped with a water heater. For the water to be clean for the consumers, it must pass through a fine particle filter, pipes with ball valves and one main valve that allows water to pass to the consumer. A freshwater tank contains vents that prevent water from taking on unsuitable conditions. Hot water supply is performed, so that part of the pipe from the drinking water tank is bought to the boiler and goes to the consumers. After installation, the water system must be tested for pressure 1.5 times higher than the operating pressure.

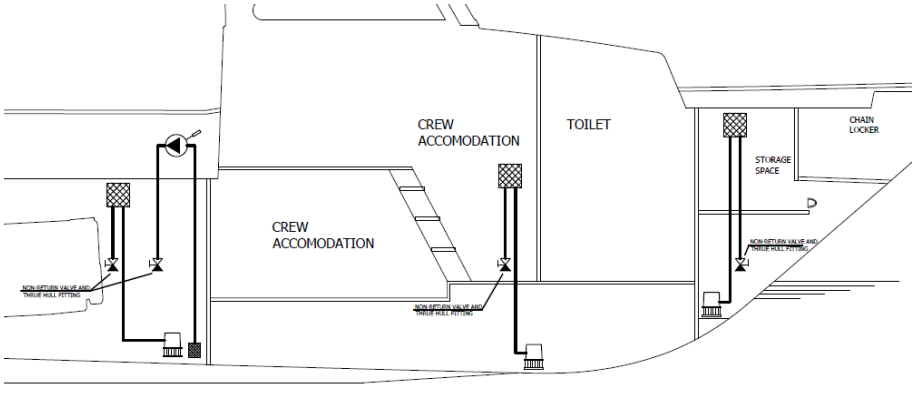

Figure 4. Bilge system

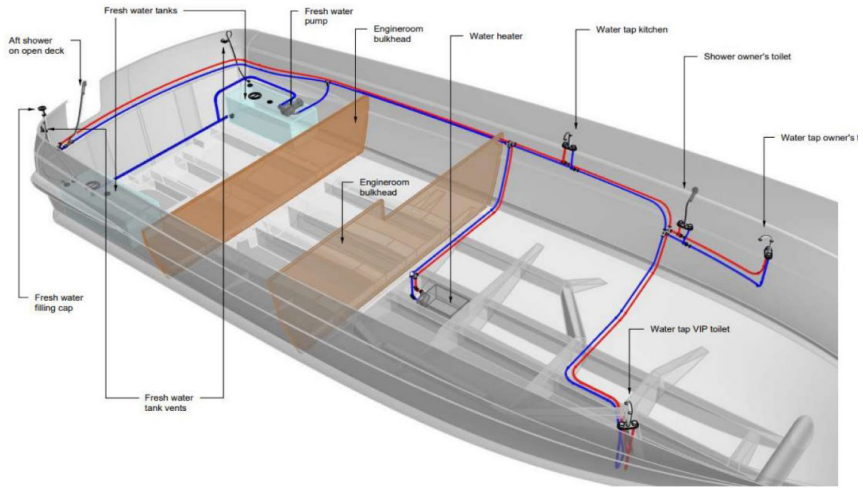

Figures 5. Fresh water system

5. Conclusion

This paper describes the procedure and relevant rules and guidelines for preparing technical documentation of the polyvalent vessel. General characteristics define documentation prepared in advance, focusing on the purpose of the vessel and equipment it will contain. Documentation for polyvalent vessels has to consider rules that apply to different operating types, e.g., stability of workboats and passenger boats. The content of this paperwork is a guideline for preparing and selecting applicable rules and regulations, and it can serve in the early stages of the design.

6. Acknowledgements

This research is supported by funds from the supporting research at the University of Rijeka for the project " Development of Methodology for Ship Design and Production towards Industry 4.0. Concept"

7. References

1. Croatian Register of Shipping. (2020) *Rules for the classification of ships.* Available from*: https://www.crs.hr/rules-imo-and-eu-regulations/crs-rules-and-standards/rules-for-the-classification-of-ships* [Accessed 3th July 2020].
2. Međunarodna organizacija za standardizaciju (2004) *HRN EN ISO 12215-1:2004: Mala plovila - konstrukcija trupa i dimenzije konstrukcijskih elemenata* (ISO 12215-1:2000: Small craft - Hull construction and scantlings Part 1: Materials: Thermosetting resins, glass-fibre reinforcement, reference laminate).
3. Ministry of the Sea, Transport and Infrastructure (2020) *Ordinance on amendments to the Ordinance on Boats and Yachts.*
4. Ministry of the Sea, Transport and Infrastructure (2020) *Ordinance on Boats and Yachts*.
5. Međunarodna organizacija za standardizaciju (2004) *HRN EN ISO 12216:2004: Mala plovila - Prozori, okna, grotlašca, vidnici i vrata - Zahtjevi za čvrstoću i vodonepropusnost* (ISO 12216:2002 Small craft - Windows, portlights, hatches, deadlights and doors - Strength and watertightness requirements).
6. Međunarodna organizacija za standardizaciju (2015) *HRN EN ISO 12217-1:2015: Mala plovila - ocjenjivanje i razradba stabiliteta ili plovnosti – 1.dio: Plovila bez jedara duljine trupa 6m ili više* (ISO 12217-1:2013: Small craft-Stability and buoyancy assessment and categorization - Part 1: Non-sailing boats of hull length greater than or equal to 6 m).
7. Međunarodna organizacija za standardizaciju (2013) *HRN EN ISO 10088:2013: Mala plovila - Trajno ugrađeni sustavi goriva* (ISO 10088:2013: Small craft - Permanently installed fuel systems).
8. Međunarodna organizacija za standardizaciju (2004) *HRN EN 8849:2004 – Mala plovila - Elektromotorne kaljužne crpke na istosmjernu struju* (ISO 8849:2003: Small craft - Electrically operated direct-current bilge-pumps).
9. Međunarodna organizacija za standardizaciju (2001) *HRN EN ISO 9093-1:2001: Mala plovila - Oplatni ventili i prolazi* (ISO 9093-1:1994: Seacocks and through-hull fittings).
10. Međunarodna organizacija za standardizaciju (2004) *HRN EN ISO 8099:2004: Mala plovila - Sustav za prikupljanje sanitarnog otpada* (ISO 8099:2000: Small craft - Toilet waste retention systems).

ISSN 0554-6397
Prethodno priopćenje
(*Preliminary communication*)

Patrik Kubaska
E-mail: pkubaska969@gmail.com
Tin Matulja
E-mail: tin.matulja@riteh.hr
Marko Hadjina
E-mail: hadjina@riteh.hr
Faculty of Engineering University of Rijeka, Vukovarska 58

Carbon Mast Structural Damage Detection Using Ultrasonic NDT Method

Abstract

Glass and carbon fibers as materials have become the primary choice in the construction of smaller vessels. The advantages of these materials are good mechanical properties, they are relatively light materials that today anyone with a little knowledge can handle and also, financially speaking, they are materials that are affordable to almost everyone. One of the disadvantages is that composite materials are not homogeneous. This would mean that irregularities can be observed in the cross section of the laminate of such composite vessel or equipment. These irregularities are usually negligible because they simply belong to the property of composite materials. The problem arises when imperfections are caused by human factors or the action of some external force such as residual air in the laminate or delamination. Such imperfections during navigation can cause catastrophic damage. Although visible damage may seem small, it is very likely that there is much greater damage to the laminate that is not visible because it is located somewhere between the layers of fibers. Various methods exist for detecting such damage and imperfections, which can be invasive or non-invasive. The focus of this paper is on detecting the magnitude of damage in the laminate of the carbon mast of a racing sailboat Melges 32 using a non-invasive ultrasonic testing method. The Avenger EZ device was used for testing only.

Keywords: Carbon mast, Laminate, Damage detection, NDT method, Ultrasonic testing

1. Introduction

This paper describes the procedure of ultrasonic testing of the carbon fiber mast of a Melges 32 sailboat for the purpose of damage repair. The first part of the paper explains the basic features of composite materials, especially those containing carbon fibers, as well as methods for testing composite laminates. In the continuation of the paper, the procedure of ultrasonic testing of materials is described in more detail, as well as the equipment needed to perform the testing itself. Finally, the carbon mast of

the Melges 32 sailboat was tested to determine the extent of the damage and to repair the damage itself.

2. Composite materials

Composite materials are obtained by joining materials together to form a material that has better mechanical properties than separate materials. The characteristic of composite materials is that they usually have better specific strength, better modulus of elasticity and better heat resistance. When making composite materials, basic materials are selected that have satisfactory characteristics for the required purpose. Composite materials can be divided according to the type of matrix and according to the type of reinforcement.

According to the type of matrix, composite materials are divided into:
- Ceramic matrix composites (CMC)
- Polymer matrix composites (PMC)
- Metal matrix composites (MMC)
- Carbon-Carbon Composites (CCC)

According to the type of reinforcements, composite materials are divided into:
- Fiber-reinforced composites
- Particle reinforced composites
- Structural composites

The main role of the matrix is to interconnect the reinforcement and transmit force to it, give shape to the composite and protect the material from external forces while the role of reinforcement is to improve the strength and modulus of elasticity of the composite material itself.

2.1. Carbon fiber composites

Carbon fiber composites consist of carbon fibers and a polymer matrix, with the polymer matrixes being divided into plastomers and durometers.

Plastomers:
- Polyethylene (PE)
- Polypropylene (PP)
- Polyamide (PA)
- Acrylonitrile butadiene styrene plastic (ABS)

Duromers:
- Epoxy resin
- Vinyl-ester resin
- Polyester resin

Epoxy resin is most commonly used as a matrix in carbon fiber reinforced composites. The properties of such a composite largely depend on the length and diameter of the carbon fibers, the fiber orientation, the fiber to matrix ratio in the composite, and the mechanical properties of the fibers and matrix themselves. Figure 1 shows some of the possible orientations of the carbon fibers in the matrix.

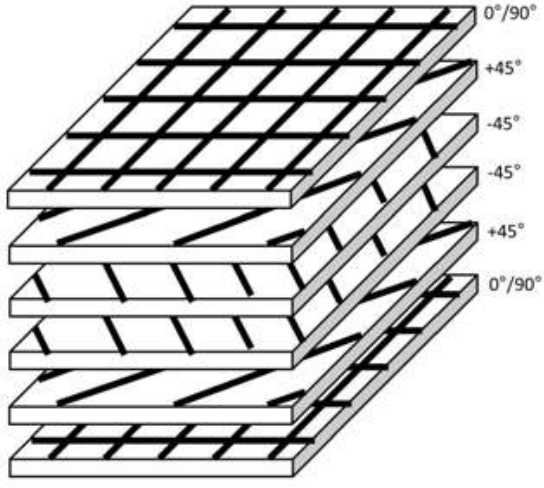

Figure 1. Fiber orientation

2.2. Testing of composite materials

Carbon fiber composite laminates often contain imperfections that can cause damage due to external loads. In order to eliminate the possibility of damage, it is necessary to examine the laminate. Test methods are divided into invasive and non-invasive. Invasive methods are also destructive methods because a sample is taken for testing the laminate, and the sampling itself creates damage in the laminate. For composite materials, non-invasive laminate testing methods are far more acceptable.

Basic division of non-invasive methods:
- Visual inspection
- Tapping method
- Ultrasound method
- Radiography
- Eddy-current method
- Thermography

The primary noninvasive method of testing laminate is visual inspection. Although composite laminates hide imperfections and damage well, it is possible to determine the

location of some significant damage with the help of visual inspection. A slightly more advanced method would be the tapping method. With the tapping method, a blunt object is tapped on the surface of the laminate and, with careful listening, a change in the sound produced is sought, which would indicate an imperfection in the laminate. Although this method cannot provide a detailed picture of the condition of the laminate, it is still used because it very quickly gives an idea of the size and location of imperfections in the laminate without the use of expensive test equipment.

Radiography uses an X-ray generator that penetrates the laminate and on the other hand comes into contact with a detector or X-ray sensitive film. In some places, X-rays are more absorbed into the material, and in some less, so a detailed picture of the condition of the laminate is obtained. The disadvantage of this method is that X-rays are harmful to humans and other living things.

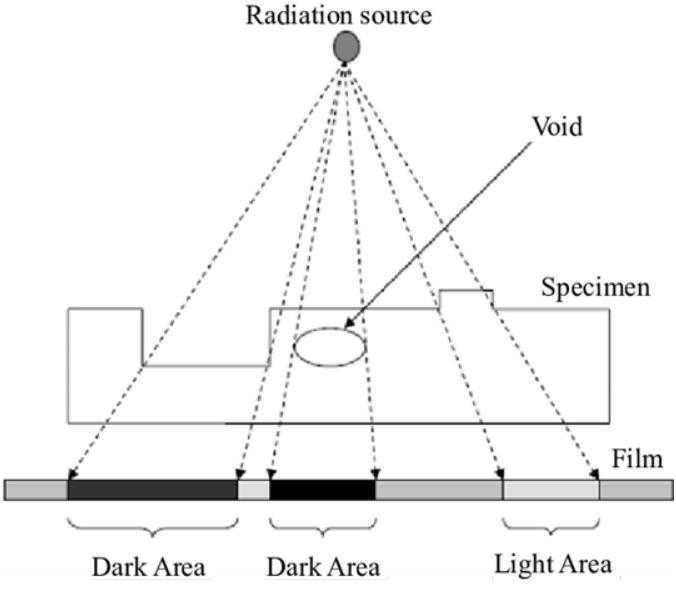

Figure 2. Radiography

Eddy current method is less commonly used in composite laminates and more commonly in metal inspection.

The reason for this is that in this method a coil that generates a magnetic field is brought close to the material. A magnetic field near an electrically conductive material induces an electric field in that material which also creates its own magnetic field that interferes with the original magnetic field in the coil. This interference changes with respect to material thickness and internal imperfections. Although carbon is an electrically conductive material and it is possible to test laminate by this procedure, this method is still more used in metal testing.

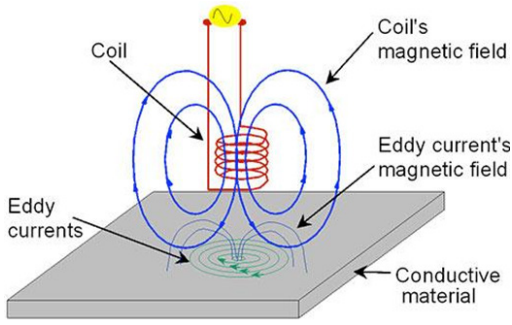

Figure 3. Eddy current method

In thermography, a special camera measures the radiation of the material in the infrared part of the electromagnetic spectrum. According to black body radiation theory, all bodies that have a temperature above absolute zero radiate in the infrared spectrum. Thermography is a quick and easy way to test a material that instantly gives a picture of the condition of the material over a large area, but if it is imperfections and damage that are deep in the material then a much better picture of the condition of the material is obtained using the ultrasonic test method described in the next section.

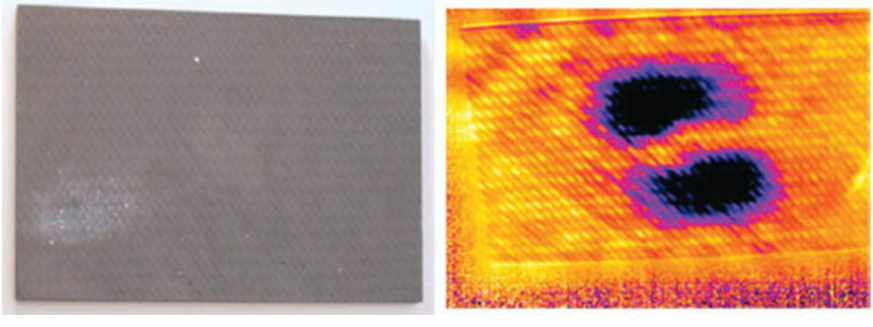

Figure 4. Termography

2.3. Ultrasonic testing of composite materials

Ultrasonic testing of solid materials is used to detect material imperfections and microcracks. It is based on the fact that solids are good conductors of sound waves. Sound waves are reflected within the material from its sides, and at the same time they are reflected from all imperfections in the material. The interaction of the material itself and the sound waves is better the smaller the wavelength of the sound. This also means that higher frequency waves are used. This material testing method is characterized by frequency waves from 0.5 MHz up to 25 MHz. The reason for this is that the interaction of waves is most pronounced if a wave of a certain wavelength comes into contact

with an imperfection that is similar in magnitude to the wavelength of that sound. The observed laminates in composite vessels are usually a few millimeters thick, so it is necessary to adjust the sound wavelength so that it is in the range of a few millimeters. Equation 1 defines the sound wavelength for a given speed of sound and frequency. The speed of sound in air is approximately 343 m/s, but this value is not applicable in this case. As explained earlier, solid materials are good conductors of sound, which means that the speed of sound in solid materials is much higher than the speed of sound in air, so it is necessary to adjust the value of the speed of sound in the equation for the observed material. In case of carbon laminates that would be 3070 m/s.

$$\lambda = \frac{c}{f} \tag{1}$$

c = Speed of sound [km/s]
f = Frequency [MHz]
λ = Wave lenght [mm]

The method of ultrasonic testing of materials is mainly based on two different procedures. The first procedure would be based on the measurement of reflected sound waves (pulse-echo) while the second procedure would be based on the measurement of waves that have completely passed to the other side of the material (through-transmission). In practice, the method of measuring reflected waves is used much more for the reason that the measurement requires access to the material from only one side. The reflected wave method is also used to determine the speed of sound through the observed material. If the thickness of the material and the time required for the transmitted sound wave to return to the piezoelectric element are known, it is very easy to calculate the speed of sound through that material.

$$c = \frac{2d}{t} \tag{2}$$

c = Speed of sound [m/s]
d = Thickness of material [m]
t = Time [s]

Compared to other methods of non-invasive testing of solid materials, the ultrasonic method has its advantages and disadvantages.

Advantages:
- High sensitivity to imperfections inside the material
- No preparation of the observed material is required
- The depth to which the wave penetrates is much greater than with other methods
- High precision in determining the size and position of imperfections
- Minimum equipment required for testing (usually portable equipment)
- The test procedure is not harmful to the material or the people conducting the test

Disadvantages:
- High sensitivity to surface imperfection and surface curvature of the material
- The surface of the material must be accessible for testing
- A medium is required between the surface of the material and the piezoelectric probe
- Materials that are not homogeneous are difficult to examine
- Imperfections in the material that are oriented in the direction of sound are almost impossible to detect
- Materials that are very thin (<1mm) are almost impossible to test with this method

2.4. Testing equipment

The ultrasonic material testing device is composed of several parts. The basic parts would be a central unit and a piezoelectric element. The central unit consists of an ultrasonic generator that transmits electrical pulses and a screen that displays the results obtained. The operation of a piezoelectric element is based on the piezoelectric effect of crystals such as quartz. Crystals like quartz have the ability to convert electricity into vibrations and vice versa.

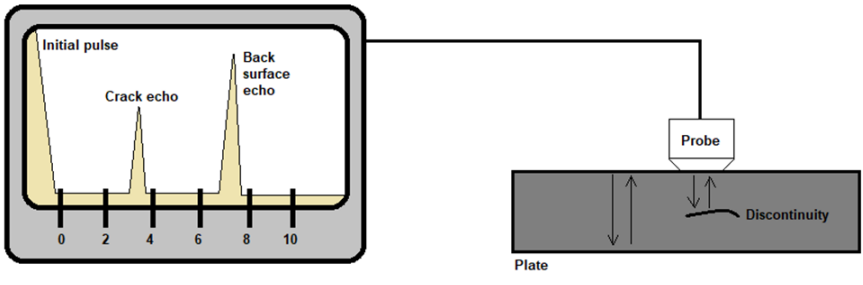

Figure 5. Ultrasonic testing equipment

The piezoelectric element is often referred to as the active element. The operation of the element itself is based on the Lippmann effect. Gabriel Lippmann was a French physicist who found that in some materials, such as certain crystals and some ceramics, polarization occurs at the ends of the material due to the execution of elastic deformation by some force. This phenomenon is especially pronounced if the ends of this material are cut straight. Lipmann also found that there is a reverse phenomenon. If the crystal is placed in an alternating electric field, an elastic deformation of the material occurs, which is called electrostriction.

In the event that the frequency of the alternating electric field coincides with the natural frequency of the material, vibration and resonance of the crystal occur. In some

crystals this is quite pronounced, such as tourmaline whose frequency reaches a few hundred MHz.

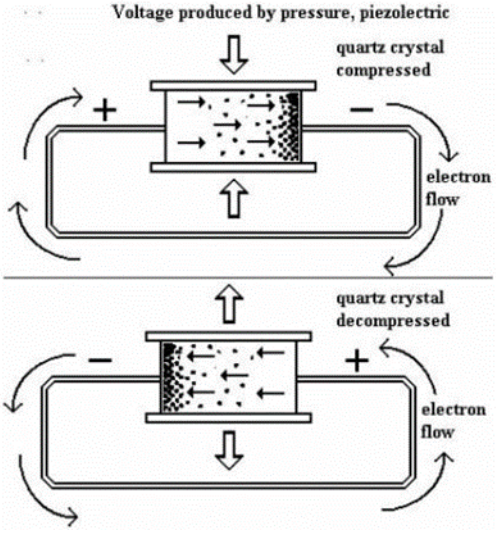

Figure 6. Lippmann effect

3. Pulse-echo method

The pulse-echo method is the method most commonly used in material testing. During the testing of the material, the ultrasonic generator emits short-term pulses of electricity that come through a conductor to a piezoelectric element that is in contact with the surface of the material. The moment an impulse of electricity reaches a piezoelectric element, it converts that impulse of electricity into mechanical energy of vibrations. The vibration is transmitted through the observed sample until it is reflected from some imperfection or from the back surface of that sample. The reflected vibrations are returned back to the piezoelectric element which converts the received vibrations into a pulse of electricity. This pulse travels back to the central unit where it is displayed on the screen.

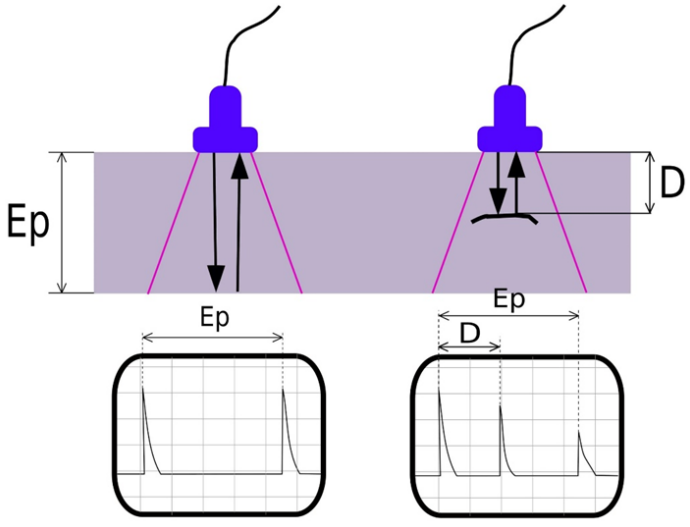

Figure 7. Pulse-echo method

In the pulse-echo method, there are two types of probes with a piezoelectric element that are most commonly used. They are divided into probes with one element and probes with two elements. Single-element probes use the same piezoelectric element to transmit and receive vibrations while two-element probes have one piezoelectric element to transmit vibrations and another element to receive vibrations.

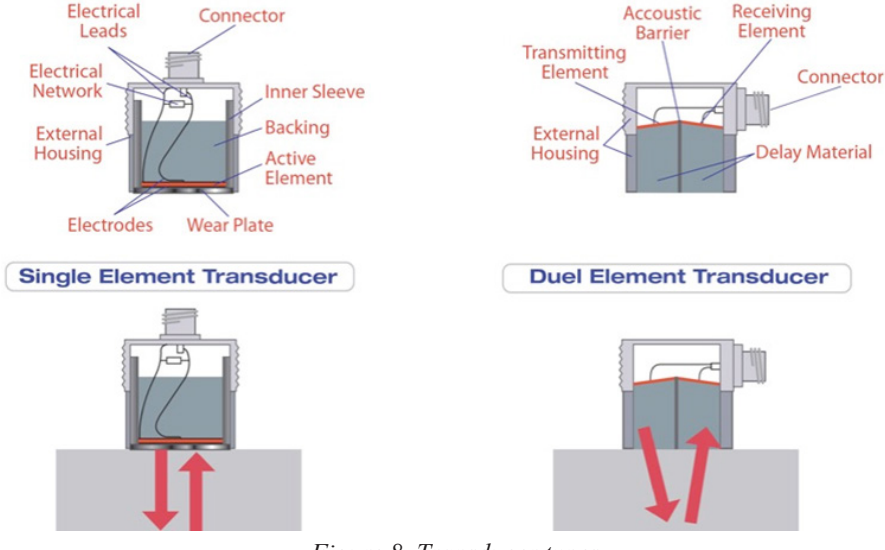

Figure 8. Transducer types

Single-element probes are most commonly used to test for imperfections in metals and delamination in composite materials while two-element probes are most commonly used to detect damage caused by corrosion on metal or to test very thin materials such as sheets because they have much less interferences.

4. Testing and results

The acquired theoretical knowledge about the method of ultrasonic testing of solid materials was applied in the detection of structural damage in a mast made out of carbon fiber. The mast, as one of the basic parts of a sailboat, is constantly loaded with forces during sailing. It is loaded with lateral forces of variable intensity due to various and sudden wind gusts and is also under constant pressure load due to the steel rigging.

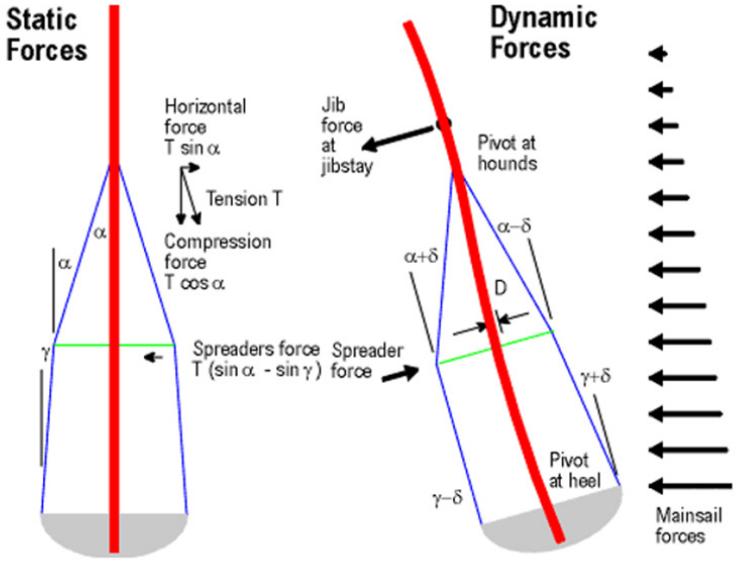

Figure 9. Forces on sailboat mast

The analyzed mast is the mast of a Melges 32 class sailboat. It is a two-part mast made of carbon fiber. The reason why the mast is designed in two parts is primarily to make it easier to transport. Damage was caused to the upper part of the mast during sailing in strong winds. At the time of sailing downwind there was damage in the rigging which caused a short-term torsional load of the mast and shortly after the rupture of the upper section of the mast into two parts.

Masts are generally not designed to withstand torsional loading because it almost never occurs under normal conditions.

Figure 10. Mast damage

At first glance, the damage to the mast is only near the site of the section rupture. However, as mentioned earlier, the problem with composite materials is that most often internal damage is many times greater than it is apparent.

An Avenger EZ ultrasound scanner was used to determine the size and type of damage. It is a hand-held portable device that uses the pulse-echo method to find damage. A piezoelectric probe operating at a frequency of 5 MHz was used for the measurement. Calibration of the device itself is relatively simple when it comes to testing homogeneous materials such as steel and aluminum. When working with composite materials, the process is somewhat more complicated. It is necessary to have pre-made pieces of a similar laminate as the mast for calibration. The wall thickness of the mast was measured with a movable scale in several places and an average thickness of 6.5 mm was obtained. Since the mast is mostly pressure loaded, most of the layers in the laminate have fibers oriented in one direction that go from the top of the mast all the way to the lower end of that mast section.

Pieces of approximately the same 6.5 mm thick laminate were made by hand laminating using a vacuum bag. It is important that the calibration pieces have similar thickness and structure as the mast. The device was roughly calibrated on the made piece of laminate and was subsequently calibrated on the part of the mast that was not damaged. Since the mast wall thickness is known to average 6.5 mm, this size was taken as a reference. Any larger deviation from the ideal 6.5 mm requires more attention when testing. The ultrasound examination was started approximately 75 cm from the rupture site of the mast and gradually moved closer to that rupture site with the probe. Before the measurement, the probe is coated with gel so that there is no

air between the surface of the material and the probe and in order to create the best possible contact of the probe with the surface, which also results in better transmission of sound waves into the material itself. In contact with the material surface, the device displays graphically the sent and received wave as well as the value in millimeters to the first obstacle. In this case, the obstacle was the inner side of the mast wall, so a value of 6.28 mm was obtained.

Figure 11. Result 1

Figure 11 shows the three signals received. The first and most pronounced signal is a transmitted wave that bounced off the surface of the mast wall without entering the material itself. This wave needs to be filtered out of the measurement for the reason that otherwise the device will show the wrong wall thickness and later the wrong place and size of the imperfection in the material. The second signal shows a wave bounced off the inner surface of the mast wall to a depth of 6.28 mm. This is the signal that needs to be recorded on the mast to know the exact position where the damage does not exist. The third and smallest signal is not common, but occurs if the laminate is well made and it shows a wave that has already bounced off the inner surface of the mast

wall and once again made its way all the way through the mast wall again and once again bounced off the inner surface of the mast and back into the ultrasonic probe. The obtained value is approximately twice the mast wall thickness.

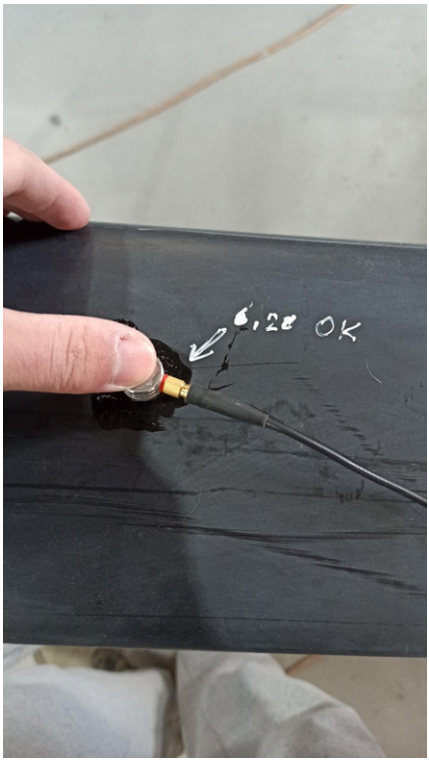

Figure 12. Position 1

Figure 11 and figure 12 show ideal conditions where damage does not exist and only the thickness of the mast wall is measured. Figure 13 shows a situation where the damage in the wall of the mast is close to the surface from which we are measuring. Ultrasound no longer shows at what depth the inner surface of the wall is but only shows the location of the damage. It can be concluded that it is a case of delamination. The layers of laminate are separated from each other and between them there is a layer of air that does not allow sound to travel freely through the material.

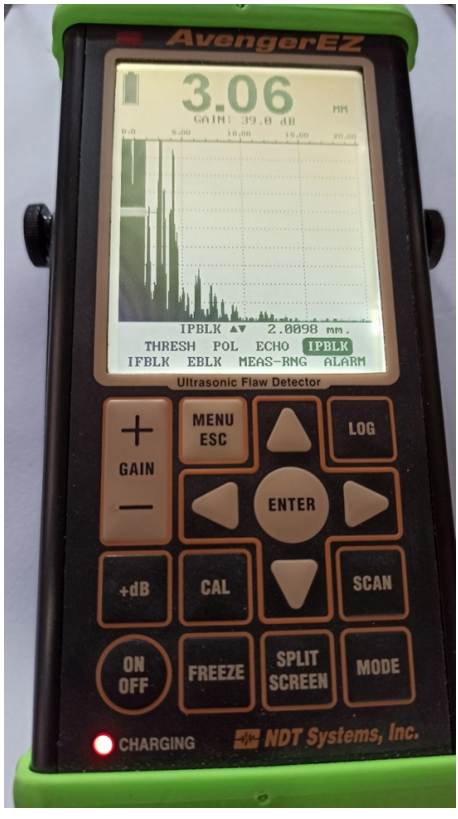

Figure 13. Result 2

The measuring position as well as the obtained value are marked on the surface of the mast in order to finally get a detailed picture of the magnitude of the damage to the mast.

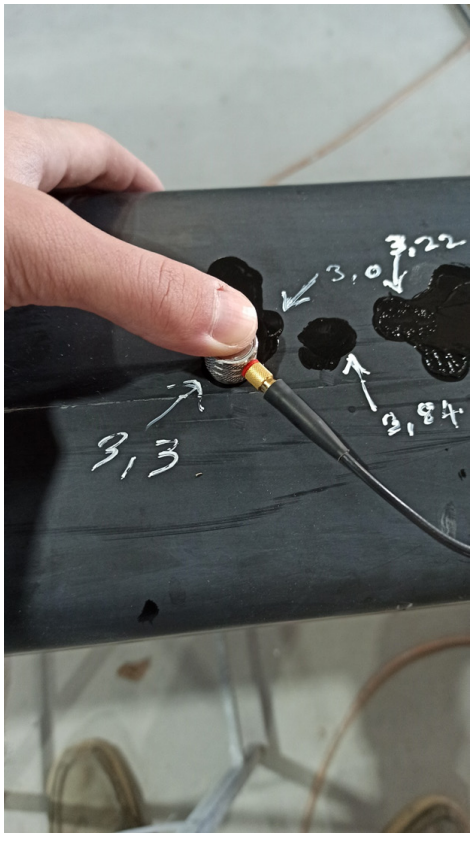

Figure 14. Position 2

In certain situations, the measurement result was not completely clear at first. As shown in figure 15 , the feedback signal from the inner surface of the mast wall is clearly visible at 7.16 mm but there are two signals also visible near the outer surface of the mast wall.

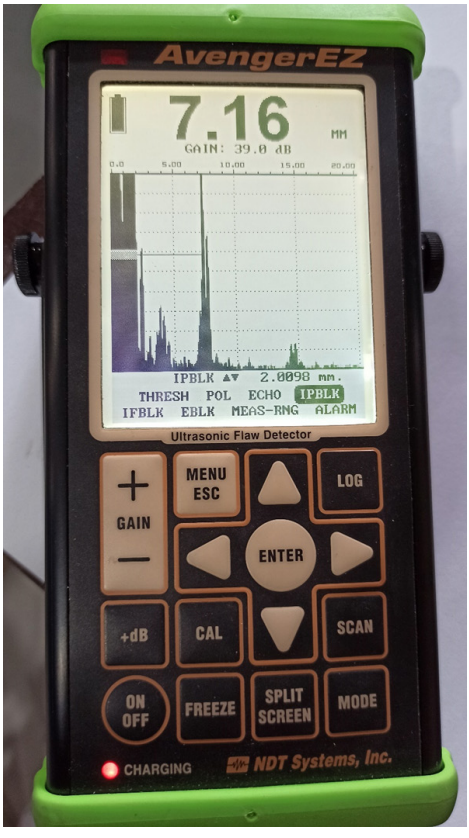

Figure 15. Result 3

The measuring point was marked on the mast in order to get a detailed picture of the condition of the mast and to determine later during the repair what kind of irregularity it is, considering that the ultrasonic examination did not give a concrete result. During the repair, that place on the mast was sanded and it was determined that it was an imperfection that occurred during the production of the mast in the factory, and that imperfection was filled with some kind of epoxy filler.

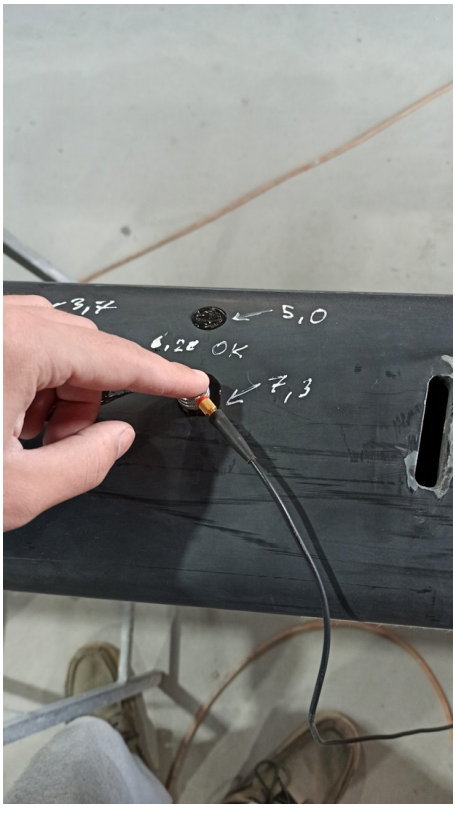

Figure 16. Position 3

After the mast was examined in a number of positions, an insight was gained into the magnitude of the damage itself. The damage, which at first glance seemed to be localized only around the rupture site, actually extends approximately 60 cm above the rupture site. The test was also performed on the lower part of the broken section and the obtained results indicated that the internal damage on the lower part is much less than on the upper part of that mast section. Figure 17 shows the amount of damage at the top of that mast section. All to the left of the red line is a wall that has layer delamination.

Figure 17 Magnitude of damage 1

The lower part of this section of the mast shows slightly less damage, but it is interesting to note that the place where the internal damage ends is not a straight line but in both parts of the mast is a curved line, which could indicate that it is indeed damage caused by torsional load. on the mast. Figure 18 shows the lower part of that mast section. Anything to the left of the red line is damage.

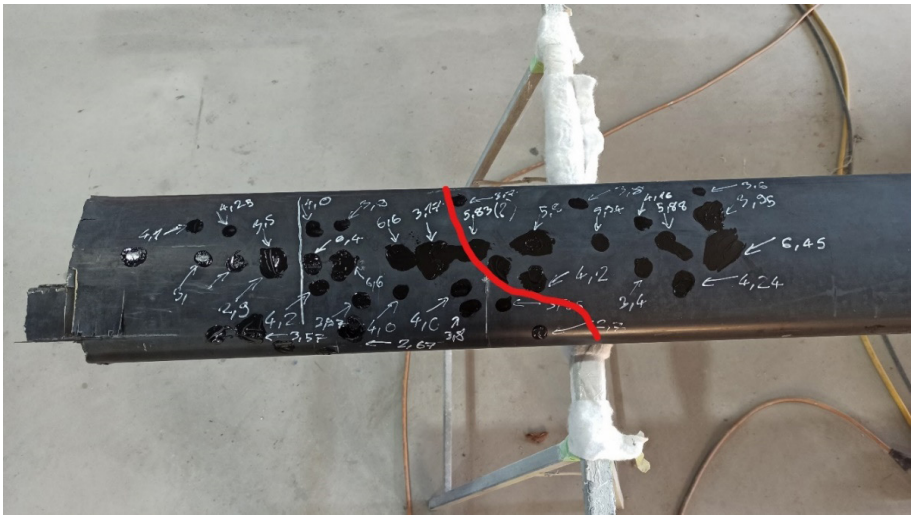

Figure 18 Magnitude of damage 2

5. Conclusion

When working with nonhomogeneous materials, such as composite materials, there can always be unpredictable imperfections in the material which can cause major damage. Today, composite materials are used in the manufacture of airplanes, boats, cars, sports equipment ... It is not uncommon for material fatigue or damage to occur due to the action of some external force on the material. Damages are difficult to notice in composite materials because they are most often hidden under the surface. Regular material control is very important, primarily visual inspection, and certainly material control with the help of some of the non-invasive methods. The ultrasonic testing method has proven to be one of the better methods because it is not dangerous for the operator and the material being tested, the equipment is usually small enough to be carried in the hand and also gives a very detailed insight into the condition of the material. Delaying regular material inspections can lead to catastrophic consequences such as the sinking of a vessel or the crash of a plane where in both cases there could be human casualties. Through the practical part of this paper, it was found that visual inspection of the material alone is not sufficient. The ultrasonic method determined that the damage to the laminate of the mast was many times greater than it was at first sight. By using the ultrasonic method, it is possible to precisely locate the position of the damage in the structure of the composite material. The results should be checked multiple times as it is possible to get wrong readings due to surface imperfections or curvature. The results may indicate that the mast broke during torsional load which could be possible to avoid with different composite laminates such as laminates which use more biaxial carbon fibers where the torsional load on the mast would be oriented along the fibers. It can be concluded that the damage happened because the mast was not designed to withstand a torsional load. Results of these kind of non-destructive testing's should be used to improve the design and structure of future sailboat masts.

6. Acknowledgments

This research is supported by funds from the supporting research at the University of Rijeka for the project " Development of Methodology for Ship Design and Production towards Industry 4.0. Concept"

7. References

1. Kunej, W. (2003) Poliesterski kompoziti. Zagreb, Metalmineral d.d.
2. Wanberg, J.(2009) Composite Material Fabrication Handbook #1. Stillwater, Wolfgang Publications, Inc.
3. Non destructive testing of composite materials in aviation. (2021). Available from: https://www.skybrary.aero/index.php/Non_Destructive_Testing_of_Composite_Materials_in_Aviati on, [Accesed 7th August 2021].
4. Krautkramer, J.; Krautkramer, H (1990) Ultrasonic Testing of Materials. Berlin, Springer-Verlag.

ISSN 0554-6397
Stručni članak
(*Professional paper*)

Rajko Rubeša
E-mail: rajko.rubesa@gmail.com
Shipyard "3.MAJ" d.d., Liburnijska 3, Rijeka, Croatia
Marko Hadjina
E-mail: hadjina@riteh.hr
Tin Matulja
E-mail: tin.matulja@riteh.hr
Faculty of Engineering University of Rijeka, Vukovarska 58, Rijeka, Croatia

Criteria for Evaluation the Technological Level of Ship Pre-Outfitting in Shipyard

Abstract

In today's highly competitive shipbuilding business, gaining a competitive advantage between shipyards is extremely important. In order to have a competitive and sustainable shipyard, it is important for the management to continuously monitor and raise the productivity, efficiency and quality of the production process. One of the major issue in today's shipbuilding is how to organize and conduct the efficient ship outfitting process as one of the most complex task within ship design, supply chain and production activities, particularly for high value added ships. To be able to manage, improve and optimize ship outfitting process it is necessary to establish its current technological level and relevant activities. Hence, in this paper authors are analysing the ship outfitting process with special attention to ship outfitting prior to ship launching, with a purpose to define and explain the criteria to be used for such technological level evaluation.

Keywords: shipbuilding, technological level, outfitting, evaluation, efficiency, sustainability

1. Introduction

In today shipbuilding, especially for complex types of ship with high added value the outfitting, and equipment supply process, the shipyards try to become successful and competitive on the world shipbuilding market [1]. Thus they have to build quality ships, to enable a lower cost of the production process and to shorten delivery time of the ship. Shortening the time in the shipbuilding process by using the pre-outfitting concept is one way of reducing total ship production time and improving efficiency and cost performance [2]. But pre-outfitting could be problematic for some shipyards

and ship types due to obstacle in technological and production areas in shipyards. In this paper will be analysed particular criteria of using ship pre-outfitting in shipyards to evaluate their level of advance outfitting. The criteria will evaluate obstacles in shipyard such as shipbuilding preparation process, technological requirements and technological limitation through particular important sub-criteria. The result will be evaluation the level of pre-outfitting capabilities in observed shipyard and finding critical point that shall be improved to achieve higher level of advance outfitting usage which lead to shorten the time in ship outfitting process and reduce the outfitting cost.

2. Overview of outfitting process

In general, the process of ship outfitting (Figure 1) is typically divided into two separated outfitting stages: pre-outfitting, otherwise known as advanced outfitting and on board outfitting [2].

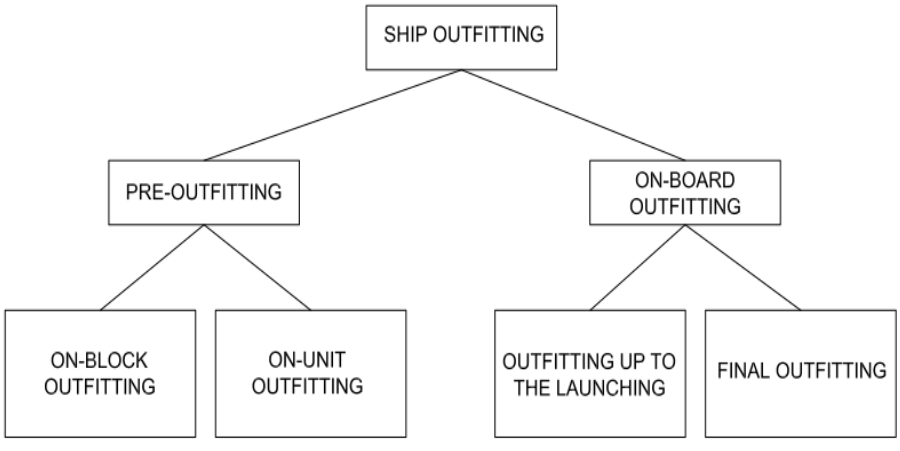

Figure 1 Breakdown structure of outfitting stages

For pre-outfitting process is characteristically that it takes place in time almost simultaneously with the hull construction and is divided into two independent outfitting stages: On-blocks outfitting and on-unit outfitting, otherwise known as modular outfitting. On board outfitting is also divided into two separated outfitting stages: on board outfitting up to the launching and final outfitting that is performed on board after launching.

On-blocks outfitting relates to the outfitting on panels, hull assembles and blocks with numerous parts of equipment such as pipelines, cable trays, ducts, penetrations through the structural parts for pipes, cables and ducting, stairs, ladders, railings, manholes, hatches and etc. Detail definition of on-block outfitting is depicted in Chapter 3.

On-unit outfitting represents the assembling of ship's equipment in workshops as assembly unit, machinery unit and structural unit [3]. Detail definition of on-block outfitting is depicted in Chapter 3.

On board outfitting will begin immediately upon block's erection on the building berth, where it continues with the installation of ship equipment up to the launching. The last stage of ship outfitting comprises final outfitting that is performed after launching when are installed the ship's equipment that are subjects of damage, such as instruments, equipment for communication, navigation and signals, electronic and computer equipment, lifesaving equipment and equipment that are not installed during the early outfitting stages.

3. Terminology definition

Because different countries, companies, and even people use different words to explain or describe the same item, it is necessary to provide definitions for the use of specific words [4]. The confusion that can result from the lack of clear definition can be appreciated by reference in chapters 3.1, 3.2 and 3.3. The following definitions applicable for shipbuilding process in overall are described in this paper.

3.1. Terms applicable for outfitting

OUTFITTING. A broad definition of all non-structural equipment and systems which are to be installed in or on a ship, including machinery.

PRE-OUTFITTING (ADVANCED OUTFITTING). The installation of outfit systems and components on a structural block or outfit unit prior to shipboard erection. It happens at an earlier stage of construction of the ship than is traditional as a means of shortening the construction time, and to increase productivity. It also enables the traditional outfitting crafts manning peak to be smoothed out.

GROUND OUTFITTING. Outfit installation during on-unit or on-block outfit stages.

ON-UNIT OUTFITTING. Outfit assembly and installation on an outfit unit prior to erection onboard.

ON-BLOCK OUTFITTING. Outfit installation on a structural block prior to erection onboard.

ON-BOARD OUTFITTING. Outfit installation following structural block erection. This means outfitting on the berth or in the dock before ship launching.

FINAL OUTFITTING. Outfit installation on-board which means outfitting of the ship along the quay after ship launching.

ZONE. An assigned area or compartment in the shipyard and/or onboard the ship for the purpose of organizing information, planning, material, and resources to support the design and construction of the ship.

UNIT. A packaged group of outfit, equipment and machineries designed to be treated as a single component, installed on common supports and foundation and manufactured in workshop independently of the hull construction.

ON UNIT. Term used to identify the activity of installing a group of outfit items into a package consisting of equipment, support, pipe, wiring**,** gratings, and controls.

ON BOARD. Term used to identify the activity of installing units or individual outfit items in or on a ship on the building berth or afloat.

3.2. Terms applicable for hull construction

SINGLE PART. A structural item which is fabricated from plates or shapes and after cutting will be incorporated with other single part into a subassembly, assembly or block.

SUBASSEMBLY. A structural item which is fabricated from processed plates and shapes, and which when completed will be incorporated with other subassemblies into an assembly or block.

PANEL. A structural item consisting of two or more butt welded plates with fillet welded longitudinal shapes.

FLAT PANEL BLOCK. A structural item consisting of a single panel made up from individual plates, shapes, and subassemblies, such as deck, shell, bulkhead, etc.

ASSEMBLY. A structural item consisting of a single panel made up from individual plates, shapes, and subassemblies, such as deck, shell, bulkhead, etc.

BLOCK. Hull structural interim product which can be erected as a block or combined as grand block. It consists of one or more subassemblies/ assemblies.

GRAND BLOCK. Assembly of two or more structural blocks mated prior to onboard erection.

RING UNIT. A structural item consisting of large and heavy types of blocks. A ring unit is an assembly of a number of conventional blocks between two cross-sections.

3.3. Terms applicable for pre-outfitting

ASSEMBLY UNIT. Steel assembly consist of steel parts of ship's equipment without mechanical or electrical drive such as pipe system supported on a common hanger system, outfit for walking such as platform, walkway and ladder, Figure 2.

Figure 2. Assembly unit

MACHINERY UNIT. Ship specific assembly consisting of one or more several outfit systems including all mechanical and electrical components and subsystems in an area. That means fabrication indoors close to the workshop equipment, Figure 3.

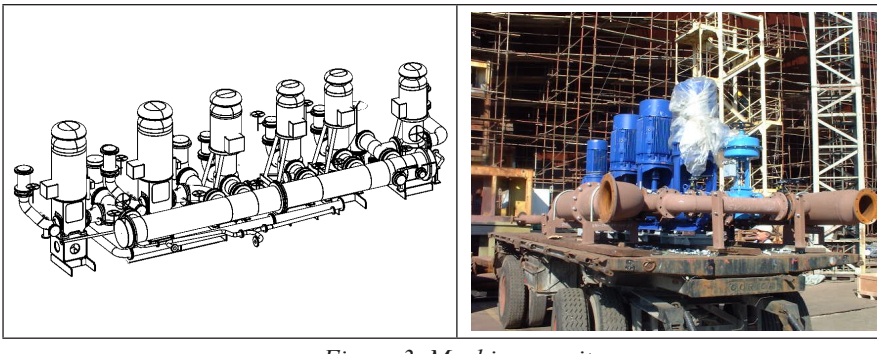

Figure 3. Machinery unit

SYSTEM UNIT. Assembly consisting of all mechanical and electrical components making up a single subsystem on a common foundation, Figure 4.

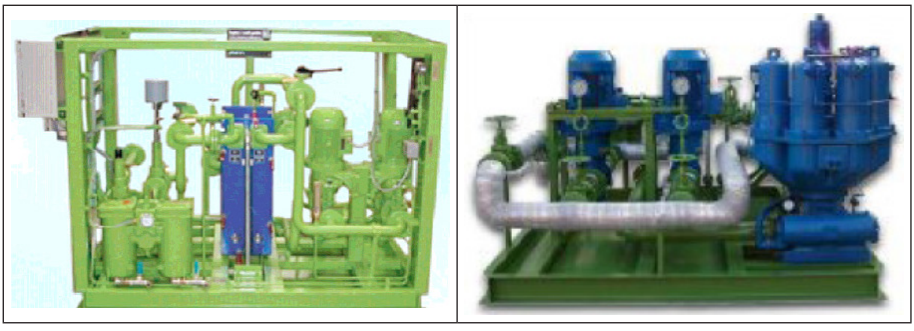

Figure 4. System unit

STRUCTURAL UNIT. Structural foundation and grating support for an outfit unit, Figure 5.

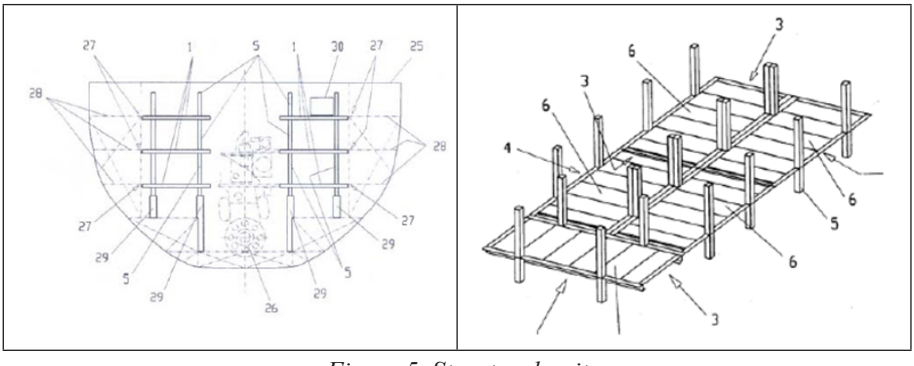

Figure 5. Structural unit

STRUCTURAL MACHINERY UNIT. Assembly consisting of a standard structural unit, one or more system units, and all ship's distributed systems in an area. The structural machinery unit design is based upon machinery unit structural and system interfaces, Figure 6.

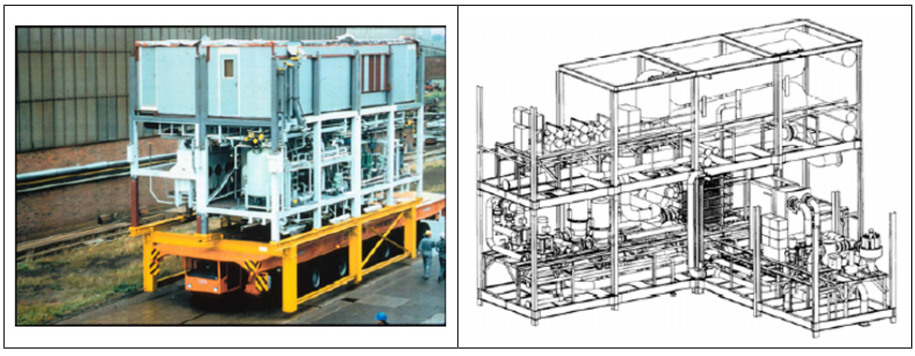

Figure 6 Structural machinery unit

PRE-OUTFITTED BLOCK. Block or sub-block outfitted before the block is erected at the berth or in the dock. Therefore, all designers always use the proper and latest version of the 3D model, Figure 7.

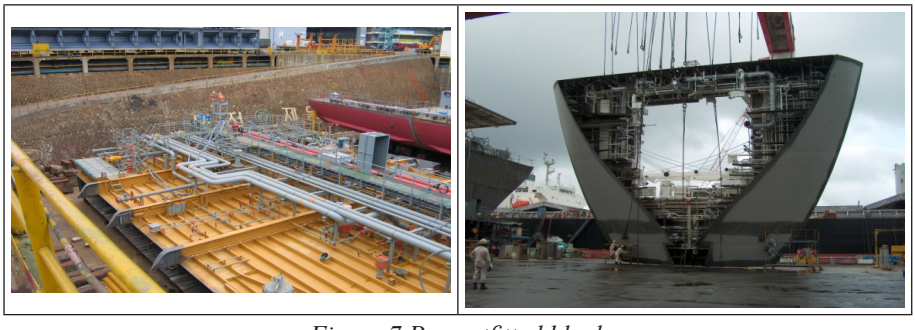

Figure 7 Pre-outfitted block

4. Criteria for evaluation the level of ship pre-outfitting

There are no clear and detail delimited the activities and recommended equipment that shall be installed in pre-outfitting stage. It depends on technological level of shipyard and its production limitations. In this paper are analysed the criteria for evaluation the level of pre-outfitting process in particular shipyards shown in Figure 8.

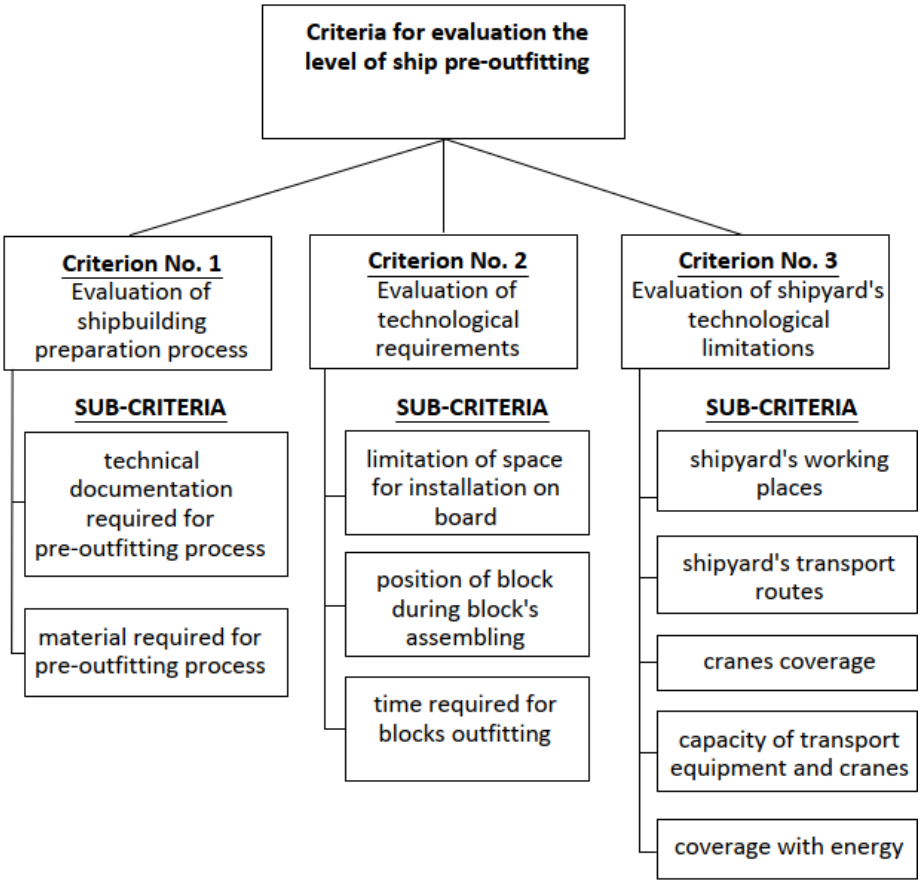

Figure 8 Breakdown structure of criteria for evaluation the level of ship pre-outfitting

The criteria for evaluation the level of pre-outfitting is divided in three main criteria: criterion for evaluation the shipbuilding preparation process, criterion for evaluation the technological requirements and criterion for evaluation the shipyard's technological limitations. Each criterion is divided in particular sub-criteria. Criterion for evaluation the shipbuilding preparation process is divided in two sub-criteria: sub-criterion for evaluation the technical documentation required for pre-outfitting process and sub-criterion for evaluation the material required for pre-outfitting process. By evaluating the technical documentation required for pre-outfitting process is rated the technical documentation suitability for ship pre-outfitting, while by evaluating the material required for pre-outfitting process is rated material preparation suitability.

The higher rate means greater justification of shipbuilding preparation process for the application in pre-outfitting process.

Criterion for evaluation the technological requirements is divided in three sub-criteria: sub-criterion for evaluation the limitation of space for installation on bord, sub-criterion for evaluation the position of block during block's assembling and sub-criterion for evaluation the time required for blocks outfitting. By evaluating the limitation of space for installation on board, the capability of space on board suitable for ship equipment and outfitting installation is rated. By evaluating the position of block during block's assembling, the possibility of ship equipment and outfitting installation during block's assembly process is rated. By evaluating the time required for blocks outfitting, the technological stage of ship euipment and outfitting installation during block construction is rated. The higher rate means greater satisfaction of technological requirements suitable for the application in pre-outfitting process.

Criterion for evaluation the shipyard's technological limitations is divided in five sub-criteria: sub-criterion for shipyard's working places dedicated for pre-outfitting, sub-criterion for shipyard's transport routes for the purpose of pre-outfitting, sub-criterion for cranes coverage on pre-outfitting place, sub-criterion for capacity of transport equipment and cranes for the purpose of pre-outfitting and sub-criterion for coverage with energy on pre-outfitting place. By evaluating the shipyard's working places dedicated for pre-outfitting, the suitability of working places on board for ship equipment installation are rated. By evaluating the shipyard's transport routes for the purpose of pre-outfitting, the capability of transport routes suitable for ship pre-outfitting are rated. By evaluating the cranes coverage on pre-outfitting place, the capability of cranes coverage suitable for ship pre-outfitting are rated. By evaluation the capacity of transport equipment and cranes for the purpose of pre-outfitting, the capability and the capacity of transport equipment and cranes suitable for ship pre-outfitting are rated. The evaluation of the energy coverage on pre-outfitting places, the level of energy coverage suitability for ship pre-outfitting is rated. The higher rate means less shipyard's technological limitations in pre-outfitting process.

5. Conclusion

Pre-outfitting is a way to shorten the time of the shipbuilding process and reduce costs, without investment in new facilities, machines and tools, and may increase competitiveness of shipyard. On the basis of the results obtained by this research, it is possible to measure cost benefit results as a consequence of using the pre-outfitting concept within the shipbuilding process. In this paper the clear terms and definitions used for advanced outfitting are defined. To avoid confusion between various terms and definitions the authors suggest using them as a standard. The main goal of proposed approach is possibility to evaluate the level of pre-outfitting capabilities in any particular shipyard as well as to find critical point that shall be improved to achieve higher level

of advance outfitting usage which will be visible through: maximising work during most productive stage of outfitting (On-unit or On-block), minimising work during less productive stage of outfitting (On-board), maximising work under cover, maximising access to working place, minimising material handling and transport, minimising non-productive activities, maximising productivity of available manufacturing process, to ensure all necessary resources are readily available at work times scheduled (such as: drawings, materials, tools, facilities and manpower), to exploit benefit of engineering, material and production standards. Furthermore, the authors suggest continuing this research by evaluating technological level of shipyard by rating its overall technological capability.

Acknowledgements

This research is supported by funds from the support research at the University of Rijeka for the project "Development of Methodology for Ship Design and Production towards Industry 4.0. Concept"

References

1. Storch, R.L. et al. (1995) Ship Production. New Jersey, SNAME.
2. Fafandjel, N., Rubeša, R., Mrakovčić, T. (2008) Procedure for Measuring Shipbuilding Process Optimisation Results after using Modular Outfitting Concept. Strojarstvo/Journal for theory and application in mechanical engineering. 50 (3), 141-150.
3. Rubeša, R., Fafandjel, N., Kolić, D. (2011) Procedure for estimating the effectiveness of ship modular outfitting. Engineering Review. 31 (1), 55-62.
4. Jaquith, P. E. Et al. (1997) A Parametric Approach To Machinery Unitization In Shipbuilding. The National Shipbuilding Research Program. Paper No. 21.

ISSN 0554-6397
Stručni članak
(*Professional paper*)

Davor Bolf
E-mail: dbolf@riteh.hr
University of Rijeka, Faculty of Engineering, Vukovarska 58, Rijeka, Croatia
Peter Rogelj
E-mail: peter.rogelj@upr.si
University of Primorska, Faculty of Mathematics, Natural Sciences and Information Technologies, Glagoljaška 8, 6000 Koper, Slovenia
Adrian Tomić
E-mail: atomic.worldpeace@gmail.com
Albert Zamarin
E-mail: zamarin@riteh.hr
University of Rijeka, Faculty of Engineering, Vukovarska 58, Rijeka, Croatia

Application of a General Purpose Software Package on Shear Forces and Bending Moment Calculations in Ship Structure

Abstract

The calculation of shear forces and bending moments are the basis of every ship design documentation. It is essential for determining the strength of the ship and the reliability of the structure itself. Nowadays, due to a sheer volume of data, this calculation is performed exclusively with the help of specialized software packages. Such shear force and bending moment curves can often be obtained within the software packages specially designed for checking the ship's design according to specific classification societies' rules. Usually, they already have built-in formulas and guidelines to execute that task properly. However, such software packages often do not meet all the end user's needs. For example, for the initial project stage, special software packages with the functionality of easy designing of a ship form are usually used, while the aforementioned packages are used in later design stages when performing stability and structure checks. This transition often requires converting files into the appropriate type from one software to another. The Rhinoceros program is widespread in the shipbuilding profession, and it is often used in the initial stages of the project. It also allows automation of the process with the help of integrated scripts. Therefore, the authors have decided to examine the possibility of using Python scripts within the Rhinoceros software package. The mentioned script will calculate the transverse forces and bending moment based on the previously modelled hull.

Keywords: shear forces, bending moment, Rhinoceros, Python

1. Introduction

It is of utmost importance to know the exact loads and material characteristics used in the calculation to design any ship structure properly. The loads on a ship can be classified according to the level of structure at which they act, [1], i.e., the hydrostatic pressure is acting on the ship's hull on a global level, while windlass forces, various equipment weight and operating forces tend to transfer the load on a smaller area of the structure; thus these forces can be considered local. The calculation of shear forces and bending moment acting along the length of a ship is essential for designing a longitudinal structure, [2], therefore, being an essential step in calculating the ship's longitudinal strength. However, these forces can and are usually also used in later design stages while calculating the strength of the localized structural elements.

In order to calculate ship longitudinal strength (and shear forces and bending moment), the users can choose among several specialized software packages already available on the market, usually as a part of the classification society. Some of them are software packages tied to a particular classification society, like BV Veristar, LR SEASAFE, [3], [4], [5], and others are independent, i.e., EcoLoad Master from Greenship technology company, [6]. However, even such software abides by the rules of the classification societies. Specialized hydrostatic programs are also usually capable of calculating the still water, shear force and bending moment distribution along the ship length, [1]. However, they usually do not provide open-source access, and the customization of the inputs and outputs is mostly limited. The small independent design offices often rely on software packages for 3D modelling and easy drawing extraction such as Rhinoceros (Rhino) and AutoCAD, often not specially customized for shipbuilding application, using them as a comprehensive tool for designing the hull structure, machinery, systems and equipment, [7], rather than investing in several specialized software programs.

Rhino is usually used as starting tool, often in the initial design phase of the project. The modelling in Rhino is based on NURBS (Non-Uniform Rational B-Splines) mathematical model. The modelling is relatively easy and intuitive, as it can create the simplest geometrical forms and organic 3D shapes and free surfaces. Therefore, it is often used to model the ship hull and design the ship superstructure in the early stages of the design process, [8].

The benefit of Rhino is the ability to interact and automate the design process using some of the well-known and widely used programming languages, such as Python, C++ or Visual Basic, [9]. This automated modelling process is often started and implemented using the scripting process, capable of executing all 3D modelling commands without using the graphical user interface. The connection between the modelling and scripting in Rhino can be achieved using *rhynoscriptsxntax* module package, [10]. The authors have used Rhinoceros 7, which has integrated IronPython package with the ability to connect Python and .Net framework, to evaluate the possibility of calculating the shear forces and bending moments using the Python script with 3D modelling tool on

Windows operating platform. Three different calculation methods were investigated and compared to the results obtained with a standard software package used in the well-known design office.

2. Basic principles of calculating longitudinal shear force and moment distribution

The concept of the "hull girder" model falls under the primary level of ship structural loadings and responses. The ship is simplified and idealized as the thin-wall box beam with several assumptions and simplifications: there is only one variable with loads and deflections having the single value at any cross-section, the hull girder remains elastic with relatively small deflections, any dynamic forces and effects are either neglected or substituted with equivalent static forces, and finally, the vertical bending is predominant, and finally, bending strain is linear, [1].

In order to calculate the resultant load on the ship q_x, the weight distribution curve, q_t and buoyancy distribution curve, q_u, must be determined. The weight distribution curve is obtained by adding the weights acting on each cross-section along the length of the hull, and the buoyancy curve is usually obtained by calculating the volume of the immersed area of the hull on that same cross-sections. The static equilibrium is achieved if the buoyancy force is equal to the weight of the ship, as shown in the following equation:

$$\int_0^L q_t \, dx = \int_0^L q_u \, dx, \tag{1}$$

where L is the length of the ship, and the position of the longitudinal centre of buoyancy must be in coincidence with the longitudinal centre of gravity, [1].

Thus, it is possible to calculate and draw shear force Q_x and bending moment M_x on any given position x along the length of the ship (Figure 1) according to equations 2 and 3:

$$Q_x = Q_u - Q_t = \int_0^x (q_u - q_t) \, dx = -\int_0^x q_x \, dx \,, \tag{2}$$

$$M_x = M_u - M_t = \int_0^x \int_0^x (q_u - q_t) \, dx \, dx = -\int_0^x \int_0^x q_x \, dx \, dx \,, \tag{3}$$

where Q_u, M_u are shear force and moment respectively, resulting from buoyancy, and Q_t, M_t are shear force and moment respectively, resulting from weight distribution.

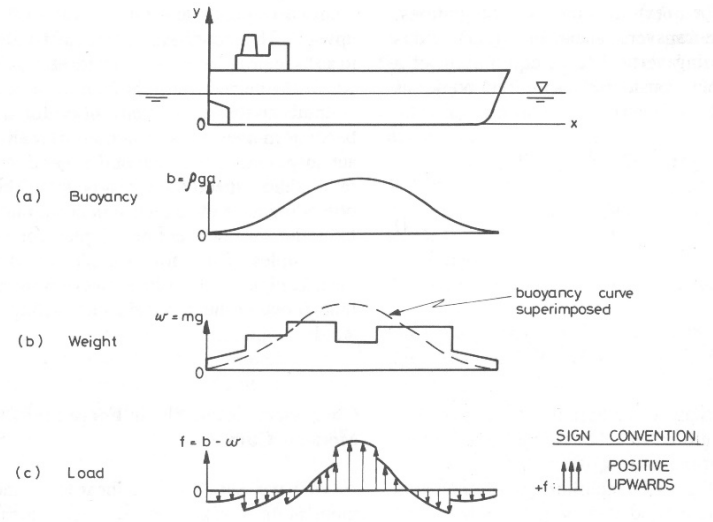

Figure 1: Summary of hull girder bending [1]

The starting step of shear forces and moment calculation is determining weight distribution along the length of the ship. The loads are usually grouped to form logical units, such as hull weight, machinery section, fuel, water, crew and provisions, passengers and cargo, plus a safety margin for the weights that can be underestimated, [2]. The weight of the hull can easily be extracted by using a preliminary 3D model of the structure or in early design stages by any given equation for preliminary calculation of the weight i.e. from literature sources, [2], [11]. Other loads, which are not positioned through the complete length of the ship, are then added to the hull weight by positioning them on the exact longitudinal position with correct weight length and weight amplitude, thus forming the weight distribution diagram.

Before calculating the buoyancy distribution diagram, it is essential to determine the correct waterline using the convergence method described in the literature, [2]. The proposed starting waterline must be corrected with one parallel translation and one angular rotation. Buoyancy can be calculated and checked against the weight distribution upon creating the waterline. When the equilibrium is achieved, meaning that the weight of the ship is equal to the total upwards buoyancy and these two forces coincide, [1], shear forces and moment can be calculated. The principle method flowchart is presented in Figure 2.

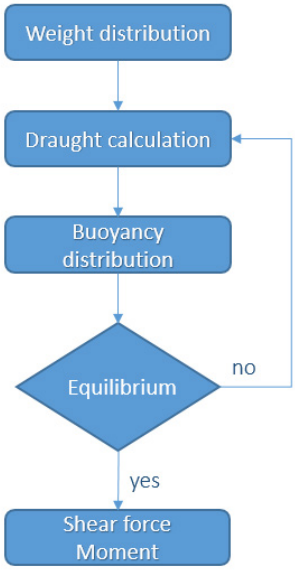

Figure 2: Design flowchart for shear force and bending moment calculation

The method mentioned above can be applied for still water as well as for wave loads. The method usually includes integration of the load curve using numerical integration formula i.e. trapezoidal rules or Simpson's One-Third Rule, [1], which can be used for hand calculation and for calculation executed using some specialized computer program.

3. Using *rhynoscriptsyntax* with Python code within Rhinoceros model

The shear force and moment calculation was used to test and verify calculation capability with an integration of Python within the Rhino models. The design principle from Figure 2 was incorporated into the Python script embedded within the Rhino model. To verify the script, authors have created the hull shape using Rhino modelling tools and have tried three different approaches, resulting in the creation of three versions of Python scripts. Version A and version B mainly focus on an analytical calculation using the numerical integration and following the workflow and equations from the literature, [2]. In contrast, version C used the graphical solution, relying mainly on the command available in Rhino and executed through the functions from *rhinoscriptsyntax* module. Versions A and B focus on calculating the buoyancy by using a determined number of sections through the hull length, where for version A, the number of sections was 20, and for version B, the number was user-defined. Upon defining the hull sections,

the total buoyancy of the hull was calculated using Simpson's One Third Rule. In version C, the hull geometry was graphically closed with a waterline surface, and by using the *rhinoscriptsyntax* module, the volume formed by the hull surface and closing waterline was formed. The flowchart of version C is shown in Figure 3, and usage some of the most used functions are briefly listed and explained through this chapter.

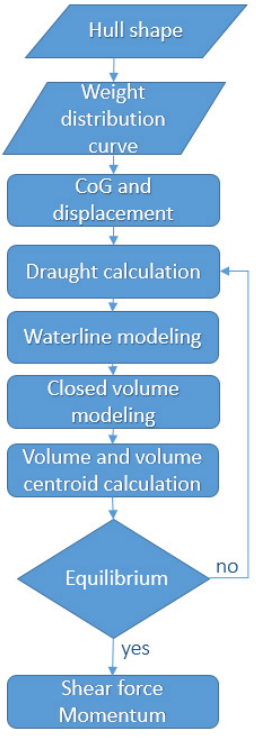

Figure 3: Design flowchart for version C

The Phyton script modules *math* and *rhinoscriptsyntax* were imported into the program using the **import** command. The *rhinoscriptsyntax* module enables the usage of Rhino command through Python scripting language, and *math* module enables some mathematical functions to be executed without the need of scripting these functions.

The ship particulars length over all (L_{oa}), hull breadth (B_{oa}) and a total height of the hull surface were defined through the function *BoundingBox(obj)*, where *obj* is 3D object obtained with *GetObject()* function through the user selection of the hull surface in the Rhino model. *GetObject()* function was frequently used to determine the graphical objects selected by the user in the graphical user interface (GUI) of Rhino software. The same function was later used to select the weight distribution curve and determine its parameters by selecting the curve using the object type filtering expression within

the *rhinoscriptsyntax* module, within the ***if*** statement in form (**if** *rs.IsCurve(graph):)*, where *graph* is the selected diagram. The points of the curve object were also extracted by creating the new list of points with the help of the *CurvePoints(graph)*. The weight distribution curve was then plotted in scale and closed. Redrawn and scaled curve was used to calculate the area under the curve, equal to the ship's displacement, with *CurveArea()* function. The centre of gravity coincides with the curve area centroid, easily extracted with *CurveAreaCentroid()*function. The same functions and principles were applied to extract the frame area and centre of buoyancy.

The waterline was created at half of the hull shape height and interpolated by the Rhino script in several iterations. The final version of intersecting waterline plane was created using the bounding box limiting planes and calculated waterline curve. The waterline surface was created with the surface command *AddSrfPt* and used as the intersection surface to create the volume with the hull surface model. With syntax line *rs.Command("-_CreateSolid")*, the selected curves (waterline and hull surface) joined in the solid, closed volume and thus, enabling extraction of the volume and centre of buoyancy with use of functions *SurfaceVolume()* and *SurfaceVolumeCentroid()*.

These values were compared with total displacement and longitudinal centre of gravity extracted from the weight distribution diagram. The shear force and momentum curves were drawn when the equilibrium was achieved.

The final frame area curve was calculated and drawn using previously described methods upon achieving the equilibrium. Two curves, frame area curve and weight distribution curve, were adjusted to have the same number of values on the abscissa axis and then the unknown values were interpolated using the linear interpolation. The curves were subtracted and plotted into the Rhino 3D model space.

4. Python within Rhino script execution method

From the user's point of view, several steps were taken. In order to commence calculation, a proper hull shape had to be selected. Hull shape geometry and weight distribution curve (diagram) were created (or imported) to Rhino. The imported or created geometry was checked for gaps prior to the script execution. If needed, surfaces were recreated using the *Patch* and *Loft* commands in Rhino and *ShowEdge* command crucial for visualization of any possible gaps in the model. The weight distribution diagram was inserted into the same model as the hull shape.

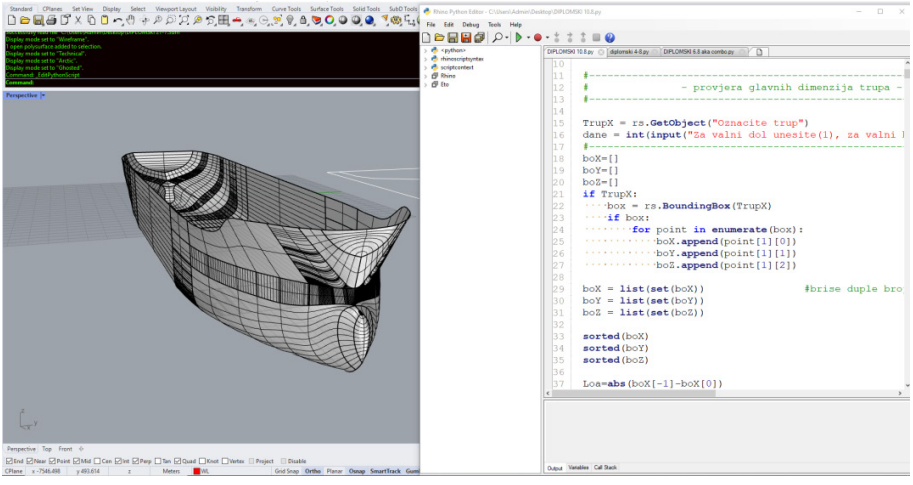

```
#-------------------------------------------------------------------
#                  - provjera glavnih dimenzija trupa -
#-------------------------------------------------------------------

TrupX = rs.GetObject("Oznacite trup")
dane = int(input("Za valni dol unesite(1), za valni
#-------------------------------------------------------------------
boX=[]
boY=[]
boZ=[]
if TrupX:
    box = rs.BoundingBox(TrupX)
    if box:
        for point in enumerate(box):
            boX.append(point[1][0])
            boY.append(point[1][1])
            boZ.append(point[1][2])

boX = list(set(boX))                    #brise duple bro
boY = list(set(boY))
boZ = list(set(boZ))

sorted(boX)
sorted(boY)
sorted(boZ)

Loa=abs(boX[-1]-boX[0])
```

Figure 4: Rhino GUI with Python script editor [8]

Upon inspection and after finalizing model preparation, the initiated the script within *Tools* toolbar by choosing the *PythonScript -> Run…* command and selecting the appropriate Python script from the working folder. The model and loaded script are visible in Figure 4.

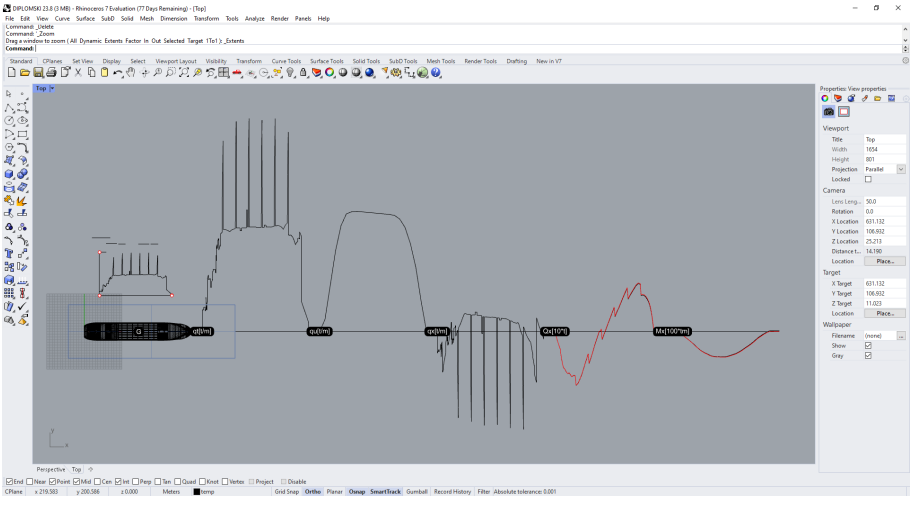

Figure 5: Output curves in Rhino 3D model space [8]

Several inputs were required prior to commencing the scripted calculation. The script guided the user through the necessary actions, selection of hull surface and

diagram selection process and diagram scaling. After the initial inputs, the script commenced the calculation and output diagrams were created in the Rhino 3D model space (Figure 5).

The script recreates the weight distribution diagram; it is only created using the appropriate scale. The frame area curve and load curve q_x were also created, as well as shear force and bending moment curves stacked from left to right in Figure 5. If needed, the moment envelope can be created by the user using the appropriate scale for moment (1 m in model space equals 100 tm).

This method was used to test all three versions and compare them to the approved and finalized calculation for the chemical tanker provided by the design office of the well-known shipyard, called the reference case. The weight distribution curve was taken from the shipyard's documentation, and the hull was remodelled according to the lines plan of the ship. The ship's particulars are shown in Table 1 and general arrangement of the vessel in Figure 6.

Table 1: Main particulars [8]

Length overall	195.20 m
Length between perpendiculars	187.30 m
Breadth moulded	32.20 m
Depth moulded	17.80 m
Design draught	12.00 m
Deadweight at design draught	49000 t

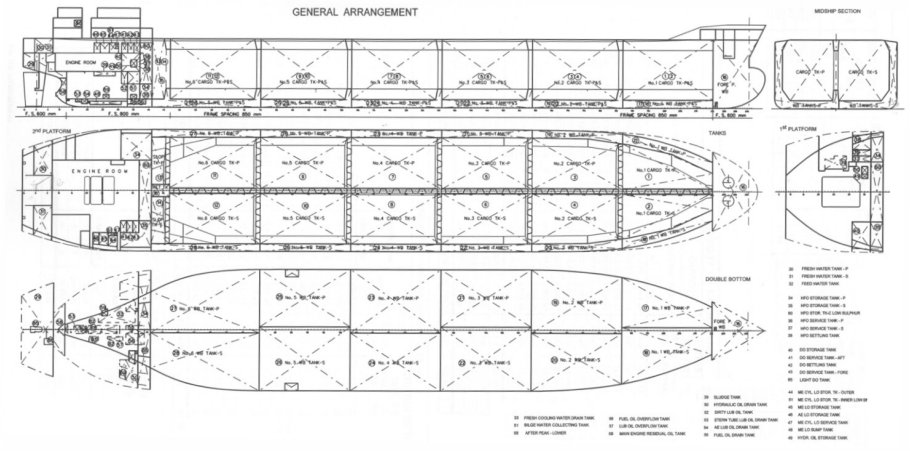

Figure 6: General arrangement of the case study ship [8]

5. Results and discussion

The shear force curves for each version were plotted and compared to the reference case, as seen in Figure 7. The comparison in the shear force diagram between the reference case and user versions of the program showed a 45.76 t greater value in favour of version C, while version B and version A had smaller values from the reference case by 82.12 t, and 337.14 t, respectively. Closer to the bow, the difference in maximum values was more significant. Version C had the biggest difference to the reference case with the value of 450.17 t, while version A had the smallest deviation of 117.20 t and version B intermediate 304.25 t. These values were smaller than the maximal value of the reference case in the bow area. The starting values of versions C and B were almost overlapping the reference curve, but the difference becomes more significant through the ship's length.

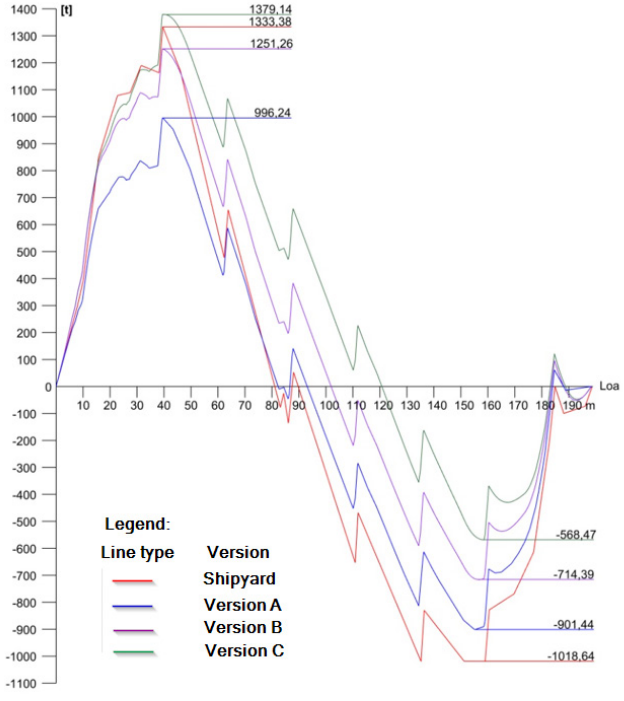

Figure 7: Comparison of shear force curves to reference case [8]

A similar issue was observed when looking at the bending moment curves (Figure 8). Version A, although with the most significant difference in maximum moment value (854 tm) but has the position of the momentum along the length of the ship almost at the same x coordinate, while version B and version C have maximal value closest to the

reference case (641.4 tm and 587.8 tm respectively). The bending moment maximum for version C is shifted well forward, as seen in Figure 8.

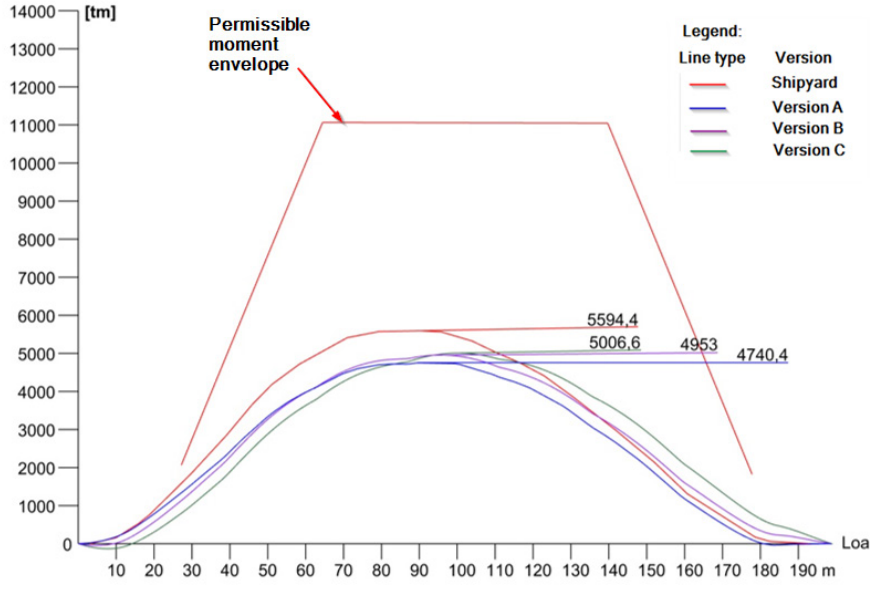

Figure 8: Comparison of bending moment curves to reference case [8]

While the smallest difference in shear force maximum values between the reference case and version C was 3,4% at the stern part, the percentage was increased in the bow area with a value difference of 44%. Version B has a 6% difference at the stern and 30% at the bow. The smallest difference of 10.5% for the bending moment values between version C and reference value cannot be omitted. Further investigation is needed to establish the reason of these deviations.

6. Conclusion

The authors have presented a methodology of determining the shear forces and bending moments based on scientific methods and tools that differ from the classical approach, primarily in using a generic 3D software package in conjunction with open source Phyton software to facilitate the calculation procedure.

The values were compared with the reference case, and even though the curve shapes match the reference case, there are differences in values that cannot be easily omitted. Authors have found several possible reasons that can influence the values:

Differences between the input geometry can have a significant influence on final values. The hull geometry was modelled in Rhino 3D using the lines plan, and the hull

shape was corrected and adjusted to have closed surfaces and work properly with the script. The geometry used by the authors was slightly simplified, especially around the bulbous bow, where the shape differs from the lines plan.

The authors have used a simplified interpolation method, linear interpolation, appropriate for the weight distribution curve. However, using this method on the buoyancy curve can lead to significant errors. In the authors' opinion, improving the iteration and integration methods can also lead to more accurate values.

To fully validate software and troubleshoot possible errors, several cases and several ships will have to be considered and studied in future work.

Acknowledgements

This research is supported by funds from the support research at the University of Rijeka under project UNIRI tehnic 18-159 "Development of Methodology for Ship Design and Production towards Industry 4.0. Concept"

References

1. Hughes, O. F. (1988) *Ship structural Design*. New Jersey, SNAME.
2. Uršić, J. (1991) Čvrstoća *broda I. dio.* Zagreb, Sveučilišna naklada d.o.o.
3. Bureau Veritas (2019) *Bureau Veritas Rules for the classification of Steel Ships, Part B Hull and Stability*, Paris, BV.
4. Marine and Offshore (2021) *Veristar Stability Software – Intact and Damage Calculation* Available from: https://marine-offshore.bureauveritas.com/veristar-stability-software-intact-and-damage-calculation [Accesed 28th October 2021].
5. LR SEASAFE (2021) *Providing certainty for critical marine calculation* Available from: https://www.lr.org/en/lr-seasafe/ [Accesed 28th October 2021].
6. Green ship technologies - Marine Software (2019) *Marine Software,* Available from: https://www.greenshiptech.com/marine-software/ [Accesed 28th October 2021].
7. Rhinocheros (2021) *Rhino for the Marine Industry* Available from: https://www.rhino3d.com/for/marine/ [Accesed 28th October 2021].
8. Tomić, A. (2021) *Proračun uzdužne* čvrstoće *broad primjenom općih programskih paketa*, *Croatia.* Masters thesis, University of Rijeka, Faculty of Engineering.
9. van Oers, B., van Hees, M., Stapersma, D., Hopman, H. (2008) Combining a Knowledge System with Computer-Aided Design. *Ship Technology Research*. 55(2), 51-59.
10. Rhino Developer Docs (2021) *What is Rhino.Python*. Available from: https://developer.rhino3d.com/guides/rhinopython/what-is-rhinopython/ [Accesed 28th October 2021].
11. Lamb, T. (2003) *Ship Design and Construction, Volumes I and II*. New Jersey, SNAME.

ISSN 0554-6397
Prethodno priopćenje
(*Preliminary communication*)

Ivan Sulovsky
E-mail: isulovsky@riteh.hr
Jasna Prpić-Oršić
E-mail: jasnapo@riteh.hr
Faculty of Engineering, University of Rijeka, Vukovarska 58, 51000 Rijeka

Seakeeping Analysis of a Double Ended Ferry

Abstract

Awareness of environmental protection is increasing, especially in recent years when warnings of imminent climate change have begun to appear in public space. In addition to one of the most significant environmental pollutants, global maritime transport is also mentioned, where environmental pollution is explicitly in the form of exhaust gases from marine propulsion engines. The trend of developing environmentally friendly, so-called "eco" ships is on the rise, primarily in the development of electric ferries designed to transport passengers and vehicles on short routes. This paper deals with a seakeeping analysis of a double ended ferry which is intended for sea route between Brestova and Porozina in the North Adriatic. The adopted dimensions and shape of the ship, the characteristics of sea waves for the adopted spectrum will be presented, and then the obtained results, considering the limits of the ship operability related to passenger comfort and cargo safety. The analysis was performed using computer software "Sesame HydroD". A seakeeping estimation for the ferry is finally adopted and possible directions for future developments are proposed.

Keywords: Seakeeping, electric ferry, Sesame HydroD

1.Introduction

The development of double ended ferries with electric propulsion has certainly taken an important roll in shipbuilding in recent years. Efforts were made in the comparison of basic parameters for double-ended ferries [5] for new hybrid design in the future. In this paper, insight in seakeeping behaviour of such vessel is shown. Seakeeping analysis was done for double-ended ferry which is intended for route beetween Brestova and Porozina in North Adriatic sea. Analysis was done using DNV's software *Sesame HydroD,* using *Wasim* module. *Wasim* is a time-domain 3D-BEM code using rankine approach. ITTC wave spectrum is chosen with main parameters derived from [2]. Performed analysis was done for one loading condition and one service speed.

Inputs that are necessary for this type of analysis, with this software, are hull form, center of mass and desired speed. Hull form has the biggest impact on seakeeping performance where length of a ship plays the most significant role. Optimization of hull forms in terms of seakeeping are usually not „fine tunings“ but rather changes of main dimensions, form coefficients or mass redistribution. Results of the presented analysis are shown in common way of *RAO's* of a vessel with some time domain diagrams. If one is to say „*this vessel has good seakeeping characteristics!“* what is the physical and mathematical evidence for this statement? It is when *operability* of the vessel enters the game. Operability of the vessel simply shows *how practical would this ship be on certain sea state.* To evaluate operability, appropriate criteria and their limiting values needs to be adopted. In this analysis limiting criteria is adopted with regards to comfort of passengers and crew, and safety of transported cargo. Comfort during the trip is assesed considering roll motions while cargo safety considering vertical accelerations. Operability assesment for this type of ship would be more precise if real seakeeping performance criteria were developed. Roll motion resctriction is adopted from [4], while simple methodology for pitch and heave restriction calculation are presented with very basic formulations. Lashing sytems on ferries and Ro-Ro ships require careful attention during design proccess. While further investigations of seakeeping and maritime characteristics are needed for this type of ship, this work represent small but valuable contribution for having an insight in ship behaviour in real conditions.

2. Input data and environment modeling

To perform numerical seakeeping analysis, two groups of data are necessary. Firstly, it is important to define ship hull form, which most often meets the requirements for displacement or/and draught. Among hull form, it is also necessary to perform weight study to get information about center of gravity of the ship and mass moments of inertia. Basic CAD model of the double ended ferry was prepared by the company Flow Ship Design d.o.o, Figure 1, along with weight study.

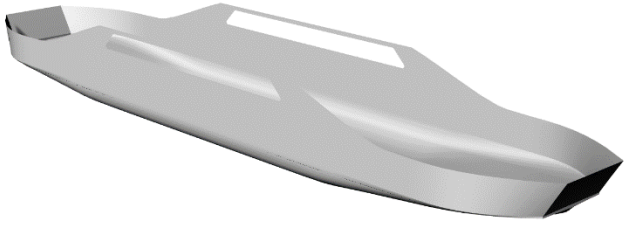

Figure 1. Double ended ferry CAD model [2]

Loading condition that is considered for seakeeping analysis is the "worst" probable condition while the ship is intact. This loading condition includes maximum number of passengers and trucks. Parameters for this loading condition and main dimensions are as follows, [7]:

$\Delta = 2780$ t	$L_{OA}=101.9$ *m*
$T = 2.5$ m	$L_{PP}=92.7$ *m*
$L_{CG} = 46.0$ m	$B=20$ *m*
$V_{CG} = 5.3$ m.	$D_{MainDeck}=3.8$ *m*

Also, analysis was performed with service speed of 12.0 knots. The meshed Double-ended ferry hull that is done in *Wasim* is seen on Figure 2. Regarding viscous roll damping, quadratic damping coefficient is employed to account for the vicsous effects on roll motion. [9]

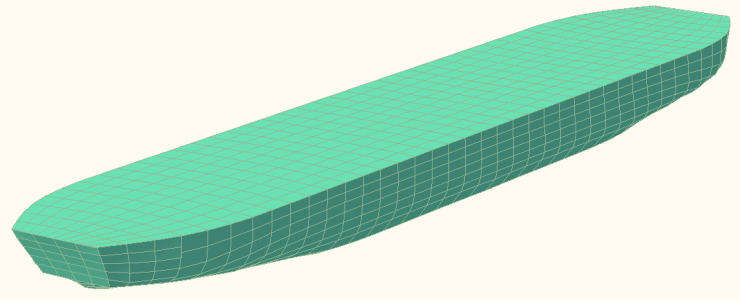

Figure 2. Hull mesh

The sea characteristics were modeled through ITTC (Bretschneider) spectrum that is most used in these types of analysis [1], [8]. Although JONSWAP spectrum could be more appropriate for this area, due to inconsistencies in data ITTC spectrum is chosen [10]. The significant wave height *Hs* was taken as 0.8 meters with average period *T* of 4.6 seconds, which correlates to sea state 4 (four). The spectrum is shown in figure 3.

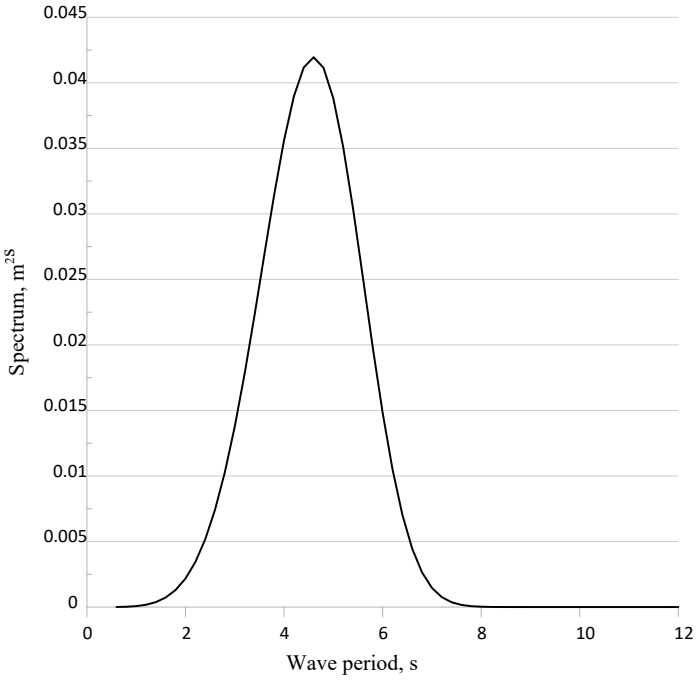

Figure 3. ITTC 57 wave spectrum

Figure 4. shows sea route for which this ferry is intended. Route between Porozina, southernmost village of Island Cres and Brestova that is located on Istrian peninsula. Total length of the route is around 2.5 nm with high traffic in the canal.

Figure 4. Route Brestova – Porozina [3]

Geographical characteristics of this sea passage dictates the wind directions, which usually cause beam seas which can be the most challenging, unpleasant, and dangerous of all conditions to navigate. Seven wave directions were considered in the analysis, ranging from stern to bow with step of 30 °, figure 5.

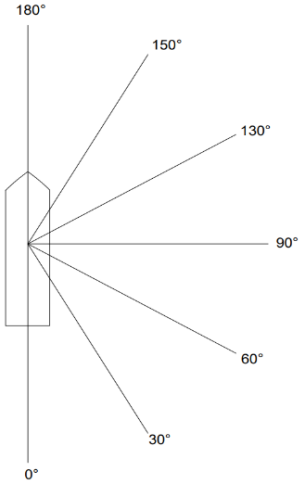

Figure 5. Wave directions applied in calculations

3. Operability criteria

For the sake of seakeeping evaluation of a ship, operability and usability of the ship should be considered. For double ended ferry there are two goals that must be met:

◊ Passenger and crew comfort
◊ Cargo safety

According to these two goals, the corresponding criteria will be defined. In [4], limiting value for roll motion for transit passengers is **2.5 ° RMS**[1] . This value will be adopted for overall crew and passenger comfort. Regarding cargo safety which in this case are road vehicles, limiting value is defined in the following way:

According to [6], section 3.4.3, maximum securing load for road vehicles of more than 3.5 tonnes should be not less than **100 kN**. Having that value in mind it is possible to calculate critical acceleration from equation:

$$F_{msl} = ma_{kr} \tag{1}$$

[1] RMS – root mean square is defined as the square of the mean square values

m = 18750 kg, average mass of road truck

F_{msl} = 100 000 N, maximum securing load

Which gives us our limiting value for acceleration:

a_{kr} = ***6.4 m/s²***

Short summary of operability criterias with their associated limit values are listed in table 1.

Table 1. Limiting values for operability assessment

Operability criteria	***Limiting value***
Passenger and crew comfort	*<RMS roll* 2.5 °
Cargo safety	*<6.4 m/s²*

There are however other possible operability criteria that would be of interest. Ramp accessibility during vehicle boarding when the ferry is operating in unprotected ports could also be a potential operability limit, especially in the port of Brestova that is relatively unprotected of waves and wind. The influence of wind should also not be neglected, especially when the vessel is approaching the pier. Due to relatively small windage area, wind drift and heeling of the vessel should be canceled out, or at least minimised by steering manouvers from the captain

4. Results

Seakeeping analysis was carried out with DNV's software for hydrodynamic analysis SESAME HydroD. Simulation is carried out in time domain but it can be transformed into frequency domain via fourier transformations. The code is based on Rankine panel method which solves fully 3-dimensional radiation and diffraction problem. Potential flow codes are still the most prevalent numerical choice for evaluations of seakeeping properties of ships for it's low computational costs. It is however unable to accurately resolve the nonlinearity of waves and rigid body motions, wave breaking, etc. Snce it is common practice to display the seakeeping properties of a ship with response amplitude operators (RAO) that are defined in equation (2), RAO's for roll, pitch and heave are presented.

$$RAO = \left|\frac{R_a}{\zeta}\right|^2 \tag{2}$$

Response amplitudes for heave and pitch will be shown for head waves including encounter angles from 120° up to 180°. Roll amplitudes will include encounter angles from 30° up to 120°. In figure 6. no significant peaks for heave motion is visible. Regarding pitching, on figure 7. there are peaks in the range of 1-1.5 rad/s of encounter frequency but with no significant amplitudes. Regarding roll motions, as expected, amplitudes are highest for beam seas as it is clear on figure 8.

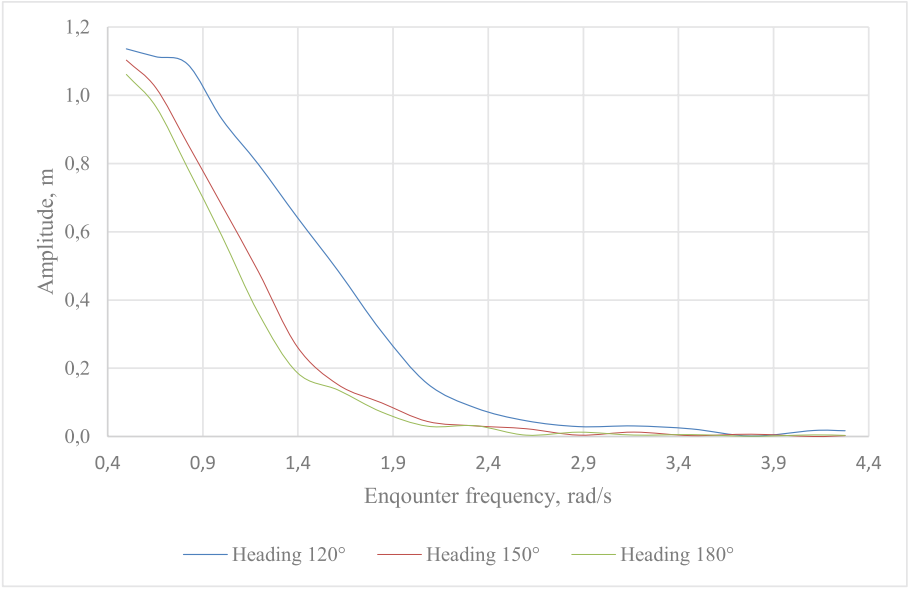

Figure 6. RAO's for heave motions

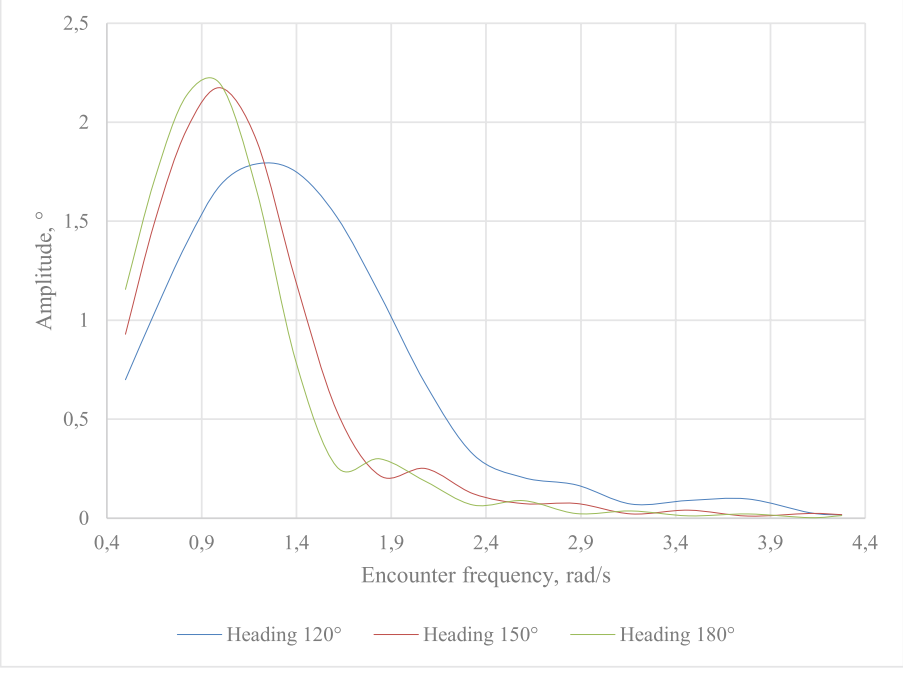

Figure 7. RAO's for pitch motions

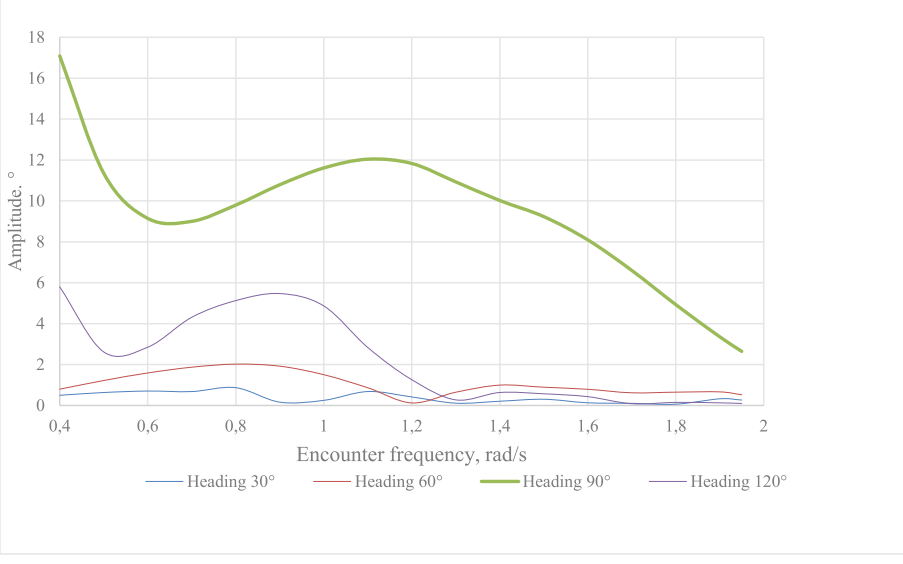

Figure 8. RAO's for roll motions

In Sesame HydroD software, graphical postprocessing options are available. Figures 9. and 10. show ship response for head and beam seas.

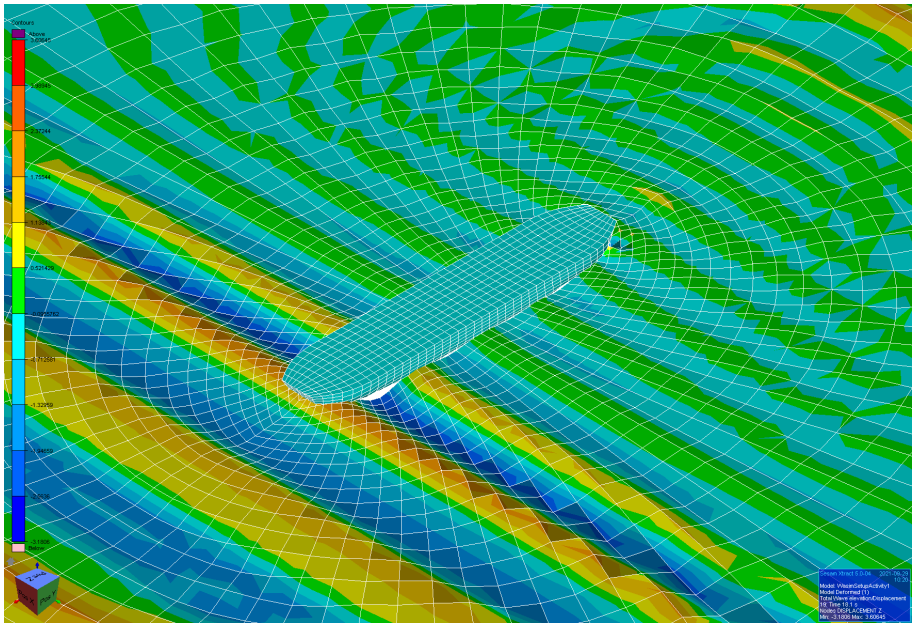

Figure 9. Graphical excerpt from Wasim – head seas

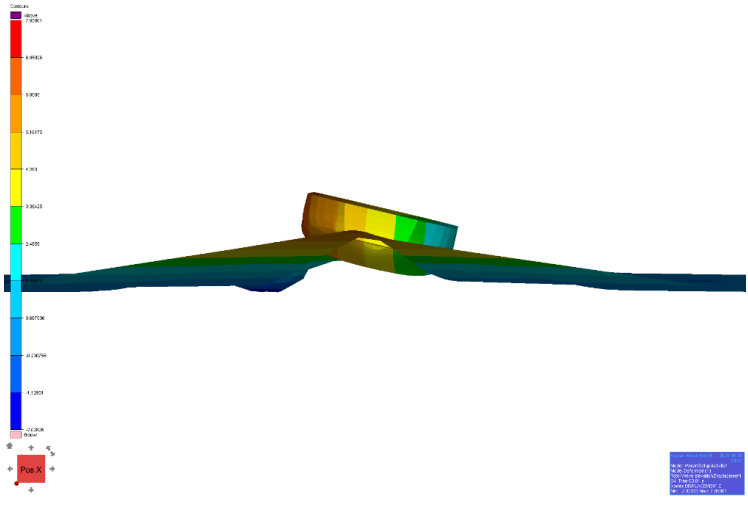

Figure 10. Graphical excerpt from Wasim – beam seas

4.1. Operability assesment

Given that sea and wind statistics for the area of navigation (Vela Vrata) are missing for this analysis, probability of occurrence of wave heights and directions will be ommited.

4.1.1. Passenger and crew comfort assesment

Observing RAO's for roll motion from figure 8. it is clear that the heaviest response is to be expected in beam seas. Therefore, roll response spectrum for beam seas is shown in figure 11. with it's corresponding value of zero moment.

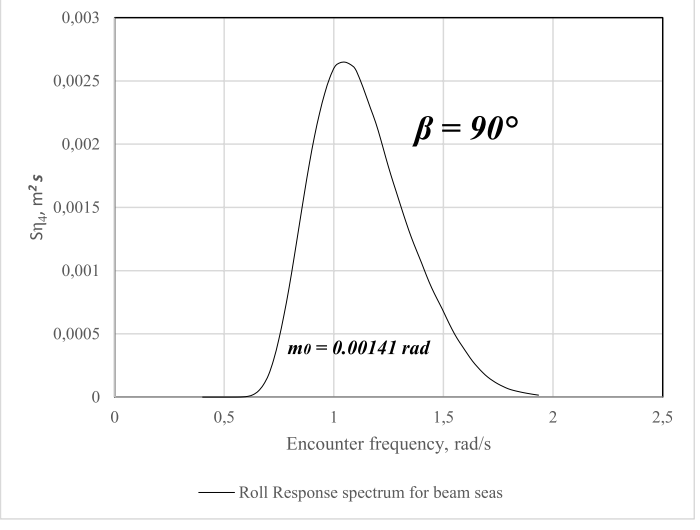

Figure 11. Roll response spectrum for beam seas

Since the relation beetween *rms* and zero moment is:

$$\sqrt{m_0} = rms \tag{3}$$

First operability criteria for passenger and crew comfort, for the given weather conditions, is satisfied:

$$\mathbf{2.119° < 2.5°}$$

4.1.2. Cargo safety assesment

Regarding **cargo safety** as an operability criteria, vertical accelerations were examined at the front point on the ship at the garage deck, where position of trucks is highly probable. Point coordinates are 70 meters from aft perpendicular, 5 meters above baseline and in the centerline . Response spectrum of vertical acceleration is shown on figure 12. with it's corresponding moment. Among calculation in frequency domain, time simulation of voyage in duration of 20 minutes is carried out with paying attention to variability of vertical accelerations, figure 13. Maximum expected accelerations are found to be around 0.55 m/s^2. It can be concluded that due to the small wave height and short wave periods, acceleration amplitudes are not large.

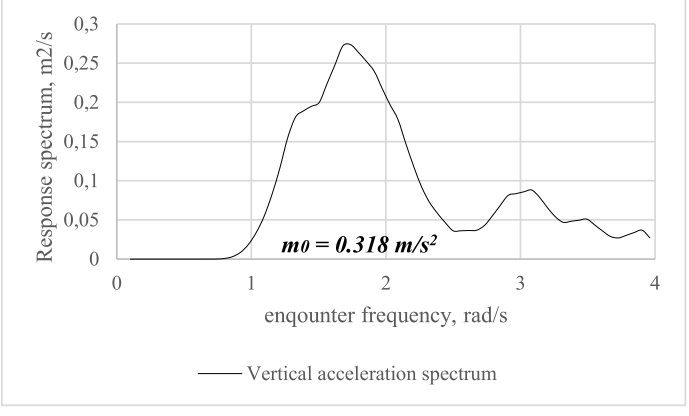

Figure 12. Pitch accelerations – excerpt from HydroD

According to (2), operability criteria for cargo safety is also satisfied:

$$\mathbf{0.563\ m/s^2 < 6.4\ m/s^2}$$

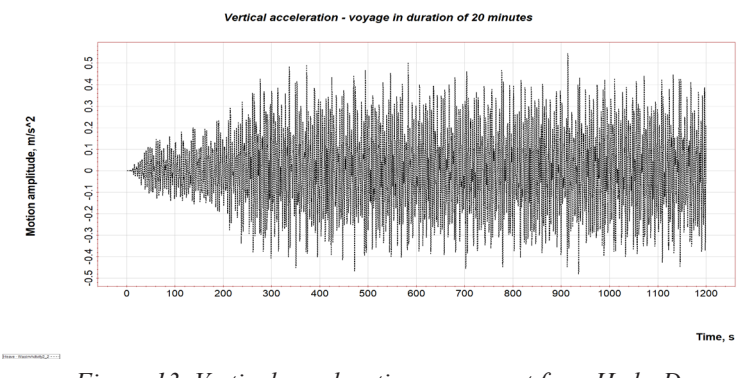

Figure 13. Vertical accelerations – excerpt from HydroD

5. Conclusions

The development of a database for seakeeping and overal maritime characteristics of double-ended ferries is surely needed, given the latest efforts in the field of „eco-ships“. This work shows a methodology for estimation of seakeeping characteristics of such ships where further developments and improvements are possible. Key improvements would include development of operability criteria for „eco-ships“ such as heave vertical motion limit for ramp accesibility during vehicle boarding and an investigation of scatter diagram of weather conditions for navigational routes of these kind of ships. These data, with the seakeeping calculation for the whole range of ship speeds and wave headings, will allow us to estimate operability index and compare several desing options. The analysis in this work showed favourable seakeeping characteristics for navigation in sea passage Vela Vrata, with no need for implementing motion stabilizers other than standard bilge keels. Roll amplitudes are in acceptable range, satisfying more sensitive passengers on board. Vertical acceleration is also observed and no significantly high values are found. Since the sea state adopted in this analysis has relatively small significant wave height, these results were to be expected. Lastly, since electrial propulsion is implemented in this ship, it would be of great importance to have an insight into attainable ship speed during rough weather for estimating needs for batteries on bord.

Nomenclature and units

Δ - ship displacement, t
T - draught, m
L_{CG} - longitudinal center of gravity, m
V_{CG} - vertical center of gravity, m
Hs – significant wave height, m
T – mean period, m
m – average vehicle weight, kg
Fmsl – maximum securing load, N
a_{kr} *- critical accceleration, m/s²*
RAO – response amplitude operator
Ra – response amplitude, m, °
ζ – wave amplitude, m
m_0 – zero moment
rms – root mean square as roll criteria, °

Acknowledgements

This work was done as a part of *Maritime Environment-Friendly TRanspOrt systems (METRO)* project, with main objective to improve the quality, safety and environmental sustainability of marine and coastal transport services and nodes by promoting multimodality in the programme area. Lead partner is University of Trieste – Department of Naval Architecture with Faculty of Engineering being one of the partners.

This work has also been supported by the Croatian Science Foundation under the project project IP-2018-01-3739. This work was also supported by the University of Rijeka (project no. uniri-tehnic-18-18 1146 and uniri-tehnic-18-266 6469).

References

1. Bretschneider, C.L., 1959, "Wave variability and wave spectra for win-generated grav-ity waves", Technical Memorandum No. 118, Beach Erosion Board, U.S. Army Corps of Engineers, Washington, DC, USA.
2. D. Zorović, R. Mohović, Đ. Mohović. "Prilog određivanju duljine vjetrovnih valova na Jadranu, ISSN 0479-6255, "Naše more" 50(3-4)/2003
3. Excerpt from online database of world maps:
   Available from: https://www.google.com/maps
4. Ghaemi, Hossein & Olszewski, Henryk. (2017). „Total Ship Operability-Review, Concept and Criteria" Polish Maritime Research. 24. 74-81. 10.1515/pomr-2017-0024.
5. L. Josip Novak, D. Majnarić, R.Dejhalla, A.Zamarin "An Analysis of Basic Parameters of Ro-Pax ships and Double-ended Ferries as Basis for New Hybrid Ferries Designs, September 2020 Journal of Maritime & Transportation Science Special edition (3):33-48 DOI: 10.18048/2020.00.02
6. Maritime and Coastguard Agency, "Roll-on/Roll-off Ships-Stowage and Securing of Vehicles", TSO, London, 2003.
7. METRO-Double ended Ferry-TRIM & STABILITY BOOK_REV1
   Available from: Double+ended+Ferry-TRIM+%26+STABILITY+BOOK_REV1.pdf
8. METRO, WP 5 / Act. 5.1 Navigational, Meteorological and Oceanographic Analysis, prepared by the Faculty of Maritime Studies, University of Rijeka
9. M. Himeno, Yoji. (1981). „Prediction of Ship Roll Damping. A State of the Art." University of Michigan Department of Naval Architecture and Marine Engineering, (Report). 87.
10. Tucker, M.. (2001). Waves in Ocean Engineering. Ocean Eng. Book Ser.. 5. pp 150-210

ISSN 0554-6397
Prethodno priopćenje
(*Preliminary communication*)

Toni Holjević
E-mail: toniholjevic@gmail.com
Tehnički fakultet Sveučilišta u Rijeci, Vukovarska 58, Rijeka, Croatia
Vanja Travaš
E-mail: vanja.travas@gradri.uniri.hr
Građevinski fakultet Sveučilišta u Rijeci, Radmile Matejčić 3, Rijeka, Croatia
Lado Kranjčević
E-mail: lado.kranjcevic@riteh.hr
Siniša Družeta
E-mail: sinisa.druzeta@riteh.hr
Tehnički fakultet Sveučilišta u Rijeci, Vukovarska 58, Rijeka, Croatia

Analysis of Microplastic Particle Transmission

Summary

The progressive increase in the mass of microplastics in the ecosystem obliges us to urgently define measures to reduce its adverse effects, which primarily requires an understanding of the genesis of its presence and the dynamics of expansion through the biosphere. This paper aims to contribute to the understanding of the dynamics of microplastic particle motion, especially in the context of deposition rate with respect to microplastic material density, microplastic particle size and especially with respect to microplastic particle shape (which significantly affects shape resistance forces). For this purpose, an overview of existing works in the field of modeling the motion of microplastics is given, and a numerical model for modeling the transport of microplastic particles in an inhomogeneous fluid velocity field for laminar flow is formed. The proposed model is thus based on a system of two nonlinear ordinary differential equations.

Keywords: microplastics, precipitation, physical model

1. Introduction

Plastic is today one of the most important and most commonly used materials in the world. In the manufacturing process it is often a cheaper and lighter material than the available alternatives. However, increasing amounts of inadequately disposed plastic waste combined with an extremely long decomposition time have resulted in its increased accumulation in the environment.

According to the European Parliament [1], only 32.5% of plastic waste is recycled, 42.6% is incinerated, releasing significant amounts of toxins such as mercury and nitrous oxide, and carbon dioxide into the atmosphere with energy production, and only 24.9% are delayed. The data refer to plastic that has been adequately disposed of. Due to different parameters such as wind speed, temperature, earth rotation, salt concentration and the like, there are five main vortices in the oceans: North Pacific, North Atlantic, South Pacific, South Atlantic and Indian Ocean vortex. Sea currents collect plastic from the shores of continents and carry it towards the centers of the vortex, so there are huge amounts of plastic of different dimensions in the centers, which destroy flora and fauna. Plastic is so widespread in the seas and oceans due to currents, that it can be found in all parts of the world regardless of the presence of people in the area, so the parts have been found even in Antarctica.

The categorization of plastics accumulated in aquatic environments is defined according to sample size. The sample size is the maximum distance that can be measured between two points of the particle, which defines the characteristic dimension of the sample d_p [L]. Although there are different categorizations of plastics by size, in recent times the most common is the one in which samples are classified into 4 categories: (i) macroplastics for samples with a d_p greater than 200 mm, (ii) mesoplastics for samples with a d_p in in the range of 5 to 200 mm (iii) microplastics for samples in which d_p is in the range of 0.001 to 5 mm and (iv) nanoplastics for samples in which d_p is in the range of 1 to 100 nm.

In this paper, microplastics and its behavior in aquatic environments are considered. An overview of previous works in the field of modeling the motion of microplastic particles is given. Based on current knowledge about the behavior of microplastics in aquatic environments and the dominant forces influencing the process, a numerical model was formed and a simulation was performed for controlled conditions.

2. Previous achievements in modeling the movement of microplastics

Microplastic research is mainly related to the collection and analysis of particles, while a small number of papers deal with simulating the movement of microplastics due to very complex processes that cannot be unambiguously determined. Therefore, each survey contains a number of simplifications that allow the calculation of average values. The movement of microplastics can be horizontal due to winds and sea currents, and vertical due to the sinking of particles after their mass changes. In most cases, the particles move in both directions, and there is a vortex depending on the weather. Therefore, some of the works deal with one or both forms of movement.

Research [2] includes measurements and modeling of the vertical distribution of microplastics in the Atlantic Ocean. The collection was performed using a pump filtration device and then the particles were analyzed by Raman spectrometry. Concentrations ranged from 13 to 501 pieces per m^3. The largest number of particles had a size of 10 to

20 μm. The numerical model was made with polyethylene particles in the dimensions of 10, 100 and 1000 μm. The vertical distribution is based on an advective transport model that includes buoyancy and turbulent mixing forces that cause the microplastic particles to move. The vertical velocity depends on the difference in density of the polymer and seawater. The shape of the particles is assumed to be spherical. Particle distribution was calculated with a one-dimensional equation for depths up to 250 m. The results show that most particles are located in the upper layers, and indicate a correlation between particle dimensions and position in the water column.

As part of [3], simulations of the movement of microplastics on the ocean surface were made, based on satellite images and measurements, in order to place devices for removing microplastics from the sea in an appropriate place. The analysis was performed on the surface of all seas and oceans on planet Earth. The authors have placed 29 "sinks" for microplastics in the domain, which were proposed as part of the The Ocean Cleanup project. During the optimization process, the locations of the microplastic outlets were changed, in order to find the positions that would result in the largest amount of collected particles. The grid on which the search was performed was 1° × 1°. The amount of plastic that entered depended on the amount of poor waste management in each country based on previous research, taking into account the exponential increase in the amount of plastic over the years.

Paper [4] compares the results of modeling and collection of microplastics in the northern Italian part of the Adriatic Sea. In particular, the influence of the river Po is analyzed, which has a flow in the range of 100 to 11550 m^3/s and carries with it significant amounts of microplastics. The amount of microplastics from water at 24 locations and sediment at 9 beaches in the area of the tidal cycle was analyzed. Measurements have shown that the average amount of particles at sea locations is 84 particles per m^3 and 78 particles per kilogram of sediment on the beach. The model made in the ICHTHYOP program includes the movement of microplastics through particles in the Lagrange model, and includes a 3D model based on horizontal and vertical dispersion, advection and buoyancy force. Assumptions about particles that are spherical in shape, 1 mm in diameter and density 0.91 g/mL, and assumptions about the concentration of 10 particles per m3 in the amount of water coming with the river Po were used. The Po River itself is assumed in the model as a point source. ROMS, SWAN and COAWST programs were used to model the sea flow. The paper concluded that tourism is a significant source of plastic waste that is not included in the model, so the results do not match to a greater extent. In a scientific study [5], the concentration of plastic in the surface layer of the Adriatic Sea was calculated. Calculations include combinations of terrestrial and marine litter inputs, the Lagrange model MEDSLIK-II, AFS ocean current simulations, and ECMWF wind analysis. Rivers entering the Adriatic Sea and larger cities are taken as plastic entry points. This model allows the particles to remain on shore. The calculation was made so that 10,000 virtual particles are introduced into the model over a period of 10 days. Figure 1 shows the results obtained. This research covers all dimensions of plastic particles, not just microplastics.

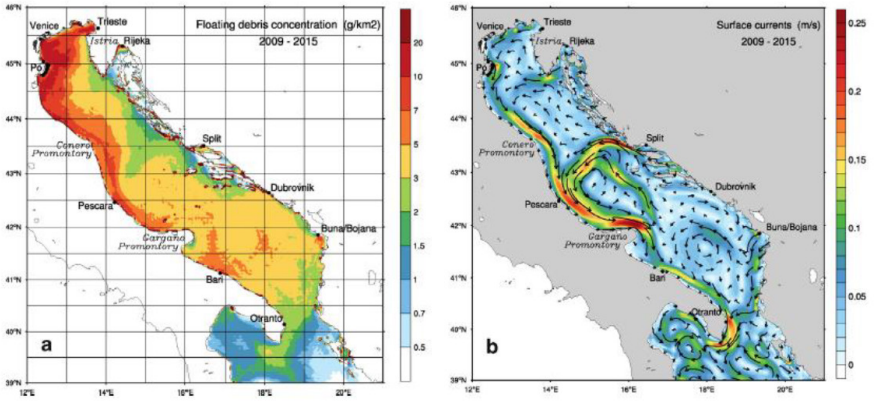

Figure 1. Expected average values of microplastics and sea speed for the period 2009-2015.

3. Numerical model of microplastic motion

When describing the vertical motion of microplastic particles, it can be found in conditions of sinking (negatively buoyant plastic) and conditions of emergence (positively buoyant plastic), which is predominantly influenced by the density of microplastics ρ_p and the density of the recipient ρ_f. The size and shape of the microplastic particle affect the amount of resistance force of the shape that occurs in the case of relative motion between the fluid and the particle itself. Challenges in modeling relate to defining shape factors for a randomly selected microplastic particle. For this purpose, the reduction principle is applied in which the shape of the particle is categorized according to the number of dominant dimensions. Based on this approach, we distinguish microplastic particles categorized as 3D, 2D, and 1D objects. Based on the above reduction approach, a mathematical and numerical algorithm for the integration of the equations of motion of microplastic particles of generalized shape was developed, taking into account the change in the resistance factor of the shape of the microplastic particles. This paper provides an overview of the model results for the described input parameters, but will not go into detail describing the model algorithm. Based on the above model, a numerical analysis of water flow and movement of microplastic particles in the experimental bed of the hydrotechnical laboratory of the Faculty of Civil Engineering in Rijeka was performed. The purpose of the analysis is to prepare an experimental procedure through which the different conditions of microplastic particle transport under open flow conditions will be investigated and the calibration of the numerical model will be enabled.

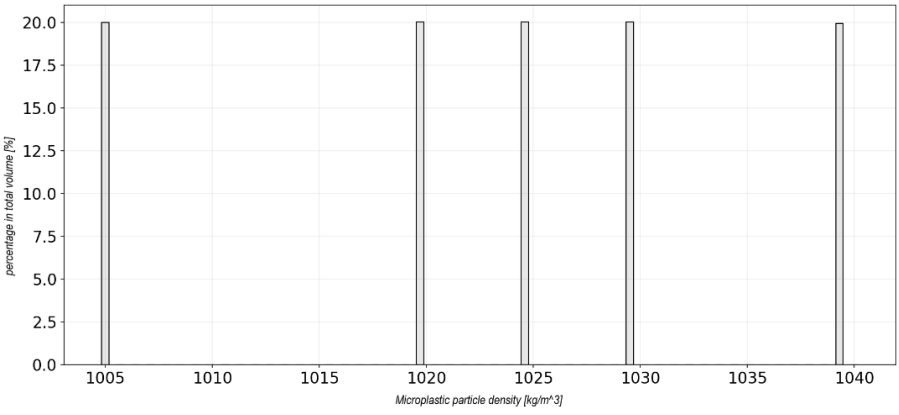

Figure 2. Microplastic particle density

A numerical model was performed for 2000 microplastic particles. The default particle density distribution is seen in Figure 2. The characteristic particle size is given by a uniform statistical distribution through which the characteristic particle size of the microplastic is given between the limits of 0.1 to 3.0 mm (Figure 3). The sphericity index of microplastic particles is defined in three categories: 3D, 2D and 1D samples. Water density is defined with an amount of 1000 kg/m^3. The spatial domain of the model was defined according to the dimensions of the experimental riverbed (length 12.5 m, width 0.309 m and height 0.45 m). An exponential velocity profile with a maximum velocity on the water surface of 0.3 m/s is given by the height of the cross section. The duration of the simulation is 60 s, and the time step is 0.5 s.

The spatial distribution of sedimented microplastic particles can be observed by applying statistical analysis [6] in a way that defines the probability of deposition for a particular group of microplastic particles or for particles that have the same or similar sphericity factor ψ . For these purposes, the bottom of the spatial flow domain is divided into 25 0.5 m segments in which the deposition of precipitated particles is performed. The sediment probability density function thus defines the probability that a particle from a particular grouping is located at a particular part of the bottom of the spatial flow domain. As 3 categories of shapes were considered, three separate density functions were defined.

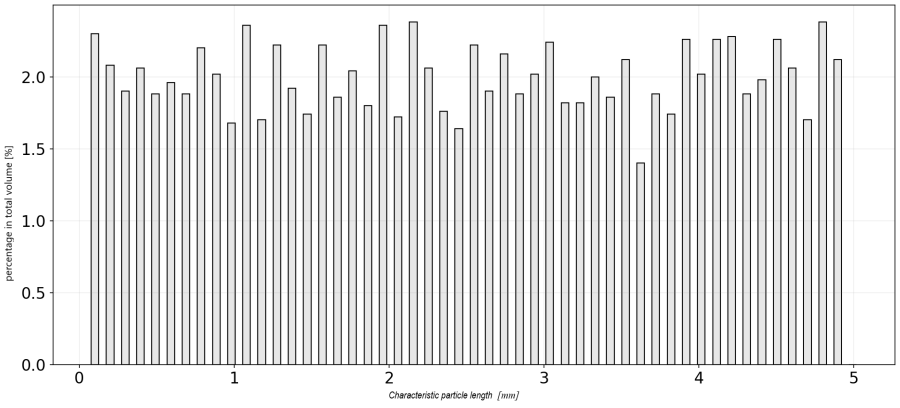

Figure 3. Characteristic particle length of microplastics

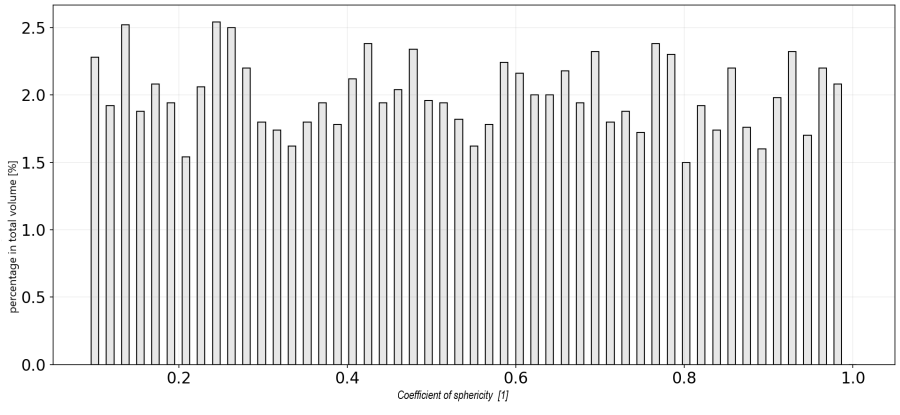

Figure 4. Coefficient of sphericity of microplastic particles

Figure 5 shows the results of the numerical analysis. The graph above shows the position of the particles for the final moment of the simulation t = 60 s, together with the flow velocity profile according to the previously defined model. The lower graph on the left ordinate shows the time to the moment when the particle touched the bottom of the spatial domain, and on the right ordinate there is the probability of deposition of three examined groups of particles according to the given sphericity index. On the graph, particles of different densities are shown in a different color. Particle density ranges from 1020 to 1100 kg / m^3.

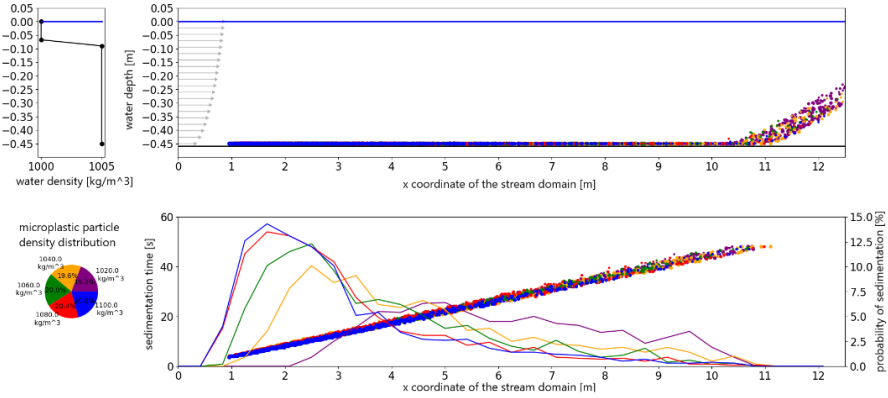

Figure 5. Results of the numerical model for t = 60 s

The particles with the highest density (blue color) precipitated the earliest, that's why their concentration is the highest in the first part of the spatial domain. The rest of the particles precipitated closer to the end of the spatial domain of the flow, which should be taken into account when defining the laboratory experiment in order to facilitate the monitoring of the results. Numerical results show the justification of the assumption about the possibility of spatial differentiation of particles through experimental analysis.

4. Conclusions

The paper briefly presents the global problem of microplastic accumulation in the environment, and especially in the seas and oceans. A presentation of some of the model tests of microplastic movement performed so far is given, and a numerical algorithm for the analysis of microplastic deposition in an open watercourse is proposed. The domain of the numerical model is given according to the parameters of the experimental channel located at the Faculty of Civil Engineering in Rijeka, and this choice is motivated by the planned experimental tests. The results of the numerical model confirmed the assumption about the possibility of spatial differentiation of the deposition of particles of different shapes. The proposed numerical model provides the possibility of modeling 3 dominant parameters that determine the dynamics of microplastic particle motion (density, size and shape). In the following research, it is planned to complete the development of the experimental channel and check the results of the model on real observations.

References

1. Europska komisija. (2021) *Komunikacija komisije europskom parlamentu, vijeću, europskom gospodarskom i socijalnom odboru i odboru regija*. Available from: https://eur-lex.europa.eu/resource.html?uri=cellar:2df5d1d2-fac7-11e7-b8f5-01aa75ed71a1.0004.02/DOC_1&format=PDF [Accessed 10. ožujka 2021].
2. Enders, K., Lenz, R., Stedmon, C. A.,Nielsen, T. G. (2015) Abundance, size and polymer composition of marine microplastics ≥10 μm in the Atlantic Ocean and their modelled vertical distribution. *Marine pollution bulletin.* 100(1), 70-81.
3. Sherman, P., Van Sebille, E. (2016) Modeling marine surface microplastic transport to assess optimal removal locations. *Environmental Research Letters*. 11(1), 014006.
4. Atwood, Elizabeth C., Falcieri, F. M., Piehl, S., Bochow, M., Matthies, M., Franke, J. (2019) Coastal accumulation of microplastic particles emitted from the Po River, Northern Italy: Comparing remote sensing and hydrodynamic modelling with in situ sample collections. *Marine pollution bulletin.* 138, 561-574.
5. Liubartseva, S., Coppini, G., Lecci, R., Creti, S. (2016) Regional approach to modeling the transport of floating plastic debris in the Adriatic Sea. *Marine pollution bulletin*. 103(1-2), 115-127.
6. Kooi, M.; Koelmans, A.A. (2019) Simplifying Microplastic via Continuous Probability Distributions for Size, Shape, and Density. *Environmental Science & Tehnology Letters*. Vol. 6, 551-557.

ISSN 0554-6397
Izvorni znanstveni članak
(*Original scientific paper*)

Šimun Sviličić
E-mail: ssvilicic@fsb.hr
Smiljko Rudan
E-mail: smiljko.rudan@fsb.hr
Faculty of Mechanical Engineering and Naval Architecture, University of Zagreb, Ivana Lučića 5, Zagreb, Croatia

Assessing the Compression Fatigue of the Welded Test Specimens

Abstract

The focus of this paper is on compression fatigue life in welded test specimen. Considered test specimen is highly complex due to multi-layer welding and production errors affecting its topology. Test specimen is made from S355 steel which is used for both base material and weld. Compression fatigue analysis is seldom performed as compression positively affects fatigue life. At the same time, during MAG welding residual stresses affect the fatigue life, decreasing it significantly. Finite element method (FEM) is applied to estimate compression fatigue life of the welded test specimen and obtained fatigue curve is compared to the experimental curve. Experimental curves are given for different stress ratios: R= -1, and R= -∞. Analysis consists of thermal and structural analysis using FEM method and fatigue analysis which is based on FEM results. FEM thermal simulation of welding with constant initial temperature is performed first and followed by nonlinear structural analysis for assessment of the residual stresses due to heat expansion. Fatigue parameters are determined using Universal slope method.

Keywords: compression fatigue, R ratio, MAG welding, residual stress, coupled thermal-mechanic, S355

1. Introduction

Extensive research is done for the analysis of tensile fatigue. At the same time, compression and its effects are usually not considered due to its beneficial influence on fatigue life. General rule is that compression closes crack, opposed to tension which opens it [1]. This is true for cases when only compression exist but in other cases, such as in welding, this statement is not valid. Here, physical effects exist that cause residual stress such as phase transformation and distortion of crystal surfaces due to

material melting. During welding, weld is contracting in all directions: longitudinally, transversely and through thickness. Longitudinal stress causes weld distortion inwards which consequently causes tensile transversal stress in the middle of the weld [2]. This effect can be seen in Figure 1.

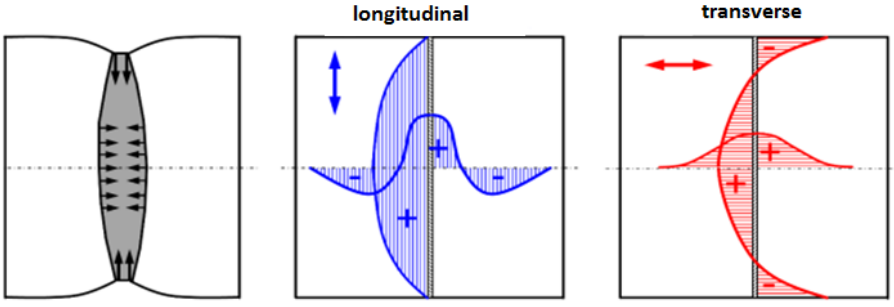

Figure 1. Weld stress [3]

Phase material transformation, volume of material, boundary conditions and geometry shape are critical variables which define residual stress. Influence of compressive, tensile, and residual stress is shown in Figure 2.

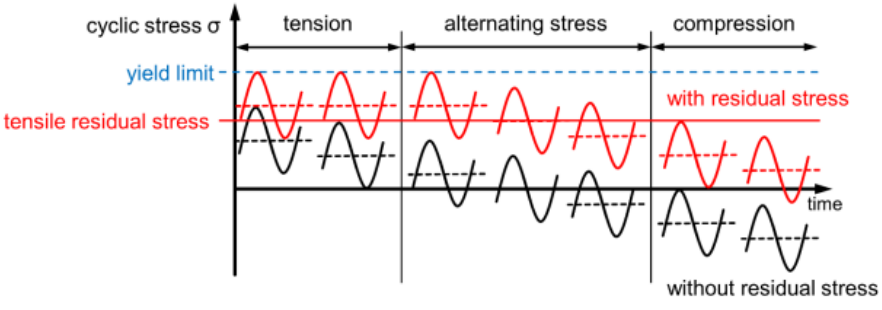

Figure 2. Influence of stress character on fatigue life [3]

Fatigue life is important parameter in designing a product, but it is hard to calculate it in real life due to many factors that influence it. Also, experimental tests are expensive, require a lot of time and resources so experimental data is often lacking. In order to investigate it more, Hamburg University of Technology conducted experiments on welded specimen submitted to alternating and compressive stress cycles, R= -1, and -∞ [4]. Test specimens were extracted from two different plates with different thickness, 25mm and 10mm respectively, with length of 250mm (both) and the width of 55mm. Dimensions of the test specimen are shown in Figure 3. During welding, U-profiles are welded on the sides so that additional deflection should not occur.

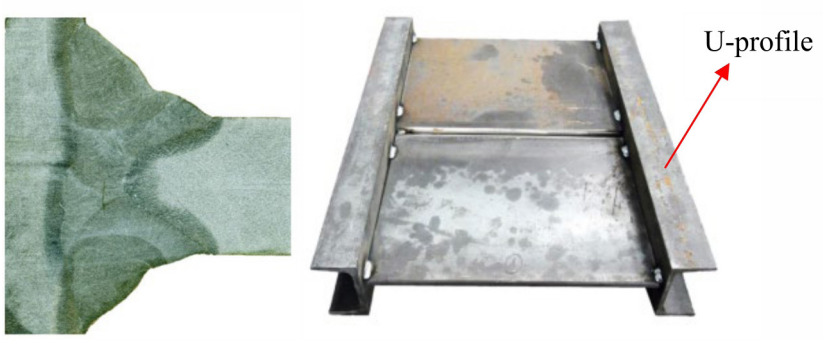

a) Test specimen *b) Set-up*

c) Dimensions

Figure 3. Test specimen [4]

Also, process of welding was monitored, and temperature measurements were done, Figure 4 [4].

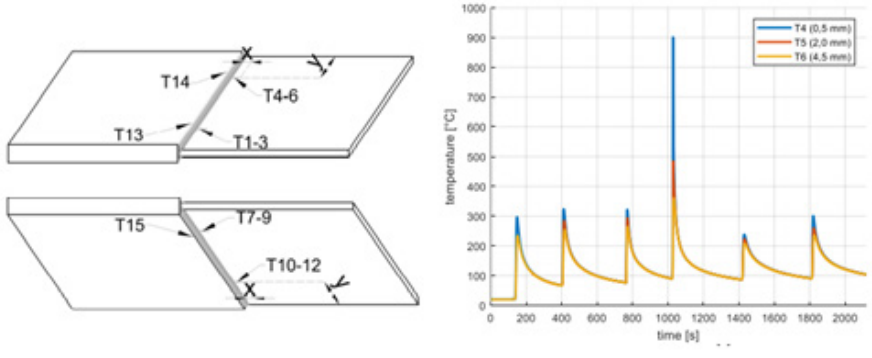

Figure 4. Thermal measurements [4]

Due to residual stress, test specimen is deformed and additional plates are introduced to minimize secondary bending during tensile test, Figure 5.

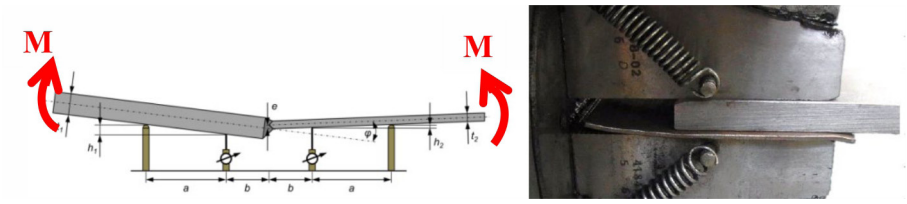

Figure 5. Test specimen deformation [4]

Residual stress is measured by two experimental methods: X-ray method and hole drilling method [3]. Hole drilling method is the most popular method for assessing residual stress [5]. Method has high variety of uses, such as in the analysis of tubular steel joints [6], or by combining it with digital image correlation for fatigue calculation [7]. For non-destructive test, X-ray method is the most popular, but accuracy is only valid up to several microns of depth [8].

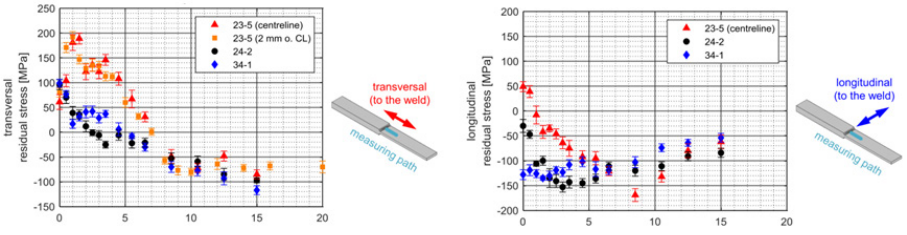

Figure 6. Residual stress [3]

There are numerous physical processes occurring during the welding (phase transformation, high thermal loads), so material properties can vary [9]. Due to uncertainty in material data properties, well known steel S355 was used [10] and metal active gas welding was chosen as a manufacturing process. Both plates and weld are made from the same already mentioned material. Fatigue calculations are commonly focused on the high cycle's fatigue, between 10^5 and 10^7 cycles while load amplitudes are constant. In the case of low cycle fatigue, calculations are based on the accurate plastic strain value which presume very accurate elastoplastic model [11]. In this work, elastoplastic model is not calibrated and tested so low cycle fatigue will not be in focus of research. Opposed to the low cycle fatigue, very high cycle fatigue with number of cycles $>10^7$ is not driven by the strain but instead by the stress. In the high cycle regime, additional factors such as surfaces treatment [12], surface integrity [13], inclusion size [14] and others are influencing the results. Even though these factors make more influence in the area of very high cycle fatigue ($>10^7$), they can start to influence around 10^6 cycle area, but this will not be covered in this article.

Goals of this research are:

- determine residual stress of the welded specimens due to high temperature and thermal expansion,
- compare residual stress values to measured values in [3],
- study influence of residual stress on the full compressive load and fatigue life in fully compressive load, R= -∞,
- compare fatigue curve obtained by numerical simulation with experimental one.

Results obtained by numerical calculation with FEM method will be compared to the experimental results done on Hamburg University of Technology [4].

2. Methodology

A methodology for fatigue life estimation based on FEM analysis using multiple ABAQUS solvers will be presented. Starting reference is the experimental test published in doctoral thesis [3] and results published by Maarstruct report [4]. Full simulation schematic is shown in Figure 7. Procedure is next:

1. First step is heat transfer analysis which consists of 12 steps: 6 steps for weld passes and 6 cooling steps in between each weld pass. Result of this analysis are nodal temperatures on the test specimen.
2. Second step is welding structural analysis: thermal expansion where nodal temperatures from previous step are applied to the identical structural mesh. Here, stress during welding is calculated due to thermal expansion.
3. A third step, structural analysis: tensile test is test where test specimen is subjected to tensile load with residual stress incorporated from previous step.
4. Last step is the fatigue analysis where stress field is transferred from structural analysis: tensile test to fatigue calculation software, FE-SAFE. Here, number of cycles until failure are calculated for every nominal load applied.

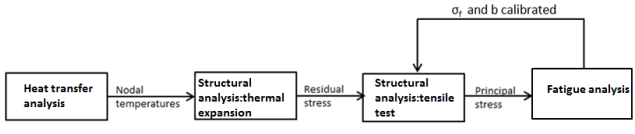

Figure 7. Schematic of simulation method

Despite the advanced approach presented, many variables could affect the accuracy of the results. Some of them are: material property data, manufacturing process deviations, symmetry condition, inadequate fatigue parameters etc. So initially, Basquin equation parameters are calibrated for R= -1 with less than 5% correction. Referent curve and corresponding loads are shown in Figure 8. After this, tensile test is done for full compression, R= -∞ by using fatigue parameters previously calibrated for R= -1.

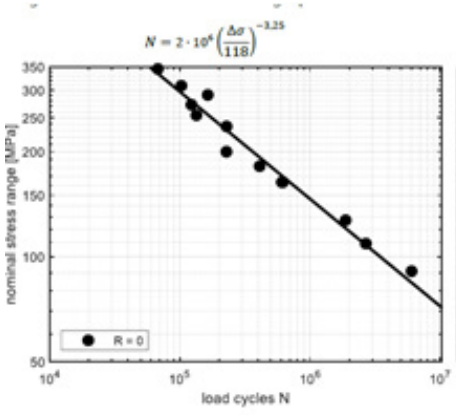

Fmin [kN]	Fmax [kN]	Nominal stress range [MPa]	Load cycles N
0	160	290,91	163830
0	150	272,73	122683
0	170	309,09	102600
0	190	345,45	67796
0	130	236,36	228488
0	110	200,00	227921
0	70	127,27	1874139
0	50	90,91	6023907
0	90	163,64	607880
0	60	109,09	2682988
0	140	254,55	134052
0	90	163,64	617751
0	100	181,82	409970

Figure 8. Reference experimental curve [4]

2.1. Heat transfer analysis

Heat transfer analysis solves heat generation problem in solids under thermal load. This solver can solve both steady state and transient cases. In welding simulation, only transient case should be considered due to variable heat input. Nonlinearities in this type of analysis comes from either nonlinear boundary conditions or from material properties that are temperature dependent. Nonlinearity from material properties is usually mild because properties do not change rapidly with the temperature. Formula for heat transfer analysis can be written through energy balance equation:

$$\int_V \rho \dot{U}\, dV = \int_S q dS + \int_V r\, dV \tag{1}$$

where V is a volume of solid material, S surface area, ρ is the density of the material, $\dot{U}$ is the material time rate of the internal energy, q is the heat flux per unit area of the body and r is the external heat source. Here, it is assumed that analysis is uncoupled in the sense that temperature of the material does not depend on strains and displacements of the body. Heat is inputted in the analysis through constant temperature method using "death and birth element" method. This means that analysis is introducing elements at a constant temperature which is equivalent to the melting temperature. In order to solve this, diffusive elements are used which allows heat storage and heat conduction. These elements only have temperature degrees of freedom. Output results are the nodal temperature. To define heat transfer analysis, data on conduction, convection, and thermal capacity should be provided [10].

2.2. Structural analysis

Structural analysis solves equation:

$$\left[K_T\right]\left\{\Delta u\right\} = \left\{F\right\} - \left\{F^{nr}\right\}, \tag{2}$$

where $[K_T]$ is tangent stiffness matrix, $\{\Delta u\}$ is displacement increment, is external load and $\{F^{nr}\}$ is internal force vector. Solver iteratively solves this equation based on Newton – Raphson method by gradually increasing load at each increment and calculates equilibrium equations. When equilibrium iteration is within specified tolerance, solver is continuing to the next increment. Maximum size of the increment is defined by the load amplitude input, in this case temperature. Incremental plasticity theory with isotropic hardening is used which defines post-yield behavior by defining true stress-strain diagram after yield. Plastic curves and thermal expansion coefficients are defined for this problem as temperature dependent [10].

2.3. Fatigue calculation

There are multiple ways and equations how to calculate fatigue and usage of them is based on assumptions, material, and recommendations. Here, calculations are based on the Basquin equation [15]. Since stress ratio is different than -1, mean stress effect exists. Brown Miller algorithm was used following the recommendations [16].

$$\sigma_A = \sigma_f^{'} N^b, \tag{3}$$

where σ_A is stress amplitude, N number of cycles, σ'_f and b are Basquin parameters. Output parameter is number of cycles until failure.

3. Results

Due to limited computational resources, total simulation time is reduced with factor of 2 by increasing air convection coefficient from standard 10 W/m^{2}K to 40 W/m^{2}K. Other parameters for heat transfer analysis are: conduction set to 45 W/m^{2}K and specific heat set up to 455 J/kg K at a room temperature. Width of test specimen, Figure 9, is reduced with the usage of symmetry boundary condition from 55mm to 27.5mm. Elements that are used for heat transfer analysis are second order hexahedral DC3D20 with average element size in each direction is 8mm and critical weld areas are locally refined. The melting temperature of the weld is 1450 ^{o}C. Focus during the meshing is on the weld and the critical area which is transition from the weld to the thinner plate.

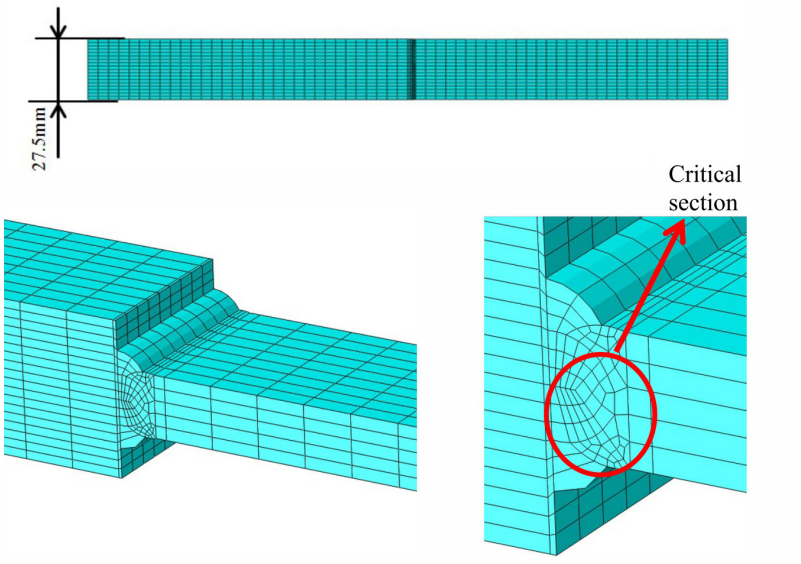

Figure 9. Test specimen dimensions and mesh (zoom on the right)

In Figure 10, temperature distribution is compared between actual measurement on the Hamburg University of Technology [4] and simulation measurement. Results are given for the same points, shown in Figure 4. Three points are measured on different locations: 0.5mm, 2.5mm and 5mm from the weld. Correlation of the results is excellent between measurement and reduced heat transfer simulation. With this, it can be said that increasing air convection coefficient α is justified.

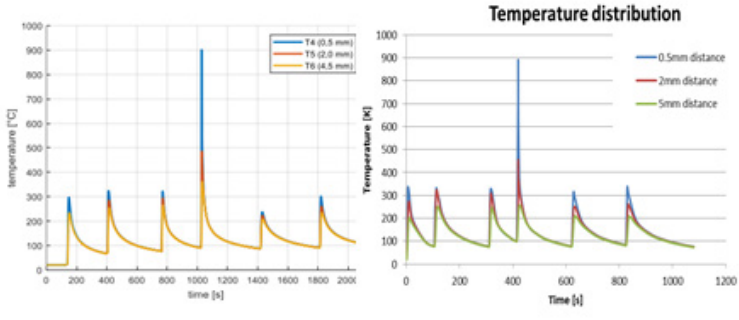

a) *b)*

Figure 10. Thermal distribution: a) measurement [4], b) simulation

Temperature results are applied on the compatible structural mesh. Boundary conditions are shown in Figure 11. For the heat transfer analysis, only symmetry boundary conditions are applied. For the structural analysis: thermal expansion, two additional nodes are constrained as shown in Figure 11 a). Reason why they are fixed is that in actual welding, additional U-profiles are spot welded on the side to prevent rotation and displacement of the plate in these sides (Figure 5). Without those additional boundaries, test specimen would freely rotate. For tensile test, only symmetry and fixation on the surface is used. Linear expansion coefficient is equal to 1.2

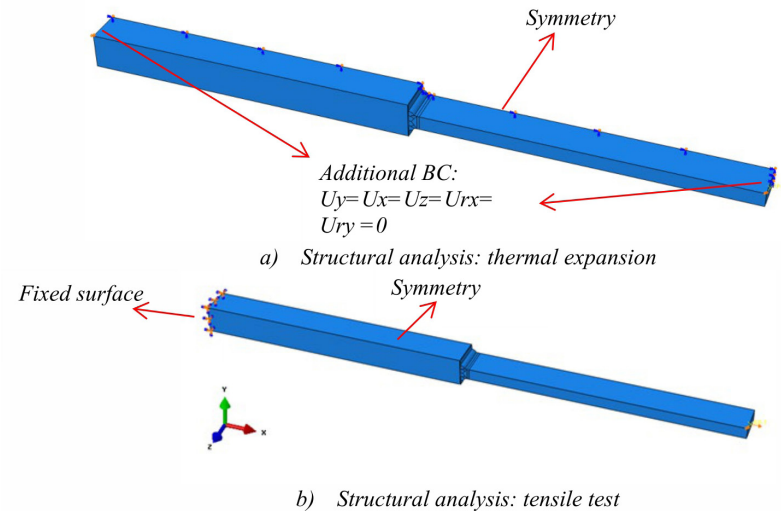

Figure 11. Boundary conditions

Simulation showed model angular deformation is similar to the test specimen angular deformation after welding (Figure 12). Test specimen is bending due to the thermal expansion [4].

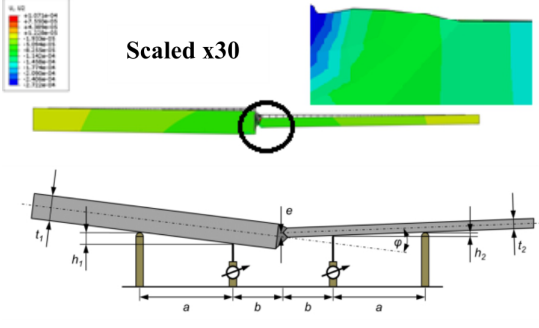

	Angular deformation [°]
Experiment	0.33
Simulation	0.304

Figure 12. Deformation after welding

Progression of plastic deformation during time is presented in Figure 13. Plastic deformation is occurring in different zones at a different time depending on the welding progress. This is causing asymmetrical plastic deformation and residual stress. It can be seen on Figure 13 that area with elements where Weld pass 1 is applied has much higher plastic strain than on the last Weld pass 6. Reason why is that even though largest percentage of plastic strain is caused during phase transformation and melting, neighboring welds are influencing development of plastic strain which is rising. Weld 1 does not experience only phase transformation during welding but also temperature increase during surrounding weld passes. On the other hand, Weld pass 6 is the last welding pass so it will only experience phase transformation.

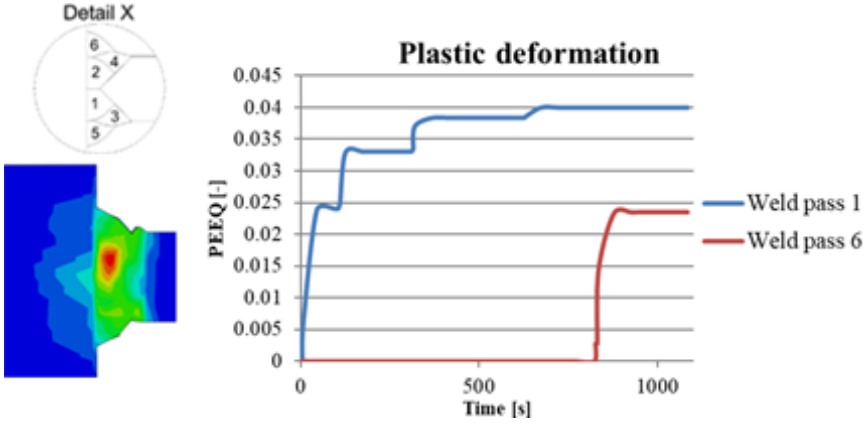

Figure 13. Plastic deformation zones

Longitudinal stress is shown in Figure 14 and it is compared with the measurement from [3]: both hole drilling and X-ray methods are compared with the simulation.

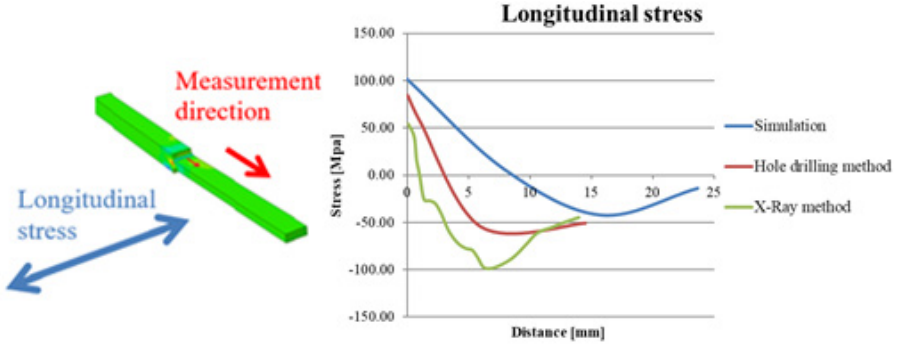

Figure 14. Longitudinal stress

Simulation differs from both measurement methods at the proximity of the weld and the gap is smaller away from the weld. Longitudinal stress is not critical in this case because it will not superimpose with the stress from tensile test.

Transverse stress is the most important as it has the same direction as the stress caused by the tension that will be applied afterwards. It can be seen in Figure 15 that results in proximity to the weld are extremely close, <2% difference, which is important because this is the location of critical section. Away from the weld, stress results differ which could be result of using the same material properties for heat affected zone and the rest of the specimen.

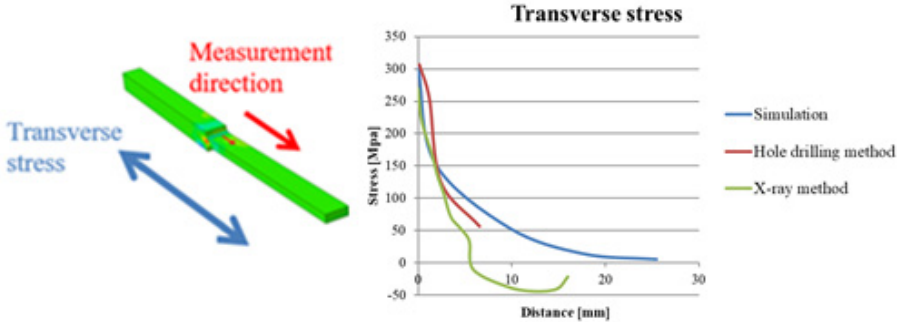

Figure 15. Transverse stress

Results given by FEM method are applied in the numerical software FE-SAFE for fatigue calculation. Fatigue life curve and corresponding cycles are calculated with the Basquin equation while Brown Miller algorithm is used for the mean stress correction. Plastic deformations are not used in fatigue calculation because they occurred only during welding and force used in tensile test is too low to cause further plastic strain increase. This means that plastic strain will not cycle but instead will have a constant value.

Values for fatigue parameters are initially calculated by Universal slope method (modified by Mason and Muarlidharan [17]).

$$\sigma_f^{'} = E \cdot 0.623 \left(\frac{\sigma_m}{E} \right)^{0.832} \tag{4}$$

$$b = -0.09 \tag{5}$$

where $\sigma'_f = 885$ and b= -0.09 are results from (4) and (5). Angular deformation is captured with FEM while linear misalignment will be applied as factor:

$$k_{m,e} = 1 + 3\frac{e}{t} = 1.033 \tag{6}$$

Linear misalignment is hard to physically model for small deformations, less than 1mm [18] but instead, it is usually implemented as a factor [19]. Also, it is shown that this is acceptable [20].

Initial results are calculated for the stress ratio of R= -1 and compared to the referent curve, Figure 8. Fatigue life calculations estimates 290000 cycles until failure for a nominal stress of 200 MPa. With this, small calibration of the Basquin parameters calculated by Universal slope method should be done. Only σ'_f is calibrated by a little margin, from 885 to 878. Second parameter, b which defines fatigue life curve slope was not calibrated.

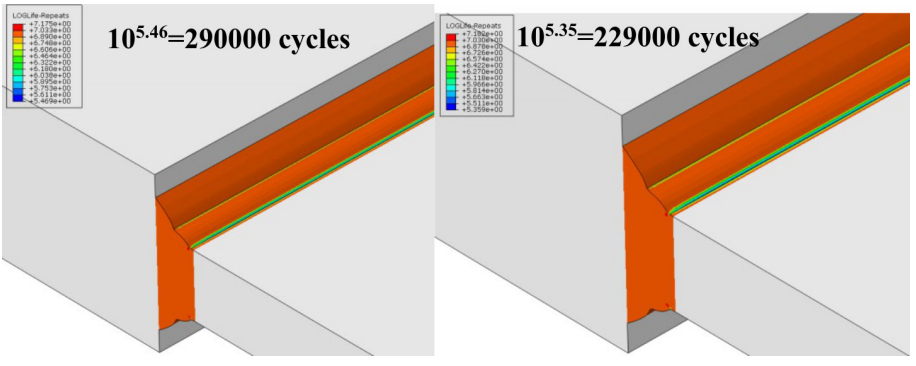

a) σ'_f *=885* *b)* σ'_f *=878*

Figure 16. Fatigue life calibration for R=-1: a) calculated σ'_f *and b) calibrated* σ'_f

Finally, results comparison for the full compression, R= -∞ are shown in Figure 17. It can be noticed that in lower area of fatigue, $<10^6$ cycles, results are close enough with the difference of 10%, but when going into area above 2 million cycles, results diverge significantly, >100%. Reason for this cannot be known without additional test of material properties and their dependency on temperature, surface treatment factors (having an increasing influence at higher number of cycles), etc. This is out of the scope of this article and could be done in future research.

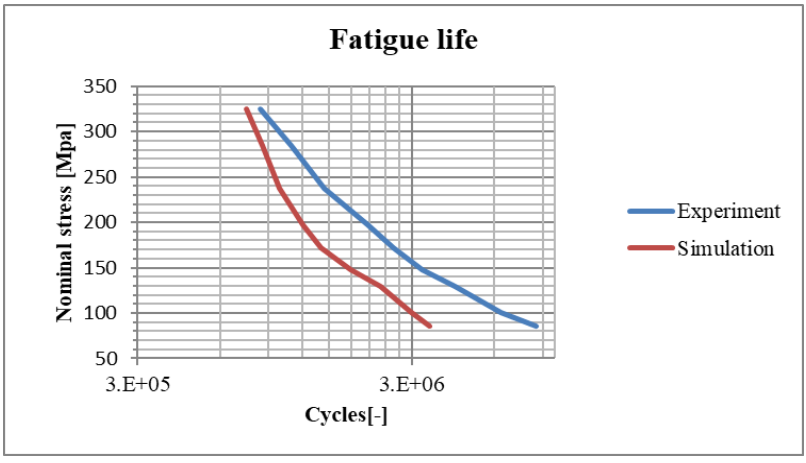

Figure 17. Comparison of the results for R= - ∞

4. Discussion

Deviation from experimental testing can occur from many different reasons. One of them is lack of fatigue data and repeatability of the test specimen testing. Second reason is control of manufacturing and geometrical sensitivity of the test specimen. Additional parametric study was done to test the sensitivity of results on the weld geometry. High discrepancy between maximum stresses in the case of local weld radius change was noticed. In the parametric study, nominal force of 160 kN was applied as a tensile force and two radii are changed: between Weld pass 4 and Weld pass 6 and between thinner plate and Weld pass 6. It can be seen that for a small change of radius, 0.0035 to 0.0045mm, stress can increase from 450 to 541 MPa which is over 20%.

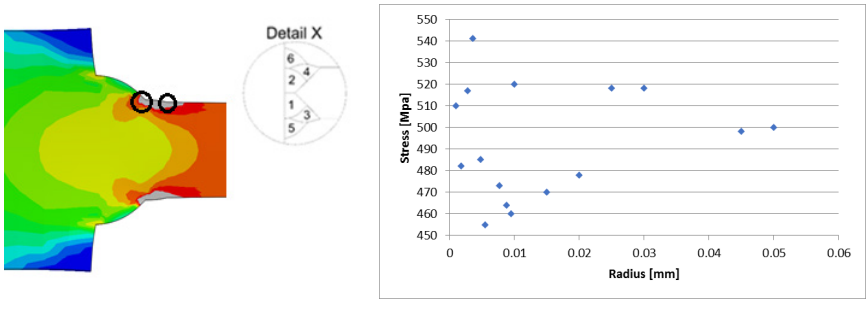

Figure 18. Geometrical sensitivity

Factors of surface treatment are not included in the analysis which can also lead to the wrong results in the higher fatigue area.

5. Conclusions

Compression fatigue calculation is presented in the paper.

Heat transfer analysis using constant temperature reached satisfactory results. Temperature measurement in experiment and simulation differ by less than 5% so it can be concluded that chosen material model with time reduction captures heat transfer behaviour correctly leading to correct analysis.

Structural analysis: thermal expansion, showed different results than those measured. Longitudinal stress showed rather high deviation from measurement, but transversal stress showed good fit close to the weld root. Away from the weld, results differ. It is suspected that heat affected zone is not adequately modelled or elastoplastic material model is not adequate. Further research should focus on modelling heat affected zone with different material properties and investigate elastoplastic model and its dependency on temperature.

Even with rather inaccurate longitudinal residual stress, fatigue analysis showed satisfactory results for less than 1 million cycles. Difference between simulation and experiment was in the range between 10 and 20 %. This is because transverse stress is more important, and it was much closer to the measurements. Higher number of cycles diverged from the testing with giving only half of number of cycles that experiment gave. This could be due to numerous reasons: beneficiary behaviour of multiple factors such as surface treatment on the fatigue life or limitation in fatigue algorithms for the analysis. Additionally, slope of the fatigue life curve which depends on the Basquin parameter *b* should be further calibrated.

Nomenclature

Abbreviations:

MAG	Metal active gas
FEM	Finite element method
SN	Stress-Number of cycles

Latin Symbols:

b	Basquin exponent (-)
$k_{m,e}$	linear misalignment factor (-)
N	number of cycles (-)

Greek symbols:

α	convection transfer coefficient (W/m^{2}K)
σ	stress (MPa)
σ'_f	Basquin parameter (MPa)
σ_m	mean stress (MPa)

Subscripts:

x longitudinal direction
y transverse direction
z thickness direction

6. References

1. Lietaert, K., Cutolo, A., Boey, D. & Van Hooreweder, B. (2018) Fatigue life of additively manufactured Ti6Al4V scaffolds under tension-tension, tension-compression and compression-compression fatigue load. *Scientific Reports.* 8, 4957. Available at: https://doi.org/10.1038/s41598-018-23414-2 [Accessed on 16. March. 2021].
2. Dev, A. & Saha, M. (2017) Ship Repairing Time and Labour. *MARTECH 2017; 12th Biennial International Conference and Exhibition Towards 2030: Maritime Sustainability through People and Technology.* Available at: https://ssrn.com/abstract=3753689 [Accessed on 16. March. 2021].
3. Friedrich, N. (2021) *Approach to consider welding residual stresses in fatigue analysis using numerical simulations*. Ph. D. Technischen Universität Hamburg.
4. Freidrich, N. & Ehlers, S. (2018) Fatigue life prediction of welds for different stress ratios R. *Marstruct*. Available at: http://www.marstruct-vi.com/marstruct2021/structure.aspx [Accessed on 3. March 2020].
5. Schajer, G. S. & Whitehead, P. S. (2018) *Hole-Drilling Method for Measuring Residual Stresses*. Synthesis SEM Lectures on Experimental Mechanics. Available at: https://doi.org/10.2200/S00818ED1V01Y201712SEM001 [Accessed on 20. March. 2021].
6. Van Puymbroeck, E., Nagy, W., Fang, H. & De Backer, H. (2018) Determination of residual weld stresses with the incremental hole-drilling method in tubular steel bridge joints. *Procedia Engineering.* 213, 651-661. Available at: https://doi.org/10.1016/j.proeng.2018.02.061 [Accessed on 21. March 2021].
7. Peng, Y., Zhao, J., Chen, L. & Dong, J. (2021) Residual stress measurement combining blind-hole drilling and digital image correlation approach. *Journal of Construction Steel Research*. 176, 106346. Available at: https://doi.org/10.1016/j.jcsr.2020.106346 [Accessed on 21. March 2021].
8. Lai, H. & Wu. W. (2020) Practical examination of the welding residual stress in view of low-carbon steel welds. *Journal of Materials Research and Technology*. 9(3), 2717-2726. Available at: https://doi.org/10.1016/j.jmrt.2020.01.004 [Accessed on 21. March 2021].
9. Winczek, J., Gawronska, E., Gucwa, M. & Sczygiol, N. (2019) Theoretical and Experimental Investigation of Temperature and Phase Transformation during SAW Overlaying. *Applied Science*. 9(7), 1472. Available at: https://doi.org/10.3390/app9071472 [Accessed on 23. March 2021].
10. Piekarska, W., Saternus, Z., Sapieta, M. & Kopas, P. (2020) Numerical and experimental analysis of a laser welded joint made of dissimilar materials S355 and 304 steel. *IOP Conference Series Materials Science and Engineering*. 776(1), 012075. Available at: https://iopscience.iop.org/article/10.1088/1757-899X/776/1/012075 [Accessed at 25. March 2021].
11. Zhang, J., Li, W., Dai, H., Liu, N. & Lin, J. (2020) Study on the Elastic–Plastic Correlation of Low-Cycle Fatigue for Variable Asymmetric Loadings. *Materials*. 13(11), 2451. Available at: https://doi.org/10.3390/ma13112451 [Accessed on 27. March 2021].
12. Song, Z., Gao, W., Wang, D., Wu, Z., Yan, M., Huang, L. & Zhang, X. (2021) Very-High-Cycle Fatigue Behavior of Inconel 718 Alloy Fabricated by Selective Laser Melting at Elevated Temperature. *Metals*. 14(4), 1001. Available at: https://doi.org/10.3390/ma14041001 [Accessed on 1. April 2021].
13. Fu, H. & Liang, Y. (2021) Study of the Surface Integrity and High Cycle Fatigue Performance of AISI 4340 Steel after Composite Surface Modification. *Metals*. 9(8), 856. Available at: https://doi.org/10.3390/met9080856 [Accessed on 2. April 2021].
14. Li, S. X. (2013) Effects of inclusions on very high cycle fatigue properties of high strength steels. *International Materials Reviews*. 57(12). 92-114. Available at: https://doi.org/10.1179/1743280411Y.0000000008 [Accessed on 2. April 2021].
15. Wen, X., Wang, P., Dong, Z., Liu, Y. & Fang, H. (2018) Nominal Stress-Based Equal-Fatigue-

Bearing-Capacity Design of under-matched HSLA Steel Butt-welded Joints. *Metals*. 8(11), 880. Available at: https://doi.org/10.3390/met8110880 [Accessed on 4. April 2021].
16. Barraza, J., Monarrez, M. R. & Molina, R. (2020) Fatigue-Life Prediction of Mechanical Element by Using the Weibull Distribution. *Applied Science*. 10(18), 6384. Available at: https://doi.org/10.3390/app10186384 [Accessed on 5. April 2021].
17. Muralidharan, U. & Manson, S.S. (1988) A Modified Universal Slopes Equation for Estimation of Fatigue Characteristics of Metals. *Journal of Engineering Materials and Technology*. 110(1), 55-84. Available at https://doi.org/10.1115/1.3226010 [Accessed on 5. April 2021].
18. Ottersböck, M.J., Leitner, M., Stoschka, M. & Maurer W. (2019) Analysis of fatigue notch effect due to axial misalignment for ultrahigh-strength steel butt joints. *Welding in the World*. 63(1). 851-865. Available at: https://doi.org/10.1007/s40194-019-00713-4 [Accessed on 7. April 2021].
19. Xing, S. & Dong, P. (2016) An analytical SCF solution method for joint misalignments and application in fatigue test data interpretation. *Marine structures*. 50(1). 143-161. Available from: https://doi.org/10.1016/j.marstruc.2016.07.006 [Accessed on 7. April 2021].
20. Taras, H. & Unterweger, H. (2017) Numerical Methods for the fatigue assessment of welded joints: Influence of misalignment and geometric weld imperfections. *Engineering Structures*. 9(1). 9-24. Available at: https://doi.org/10.3846/2029882X.2017.1299968 [Accessed on 7. April 2021].
21. Niesłony, A. & Böhm, M. (2013) Mean stress effect correction using constant stress ratio S–N curves. *International Journal of Fatigue*. 52. 49-56, Available at: https://doi.org/10.1016/j.ijfatigue.2013.02.019 [Accessed on 9. April 2021].

7. APPENDIX

Opposed to the complex study shown in the article, two other approaches were tried in order to see can the compressive fatigue be solved with less complex methods and possibly save significant amount of time.

7.1 Analytical approach

First approach is done by linear regression [21] which takes into the account mean stress correction:

$$N = 2 \cdot 10^6 \cdot \left(\frac{\Delta\sigma}{118}\right)^{-3.25} \tag{7}$$

$$\Delta\sigma_{eg} = \frac{\sigma_a}{1-\frac{\sigma_m}{R_m}} \tag{8}$$

where $\Delta\sigma$ is equivalent stress amplitude, R_m tensile strength, σ_m mean stress and N number of cycles. Here, Morrow mean stress correction is taken.

$$\frac{N_{R\neq-1}}{N_{R=-1}} = \frac{2\cdot 10^6 \cdot \left(\frac{\sigma_{a,R\neq-1}}{118\cdot\left(1-\frac{\sigma_{m,R\neq-1}}{R_m}\right)}\right)^{-3.25}}{2\cdot 10^6 \cdot \left(\frac{\sigma_{a,R=-1}}{118}\right)^{-3.25}} => N_{R\neq-1} =$$

$$N_{R=-1}\cdot\left(\frac{\sigma_{a,R\neq-1}}{\left(1-\frac{\sigma_{m,R\neq-1}}{R_m}\right)\cdot\sigma_{a,R=-1}}\right) \quad (9)$$

With this formula, mean stress effect is taken into the account so fatigue curves can be cone for different stress ratios R=-1, -∞ or different stress amplitudes

Disadvantages of this approach is that does not include any physical effect or any residual stress nor mean stress amplitude changes value with the change of load direction (tension/compression). Results approximated for R=-∞ are shown in Figure 19.

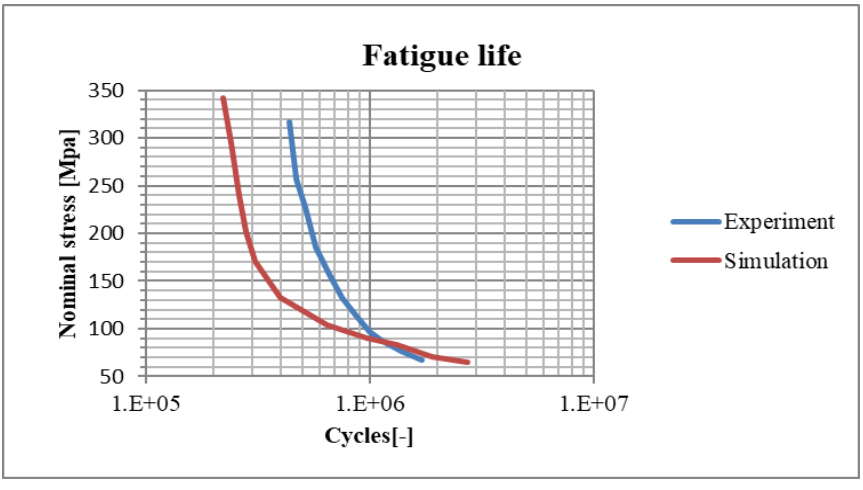

Figure 19. Fatigue curve for R=- with first approach

Results in Figure 19 show that the slope of the tested curve is completely different then the experiment and it will accurately predict only zone around 5 million cycles. Opposed to the experimental curve which has big slope due to residual tensile stress, curve gain by first approach is not showing this behaviour. This approach should not be regarded as valid.

7.2 Elastic approach

Second approach combines linear elastic FEM model by using second order hexahedral elements, C3D20 and fatigue calculation. Design of test specimen, Figure 8 is reversely engineered from the presented test specimen [4] and this will be used for calculation. Newly designed test specimen is shown in Figure 20.

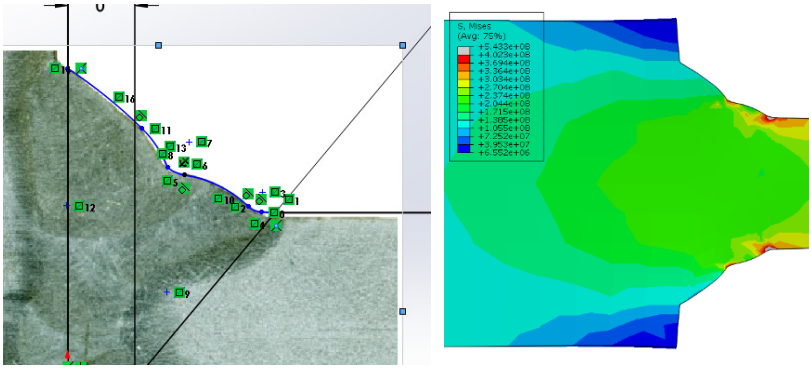

[3]

Figure 20. Reversible test specimen

Fatigue curve is first calibrated for the R= -1 curve and then it was used for R= -. For nominal stress of 200 MPa, maximum stress goes up to 400 MPa which leads to the stress concentration of 2. In order to get fatigue curve, fatigue parameters will need to be solved. For this fatigue area, Basquin equation is used so parameters that are calibrated are σ_f and b.

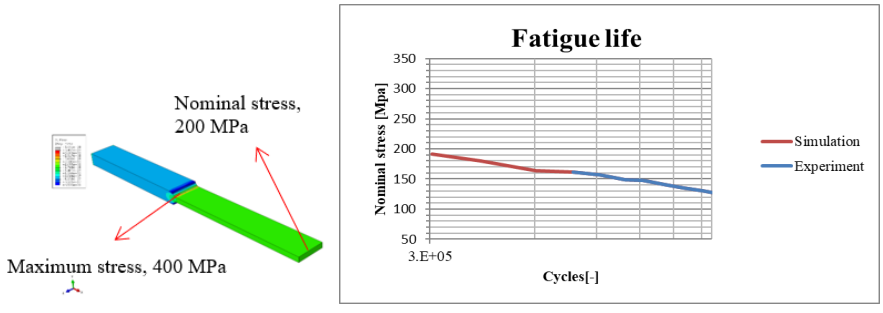

a) FEM model *b) Fatigue curves for R=-1*

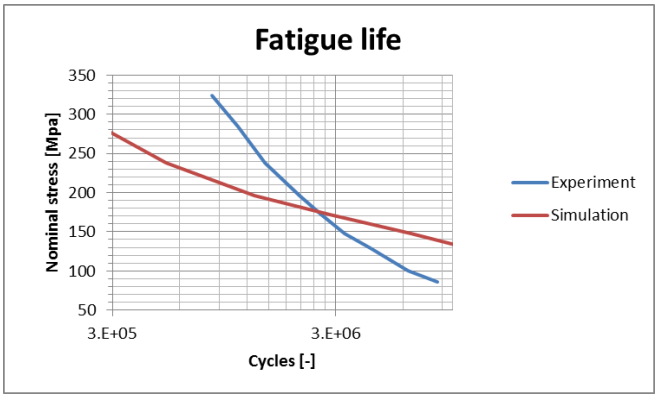

c) Fatigue curves for R= -∞

Figure 21. Second approach

Disadvantage of this approach is that no physical effect is model but instead, replaced with artificially increased value of Basquin parameters by calibrating it with reference R= -1 model. Curve shown in Figure 21 for R= -∞ is not accurately representing the fatigue live. For low cycle's fatigue, it is undervaluing the life and for higher cycles fatigue it is overvaluing the life. Again, reason behind this is that residual stress from welding is missing as a physical effect. This approach should not be regarded as valid.

ISSN 0554-6397
Prethodno priopćenje
(*Preliminary communication*)

Jerko Škifić
E-mail: skific@riteh.hr
Tibor Jaklin
E-mail: tjaklin@riteh.hr
Tehnički fakultet Sveučilišta u Rijeci, Vukovarska 58, 51000 Rijeka, Croatia

Weather Downtime Assesment for Complex Offshore Projects

Abstract

Analysis of the expected downtime in complex offshore operations is performed with metocean analysis of the area of interest which is then compared to the operative limits defined by installation analyses. The metocean conditions are commonly represented by seastate hindcast time series. On the other end, the operative limits can be defined as maximum allowable sea state, as well as the maximum allowable vessel motion. This paper presents the methodology to evaluate the operative weather downtime based on classical operative sea state limit.

Keywords: downtime analysis, offshore operations, operative limits

1. Introduction

Offshore operations and installations are exposed to harsh marine environment. Consequently, operations can be suspended which could put human safety or equipment at risk. This is particularly valid claim for many areas where adverse metocean conditions could be encountered even during statistically good season. In order to quantify expected downtime caused by environmental conditions, three classes of information need to be specified as accurately as possible:

- Precise sequence and duration of operations
- Operative limits for relevant operations and/or sequence of operations
- Metocean data

Furthermore, definition of realistic operation's sequence, suspension procedures and limiting criteria are crutial for reliable downtime estimate.

Operation characteristics and their precedence relationships should be meticulously specified during project planning phase.

Operative limits are commonly expressed in terms of maximal allowable wave height, but more detailed criteria have been developed in the last decade. This development was primarily driven by the task of reducing downtime by shifting the operative limit definition to vessel motion limiting criteria. That has proven to be effective in terms of more realistic downtime assesment compared to classical approach.

This paper presents the wheather downtime assesment methodology that uses metocean data defined either as long or synthetic hindcast time series. By comparing metocean data with operative limits, one can provide workability assessment for each step along the time series. Consequently, the downtime can be accumulated for any sequence of operations, and can be expressed with different occurrence probability.

2. Operative limits

Operative limit is defined as a combination of values of metocean parameters, that define the threshold below which the operation can safely advance.

Typically, they are expressed in terms of significant wave height H_s, frequently coupled with wave period T_p and direction. Furthermore, the limit can be defined as maximal allowable motion at relevant vessel's location e.g. stinger tip. Additionally, some operations may depend on additional limits, such as wind and ocean current limits, as well as the fog, ice coverage limits, to name a few. It is worth noting that in some cases, the operative limit can be expressed as a combination of multiple limits, vessel motion and wind limit, for example.

Most commonly, operative limit is defined as maximal allowable H_s values for predefined combination of peak period T_p and directions, obtained as result of:

- dynamic installation analyses performed for many different combination of significant wave height, peak period and direction relative to vessel's incomming direction
- dynamic analyses performed using regular wave theory with the maximum expected wave for a defined, spectral form [1], e.g. JONSWAP.

An example of those H_s limits that are results of the above analyses is given in Figure 1.

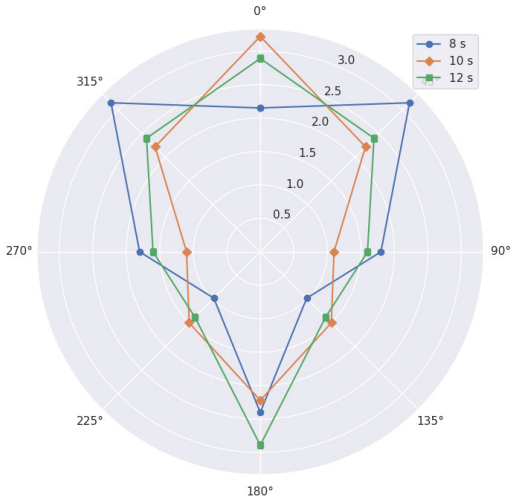

Figure 1 Limiting H_s for different peak period and incoming wave direction relative to the vessel

However, when crossed sea conditions are encountered, representative characterization of modeled environmental conditions cannot be obtained with above mentioned single collection of H_s, T_p and direction parameters [2]. In that case, a more appropriate approach requires the definition of a limiting motion for an operation, which then can be compared against a motion induced by an encountered sea state [2]. In this context, a limiting motion, lateral or vertical, refers to a relevant vessel location, and is defined as a single, or a combination of vessel motions: displacement, velocity, or acceleration.

Vessel's respond to the load of any possible sea state, can be calculated by using the Response Amplitude Operators (RAOs), which are usually provided to the vessel's Center of Gravity (CoG). They can be transferred to any vessel location P as

$$\begin{aligned} \hat{X}_P &= X_{CoG} + P_z\theta_y - P_y\theta_z \\ \hat{Y}_P &= Y_{CoG} - P_z\theta_x + P_x\theta_z \\ \hat{Z}_P &= Z_{CoG} - P_y\theta_x - P_x\theta_y \end{aligned} \tag{1}$$

where:

- X_{CoG}, Y_{CoG} and Z_{CoG} represent RAOs in complex notation for movements in X, Y and Z direction at the RAO center,
- P_x, P_y and P_z are the coordinates of the vessel location P relative to the CoG,
- θ_x, θ_y and θ_x are rotation angles around coordinate axes.

If the motion RAOs at the CoG is defined as

$$X_{CoG} = \bar{X}(\omega,\theta)e^{i(\omega t+\phi)} \tag{2}$$

where the $\bar{X}(\omega,\theta)$ denotes the vessel's motion amplitude due to a unit amplitude wave, i.e. magnitude of the response, ϕ stands for the phase shift relative to the wave, and ω represents the angular frequency, then it is easy to to calculate displacement, velocity and acceleration at any point *P*. For details, see [2].

3. Marine operations

As defined by Det Norske Veritas [3], marine operation is a *non-routine operation of a limited defined duration related to handling of object(s) and/or vessel(s) in the marine environment during temporary phases*. For the purposes of this article, the authors refer to an operation as an activity with prescribed net duration and a set of operational limits. It is worth noting that some types of operations require weather windows of a specific duration. Here, the term **weather window** [1] is defined as the time betweeen crossing of a threshold level for a metocean parameter or a set of metocean parameters and the next crossing of the same level. Complex offshore projects, depending on the scale and abstraction, can consist of hundreds of contiguous operations.

The operations can be considered *interruptible* and *non-interruptible*. That is, the execution of some an interruptible operation can be suspended at any time during its duration, if operative limits are not satisfied. The execution is then resumed when the environmental conditions allow are favorable (Figure 2). On the other hand, a non-interruptible operation must be carried out from start to finish without any delay (Figure 3).

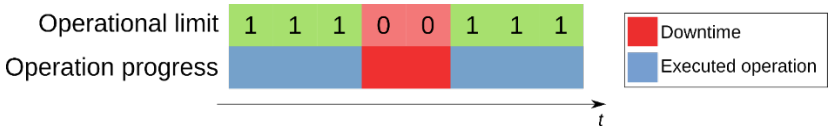

Figure 2 Example of an interruptible operation with downtime

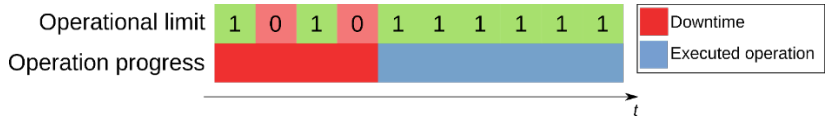

Figure 3 Example of a non-interruptible operation with downtime

Additionally, when dealing with complex projects, one has to take into an account precedence relationships, defined as a specific order in which the sequence of operations

are to be executed. Most commonly, two types of relationships are used within such a project:

- **Finish-to-Start**. This is the most common relationship used between operations. An operation B cannot start before the previous operation A hasn't ended. Here, an operation A is often referred to as an **uncoupled operation**, since the start of an operation B does not have to coincide with the end of the operation A.
- **Fixed Finish-to-Start**. Here, an operation B can only start immediately and directly after its previous operation A has ended. There cannot be any delay between the end of operation A and the start of an operation B. Not surprisingly, operation A is referred to as a **coupled operation**. More generally, one can view the sequence of operations A and B as a single operation with two different operative limits.

Figure 4 shows an example of marine project consisting of three operations, where three distinct operational limits assigned to each operation. Operations 1 and 2 are non-interruptible operations and Operation 3 is interruptible. Precedence relationship for Operation 1 and 2 is defined as Fixed Finish-to-Start, while relationship for Operation 2 and 3 is defined as Finish-to-Start.

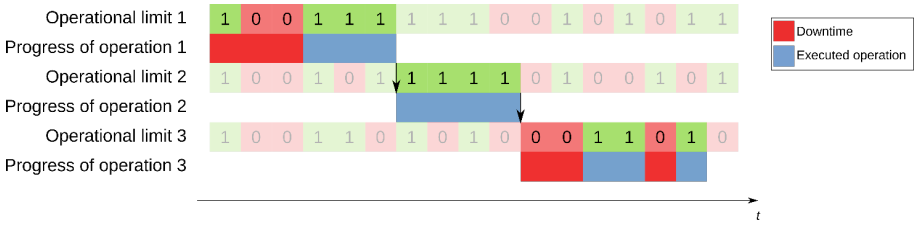

Figure 4 Example of sequence of marine operations with weather downtime. Operations 1 and 2 are non-interruptible operations, and Operation 3 is interruptible operation. Considering the precedence relationships, Operation 1 is a coupled operation, while Operation 2 is an uncoupled operation

Finally, when operation weather risk assessment is considered, the **Net Duration** (t_{ND}) of an operation is a deterministic measure defined as the time required for completion not taking into an account any delays.

Downtime (t_{DT}) is defined as a time during which an operation cannot proceed due to bad weather. **Total duration** is defined as a sum of **Net Duration** and **Downtime**, i.e:

$$t_{Total} = t_{ND} + t_{DT} \tag{3}$$

4. Hindcast time series

Nowadays, long hindcast metocean time series are available for any offshore area. Figure 5 shows an example of a significant wave height distribution per month while Figure 6 showns an example of a wave direction distribution for a specific month, both obtained for the same long hindcast time series. More precisely, Figure 5 displays distribution of significant wave heights for each month using density curves. It is worth noting that the width of each curve roughly corresponds with the frequency of data points in each month. Furthermorem the individual density curves are always built around center lines. As a consequence, density curves follow the exact same construction and interpretation. Additionally, the horizontal lines within each density curve correspond to quartiles.

Furthermore, hind cast time series typically include total sea states and their partitions. If such data can be considered representative of the metocean conditions, then the expected downtime calculations can be conducted by simulating operations' sequence for each metocean condition in hindcast time history.

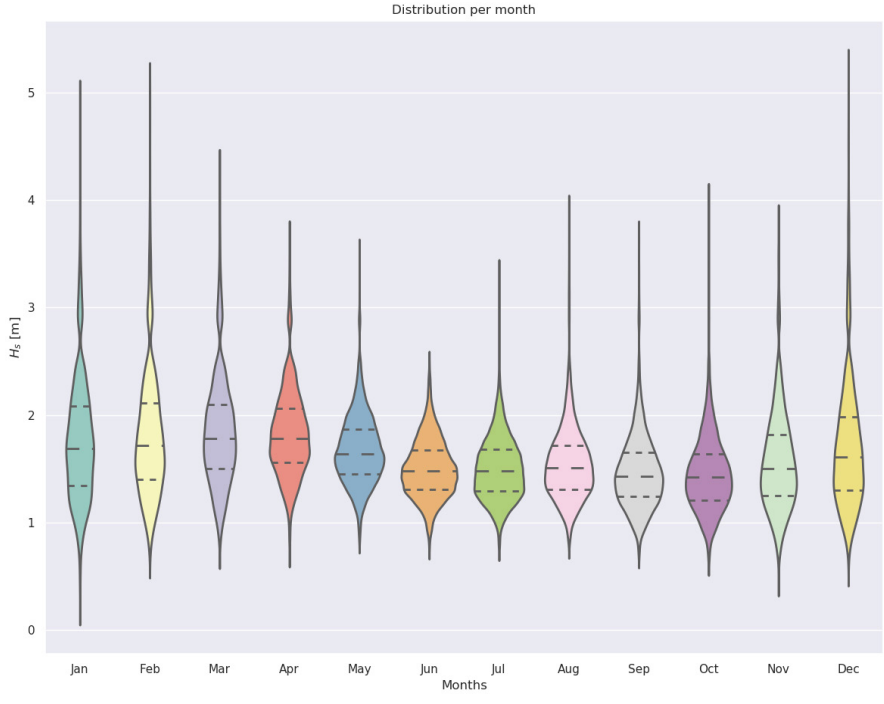

Figure 5 Example of a significant wave height distribution per month, obtained by a long hindcast time series

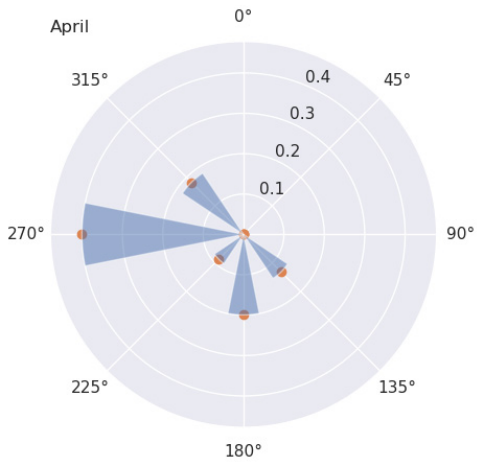

Figure 6 Example of a significant wave direction distribution for a specific month, obtained by a long hindcast time series

In some cases, recorded time series might not be long enough to guarantee statistically sane results. Or, the recorded time series doesn't contain sea states that have statistically significant occurence probability. Then, one needs to resort to generation of synthetic time series of metocean conditions with desired statistical properties. A number of models are developed, such as Box Jenkins model, Block resampling, Copula model, univariate and multivariate Markov chain models, to name a few.

Most models are designed to model up to two metocean parameters, which can be a decisive limiting factor, especially when dealing operative limits that need multiple parameters, e.g. motion limits in crossed sea conditions. However, those models provide a valuable tool for weather downtime analyses, especially in cases where operations strongly depend on temporal sequence of waves, e.g. heavy lift operations depend on the occurence of weather windows with very strict operative limits. In that case, it is common practice to generate synthetic time series at various temporal scales [4].

Usually, Markov chain models are applied to univariate metocean parameters, and are proven to properly reproduce main statistical properties, e.g. operative weather windows [10]. However, since the sea state conditions are inherently multivariate dependent phenomena, multivariate Markov models should be considered more appropriate [5]. Additionally, models using copulas are used to create realistic environmental time series by taking into an account abovementioned multivariate properties and the observed autocorrelation [6]. Copulas allow construction of model which avoid restriction imposed by models which describe pairwise families of bivariate distribution characterized by the same parametric family of univariate distributions. It is then possible to construct joint distribution requiring only marginal distributions of variables and their measures of dependence [6].

5. Weather downtime analysis

Although there exist a number of numerical methods dealing with weather downtime analysis [7], this paper will focus on an analysis by workability assessment for every time step of available hindcast time series. At this point it is of no significance if the defined hindcast time series is synthetic or not.

For this kind of analyses, compared to the synthetic time series', the long hindcast time series' are preferred. They can provide information for as many metocean parameters, and, in principle, can provide a more realistic assessment of real operative conditions, e.g. delays caused by pipe lowering and recovery.

Namely, for each time step of the time series and for each operation, one needs to establish if the sea state condition exceeds or not the operative limit. And at this point, it makes no difference if the operative limit is defined as a motion limit, limiting wave height, wind speed, or any combination of different limits, e.g. vertical displacement at the stinger tip and wind speed.

The algorithm creates a matrix of boolean values for every step of time series and for every operation, as it is shown in Table 1.

Table 1 Computed workability for each time step and each operation.

Time step	Operation 1	Operation 2	Operation 3	…	Operation N
Step 0	1	0	1	…	1
Step 1	1	0	1	…	0
Step 2	0	0	1	…	0
Step 3	0	1	0	…	0
…	…	…	…	…	…
Step N-1	1	1	0	…	0

When dealing with simple operative limits, such as wind speed coupled with or without direction, or maximal allowable wave height coupled with wave period and direction, the computational cost to determine the workability is small. One only needs to compare metocean parameters given in each time step with parameters defined in operative limit, taking into an account direction relative to vessel's heading.

On the other hand, motion limits require quite a bit of computational effort. First off, the motion estimate can be calculated by using:

- Total sea state (H_s, T_p),
- Sea state components (H_{si}, T_{pi}), where the index i denotes the i-th sea state component, and,
- Full 2D spectrum

Hindcast time series always provides the total sea state. However, its use is equivalent to that of an H_s limiting criterion. On the other hand, sea state partitions,

if available, provide more accurate description of the observed sea state conditions. Finally, the full 2D spectrum, if available, currently provides the most accurate information about the sea state condition. However, the use of this information comes at the significant computational cost [2], compared to previous levels of information available in the hindcast time series.

From the computational point of view, the approach that uses sea state partitions is considered as an optimal choice.

When operative motion limits are considered, it is necessary to presume a spectral form for an observed time series. Then, the resulting moments for any sea state spectrum described by the sum of wave partitions can be represented as the sum of the moments of the spectrum for each partition [2].

Since the moments are proportional to the square of the H_s, spectral moments can be calculated for sea states with H_s =1 m for all directions and suitable range of wave periods T_p and peak enhancement factors of the spectrum. Here, the JONSWAP spectrum is a reasonable choice, since, according to its formulation, a [8], its peak enhancement factors are a function of H_s and T_p. The result is the spectral moment expressed as a a function of wave period T_p and direction for different peak enhancement factors and moment orders. More conveniently, spectral moments are calculated for preselected periods T_p, directions and peak enhancement factors and saved as series of tables. For any possible combination of wave partitions appearing in the hindcast time series, the algorithm needs to select the appropriate table for each component and multiply the selected moment value with the square of the partition's Hs and sum the moments, which results in the moments of the resulting spectrum. For details, see [2]. Finally, the workability can be calculated by comparing the obtained result with the defined operative limit.

Large projects can consist of hundreds of operations, and, for long hindcast time series with typical time step, the workability matrix can be quite large. However, since the matrix consists of boolean values only, the actual computer memory size is quite small.

When the workability matrix has been populated, and the start of the project has been selected, all it takes is to step through time steps of the workability matrix and sum downtimes for each operation. This procedure is then repeated for each year in the workability matrix (Table 2). This approach provides, besides an average downtime, possible spread around the average which can be expressed on percentiles or as a standard deviation [9], as shown in Figure 7.

The algorithm needs to properly take into an account each operation's characteristics. For example, the sum of downtime values for non-interruptible operation include time steps where the workability is satisfied if the number of favorable consecutive time steps does not exceed the nominal duration of that operation. Additionally, Fixed Finish-to-Start precedence relationship can have a significant impact on the downtime. Finally, when dealing with pipe laying operations, one needs to take into an account the time necessary for pipe abandonment and recovery in order to properly assess downtime.

Table 2 Duration and standby for a specific project start date

Year	Total Duration (days)	Standby (Days)
1990	59.515	7.895
1991	52.355	0.735
1992	77.57	25.95
1993	52.615	0.995
1994	53.96	2.34
1995	58.705	7.085
1997	59.495	7.875
1998	59.24	7.62
1999	59.785	8.165
2000	60.91	9.29
2001	55.66	4.04
2002	63.11	11.49
2003	56.275	4.655
2004	59.83	8.21
2005	54.995	3.375
2006	56.4	4.78
2007	64.075	12.455
2008	63.995	12.375
2009	58.21	6.59
Mean	**59.3**	**7.68**

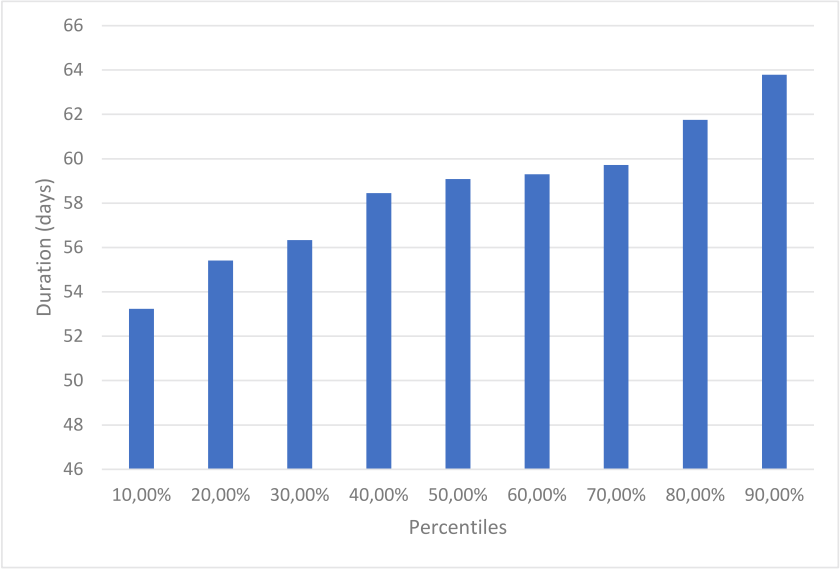

Figure 7 Calculated total duration percentiles for a specific project start date

Finally, the above procedure can be repeated for different project start dates (Figure 8), which can potentially reduce potential costs of installation project.

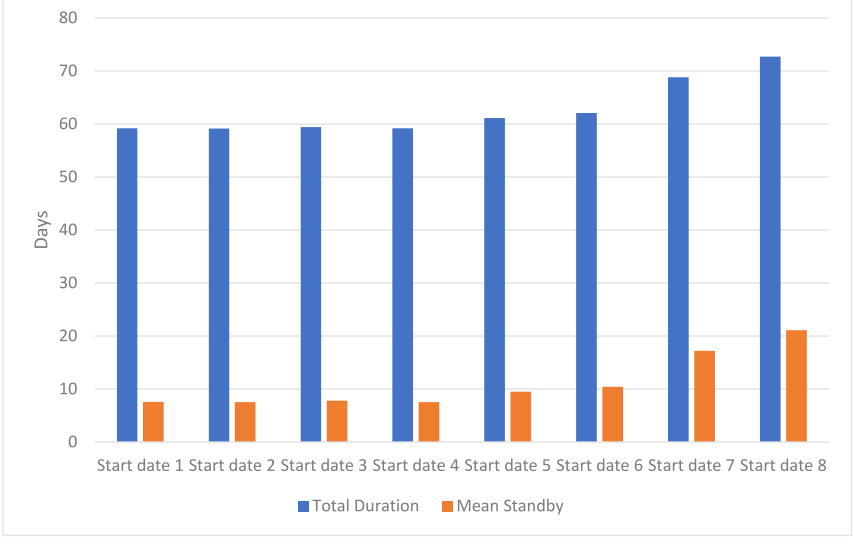

Figure 8 Calculated mean total duration and standby for preselected project start dates

6. Conclusion

Complex offshore projects require careful wheather downtime assesment, especially during early engineering phase. Wheather downtime estimated by stepping for each step of long hindcast time series has been described. The results obtained with such an algorithm have been proven to produce reallistic downtime values in real projects. In order to efficiently and reliably use this algorithm, precise operation's characteristics, along with operative limits should be defined. One has to take into an account that, if available, operative limits expressed as motion limits used in conjuction with wave partitions should produce more realistic results compared to simpler, classical representation of operative limits.

7. References

1. Det Norske Veritas, Modelling and Analysis of Marine Operations, Det Norske Veritas, 2013.
2. M. Drago, A. del Guzzo, L. Vitali i R. Bruschi, Weather Stand-by Assessment in Offshore Operations Using Motion Limit Criteria, *The 27th International Ocean and Polar Engineering Conference* , San Francisco, 2017.
3. Det Norske Veritas, Marine Operations, general, DNV-OS-H101,« Det Norske Veritas, 2011.
4. G. de Masi, R. Bruschi i M. Drago, Synthetic metocean time series generation for offshore operability and design based on multivariate Markov model, *OCEANS*, Genova, 2015.
5. B. Hagena, I. Simonsena, H. M. i b. M. Muskulus, A multivariate Markov Weather Model for O&M Simulation of Offshore Wind Parks, *Energy Procedia,* svez. 35, pp. 137-147, 2013.
6. G. Leontaris, O. Morales-Nápoles i A. Wolfert, Probabilistic scheduling of offshore operations using copula based environmental time series, *Ocean Engineering,* pp. 328-341, 2016.
7. Bruijn W. E. L. et al., Probabilistic downtime estimation for sequential marine operations, *Applied Ocean Research*, 86:257-267, 2019.
8. Det Norske Veritas, Environmental Conditions and Environmental Loads, RP-C205_2014-04, Det Norske Veritas, 2014.
9. M. Drago i M. Venturi, Probabilistic evaluation of performance and weather stand-by in offshore pipeline laying, *Proc. IMCA annual seminar*, New Orleans, Louisiana, 2011.
10. K. Anastasiou, C. Tsekos, Operability analysis of marine projects based on Markov theory*, Applied Ocean Research* 01/1996; 18(6):329-352, 1996.

ISSN 0554-6397
Prethodno priopćenje
(*Preliminary communication*)

Marin Smilović
E-mail: marin.smilovic@riteh.hr
Roko Dejhalla
E-mail: roko.dejhalla@riteh.hr
Faculty of Engineering, University of Rijeka, Vukovarska 58, HR-51000 Rijeka, Croatia

Preliminary Design of a Ship for Waste Sorting from Croatian Islands

Abstract

In the Environmental Protection Strategy of the Republic of Croatia, waste management is defined as a national priority, and the vision is a landfill-free concept. The backbones are recycling centers with sorting plants where separately collected waste will be prepared for recycling. Concept of sustainable development is a key determinant of the development of the Primorje-Gorski Kotar County (PGKC), and the fact that permanent disposal of waste of any kind will not be possible on the islands is particularly important for this County. Mixed municipal waste generated in PGKC should be first sorted at the local transshipment station on the island, and then transported by road to the county center for waste management, which is an expensive and complex process. Given that sea transport is known to be the cheapest, one possible solution would be to place a waste sorting plant on a suitable ship which would collect waste by sailing around the island, thus avoiding the need for each island to have its own sorting plant. The paper presents a preliminary design of a ship for sorting waste collected from the large islands of PGKC. The mission requirements of the ship were elaborated initially, and then a basic design of the ship was made, accompanied by the corresponding naval architecture calculations, general arrangement plan and outline specification.

Keywords: Croatian islands, waste management, ship for waste sorting, preliminary design

1. Introduction

There has been a lot of talk and writing lately about the “circular economy”, which by definition is a model of production and consumption that includes sharing, borrowing, reusing, repairing, rebuilding, and recycling existing products and materials to extend product life, and at the same time reduce the amount of waste. Circular economy strategies can have a strong impact on reducing greenhouse gas emissions and thus play a key role in combating climate change.

The circular economy is also one of the goals of the European Union (EU), which is why the European Commission presented an action plan in March 2020 [1]. The plan includes proposals for more sustainable product design, waste reduction and citizen empowerment, for example by introducing "rights to repair", with an emphasis on areas such as electronics, information and communication technology, batteries and vehicles, packaging, plastics, textiles, construction and food, water and nutrients. Basically all products from these areas require huge amounts of resources. In February 2021, the European Parliament voted on a new circular economy action plan and called for additional measures to achieve a carbon-neutral, environmentally sustainable, non-toxic and fully circular economy by 2050, including stricter recycling rules and binding targets for the use and consumption of materials by 2030. Members of the European Parliament called on EU member states to increase high-quality recycling, move away from landfills and keep incineration to a minimum.

The goal of the European Union and its waste policy is to move towards a circular economy. Its task is greater sustainability and contribution to the achievement of climate goals changing and conserving the world's resources, creating local jobs, all for the purpose of giving Europe an edge over the competition in the world. The importance of the circular economy for the European industry has recently been highlighted in the renewed EU industrial policy strategy. The transition to a circular economy will also contribute to achieving the goals of the Sustainable Development by 2030 [2].

In the paper, the situation with waste in the EU and Republic of Croatia is briefly discussed, while a stronger focus was given to the aspects of collection of waste from the large islands of the Primorje-Gorski Kotar County (PGKC). As a possible solution for the disposal of waste from large islands of this County, specially designed ship was considered. Initially, the mission requirements of the ship were elaborated, and then a preliminary design of the ship was made with the accompanying naval architecture calculations, general arrangement plan and outline specification. In that way, the need for each island to have its own plant for waste sorting could be avoided.

2. Waste management in the EU

The European Union produces more than 2.5 billion tonnes of waste each year. On July 4, 2018, new EU rules came into force with legally binding targets for waste recycling and waste reduction with fixed deadlines for EU member states that had to adapt their national legislation for the transition to circular waste in the next two years. Republic of Croatia was obliged to incorporate waste directives into its legislation by July 5, 2020. The foundations of EU waste management policy are contained in the Council of Europe Resolution on the Waste Management Strategy (97/C76/01) [3], based on the Waste Framework Directive (74/442/EEC) and other EU waste management regulations [4]. Five basic principles have been established: waste management hierarchy, self-sufficiency of the disposal plant, best available technology, proximity to waste disposal and producer responsibility.

From 2005 to 2016, the average amount of waste per capita fell by 7% in the EU, but there are significant differences between countries. Richer countries and countries engaged in tourism produce more waste. Thus, the amount of waste is growing in Denmark, Germany, Greece, Malta and the Czech Republic, and falling in Bulgaria, Estonia, Hungary, Romania and the Netherlands. In absolute values per capita, the first are Denmark, Malta, Cyprus and Germany while the Czech Republic and Slovakia produce the least waste. Denmark, for example, produces 777 kilograms of municipal waste per capita, while Croatia produces 403 kilograms. But in Denmark only 1% of municipal waste ends up on landfill while in Croatia that share amounts to 78%. In Croatia, only 21.5% is recycled and 0.1% is incinerated. According to 2016 statistics, 47% of municipal waste in the EU is recycled and composted [5]. However, practices vary between countries and many EU member states still use underground disposal for municipal waste. Underground disposal is almost non-existent in northern and western Europe (Belgium, the Netherlands, Sweden, Denmark and Germany), but as many as 12 countries dispose of more than half of their waste underground. Along with Latvia, Slovakia and Bulgaria, Croatia is above 60%. Textiles and hazardous waste from households will have to be collected separately by 2025. By 2024, bio-waste will also be collected separately or recycled at home by composting. In line with the UN Sustainable Development Goals, EU member states should aim to reduce food waste by 30% by 2025 and by 50% by 2030. In order to prevent food waste, EU member states should encourage the collection of unsold food products and their further redistribution [5].

3. Waste management in the Republic of Croatia and Primorje-Gorski Kotar County

The waste management strategy in the Republic of Croatia was adopted in 2005 with the purpose of establishing a framework within which the amount of waste generated will have to be reduced, and at the same time managed sustainably [6]. The Strategy is an integral part of the National Environmental Strategy adopted in 2002 [7], in which waste management is identified as a national priority. The idea of waste management in the Republic of Croatia is the so-called a landfill-free concept aspired to as an ideal. The Strategy and Waste Management Plan of the Republic of Croatia as its implementation document are part of the continuous waste management planning that is reflected at all levels, from national to local.

The backbone of the Waste Management Plan in the Republic of Croatia are recycling yards, recycling centers with sorting plants and composting plants where separately collected waste will be prepared for recycling.

Some of the most important measures are the encouragement of separate collection of paper, cardboard, metal, glass, plastic and bio-waste, separate collection of waste on the doorstep, introduction of incentive measures in the collection of public municipal waste collection service by composition and quantity, introduction of municipal waste

disposal fee, home and municipal composting, construction of sorting plants, IT support for monitoring waste flow and a number of educational and informative measures [8].

The concept of sustainable development is a key determinant of the development of the Primorje-Gorski Kotar County (PGKC) and its implementation in the field of waste management is given special attention. The solution to the problem of waste in PGKC consists of the establishment of a single county center for waste management (CWMC) on Marišćina in the municipality of Viškovo near the city of Rijeka, with the establishment of a network of recycling yards and transshipment stations and remediation of unregulated and inappropriate landfills throughout the County. According to the current legislation, the local self-government unit must close the landfill within one year from the day of the official commissioning of the CWMC, after which all unsorted waste would be taken to the county landfill [9, 10]. The adopted approach is fully in line with the Waste Management Strategy of the Republic of Croatia [5], and the fact that in the future permanent disposal of waste of any kind will not be allowed on the islands is particularly important.

The group of large islands in PGKC makes the islands of Cres, Lošinj, Krk and Rab. In the area of the islands of Cres and Lošinj, as well as the surrounding smaller islands (Susak, Ilovik, Unije, Srakane), the municipal activity of collecting, transporting and handling municipal waste is performed by the city company "Komunalne usluge Cres Lošinj d.o.o." [11, 12]. The collected municipal waste is disposed of at the Prižić (Cres) and Kalvarija (Lošinj) landfills. The company's most significant investment in the field of waste management is the rehabilitation of the Kalvarija municipal waste landfill in Mali Lošinj, with the construction of a transshipment station, recycling yard and composting plant and the rehabilitation of the existing waste disposal area.

Utility company "Ponikve eko otok Krk d.o.o." is an example of responsible municipal waste management [13]. Thanks to a well-thought-out strategy and systematic long-term implementation, the company has not only achieved the goals set by the Croatian Waste Management Plan, but also greatly exceeds the average recycling of municipal waste achieved at the EU level. The company manages the Treskavac landfill located in the Municipality of Vrbnik. All municipal waste from the area of the island of Krk is brought to this landfill, and next to the landfill there is a recycling yard, sorting hall and composting hall where separately collected waste is additionally separated, pressed and baled as well as composted. The sorting plant was delivered by the domestic manufacturer Tehnix d.o.o. from Donji Kraljevec, Croatia, [14]. The sorting plant was needed because it is simply not possible to separate waste so well in households that it would be immediately ready for further marketing.

On the island of Rab, the collection, transport, disposal, trading and mediation in waste management are performed by the companies "Dundovo d.o.o." (City of Rab) and "Lopar Vrutak d.o.o." (Municipality of Lopar) [15]. The Sorinj landfill is an officially unregulated landfill for non-hazardous waste, to which waste collected from the area of the City of Rab and the Municipality of Lopar has been disposed since 1969. Considering the legal regulations, the stability of the disposed waste and the impact that

the disposed waste has on the environment, the local self-government units on Rab are aware that it is necessary to rehabilitate and close the Sorinj landfill as soon as possible, which must be coordinated with location, i.e. with the beginning of waste acceptance from the area of the City of Rab and the Municipality of Lopar at CWMC Marišćina.

4. Design of a ship for waste sorting

Since the CWMC Marišćina has started operating, all utility companies from PGKC are obliged to dispose of their mixed municipal waste there. If the issue of waste on the large islands in the PGKC is considered, unsorted municipal waste should first be accepted and disposed of at the local transshipment station on the island (if any), then loaded on a truck and taken to CWMC Marišćina. Since these are islands, road transport is expensive and complex. In addition, waste disposal at the waste management center is paid per tonne of waste, and it can be expected that the price will increase over time, so this could be one of the additional motives for sorting waste on the island and significantly reducing the amount of waste which has to be transported.

Since the maritime transport is well known as the cheapest among the available transport possibilities, one of the possible solutions would be to place a waste sorting and baling plant on a purpose-built ship. The ship would call the ports on the islands, collect waste and then process it. This would avoid the need for each island to have its own sorting plant, and at the same time would greatly reduce the need for truck transport from the island. This was the main idea for the development of a preliminary ship design for the sorting of mixed municipal waste from the Croatian islands, with special consideration being given to the islands of Cres, Lošinj, Krk and Rab. The ports of calls of the ship would be the ferry port Valbiska on the island of Krk, Lopar and Mišnjak as the main and alternative port on the island of Rab, Merag on the island of Cres and the port in Mali Lošinj. Apart from the islands in PGKC, the ship could also collect and sort mixed municipal waste from other Croatian islands throughout the year.

The mission requirements of a ship were initially elaborated, and then a preliminary design of a ship was prepared with the corresponding naval architecture calculations, general arrangement plan and outline specification. The design itself is specific because there are no similar ships in the world with a plant for sorting and baling mixed municipal waste. The purpose of the ship would be to sort municipal waste without a biodegradable component (bio-waste) that must first be separated on the island. Separately collected bio-waste, which includes waste from gardens and parks, food and kitchen waste from households, catering and retail facilities, would be treated in composting plants on the islands. In the Republic of Croatia, bio-waste accounts for approximately one third of mixed municipal waste. Glass packaging would be similarly to bio-waste also separated on the island and further separately disposed. The ship would have a special plant for sorting waste, and in addition to sorting waste, it would have certain storage capacities and equipment for manipulating the output of

the sorting plant - bales of compressed waste: plastic, PET and MET packaging, paper, cardboard and RDF ("refuse-derived fuel"). RDF is a fuel derived from waste, and is produced in waste management facilities from non-hazardous unsorted municipal waste and can be used as a substitute fuel for energy production in industrial plants. This waste fuel consists of paper, cardboard, wood, textiles and small plastics, it is dry and stable and free of unpleasant odors. Due to its high calorific value, it is used as a fuel throughout the EU in various plants, from cement kilns to heating plants and thermal power plants. After collecting waste on the islands and processing it, the ship would sail to the port where bales of sorted waste would then be taken over by a collection company authorized to manage a certain type of waste.

When elaborating the mission requirements, the following main restrictions were set for the ship:

- the length and beam of the ship must be as small as possible, certainly within the dimensions of the existing ferries operating on lines between the aforementioned islands and the mainland,
- the draft of a fully loaded ship should not exceed 2.4 m due to the depth of the sea in the ports which the ship would call,
- the size of the ship must allow the installation of the entire waste sorting and baling plant,
- the waste sorting and baling plant must be shielded from the direct effects of the weather.

A sorting plant for mixed municipal waste from the company Tehnix d.o.o. from Donji Kraljevec, Croatia [14], was selected for waste sorting. Tehnix d.o.o. is one of the well-known eco-industries in the world, and their business goal is the development and production of the best technologies that achieve sustainable development and a circular economy. The company has developed and manufactured more than 300 machines and pieces of environmental equipment for which it has received hundreds of world awards and medals.

Taking into account the quantities of municipal waste shown in Table 1. [16], in cooperation with Tehnix d.o.o., a sorting plant with a capacity of five tonnes of waste per hour was selected. This is also the plant with the smallest capacity from the production program of the Tehnix d.o.o., and that capacity would be quite sufficient for the amount of waste on the islands. Figure 1. shows a waste separation and baling plant.

Table 1. Amount of waste on the islands of PGKC in tonnes per transshipment stations (data from January 2020), [16]

Month	Island of Cres	Island of Lošinj	Island of Krk	Island of Rab
January	51	286	375	280
February	36	295	408	260
March	50	419	515	300
April	82	549	709	320
May	103	562	838	360
June	186	604	1.248	680
July	282	855	1.815	800
August	325	945	2.011	824
September	172	538	1.045	371
October	90	341	715	219
November	66	300	520	200
December	53	240	455	180
Total	**1,495**	**5,935**	**10,654**	**4,794**

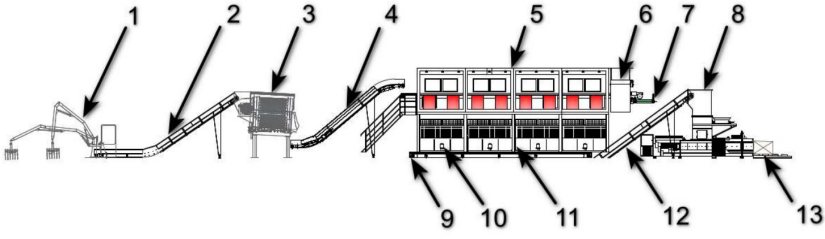

Figure 1. Waste sorting plant of Tehnix d.o.o. (1- grab; 2 - angle chain conveyor (entrance to the sieve); 3 - sieve; 4 - angle chain conveyor (exit from the sieve); 5 - four sorting cabins; 6 - magnetic separator; 7 - cross conveyor; 8 - automatic baler press; 9 - floor conveyor; 10 - pressure plate; 11 - box partitions; 12 - angle chain conveyor for baler; 13 - waste fraction bales)

The sorting plant is located on the main deck of the ship, and is designed so that the flow of material is in-line from the stern to the bow, without returning to any of the previous stations of the plant. The process begins with the delivery of mixed municipal waste by a truck that enters the ship with its rear end. The truck is weighed and then the waste is unloaded at a special waste collection point on the deck of the ship. Here the waste is picked up by a grabber and transferred to an angular chain conveyor which lifts it to a compact sieve in which the waste bags are opened. After the sieve, the waste is sent to the sorting booths by chain conveyor for manual sorting. The cabins are elevated because below them are boxes with bins for receiving sorted waste. A

total of four sorting cabins are provided, through which the conveyor passes through the middle, and on each side of the conveyor there are workers who manually separate the waste. The workplace functions in such a way that the worker stands between two bins that are at the height of the chain conveyor that brings the waste, and manually inserts a certain fraction of waste into them, which then falls down into the sorting waste bin. On the deck of the ship next to the sorting cabins there is a floor conveyor that extends the entire length of the cabins. When the receiving bins are filled with waste, they are pulled out and the contents are unloaded on that floor conveyor which takes the waste to an angular chain conveyor which inserts the sorted waste into an automatic baler. Bales with approximate dimensions of 1.2 m x 0.8 m x 1.0 m come out of the press. The size of the bale matches the dimensions of the standard European pallet, and the average mass of the bale is about 400 kg. Bales are manipulated by two electric forklifts permanently on board. For storage of bales, space is provided on both sides of the main deck and below the main deck. Workers in the sorting plant would have accommodation on board and would be treated as the ship's crew.

During the design of the ship, a round was made through the so-called design spiral, [17, 18, 19]. The following steps were considered in detail: mission requirement, main dimensions of the ship, hull shape, hydrostatic data, freeboard, arrangements, structure, resistance and propulsion characteristics, mass and center of gravity estimation and calculation of trim and stability of the ship in undamaged and damaged condition, [20, 21, 22, 23, 24, 25, 26, 27]. An energy balance analysis of the ship was also made in order to select the diesel generators that could power the electric propulsion motors as well as all other electrical systems on the ship including the sorting plant.

After passing through the various steps of the design spiral, the basic parameters of the ship shown in Table 2 were obtained.

Table 2. Basic parameters of a waste sorting ship

Length overall, m	74.0
Length between perpendiculars, m	69.1
Beam, m	17.0
Draft (maximum), m	2.4
Gross tonnage	2540
Engine power, kW	2 x 250

The three-dimensional computer model of the ship's hull is shown in Figure 2.

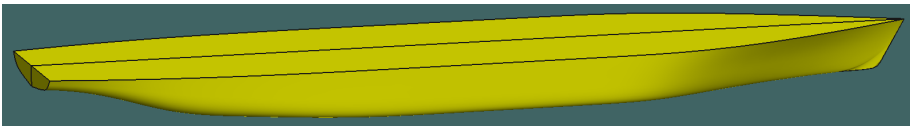

Figure 2. Three-dimensional model of the ship's hull

The ship was designed as a Ro-Ro cargo ship, with the intention to transport unit cargo in the form of bales, for the navigation area 6. The ship was designed as a twin-propelled ship, with two diesel-electric drives and Z-drive azimuthing thrusters as a means of propulsion. The electric motors of the company Tema d.o.o. from Pula, Croatia were selected, each with an individual power of 250 kW [28]. The selected speed of the ship was 10 knots, while the range was estimated at 1200 nautical miles, which allows a larger number of rounds for waste collection from the considered islands. The rules and regulations according to which the ship is designed are the rules of the Croatian Register of Shipping and other regulations applicable to ships flying the flag of the Republic of Croatia. Figure 4 shows the midship section and Figure 5 shows the general arrangement plan of the waste sorting ship.

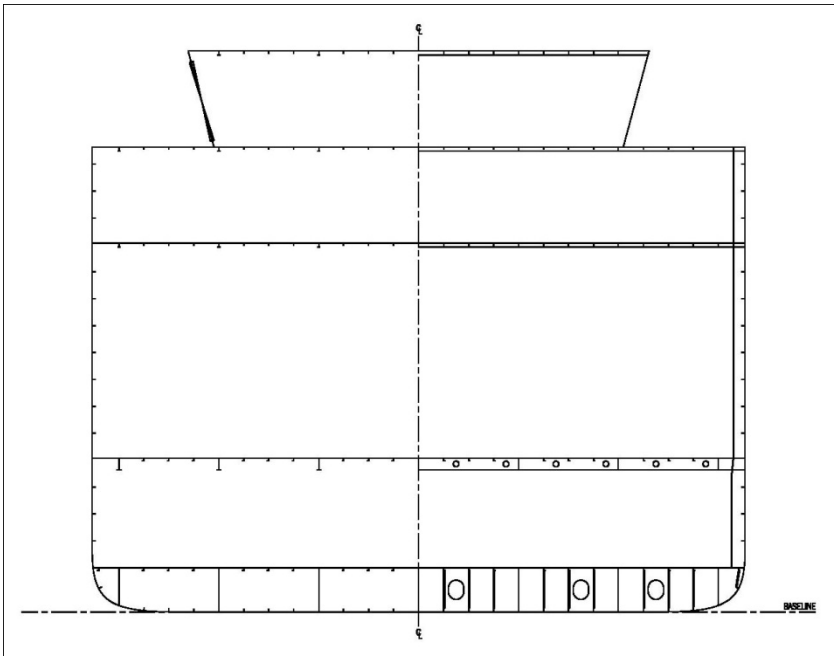

Figure 4. Midship section

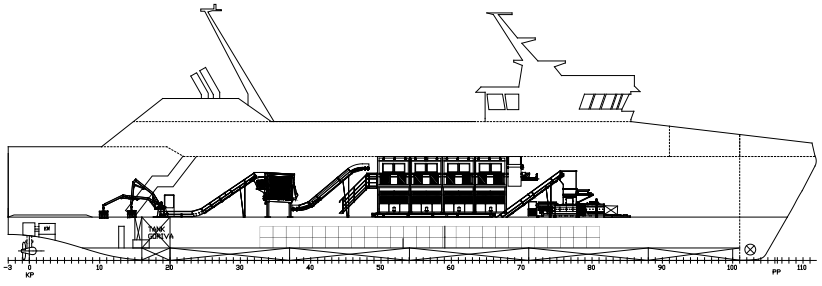

Figure 5. General arrangement plan

5. Conclusion

In this paper, the preliminary design of the waste sorting ship is presented. Preliminary design is the first phase of a ship design process in which the basis of the design are laid, and in which these basis are examined in terms of feasibility. After analyzing the process of sorting, transport and disposal of waste, a solution that could replace the plants located on the islands of Cres, Lošinj, Krk and Rab as the largest islands in the PGKC was offered.

The solution of a waste sorting ship could significantly reduce the facilities located on the islands. Currently, all waste from these islands due to lack of landfills on the islands of Primorje-Gorski Kotar County goes from transshipment stations by truck to the County Center for Waste Management Marišćina, which requires a large transport capacity of companies in charge of waste management on these islands and leads to high costs. The sorting ship can take over both this transport and sorting of mixed municipal waste, provided that bio-waste is separated at the "door", i.e. each household must separate the bio-waste and dispose it in a designated container.

The mission requirements of a ship were defined so that the ship can call to all existing ports already used for ferry lines between the island and mainland. The preliminary design shows that the idea of a ship for sorting mixed municipal waste from the Croatian islands is fully feasible.

However, the presented idea of collecting waste on the islands is narrowly focused on the ship, which is only one of the links in the entire logistics chain of collecting mixed municipal waste from islands. To complete the considered idea, bringing of waste collected on a particular island to the ship, the order of port calls around the islands, the number of calls on the islands during a week or month, then selection of a place for unloading baled waste as well as the best possible economic solution, in terms of the minimum cost for ship's operation should be additionally analyzed.

6. References

1. …, *"A new Circular Economy Action Plan A new Circular Economy Action Plan For a cleaner and more competitive Europe"*, European Commission COM(2020) 98 final, Brussels, 2020.
2. …, *"Transforming our world: the 2030 Agenda for Sustainable Development"*, A/RES/70/1, Resolution adopted by the General Assembly, United Nations New York, 2015.
3. …, *"Council Resolution on a Community strategy for waste management 97/C 76 /01"*, Official Journal of the European Communities No C 76/ 1, Brussels, 1997.
4. …, *"Council Directive on Waste 75/442/EEC, Official Journal of the European Communities No L 194/39"*, Brussels, 1997.
5. …, IUS-INFO, *"The European Parliament has adopted a new law on waste management"* (in Croatian), https://www.iusinfo.hr/aktualno/u-sredistu/33884, accessed September 2020.
6. …, *"Strategy of Waste Management in the Republic Of Croatia (Strategija gospodarenja otpadom Republike Hrvatske)"*, NN 130/05, Zagreb, 2005.
7. …, *"National Environmental Strategy (Nacionalna strategija zaštite okoliša)"*, NN 46/2002, Zagreb, 2002.
8. …, *"Waste Management Plan of the Republic of Croatia for the period 2017 to 2022 (Plan gospodarenja otpadom Republike Hrvatske za razdoblje 2017.-2022)"*, NN 3/17, Zagreb, 2017.
9. …, *"Waste management in Primorje-Gorski Kotar County"* (in Croatian), Ekoplus d.o.o., https://www.ekoplus.hr/gospodarenje.php, accessed September 2020.
10. …, *"The New Waste Management System in Primorje-Gorski Kotar County"*, City of Rijeka, https://www.rijeka.hr/en/city-government/eu-projects/closed-projects/novi-sustav-gospodarenja-otpadom-u-primorsko-goranskoj-zupaniji/?noredirect=en_GB/, accessed January 2021.
11. …, *"Waste Management Plan of the City of Cres for the Period 2017-2022"* (in Croatian), Eco Consulting j.d.o.o., Cres, 2017.
12. …, *"Waste Management Plan of the Town Mali Lošinj for the period 2017-2022"* (in Croatian), Eko Adria d.o.o., Mali Lošinj, 2017.
13. …, *"Waste Management Plan of the City of Krk for the Period From 2017 to 2022"* (in Croatian), DLS d.o.o., Krk, 2018.
14. …, Tehnix: O nama, https://tehnix.hr/o-nama/, accessed June 2020.
15. …, *"Waste Management Plan of the City of Rab for the period 2017-2022 - Draft"* (in Croatian), H-Projekt d.o.o., Rab, 2017.
16. …, Private communication, County Center for Waste Management Marišćina, January 2020.
17. Papanikolau, A. (2014) Ship Design - Methodologies of Preliminary Design, Springer, London,
18. Roh, M.-I., Lee, K.-Y. (2018) Computational Ship Design , Springer, Singapore
19. Watson, D. (1998) *Practical Ship Design"*, Elsevier Science Ltd., Oxford
20. …, *"Rules for the classification of ships"*, Edition July 2019, Croatian Register of Shipping, Split, 2019.
21. …, *"International Convention on Load Lines"*, International Maritime Organization, London, 1968.
22. …, *"International Convention on Tonnage Measurement of Ships"*, London, 1969.
23. Holtrop, Ir.J. (1977) *A statistical analysis of performance test results*, International Shipbuilding Progress – Shipbuilding and Marine Engineering Monthly, Vol. 24, No. 270, Rotterdam
24. Holtrop, Ir.J., Mennen, G.G.J. (1982) *An Approximate Power Prediction Method*, International Shipbuilding Progress – Shipbuilding and Marine Engineering Monthly, Vol. 29, No. 335, Rotterdam
25. Holtrop, Ir.J. (1982) *A Statistical Re-Analysis of Resistance and Propulsion Data"*, International Shipbuilding Progress – Shipbuilding and Marine Engineering Monthly, Vol. 3l, No. 363, Rotterdam
26. …, *"ZF Thrusters, Marine Product Selection Guide"*, https://marine.zf.com/matran/#!/search, accessed December 2020.
27. …, *"MAN MARINE Auxiliary gensets"*, https://docplayer.net/188477230-Marine-auxiliary-gensets-man-engines.html, accessed September 2020.
28. …, www.tema.hr, accessed September 2020.

ISSN 0554-6397
Konferencijski članak
(*Conference paper*)

Vladimir Pelić
E-mail: vladimir.pelic@pfri.uniri.hr
University of Rijeka, Faculty of Maritime Studies, Studentska 2, 51000 Rijeka, Croatia
Tomislav Mrakovčić
E-mail: tomislav.mrakovcic@riteh.hr
University of Rijeka, Faculty of Engineering, Vukovarska 58, 51000 Rijeka, Croatia
Radoslav Radonja
E-mail: radoslav.radonja@pfri.uniri.hr
University of Rijeka, Faculty of Maritime Studies, Studentska 2, 51000 Rijeka, Croatia
Nikola Račić
E-mail: nikola.racic@pfst.hr
University of Split, Faculty of Maritime Studies, Ruđera Boškovića 37, 21000 Split, Croatia

Technical and Ecological Aspects of Water-lubricated Stern Tube Bearings

Abstract

A ship's propulsion system has a significant impact on the ship's energy efficiency, environmental friendliness, reliability and safety. An indispensable part of a propulsion system with mechanical power transmission is a stern tube with bearings. During operation, the sliding bearings material is subjected to stresses caused by a force proportional to the total mass of the shaft and propeller. The reliability of stern tube bearings is particulary important for safety, and their durability has a significant impact on maintenance costs. Depending on the lubricant, there are bearings that are lubricated with oil or water. The permissible bearing load with hydrodynamic lubrication depends primarily on the material, the viscosity of the lubricant used and the shaft speed. Metals and their alloys with a low coefficient of friction are used for oil-lubricated bearings. Bearings lubricated with water are made of a special type of hardwood ("tree of life", lat. *lignum vitae*), rubber or various synthetic materials. The main advantages of oil-lubricated bearings are higher allowable load and durability than water-lubricated bearings. This paper analyses the technical and environmental aspects of the application of water-lubricated bearings whose main advantages are simplicity, better cooling and environmental protection.

Keywords: stern tube bearing, water-lubrication, environmental protection

1. Introduction

The reliability, competitiveness and safety of a ship depend largely on the propulsion system and the individual parts of that system. The main component of the propulsion system of most modern ships is the internal combustion engine, while the propeller is used as the propulsor. In cargo ships, slow-speed diesel engines with mechanical power transmission to the propeller are mainly used for reasons of reliability and economy in operation. A much smaller share refers to medium-speed diesel engines, steam and gas turbines with mechanical or electrical power transmission. The low rotation speed of diesel engines allows easy mechanical transmission of torque from the crankshaft to the propeller shaft. When higher speed prime movers are used, the speed must be reduced to that required for the propeller using a suitable mechanical or electrical transmission. When selecting a propulsion system, consideration is given to the energy, economic and environmental acceptability of the system as a whole and of each individual part of the system.

The prime mover largely determines the characteristics of the propulsion system, and a significant impact on safety, reliability, cost, and the environment is also exerted by the part of the propulsion system called the stern tube. The stern tube with its associated radial bearings, transmits the load caused by the mass of the shaft and propeller to the structure of the ship. In addition, depending on the design, the stern tube is equipped with appropriate seals and other elements necessary for lubrication and cooling of the bearings. Depending on the lubricant used, there are different versions that use water (freshwater or seawater) or oil to lubricate the stern tube bearings. Non-metals such as special types of hardwood and various synthetic (*polymeric*) materials are mainly used for water-lubricated bearings, while the material for oil-lubricated bearings are metals or their alloys (*bronze, lead and tin alloys*). The main advantages of water-lubricated bearings compared to oil-lubricated bearings are simple construction and maintenance, as well as environmental friendliness. Oil-lubricated bearings are durable and can withstand higher loads, but in the event of seal damage, oil leakage and marine pollution occurs.

In maritime transport, as in all other activities, we strive to achieve the highest possible efficiency, and at the same time reduce the negative impact on the environment to a minimum. MARPOL 73/78 does not allow the release of oil into the sea from ships (engine room and cargo space), except in exceptional circumstances. The IMO Polar Code, in force since January 2017, also prohibits the discharge of even the smallest quantities of oil in the Arctic and Antarctic region [1]. Recently, there has been an increase in the interest and number of commercial voyages in the North Sea, so there is a need for technical solutions that ensure the environmental friendliness of maritime transport. According to IMO requirements, in particularly sensitive sea areas and marine ecosystems, no tolerance is required for any type of pollution that might be caused by oil spills from ships. To avoid pollution when mineral lubricating oil is used in USA territorial waters, the use of biodegradable lubricating oil for the stern tube bearings is

required. Since the oil used to lubricate the stern tube bearings is a potential source of pollution and biodegradable oils are expensive, the use of water-lubricated bearings is recommended.

2. Stern tube design

In this paper, the stern tubes are distinguished according to the medium used to lubricate and cool the bearings. The stern tube bearings can be lubricated and cooled with water or oil, depending on the design and material. Until the middle of the last century, stern tube bearings made of a special type of hardwood *lignum vitae* (from Latin „wood of life) from South America were predominant. The lignum vitae contains natural oil that contributes to the self lubricating effect of the bearing.

The main reason for switching to versions with oil-lubricated bearings is the relatively short service life of water-lubricated bearings. As a rule, a bearing made of *lignum vitae* had to be replaced after five years of use. Depending on the operating conditions of the ship, bearing problems would occur much earlier, which caused additional costs and could endanger the safety of the ship. These reasons led to the use of oil-lubricated bearing systems that prevailed in the second half of the 20th century marginalizing the use of water-lubricated bearings. All stern tube bearing lubrication systems, regardless of the lubricant used, must reduce friction and provide hydrodynamic lubrication of the bearings to prevent excessive bearing wear and heating. However, the requirements for zero tolerance to pollution and the development of new technologies and materials offer water-lubricated bearings a new opportunity.

According to [2], a total of 130 to 244 million liters of oil escape from the sterntube bearing lubrication system into the sea each year. As well as [3] estimates that even under ideal conditions, at least 10 million liters of oil would leak from the stern tube into the sea each year. According to an analysis by EMSA (*European Maritime Safety Agency*) of data collected by satellites during 18 months in 2007 and 2008, 4027 possible cases of oil spills from ships were detected. Subsequent inspections from the air or from the ship confirmed that in almost 80% of the cases there was a mineral oil spill [4]. In [5], it was pointed out that due to difficult working conditions (bad weather conditions and vibrations), it is not possible to completely avoid oil leakage from the stern tube into the sea. The analysis of propeller shaft-related failures conducted in [6] showed that in the observed period of 20 years, 10% of the failures affected the aft bushing of the shaft and 4% to the forward bushing. It is also interesting to note that damage to the sealing rings accounted for 43% and 24% of the total number of failures, respectively.

It follows that achieving the goal of zero tolerance to oil pollution from the operation of ship systems depends on the application of environmentally friendly solutions. In doing so, special importance is given to materials that allow the efficient use of seawater as a lubricant for the stern tube bearings. According to [7], more

than 2000 ships in operation are equipped with THORDON bearings lubricated with seawater.

Below is a brief overview of the stern tube bearing lubrication systems using oil and water with a comparison of their characteristics.

2.1. Closed stern tube lubrication systems

Modern systems that use oil to lubricate the stern tube bearings are also called "closed" stern tube systems. In closed systems, there are two radial slide bearings in the stern tube. Oil leakage and sea penetration into the stern tube is prevented by several sealing rings (lip seals). The most common designs are with three or four lip seals on the propeller side (aft seal) and two lip seals on the engine room side (forward seal). The beginning of the use of the closed stern tube system dates back to 1948 when the Blohm & Voss company introduced the Simplex seal lubrication system for white metal bearings [8], [9].

In most versions, cooling of the bearing or lubricating oil is achieved by transferring heat from the stern tube to the sea into the aft peak tank. For this reason, the aft peak tank is always partially filled with water. The heat from the water in the tank is transferred by convection through the hull to the surrounding sea, faciliating the movement of the ship. Stern tube lubrication systems with a pump and oil cooler are less commonly used. An important part of the system is the gravity tank, which provides a higher oil pressure in the stern tube than in the surrounding sea, preventing seawater from entering the stern tube in the case of damage to the lip seals. Systems with "low" and "high" gravity oil tanks are mainly used to achieve the appropriate pressure difference when the ship is empty or loaded with cargo. With one or two gravity tanks, it is not possible to achieve an optimal pressure difference under all operating conditions. A deviation from the optimum pressure difference, especially with simultaneous damage to the seals, can lead to oil leakage or seawater penetration into the stern tube.

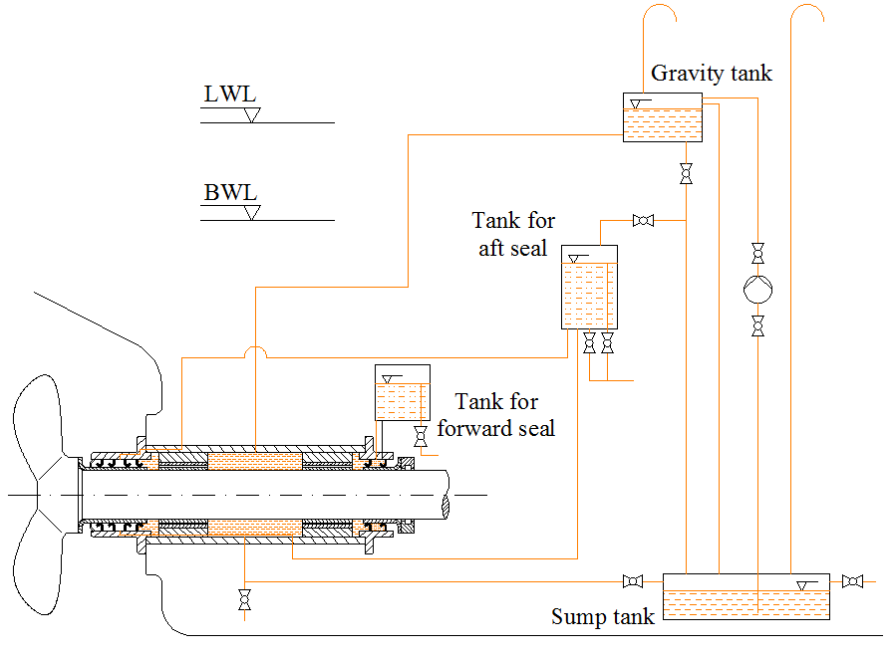

Fig. 1. Closed stern tube system with one gravity tank (source: Authors)

The closed stern tube system with one gravity tank is shown in Fig. 1. The use of only one gravity tank allows the pressure difference to be adjusted only in a limited range depending on the draft of the ship. This disadvantage is particularly pronounced in case of damage to the seals on the propeller side when the ship is immersed to the ballast water line (BWL). In this case, there is higher probability of the oil leakage from the stern tube due to the greater pressure difference.

The described disadvantage can be partially compensated by the application of the lubrication system in Figure 2 with two gravity tanks. However, even with the version with two gravity tanks, despite the greater possibility of regulating the pressure difference, increased oil leakage can occur if the seals on the propeller side are damaged.

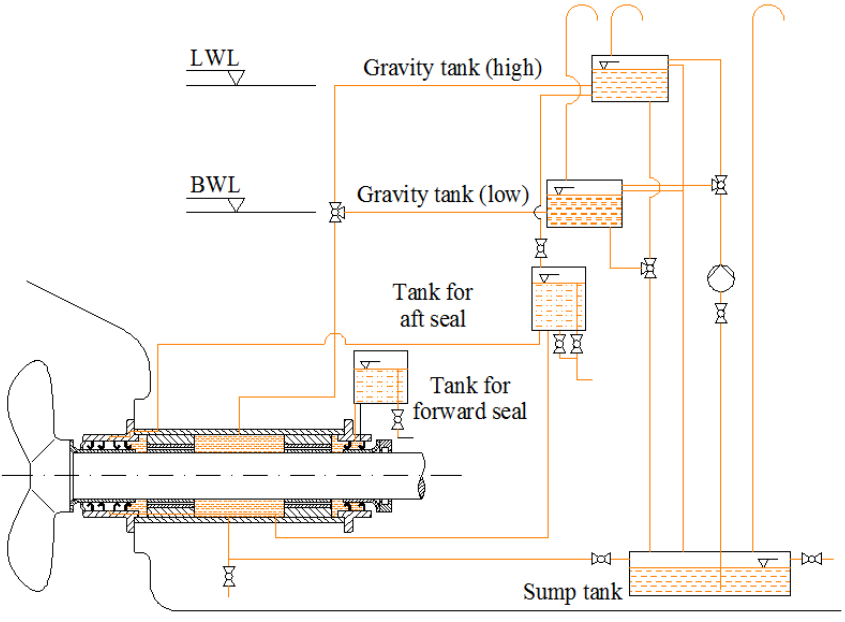

Fig. 2. Closed stern tube system with two gravity tanks (source: Authors)

Figure 3 shows the aft seal system with water, air and oil chamber. The air chamber has the function of preventing oil leakage or sea penetration into the stern tube under all operating conditions as well as in case of damage to the seal on the propeller side.

The detail of the aft seal used in the previous example is shown in Figure 4. The drawing shows a sealing system with four seals bounding the chambers filled with water, air and oil. The special part of the system shown in Figure 3 maintains the appropriate pressure in the air chamber under all operating conditions of the ship, even in case of minor damage to the outer seal. With this type of aft seal, oil leakage is not completely prevented, but is significantly reduced in the case of minor damage to the aft lip seal.

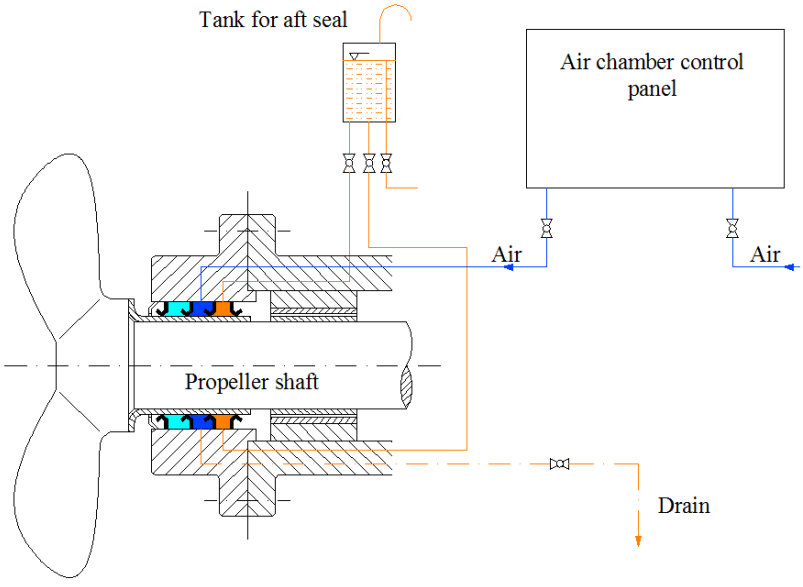

Fig. 3. Aft seal system with air chamber (source: Authors)

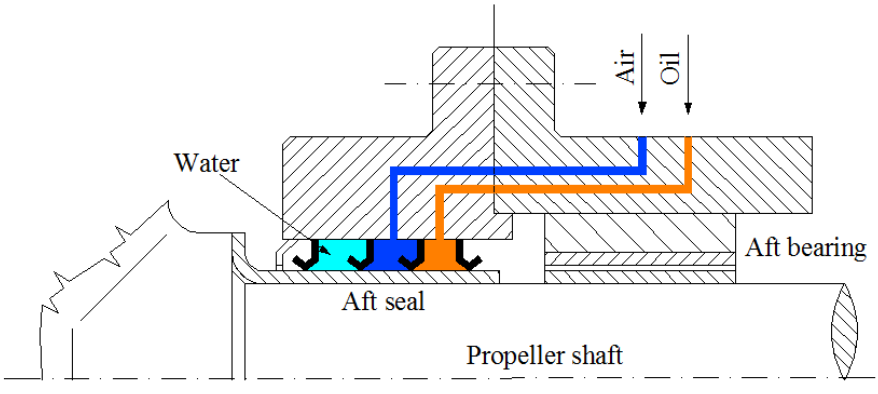

Fig. 4. Design of the aft seal with an air chamber (source: Authors)

The pressure in the air chamber adjusts to the draft of the ship. The adjustment can be manual or automatic. Automatic adjustments are especially important for vessels that have large differences in draft between load and ballast conditions. An additional input signal from a draft meter or pressure sensor is required to automatically adjust the air pressure to the ships draft.

2.2. Open stern tube lubrication systems

Open stern tube systems made of natural material, a special type of hardwood from South America, *lignum vitae*, were used intensively in the first half of the 20th century. They are characterized by their simplicity, but since the natural material is used, its mechanical properties are not uniform. Non-uniform mechanical properties, as well as the inability to adapt the material to specific requirements in some cases, lead to damage occurring much earlier, which cannot be predicted or detected by regular inspections. An example of an open stern tube with aft bearing made of *lignum vitae* is shown in Figure 5.

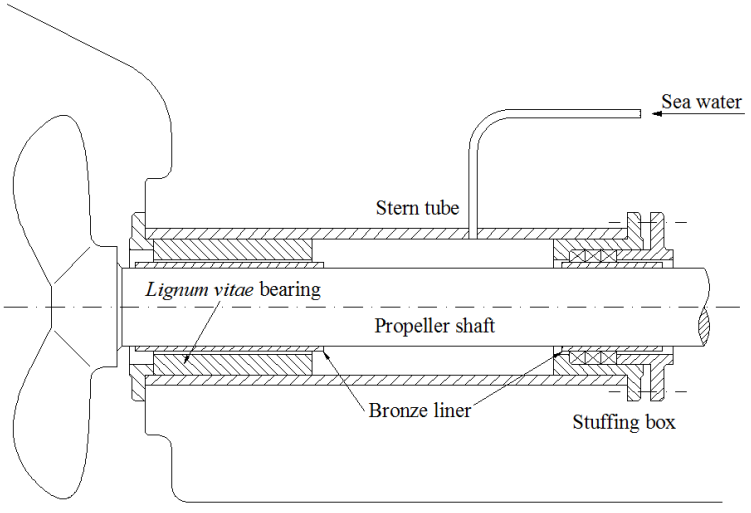

Fig. 5. Open stern tube system with bearing made of wood (source: Authors)

In the second half of the 20th century, open stern tube systems began to be pushed out of use by closed systems that use lubricating oil and relatively complex sealing systems. Closed oil systems are prone to damage on the propeller side and increase oil leakage, which cannot be completely avoided even by using complex seals. At the turn of the century, ships primarily used closed sterntube systems. However, in the 21st century, there is another opportunity to open stern tube systems in which the water-lubricated bearings are made of synthetic polymer and composite materials. In modern open stern tube lubrication systems, water or sea treatment (purification) devices are used in some cases to avoid the abrasive effect of seawater. Such a system is shown in Figure 6.

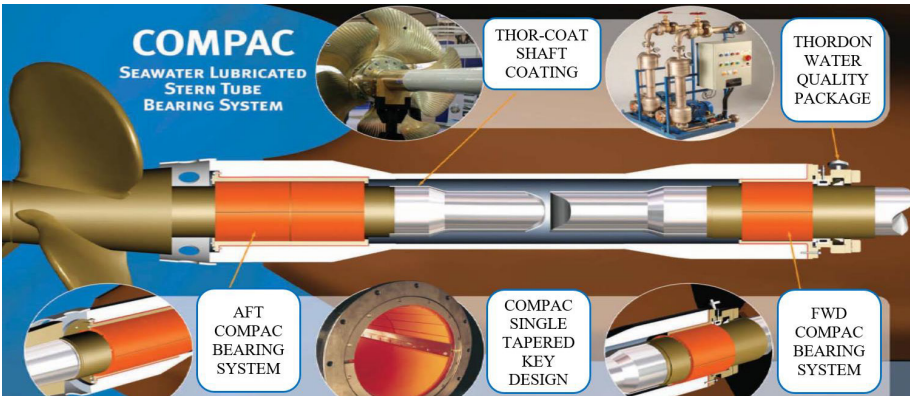

Open stern tube system with a bearing made of polymeric material (source: [7], adapted by the authors)

3. The principle of operation of fluid-lubricated bearings

The bearing must be designed to separate shaft from the bearing during rotation to minimize the operation under conditions of "dry" friction. According to the hydrodynamic principles of the sliding bearing operation, the formation of a thin lubricant layer is affected by the bearing load, the shaft speed, the lubricant used and the profile of the bearing surface. For each bearing design, there is a minimum speed at which the shaft must rotate to achieve hydrodynamic lubrication.

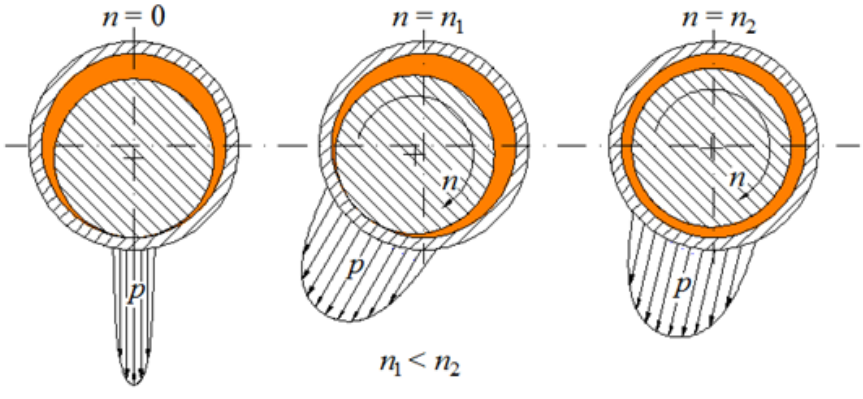

Fig. 7. Hydrodynamic lubrication principle (source: Authors)

Figure 7 shows the formation of the oil layer required for hydrodynamic lubrication of the slide bearing. At the moment when the shaft starts to rotate, a thin layer of

lubricant is formed, and when the conditions are met, the shaft journal separate from the bearing. In this way, a significant reduction in friction is achieved, resulting in lower heating and lower bearing wear. In bearings that operate according to hydrodynamic principles in normal operation, significant bearing wear occurs when the shaft rotation is started and stopped. This occurs because the bearing runs "dry" during these periods and the pressure in the oil layer is not high enough to separate the shaft from the bearing. Metal bearings use special metal alloys (bronze, white metal and others) that can withstand short-term operation under conditions of "dry" friction. Synthetic polymers and composites used for bearings have high resistance to surface pressure and wear under dry friction conditions. To protect the propeller shaft from damage coused by the corrosive and abrasive action of seawater, a replaceable bronze liner made of metal or other corrosion-resistant material is placed on the part of the shaft that comes into contact with the bearing.

Considering only the technical aspects, the application of lubricating oil generally provides better lubrication than freshwater or seawater. With oil lubrication, the conditions for hydrodynamic lubrication occur due to the higher viscosity of the oil at lower speeds. However, water has an advantage in cooling efficiency, due to its higher specific heat compared to oil. Water (freshwater or seawater) is an environmentally friendly solution and is also fully compatible with open stern tube systems.

3.1. Metal bearings

Fig. 8. Oil-lubricated stern tube bearing made of metal (source: [10])

Oil-lubricated stern tube bearings are manufactured as one-piece bearings in which a layer of white metal alloy is applied or cast onto a metal (steel) bearing bracket. An example of such a white metal alloy bearing is shown in Figure 8.

3.2. Bearings made of polymeric material

Bearings made of polymeric material are mainly made of a type of material whose characteristics correspond to the requirements of the application. The bearing bracket is usually made of steel, and its shape and dimensions are designed for quick and easy installation in the stern tube. Figure 9 shows a Thordon COMPAC type bearing designed to operate in seawater. Material properties have been selected to minimize the coefficient of friction to minimize wear under dry friction conditions. The lower half of the bearing is smooth and the upper half has longitudinal grooves for better lubrication and cooling.

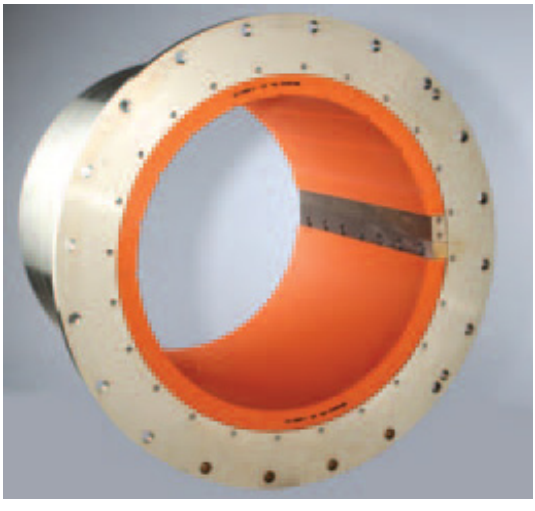

Fig. 9. Stern tube bearing lubricated with seawater (source: [11])

Figure 10 shows the design of a composite polymer bearing in which the inner layer is made of a material with high resistance to the abrasive action of the water mud to which tugs are exposed on rivers. The outer layer of the Thordon RIVER TOUGH type is designed to compensate for shock and vibration and has longitudinal grooves that allow better cooling of the bearing.

Fig. 10. Stern tube bearing lubricated with water (source: [11])

Reinforced composite plastic material that has a very low coefficient of volume expansion is suitable for use in extremely cold (North Sea) or warm (tropical) conditions. The bearing was developed by Durmax Marine. An example of the installation is shown in Figure 11.

Fig. 11. Bearing made of composite material lubricated with seawater (source: [12])

4. Technical and environmental aspects of the application of water-lubricated bearings

When analyzing the technical and environmental aspects of the application of water-lubricated bearings, attention should be paid to features such as durability, reliability, safety, investment cost, installation, maintenance, compliance with regulations and environmental friendliness. A comparison of the characteristics of the stern tube system mentioned in this paper shows that open systems using water or seawater lubricated bearings are absolutely environmentally friendly. It is undisputed that the environmental friendliness of the lubricant deserves special attention. The graph in Figure 12 shows that the leakage of lubricating oil accounts for more than 10% of the total marine pollution caused by oils [13].

The design and number of parts of the stern tube with water-lubricated bearings is much easier to manufacture and maintain, and there is no costs to purchase lubricants. Therefore, it is realistic to expect that the total cost of using water-lubricated bearings will be lower.

The significant reduction in costs when using water-lubricated bearings is supported by the fact that systems using oil-lubricated bearings to reduce the negative impact on the environment are much more complex not only in production but also in maintenance. One disadvantage of water-lubricated bearings is the inability to achieve hydrodynamic lubrication at high loads and low propeller shaft speeds. This disadvantage can be compensated by the development of new composite materials, suitable design and design of the bearing surface.

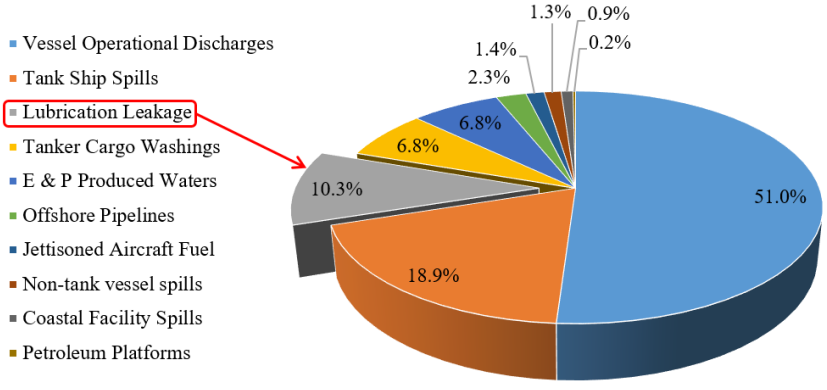

Fig. 12. Marine environment pollution by oils (source: [13], adapted by the authors)

Table 1.: Ecological acceptability of various technical solutions for lubrication of stern tube bearings (source: [13], adapted by the authors)

Enviro Solution Level	Aft Seal Configuration	Lubrication	Uses of EAL* in seawater interfaces	Risk of disscharge above limit during normal operation	Risk of discharge above limit following severe damage	
Enviro 1	No Aft Seal	Sea or Water	Compliant	Zero	Zero	Increasing Environmental Acceptance
Enviro 2	Conventional Seal	Fresh Water	Compliant	Zero	Zero	
Enviro 3	Anti Pollution – No Oil Water interference seal	EAL*	Compliant	Zero	High	
Enviro 4	Anti Pollution – No Oil Water interference seal	Mineral Oil	Compliant	Zero	High	
Enviro 5	Conventional Seal Oil Water interference seal	EAL	Compliant	Low	High	
Oil water interface seal (90% of vessels)		Mineral oil	Not compliant	NA	Very High	

** EAL – Environmentaly acceptable lubricants*

Table 1 shows the level of environmental acceptability of technical solutions that use oil or water to lubricate the stern tube bearings.

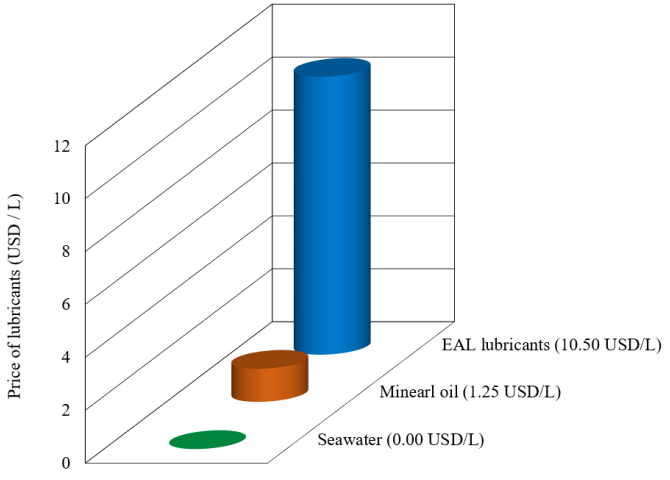

Fig. 13. Comparison of lubricant costs for stern tube bearings (source: [14] [15], adapted by the authors)

According to the data in Figure 13, a comparison of the costs associated with the use of a particular lubricant shows that the use of environmentally friendly lubricants has about eight times higher costs compared to mineral oils.

The results of the research conducted by Thordon show that stern tube bearings made of high-quality materials and lubricated with water can fully satisfy in terms of durability, reliability, safety and low maintenance costs. The research confirms the usability of water-lubricated bearings with a large (615 mm) propeller shaft diameter. Figure 14 shows the increase in the clearance of the water-lubricated bearing on a passenger ship. The measurements were performed on a ship with two propellers, and average clearance values were given for the aft bearings of the left and right propeller shafts. The results obtained show that the increase in bearing clearance is less than allowed even after 18 years of operation, and the total bearing life is estimated at 25 years.

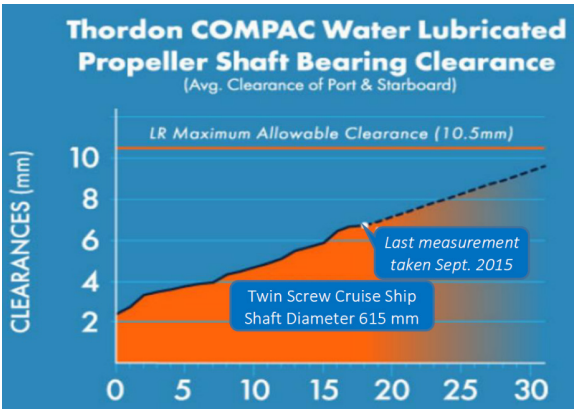

Fig. 14. Increasing the clearance of the stern tube bearing in operation (source: [14])

5. Conclusion

When choosing the optimal technical solution for stern tube bearing lubrication, one can choose between open and closed lubrication systems. All closed systems presented in this paper use lubricating oil, while the open systems use freshwater or seawater. The lubricant used has a significant impact on the complexity, durability, reliability, investment and maintenance costs of the stern tube system, and also on the environmental impact of the chosen technology.

According to the current state of development of materials and technical solutions entrusted and accepted by the shipbuilding industry, the application of oil-lubricated bearings predominates in the world maritime fleet. Their main advantage is the ability to create conditions for hydrodynamic lubrication at lower shaft speeds and higher bearing loads than water-lubricated bearings. Due to its higher viscosity, oil is technically a much more favorable lubricant than water. However, the advantages of

water as a lubricant are significantly better bearing cooling and complete environmental friendliness. Even with closed oil stern tube systems that use oil in operation, it is not possible to completely avoid the leakage of oil into the environment.

The progress made in improving the characteristics of water-lubricated bearings, as well as the contribution to environmental protection, show that their use is justified. It is expected that in the near future there will be a transition from a system using lubricating oil to systems that use freshwater or seawater for lubrication.

Acknowledgement

This work has been fully supported by Croatian Science Foundation under the projects IP-2020-02-6249 and IP-2020-02-8568.

References

1. International Maritime Organization (2017). *International Code for Ships Operating in Polar Waters*. London, IMO.
2. Etkin, D. S. (2010) Worldwide analysis of in-port vessel operational lubricant discharges and leakages. *33. AMOP technical seminar on environmental contamination and response*, 7-9 June 2010, Halifax, Canada. pp. 529-553.
3. Higgenbottom, A. (2003) Coastguard Non-Polluting Stern Tube Sealing System. RINA *International Conference for the Design and Operation of Container Ships*, 23-24 April 2003, London, UK. pp. 53-60.
4. Journel, M. (2009) CleanSeaNet: Satellite-based monitoring service for marine oil spill detection and surveillance in European waters, European Maritime Safety Agency Bulletin 104(2). pp. 48-51.
5. Sada, H., Yamajo, S., Hawkins, D. W. & Kawazoe, T. (2006) An Environmentally Compatible Lubricant for Stern Tube Shafting and Bearing Systems, *SNAME 11th Propeller and Shafting Symposium*, 12-13 September 2006, Williamsburg, Virginia, USA.
6. Smith, A. (2009) Shaft Alignment Problems Analyzed. *Marine Engineers Review,* April 2009, pp. 16.
7. Thordon Bearings Inc. (2022) *Oil Lubricated Stern Tube Discharges - The Problems and the Solution*. Available from: https://thordonbearings.com/docs/default-source/marine/documents/oil-lubricated-stern-tube-discharges.pdf?sfvrsn=c9d9e82_5 [Accessed 8 October 2022].
8. SKF Blohm & Voss Industries (2022) *Simplex-Compact Shaft Components*, Available from: http://fujimetalock.com.br/wp-content/uploads/2014/09/SKF-Blohm+Voss-Shaft-SIMPLEX-Seals.pdf [Accessed 5 October 2022].
9. Ogle, K. J. & Carter, C. D. (2015) Benefits of Seawater Lubricated Bearings to Prevent Environmental Impact from Propeller Shaft Systems in Polar Regions, *Ice Class Vessels*, 28-29 April 2015, London, United Kingdom. pp. 34-40.
10. MarineShaft (2022) *White metal*. Available from: https://marineshaft.com/casting-of-white-metal.aspx [Accessed 8 November 2022].
11. Thordon Bearings Inc. (2022) *Seawater lubricated propeller shaft bearings*, Available from: https://thordonbearings.com/docs/default-source/marine/documents/thordon-propeller-shaft-bearings-(xl-sxl-compac-rivertough).pdf?sfvrsn=fe20476e_18 [Accessed 11 October 2022].
12. Duramax Marine (2022) *Composite Water-Lubricated Stern Tube Bearings*, Available from: https://www.duramaxmarine.com/pdf/DuraBlue-Bearing_broch2019.pdf [Accessed 26 October 2022].
13. Thornhill, J. (2015) The Challenge of Stern Tube Bearings and Seals, *SNAME 14th Propeller and Shafting Symposium*, September 2015, Norfolk, Virginia, USA.
14. Carter, C. D. (2018) Seawater for Propeller Shaft Lubrication in Merchant Ships – Environmental, Operational, Legal and Shipbuilding Considerations, *6th World Maritime Technology Conference*, 4-7 December 2018, Shanghai, China.

ISSN 0554-6397
Konferencijski članak
(*Conference paper*)

Elena Miletić
E-mail: emiletic1@riteh.hr
Faculty of Engineering University of Rijeka, Vukovarska 58, Rijeka, Croatia
Lukša Radić
E-mail: luksa.radic@km.kongsberg.com
Siniša Letinić
E-mail: sinisa.letinic@km.kongsberg.com
Navis Consult d.o.o., Bartola Kašića 5/4, Rijeka, Croatia
Anton Turk
E-mail: anton.turk@riteh.hr
Faculty of Engineering University of Rijeka, Vukovarska 58, Rijeka, Croatia

Seaworthiness and Stability Analysis of a Pontoon for Holiday House

Abstract

In this paper, the methodology of seaworthiness and stability analysis of a pontoon for holiday house has described. A 3D model of the pontoon was modelled in the NAPA software to perform hydrostatic analysis. It is necessary to emphasize the fact that hydrostatic analysis has been made for several drafts and trims of pontoons. The hydrostatic analysis yielded data such as displacement, moulded volume, longitudinal centre of buoyancy, the transverse metacentric height, change of displacement, moment to change trim, and more. This part of the analysis also includes the loading scale from which we can see the deadweight at a given draft. Further, it is necessary to make weight study to get moulded displacement for pontoon for a holiday house. The pontoon also includes capacity tanks, so it is necessary to know the accurate dimensions of the tanks and their position for further analysis. It is necessary to know the exact geometry of the tanks because of the free surface effect. When calculating the stability of the pontoon, it is necessary to determine the minimum metacentric height and the maximum distance from the keel to the centre of gravity. Intact stability conditions must be met for GM limit curves and also for KG curves. Intact stability criteria of the pontoon were tested for four loading conditions: lightship, pontoon with 10% consumables without passengers, pontoon with 100% consumables with passengers, pontoon with 50% consumables with passengers. It is important to emphasize that all tasks meet the stability criteria.

Keywords: intact stability, hydrostatic analysis, loading scale, weight study, cross curves

1. Introduction

The topic of this paper is a modelling of a pontoon and calculation of pontoons buoyancy and stability. The methodology of the analysis will also be described. The pontoon is designed for tourist purposes. The purpose is to accommodate guests and it is designed as an accommodation unit, i.e. a holiday home. Floating objects are maritime objects constantly anchored or moored at sea. They are not intended for navigation. The term floating objects also includes pontoons. Their block coefficient must be greater than 0.9. Pontoons have a simple geometric or analytic shape. They have a square shape and can be used for various purposes.

Residential pontoons are designed so that the accommodation unit or a house stands on a pontoon base in accordance with the calculation of the weight and centre of gravity of the pontoon and structure, the buoyancy of the building and the strength of the structure for the given environmental conditions. Figure 1 depicts the proposed holiday house pontoon arrangement while table 1 provides basic particulars.

Table 1. Basic information about the pontoon

Length overall	L_{OA}	18.00 m
Breadth overall	B_{OA}	8.30 m
Length of waterline	L_{WL}	14.15 m
Breadth at waterline	B_{WL}	6.15 m
Depth to freeboard deck	D	1.15 m
Height	H	5.05 m
Draught	T	0.65 m
Deadweight	DWT	19.4 t

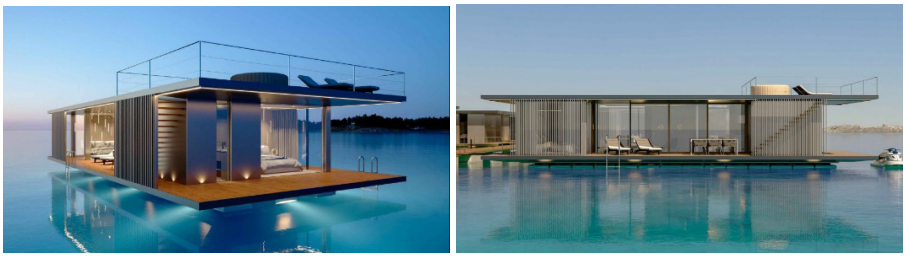

Figure 1. Pontoon for holiday house

2. Intact stability

The stability of a ship is the ability to return the ship to its initial position due to the effect of external forces, the displacement of the masses on the ship. It depends on the shape of the hull as well as the distribution of mass on board.

2.1. Stability criteria

According to the rules for statutory certification of seagoing ships of the Croatian Register of Shipping (CRS) from Annex 4, for the stability of floating cranes, pontoons, docks and ships permanently connected to the coast, the stability criteria to be met have been taken into account.

Stability of a pontoon shall be considered sufficient if:

- The area under the righting lever curves up to the angle of maximum righting lever or the downflooding angle, whichever is less, is not less than 0.08 metre-radians.
- The range of positive stability levers is at least 20° for pontoons with a length of less than or equal to 100 metres, or 15° for pontoons with a length of more than or equal to 150 metres. The range value for the length intermediate values is calculated by linear interpolation.

The downflooding angle shall be taken as the angle at which an opening through which progressive flooding may take place is immersed.

For pontoons shorter than 24 m in length and intended for navigation in “calm waters”, the Register may allow not to compute the righting lever curve for greater angles if the initial metacentric conditions for all loading conditions has a value of no less than 0.35 m. [2]

2.2. Crowding of passengers

Crowding of passengers is one of the requirements of the register for passenger ships. The angle of static inclination must not be greater than the angle of deck dive or the angle of emerge of the bilge. Furthermore, this angle of inclination must not exceed 10°.

When determining the angle of inclination due to the crowding of passengers on one side, the average weight of passengers is taken to be 75 kilograms. The assumed density of passengers on deck is 4 people per square metre. The centre of gravity of the passenger is calculated 1.0 metres above deck level in case the passenger is standing or 0.3 metres above the passenger seat in case the passenger is sitting. [3]

2.3. Weather criterion

Every ship must have the ability to withstand the effects of bad weather, as well as the effects of strong crosswinds. The same goes for a residential pontoon.

One of the criteria that must be met is that the angle at equilibrium must not exceed 16° or 80% of the value of the deck immersion angle.

Additionally, the minimum height of the freeboard that does not sink due to wind must be greater than or equal to 10 millimetres.

2.4. Openings applied for intact stability calculations

When building a ship, there is a need for caution when positioning the openings. Unprotected openings are leaky and water will penetrate unhindered when the deck floods. The residential pontoon below the main deck contains a freshwater tank, a sewage tank, a fuel oil tank, and a dry space.

With the plotting and determination of the positions of the tanks and the associated openings, the analysis begins, in which the point of immersion of the deck and the opening is determined. Flooding angle is the angle of inclination at which the opening or openings in the deck sink and progressive flooding can occur.

The analysis concludes that for a construction draught of 0.65 m, the deck floods at an angle of 12.8 degrees, and the first unprotected opening plunges into the water at 24.5 degrees as seen on figure 2.

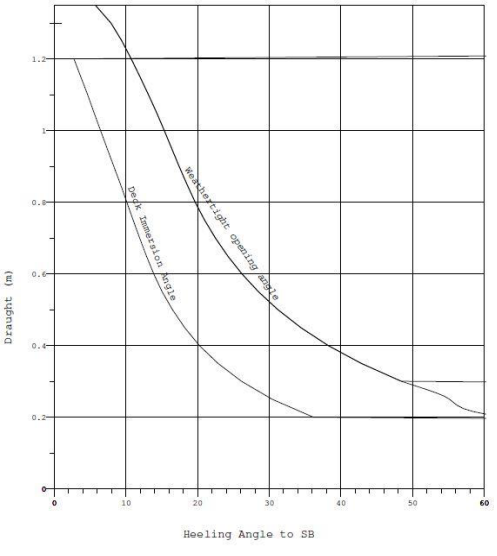

Figure 2. Deck immersion and weathertight opening angle

2.5. Deadweight scale and hydrostatics

The deadweight scale provides a method for estimating the increase in the ship's draught or determining the additional loads, that could be placed on the ship. The main use of the scale is to observe the deadweight at a given draught. In addition to presenting the relationship between draught and deadweight, it shows how the displacement depends on the density of the medium. With the same deadweight, but with a different density of water, the displacement of the ship changes.

By looking at the deadweight scale, we can see that for the project draught of 0.65 metres, the deadweight of the pontoon is 19.4 tons, given that the pontoon is located at the sea, and that it has a displacement of 59 tons.

The hydrostatic data of the residential pontoon are shown for trim values of 0 metres and trim values of -0.2, -0.1, 0.1 and 0.2 metres. The analysis took into account the thickness of the plating, which is 5 millimetres.

The analysis shows that the pontoon for a moulded draught of 0.65 metres has a displacement of 59 tons, immersed volume of 57 cubic metres, the longitudinal centre of buoyancy is 8.50 metres from the aft perpendicular, the transverse metacentric height is 5.15 metres, change of draught is 0.89 tons per centimetre and the moment to change trim is 1.1 tons meter per centimetre.

The pontoon at the trim of -0.2 meters does not have a precisely defined displacement of 59 tons. The interpolation obtained a draught value of 0.6385 metres, an immersed volume of 58.03 metres, the longitudinal centre of buoyancy is 8.86 metres from the aft perpendicular, the transverse metacentric height is 5,11 metres, the change of draught is 0.89 tons per centimetre and the moment to change trim is 1.1 ton metres per centimetre. Hydrostatic data for the trim of -0,2 m is presented in the following figure 3.

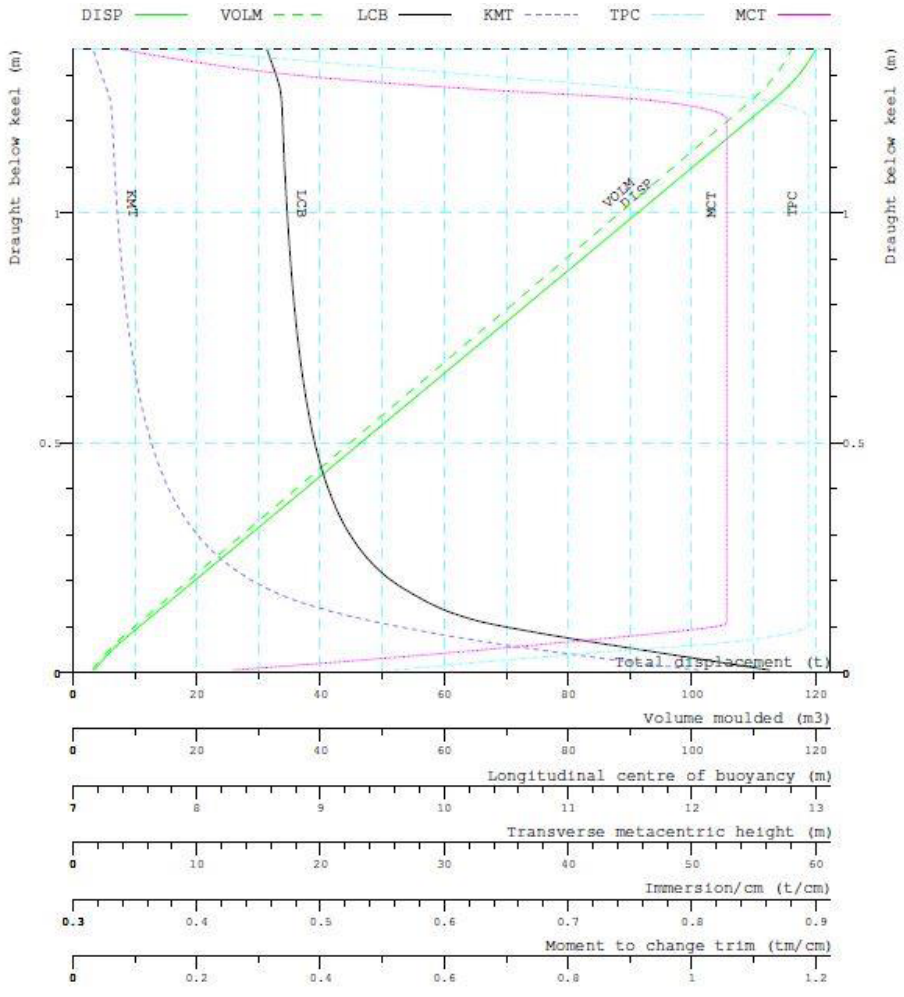

Figure 3. Hydrostatic data for the trim of -0,2 m

The pontoon at the trim of -0.1 metres for an initial displacement of 59 tons and draught of 0.65 m, immersed volume of 58 cubic metres, the longitudinal centre of buoyancy is 8.68 metres from the aft perpendicular, transverse metacentric height is 5.08 metres, the change of draught is 0.89 tons per centimetre and the moment to change trim is 1,1 ton metres per centimetre.

Interpolation showed that the pontoon at the trim of 0.1 metres has a draught of 0.6625 metres, the immersed volume of 57.26 cubic metres, the longitudinal centre of buoyancy is 8.3225 metres from the aft perpendicular, the transverse metacentric height is 5.137 meters, the change of draught is 0.89 tons per centimetre and the moment to change trim is 1.1 ton metres per centimetre.

Interpolation for the initial value of displacement of 59 tons at trim of 0.2 meters obtained the value of draught of 0.65 metres, the immersed volume of 57.5 cubic metres, the longitudinal centre of buoyancy is 8.145 metres from the aft perpendicular, the transverse metacentric height of metacentre is 5.13 metres, the change of draught is 0.89 tons per centimetre and the moment to change trim is 1.1 ton metres per centimetre.

2.6. Weight study

A very important step in both the preliminary and the final ship design stage is to asses as accurate as possible approximation of the various weight groups of the ship, and the position of their centroid. When determining the weight study, it is necessary to know the mass of each element that makes up the pontoon and where is located at, particularly the structural steel weight, but the present study takes into account other various weight groups such as for example, kitchen or solar panels on top of the deck.

Also, it is necessary to know the positions of the centre of gravity of individual masses. It is necessary to calculate the individual moments of mass (m_x, m_y, m_z) in order to obtain the centre of gravity of the masses as shown in table 2.

Table 2. Weight study of the pontoon

Opis predmeta	neto masa (kg)/jedinica	jedinica	ukupna količina	ukupna masa (kg)	x	mx	y	my	z	mz
Ormari	200	pcs	2	400	8473	3389000	0	0	2400	960000
Kuhinja	1000	pcs	1	1000	11250	11250000	1500	1500000	1850	1850000
Drveni podovi	9	m2	104	884	9191	8125278	-1000	-884000	1150	1016600
Keramičke pločice	22	m2	12	264	8510	2246640	-1500	-396000	1150	303600
Tepisi	4	m2	24	96	8513	817200	-2500	-240000	1150	110400
WC	25	pcs	2	50	8590	429500	-100	-5000	1500	75000
Bide	20	pcs	1	20	13680	273600	-2700	-54000	1500	30000
Umivaonici	20	pcs	2	40	8105	324200	-670	-26800	1675	67000
Tuš kabine	75	pcs	2	150	8495	1274175	45	6750	2150	322500
Stolice	28	pcs	2	56	8700	487200	1250	70000	1550	86800
Kauč	98	pcs	1	98	6150	602700	1350	132300	1550	151900
Stolić	50	pcs	1	50	7750	387500	1350	67500	1650	82500
Kreveti	250	pcs	2	500	7925	3962500	75	37500	1400	700000
Kuhinjski stol	50	pcs	1	50	10650	532500	-2440	-122000	1850	92500
Kuhinjske stolice	7	pcs	6	42	10650	447300	-2440	-102480	1850	77700
Ležaljke	25	pcs	4	100	7520	752000	-2425	-242500	1450	145000
Jacuzzi	1200	pcs	1	1200	13995	16794000	-410	-492000	4550	5460000
Zidni paneli	13	m2	72	936	8103	7584078	-79	-74334	2450	2293200
Nosači panela	1000	pcs	1	1000	9000	9000000	1	1000	3750	3750000
Vrata	15	pcs	5	75	7708	578100	301	22575	2150	161250
Staklene stijene	37	m2	61	2242	8986	20148073	1026	2300605	2450	5493390
Čelična rešetkasta konstrukcija	8500	pcs	1	8500	8733	74230500	-390	-3315000	3575	30387500
Fancooler	10	pcs	4	40	9000	360000	3400	136000	2450	98000
Plinska boca	20	pcs	1	20	10250	205000	3950	79000	1650	33000
Generator	120	pcs	1	120	9000	1080000	3400	408000	2450	294000
Temelji	100	pcs	1	100	9000	900000	3400	340000	1350	135000
Ograda	5	m'	80	400	11135	4454000	1	400	2790	1116000
Solarni paneli	11	m2	100	1125	6200	6975000	1	1125	4050	4556250
Ostalo	800	pcs	1	800	15000	12000000	-3580	-2864000	150	120000
Stepenice	5	pcs	15	75	16100	1207500	-1500	-112500	2450	183750
Trup ponona	16800	pcs	1	16800	8631	145000800	204	3427200	818	13742400
Margina	2000	pcs	1	2000	8631	17262000	204	408000	818	1636000
			TOTAL	39.233	9000	353080343	0	7340	1925	75531240

The total mass of the pontoon is 39233 kg, and the centre of gravity of the system has coordinates x = 9000 mm, y = 0 mm and z = 1925 mm.

2.7. Tank capacity

For further analysis of tanks loading, data on the location of tanks on the pontoon, their volume, mass and moments of inertia are required. The analysis of the weight study of tank consumables was performed on the principle of analysis of the weight study of mass, but it was supplemented by the moment of inertia for the calculation of the moment of free surfaces. The tanks considered are water tank, sewage tank or optional fuel tank. Table 3. shows capacity plan of the sewage tank with its net volume, eater plane area, longitudinal, transverse and vertical center of gravity and moments of inertia.

Table 3. Capacity plan of the sewage tank

FILL %	LEVEL FROM BASEL. m	LEVEL FROM BOTTOM m	NET VOLUME m3	W.PLANE AREA m2	CENTRE OF GRAVITY LONG m	CENTRE OF GRAVITY TRANSV m	CENTRE OF GRAVITY VERT m	INERTIA MOMENT m4
0.0	0.000	0.000	0.00	3.2	3.025	-2.575	0.001	0.3
0.1	0.001	0.001	0.00	3.2	3.025	-2.575	0.001	0.3
0.2	0.002	0.002	0.01	3.2	3.025	-2.575	0.001	0.3
0.3	0.003	0.003	0.01	3.2	3.025	-2.575	0.002	0.3
0.4	0.005	0.005	0.01	3.2	3.025	-2.575	0.002	0.3
0.5	0.006	0.006	0.02	3.2	3.025	-2.575	0.003	0.3
0.6	0.007	0.007	0.02	3.2	3.025	-2.575	0.003	0.3
0.7	0.008	0.008	0.02	3.2	3.025	-2.575	0.004	0.3
0.8	0.009	0.009	0.03	3.2	3.025	-2.575	0.005	0.3
0.9	0.010	0.010	0.03	3.2	3.025	-2.575	0.005	0.3
1.0	0.012	0.012	0.04	3.2	3.025	-2.575	0.006	0.3
2.0	0.023	0.023	0.07	3.2	3.025	-2.575	0.012	0.3
3.0	0.035	0.035	0.11	3.2	3.025	-2.575	0.017	0.3
4.0	0.046	0.046	0.14	3.2	3.025	-2.575	0.023	0.3
5.0	0.058	0.058	0.18	3.2	3.025	-2.575	0.029	0.3
10.0	0.115	0.115	0.36	3.2	3.025	-2.575	0.057	0.3
15.0	0.172	0.172	0.54	3.2	3.025	-2.575	0.086	0.3
20.0	0.230	0.230	0.71	3.2	3.025	-2.575	0.115	0.3
25.0	0.287	0.287	0.89	3.2	3.025	-2.575	0.144	0.3
30.0	0.345	0.345	1.07	3.2	3.025	-2.575	0.172	0.3
35.0	0.402	0.402	1.25	3.2	3.025	-2.575	0.201	0.3
40.0	0.460	0.460	1.43	3.2	3.025	-2.575	0.230	0.3
45.0	0.518	0.518	1.61	3.2	3.025	-2.575	0.259	0.3
50.0	0.575	0.575	1.78	3.2	3.025	-2.575	0.287	0.3
55.0	0.633	0.633	1.96	3.2	3.025	-2.575	0.316	0.3
60.0	0.690	0.690	2.14	3.2	3.025	-2.575	0.345	0.3
65.0	0.747	0.747	2.32	3.2	3.025	-2.575	0.374	0.3
70.0	0.805	0.805	2.50	3.2	3.025	-2.575	0.402	0.3
75.0	0.862	0.862	2.68	3.2	3.025	-2.575	0.431	0.3
80.0	0.920	0.920	2.86	3.2	3.025	-2.575	0.460	0.3
85.0	0.978	0.978	3.03	3.2	3.025	-2.575	0.489	0.3
90.0	1.035	1.035	3.21	3.2	3.025	-2.575	0.518	0.3
95.0	1.093	1.093	3.39	3.2	3.025	-2.575	0.546	0.3
96.0	1.104	1.104	3.43	3.2	3.025	-2.575	0.552	0.3
97.0	1.115	1.115	3.46	3.2	3.025	-2.575	0.558	0.3
98.0	1.127	1.127	3.50	3.2	3.025	-2.575	0.563	0.3
99.0	1.138	1.138	3.53	3.2	3.025	-2.575	0.569	0.3
100	1.150	1.150	3.57	3.2	3.025	-2.575	0.575	0.3

2.8. Free surfaces

The level of liquid or bulk that can be moved is called the free surface. Any weight on the ship whether added to the ship during boarding, unloading or just moving around the ship causes the moving the centre of gravity of the ship's system. When tilting, the slope of the liquid surface in the tank or the level of bulk cargo in the warehouse changes and their centre of gravity changes in the direction of the ship's tilt, which creates a moment of free surface acting in the direction of the ship's tilt and the ship's centre of gravity shifts systematically.

It is important to emphasize that due to the influence of free surface there is a loss of the actual metacentric height and a decrease in the lever of stability in relation to the initial state. The loss occurs regardless of where the liquid on board is.

2.9. KN Cross curves

Cross curves represent the distance between the points K and N at a given draught and the heel of the ship. Cross curves are used to determine the stability lever of the ship. Figure 4 depicts the KN curves with respect to drought,

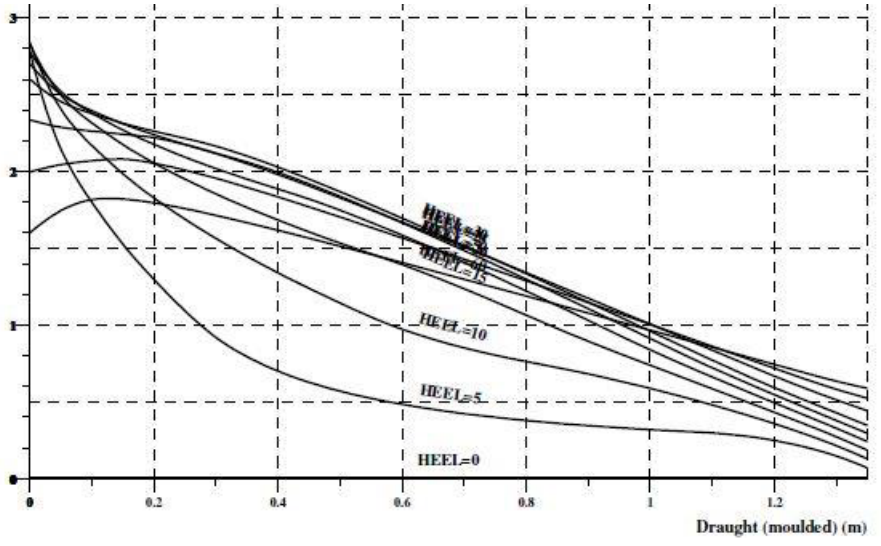

Figure 4. Pontoon KN curves

2.10. GM Limit curves

The GM limit curves show the values of the minimum metacentric height curves for a draught of 0 meters up to a moulded draught of 0.65 metres. This curve separates the area where the metacentric heights did not meet the stability criteria (restricted area) and the area of allowed metacentric heights. It should also be noted that GM limit curves are constructed without the influence of free surfaces of liquids in tanks so that to obtain accurate results one should calculate the actual metacentric height corrected for the influence of free surfaces and check whether the value obtained is greater or less than the minimum metacentric height GM.

In addition to the GM limit curves, the curves of the maximum height of the centre of gravity KG are made in the same way. They also show two areas of allowable and impermissible values according to stability criteria. They are also shown as functions of the centre of gravity of the system and the draught for a particular trim.

The determination criteria DCRI for the minimum and maximum metacentric height for the trim of 0.2 m is given in the following figure 5,

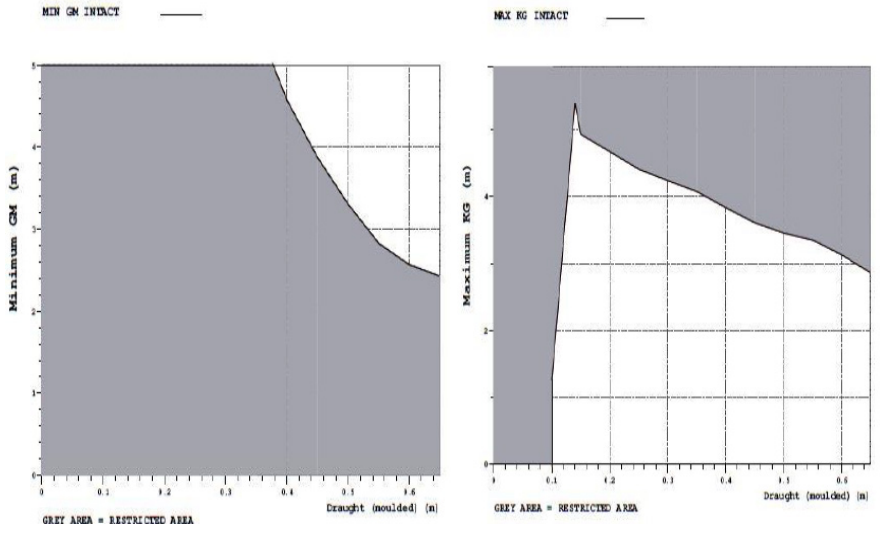

Figure 5. Minimum and maximum metacentric heights for the trim of 0.2 m

2.11. Loading conditions

A pontoon stability check will be shown for four cargo loading cases. In these cases, the percentage of tanks filled with consumables and the combination with or without the crowding of passengers on the side of the pontoon will differ. In addition, the pontoon will be exposed to a wind gust of 170 km/h.

Cases in which the criteria of stability, crowding of passengers on the side, strong wind and minimal freeboard will be examined are the case of a lightship, the case of a pontoon whose freshwater, fuel oil and sewage tank capacities are filled with 10% consumables, the case of pontoons whose tanks are filled 50% consumables and passengers are on the side of the pontoon and the case when the tanks are completely full and the passengers are piling up on the side of the deck.

2.11.1. Lightship

In the first case of the stability test, the lightship was tested, i.e. the case of pontoons of empty tanks and without passengers. In this case, there is no influence of free surfaces and the value of the corrected distance from the keel to the centre of gravity KGcorr and the corrected metacentric height GMcorr is their actual value. Intact stability criteria is provided in table 2 as well as on figure 2.

Table 4. Intact stability criteria for the lightship condition

Stability criteria	Required	Attained unit	Status
GM > 0,35	0.350 m	5.500 m	OK
Minimum range of stability > 20°	20.000°	57.573°	OK
Area under *GZmax* > 0,092 mrad	0.092 mrad	0.245 mrad	OK
Residual freeboard > 0,010 m	0.010 m	0.714 m	OK
Maximum heel caused by crowding of passengers < 10°	10.000°	0.826°	OK
Heeling angle due to wind < 16° or < 80% of the angle at which the deck dives	12.356°	1.296°	OK

In addition to the stability criteria, the value of the stability margin is also checked. Stability margin is the value when the corrected distance from the keel to the centre of gravity KGcorr is subtracted from a maximum distance from the keel to the centre of gravity KGmax, i.e. when the value of the minimum metacentric height GMmin is subtracted from the corrected metacentric height GMcorr. The margin value must be greater than or equal to zero and the difference between the two operations must be equal.

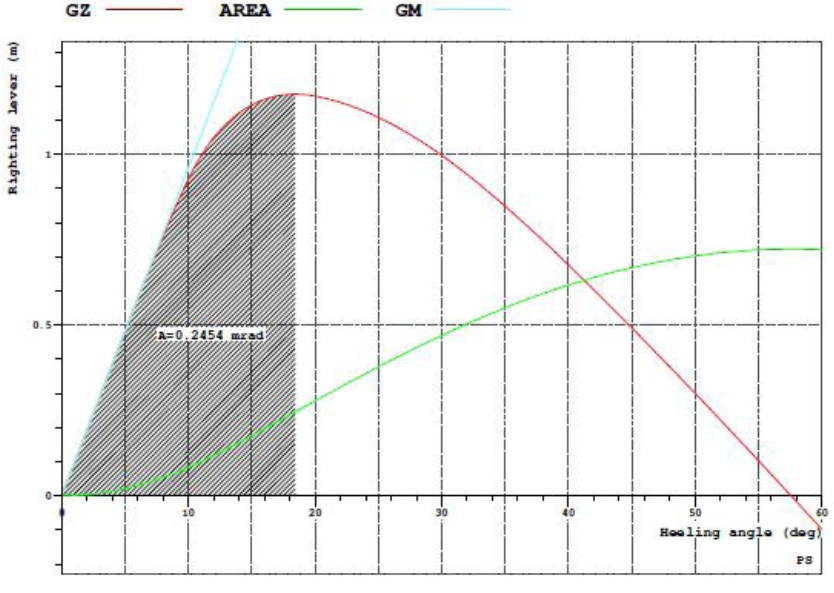

Figure 6. Intact stability criteria for the lightship condition.

2.11.2. Pontoon with 10% consumables without passengers

Another case of stability testing relates to a pontoon whose water, fuel oil and sewage tanks contain 10% liquid. This means that in this case, a moment will occur due to the influence of free surfaces.

In the diagram of the stability lever, in addition to the values of the stability lever GZ and the metacentric height GM, the values at which the openings on the deck are immersed in water and progressive flooding occur are shown. It can be seen that the opening of the freshwater tank (FW) and the opening of the empty space (BAR) is immersed in water at 33.7°. It can also be seen that the fuel oil tank opening (FO) is immersed at 38.9° and the sewage tank opening (SEW) at 41.6° as given in table 3.

Table 5. Intact stability criteria for the pontoon with 10% consumables without passengers

Stability criteria	Required	Attained unit	Status
GM > 0,35	0.350 m	5.150 m	OK
Minimum range of stability > 20°	20.000°	33.403°	OK
Area under *GZmax* > 0,092 mrad	0.092 mrad	0.236 mrad	OK
Residual freeboard > 0,010 m	0.010 m	0.691 m	OK
Maximum heel caused by crowding of passengers < 10°	10.000°	1.092°	OK
Heeling angle due to wind < 16° or < 80% of the angle at which the deck dives	12.356°	1.562°	OK

Due to the influence of the moment of free surfaces, the centre of gravity of the pontoon KG increases and the metacentric height GM decreases. During the analysis, the free surface correction is subtracted or added from the actual value of KG and GM. In further analysis, the value of the corrected distance from the keel to the centre of gravity of the pontoon KGcorr and corrected metacentric height GMcorr is taken instead of the initial value of KG and GM.

2.11.3. Pontoon with 100% consumables with passengers on the deck

The third case of loading the pontoon with cargo describes the case when the pontoon tanks are 100% full and the passengers are on the side of the pontoon as seen on figure 7.

In this case, as in the case of a lightship, there will be no impact of free surfaces, but due to the accumulation of passengers on the side of the deck, a moment is created that affects stability and the criterion of crowding of passengers on the side should be met.

The crowding of passengers is calculated by moving ten passengers weighing 75 kilograms from the middle of the pontoon to the very edge of the pontoon.

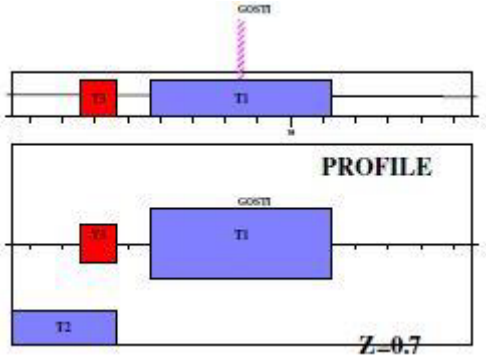

Figure 7. Schematics of the pontoon with 100% consumables with passengers on the deck

It can be seen that the sewage tank opening (SEW) is immersed in water at 23.5°, the fuel oil tank opening (FO) at 23.7°, the freshwater tank opening (FW) and the empty space opening (BAR) are immersed in water at 24.5° shown in table 4.

Table 6. Intact stability criteria for the pontoon with 100% consumables with passengers on the deck

Stability criteria	Required	Attained unit	Status
GM > 0,35	0.350 m	3.68 m	OK
Minimum range of stability > 20°	20.000°	21.007°	OK
Area under *GZmax* > 0,092 mrad	0.092 mrad	0.146 mrad	OK
Residual freeboard > 0,010 m	0.010 m	0.447 m	OK
Maximum heel caused by crowding of passengers < 10°	10.000°	3.287°	OK
Heeling angle due to wind < 16° or < 80% of the angle at which the deck dives	12.356°	6.667°	OK

2.11.4. Pontoon with 50% consumables with passengers on the deck

In the latter case, there is a test of the stability of the pontoon with 50% of the consumables in its tanks and the passengers on the pontoon. In this case, there will be two problems, namely the moment due to the influence of free surfaces and the moment due to the crowding of passengers on the side of the pontoon.

From the stability lever diagram, it can be seen that the unprotected openings of the freshwater tank (FW) and the empty space opening (BAR) are immersed in water at 28.7°. The fuel oil tank orifice (FO) is immersed at 30.2° and the sewage tank (SEW) is immersed in the sea at 30.9° presented in table 5.

Table 7. Intact stability criteria for the pontoon with 50% consumables with passengers on the deck

Stability criteria	Required	Attained unit	Status
GM > 0,35	0.350 m	4.310 m	OK
Minimum range of stability > 20°	20.000°	27.424°	OK
Area under *GZmax* > 0,092 mrad	0.092 mrad	0.201 mrad	OK
Residual freeboard > 0,010 m	0.010 m	0.600 m	OK
Maximum heel caused by crowding of passengers < 10°	10.000°	2.085°	OK
Heeling angle due to wind < 16° or < 80% of the angle at which the deck dives	12.356°	2.519°	OK

3. Conclusion and comments

In this paper, a residential pontoon is modelled. On the mathematical model of the pontoon, a stability calculation was performed for four loading conditions. The first state is a lightship, the second is a state without passengers when the tanks are 10% full. The third state is at 100% filled tanks with passengers on deck. The fourth and final state of loading is when the tanks are filled with 50% and when the passengers are on the side, more precisely on the edge of the deck.

It is important to note that for these loading conditions, factors such as the impact of free surfaces, crowding of passengers on the side and side wind gusts must be taken into account. The terms listed in the calculation represent variables that can negatively affect the results when calculating pontoon stability.

As an example, we can cite the problem closely related to free surfaces that directly affect the reduction of GM metacentric height and the centre of gravity KG of the pontoon system. As a result, the GZ stability lever decreases. For all loading conditions, the metacentric height was higher than the given criterion (GM> 0.35 m) and we can conclude that the criterion was met.

The range of positive stability levers must be greater than 20°. It is important to know that during the progressive flooding of tanks through the tank openings, the stability diagram is interrupted. The smallest dive angle of the tank opening was obtained for the case of “100% consumables with passengers on deck” where the

opening of the sewage tank (SEW) was immersed in water at 23.5°. From this, it can be concluded that the criteria are met in this part of the analysis.

The area bounded by the stability lever curve and the vertical descending from the highest point of the curve (GZmax) to the abscissa must be greater than 0.092 metre-radians. The above criterion is also met for all loading conditions.

Considering that in the worst case the minimum height of the overhang is 0.447 m, and the prescribed criterion is 0.01 m, we can conclude that the results in this part of the analysis are very conservative.

The slope caused by a wind speed of 170 km/h was in all cases less than the initial condition prescribing a slope of less than 16° or 80% of the value of the deck dive angle.

The slope criterion caused by the crowding of passengers is not specified in individual loading conditions but as a criterion that is then tested for all loading conditions. Theoretically, this could be avoided by making two groups of loading, with and without passengers. In other words, this criterion, like other moments, does not change the displacement, deadweight, draught, trim, heel and more. It depends on the number of passengers on board and their hypothetical shift. It tests what would happen if a passenger (in this case 10) moved from the symmetrical plane CL to the side. In case there are no passengers, it can be easily ignored, which is the case in two loading states (lightship and pontoon with 10% consumables without passengers).

All stability criteria are met for all loading conditions.

As these type of objects get more popular and a nice alternative for living quarters or a great way to get a family, group of friends, or work retreat out on the water, a following figure 3 presents an idea of the possible resort of such floating houses.

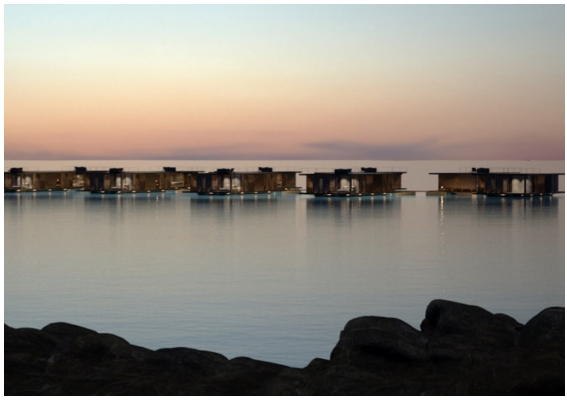

Figure 3. Floating houses resort

References

1. Miletić, E. (2020) Plovnost i stabilitet pontona za kuću za odmor. *Završni rad*, Tehnički fakultet, Rijeka.
2. Pravila za statutarnu certifikaciju pomorskih brodova. (2015) *dio 4. stabilitet*, prilog 4. Zahtjevi za stabilitet plovećih dizalica, pontona, plovnih dokova i brodova stalno spojenih s obalom, 4.1 Pontoni, 4.1.9 Zahtjevi za stabilitet, HRB. usvojeno 19. svibnja 2015. godine.
3. Pravila za statutarnu certifikaciju pomorskih brodova. (2015) *dio 4. stabilitet*, prilog 3. Dodatni zahtjevi za stabilitet, 3.1 Putnički brodovi, HRB usvojeno 19. svibnja 2015. godine.
4. Pravila za statutarnu certifikaciju pomorskih brodova. (2015) *dio 4. stabilitet*, prilog 2. Opći zahtjevi za stabilitet, 2.1 Opći kriteriji stabiliteta neoštećenog broda, 2.1.5. Kriterij jakog vjetra i ljuljanja broda (kriterij vremenskih prilika), HRB usvojeno 19. svibnja 2015. godine.
5. Uršić, J. *Stabilitet broda. I i II dio*, (1964) Fakultet strojarstva i brodogradnje, Zagreb.
6. KN curves problem. (2020) Available from: https://www.boatdesign.net/threads/kn-curves-problem.46049/ [Accessed 3. 8. 2020.]
7. Babicz, J. *Wärtsilä Encyclopedia of Marine Technology* (2015) Helsinki.
8. Dokkum, K., Katen, H., Koomen, K., & Pinkster, J. (2010) *Ship stability*. DOKMAR, Enkhuizen.

ISSN 0554-6397
Stručni članak
(*Professional paper*)

Lovro Radoš
Obrtnička industrijska i graditeljska škola, Avenija Većeslava Holjevca 13, Zagreb
Anton Turk
E-mail: aturk@riteh.hr
Dunja Legović
Tehnički fakultet, Sveučilište u Rijeci, Vukovarska 58, Rijeka, Croatia

Comparison Between the Classical Method of Inclining Experiment with the Recent Alternative Methods

Abstract

The classical method of inclining experiments has been used to determine the position of the ship's vertical center of gravity for many years. The method contains some basic assumptions, which is why the accuracy of the method has been debated in the last few years. Modern ships often have chines, or pronounced flare at fore and aft extremities, that can lead to a significant change in the waterline. The position of the metacenter changes on these ships as they incline. Therefore, the calculation of the ship's center of gravity by the classical method may be inaccurate.
In this paper, three different methods that are not based on the assumption of an unchanged metacenter are examined. Using a graphical, polar, and general method, the position of the ship's center of gravity system can be determined for any ship without determining the position of the metacenter. The three methods mentioned in this paper were observed and tested on four different ships. In addition, the results of the classical method are compared with the results obtained from recently developed methods.

Keywords: stability, inclining experiment

1. Introduction

In order to determine a ship's stability attitude, the inclining experiment is performed on a vessel to obtain the lightship weight and the coordinates of the centre of gravity. The test is applied to new constructions, and to ships that have gone through a major redesign. Inclining experiments are specified for all ships by the IMO and other international associations and mandatory as of 2009 (SOLAS Reg. II-1/5 (IMO, 2009)) for each merchant ship over 24 meters in length and for all passenger ships [1].

The procedure for determining the lightship condition centre of gravity, defined as the centre of mass of the vessel and its cargo, dates to a couple of hundred years ago. The need for such a procedure stems from the inherent errors in measured mass and position of individual items, while performing the summation of moments applied by individual loads.

The classical method has been in use almost as a dogma that was accepted by naval architects without really being questioned or doubted. Probably the reason behind it was its convenience, despite the well-known fact that the current method for calculating a ship's vertical centre of gravity following inclining experiments has its limitations in magnitude of applied heel angle and reliability accomplished for certain hull-forms (chines, knuckles, deadrise). The change in the metacentre with constant displaced volume during the incline is proportional to the change in the second moment of the waterplane area. Furthermore, the change in the waterplane area can be disregarded especially for wall-sided vessels due to equal immersed and submerged wedges of buoyancy volume thus, the so-called wall-sided assumption. However, the wall sided assumption has nothing to do with a constant waterplane area nor metacenter position.

Quite recently, three novel methods were proposed. The first method was originally proposed in a paper titled Up Against the Wall [2], where the need for an alternate method was discussed. A more thorough explanation of Dunworth's proposed method was later published as Back Against the Wall [3]. Using a preliminary experimental model validation, Beyond the Wall was presented in [4]. Note that all the papers have the "wall" appellation. As the titles suggest, an emphasis is given to challenge such a norm. It has its meaning considering that the Classical method uses the wall-sided assumption due to the hypothesis of unchanged metacentre position when the vessel is heeled. "Up against the wall" was an attempt to challenge the classical method, even more so in "Back Against the Wall", and finally a confirmation was published with "Beyond the Wall", containing numerical and model validation. The last paper was by Smith et al. [5] set out to confirm the validity of the newly-proposed method through the work-up of results to explore the potential issues of implementation and broader utility in future application.

When initial results turn out to be promising, the resources that might have been consumed by a large initial study are often better directed toward follow-up studies that further develop the idea, such as the work of Kanifolskyi and Konotopets [6]. Their method is deemed as Graphical method.

Also, an independent validation of promising initial results is essential. For the more common situation, where the idea fortunately turns out to be on-target, a validation and novel propositions may be even more useful. Therefore, the work from Karolius, and Vassalos "Tearing down the wall" [7] resulted with the method called Polar method. In this case, the "wall" is again highlighting the need to tear down the wall-sided assumption implicit in the Classical method.

When the idea is a fundamental breakthrough, this will usually be apparent from a relatively small study. However, there was some follow up work (Another blow on

the torn wall) from Ozsayan and Taylan [8] where all three methods were tested along with uncertainty analysis.

A much larger sample size does not produce much additional value. Therefore, the aim of this paper is to validate the methods on four river vessels which will be explained in the following sections.

2. Inclining experiment procedure

In order to achieve accuracy, the inclining experiment is performed free of mooring restraints, in calm weather and still water condition. Basically, by moving weights transversely as illustrated in Figure 1., the metacentric height *GM* is obtained. By using known hydrostatic curves and by reading the draft, the displacement of a vessel Δ can be readily determined. The *GM* magnitude, which dominates stability, can be estimated from the design, but the inclining test gives a more reliable value of this parameter [9].

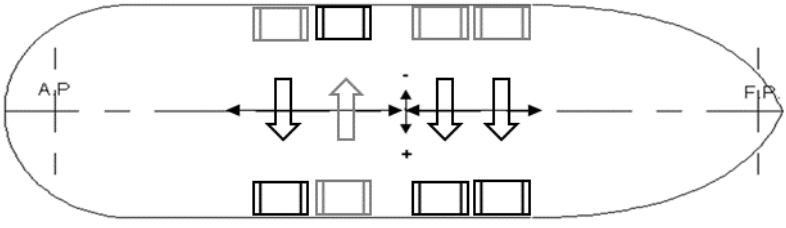

Figure 1. Sequence of weight shift

Each weight shift sequence is noted as in Table 1., where the heel values are measured typically by pendulum, but also by U-tubes or inclinometer.

Table 1. Inclining experiment calculation for each weight shift

Movement (n)	Mass Group	Direction moved P -> S or S->P	Incline Mass (t) (w)	Distance moved (m) (d)	Heeling Moment $(m) = (w) \times (d)$	Pendulum reading m (+,-)	Pendulum deflection (m) (x)	$\frac{w \times d}{x} = x_z$	Running Average $\frac{1}{n}\sum_{i=1}^{n} x_z$	Running Deviation	Deviation from Final Average
x											
x+1											
							Final sum of $\frac{w \times d}{x}$				
							Final average $\frac{w \times d}{x}$				

The heeling angle for each load movement and for each pendulum separately is determined by the expression:

$$tg\delta\theta_i = \frac{s_i}{\lambda} \tag{1}$$

where the paramteres are:
s_i - actual deflection, mm
λ - excess length of wire from the hanger to the upper edge of the measuring rod, mm

3. Inclining experiments methods

3.1. Classical method

The individual metacentric height is determined by the expression:

$$GM_i = \frac{p_i \times e_i}{\Delta \times g \times tan\delta\theta_{si}} \tag{2}$$

where the values are as follows:
p_i - weight of test load, kN
e_i - load transfer arm, m
Δ - displacement of the vessel, t
g - acceleration of gravitational force, m / s^2
$tan\delta\theta_{si}$ - mean tangent of the angle of inclination for individual measurement, °.

The position of the center of gravity of the vessel is calculated according to the formula:

$$VCG = KM - GM \tag{3}$$

where:
$VCG = KG$ - vertical center of gravity of the system, m
KM – vertical position of the metacentre, m
GM - metacentric height, m

When certain tanks have to be left partially filled, it is necessary to correct the height of the center of gravity of the system due to the influence of the free surfaces of liquids, using the expression:

$$VCG = KM - GM - FSC \tag{4}$$

in which:
FSC - free surfaces correction, m

Some individual measurements may prove inaccurate when performing the experiment, and therefore may not be taken into account when processing the experimental data. In order to detect such inaccurate measurements, it is useful to create a control graph, in which the values of the heeling moment are plotted against *tan* ϕ obtained from the pendula deflection relationship (1). An example of performing a control chart is shown in Figure 2 for portside and starboard respectively.

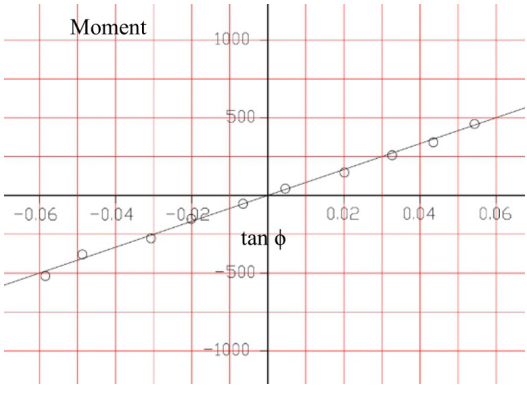

Figure 2. Moment versus tan ϕ diagram

The *GM* value can be calculated as the regression slope using a least square fit:

$$GM = \frac{1}{\Delta R_{slope}} \tag{5}$$

The Classical method is dependent on the heel angle magnitude and doesn't depend on the value of the transversal center of gravity (*TCG*) but instead it depends on the direction and extent of the metacentre shift.

Even though the three new methods specifically target the wall-sided assumption in the classical method, there is no assumption of wall sidedness in the method itself. The wall sided assumption comes from the simplified formula for calculating *GZ* for wall sided vessels. A form, in which *GZ* can be analytically derived, such as a box shaped pontoon for example, also has a change in the waterplane area when heeled which leads to subsequent change in metacentre position.

The 2008 IS Code provides, both mandatory requirements and recommended provisions relating to intact stability in which the change in metacenter position is shown to be small within the 4-degree heel limit for wall sided vessels. As mentioned in [7] a "possible problem" stems from the fact that specialized hull-forms might have excessive changes in the waterplane when heeled due to the chines, flares, and it is not an indictment of the wall-sidedness of a vessel, therefore it should be allowed even within the IMO constraints.

3.2. Generalised method [2,3,4,5]

After shifting the weights, the vessel returns to equilibrium, which means that for each moment of heeling there is a righting moment equal to the amount of heeling moment, and this equality is shown in (6).

$$\Delta \times HZ = B_M GZ \tag{6}$$

where the displacement is equal to the buoyancy force, so the equation reduces to:

$$HZ = GZ \tag{7}$$

That is, the heeling moment arm is equal to the righting moment arm, the tilt moment is:

$$M_{ng} = w \times d \times cos\varphi \tag{8}$$

when the heeling moment is divided by the displacement, the heeling moment arm is obtained:

$$HZ = \frac{w \times d \times cos\varphi}{\Delta} \tag{9}$$

Displacement, draft and initial inclination of the vessel are determined from the hydrostatic curves, after the draft has been read. For each weight movement, the slope change is determined by the excess and summed with the initial slope to obtain the actual slope. The average value of the angle of inclination is used for the calculation, for all cases of measuring the angle of inclination. Each time the weight is moved, the vessel can be tested for exact displacement, trim and heel, and the *KN* values can be determined using a specific software package or hydrostatic data. *KN* refers to the cross curves of stability, and it is defined as the distance from the keel point to the point of intersection of the two directions. The first direction is parallel to the waterline and passes through the keel point, the second direction passes through the center of gravity and is perpendicular to the first direction as seen on Figure 3 [3].

Thereafter, the arm of the upright moment and the inclination can be determined using the equations:

$$GZ = KN - VCG_1 sin\varphi - TCG_1 cos\varphi \tag{10}$$

$$HZ = KN - VCG_1 sin\varphi - TCG_1 cos\varphi \tag{11}$$

When φ = 0, then *sin* φ = 0 and *cos* φ = 1, we have:

$$TCG_1 = KN_0 - HZ_0 \tag{12}$$

Duckworth proposed plotting the *HZ* values as a third order polynomial where intercept point of y-axis for $\phi = 0$ corresponds to HZ_0.

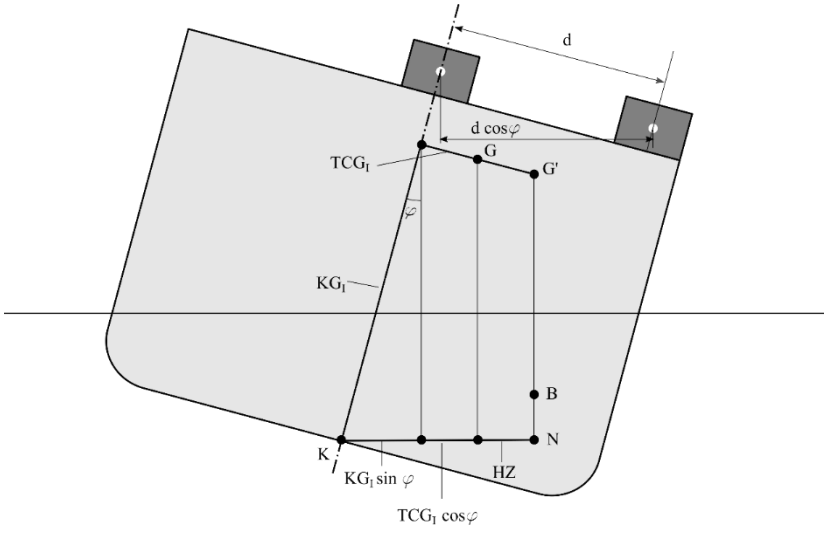

Figure 3. Overview of the generalized method as in [5]

$$VCG_1 sin\varphi = KN - HZ - TCG_1 \times cos\varphi \tag{13}$$

The proposed method does not refer to the metacenter and has no associated errors, and can be used for any shape and form and up to any angle of inclination.

3.3. Graphical method [6]

The graphical method calculates the height of the center of gravity directly through the *KN* and the heeling moment of the vessel. *KN* is determined with the help of hydrostatic data or using a software package. According to the proposed method five steps are shown in the Figure 4.

1. Draw a *KN* for the deflection of an angle equal to the slope of the vessel or of the slope of the waterline, given that the cross section of the vessel is shown vertically,
2. Draw a vertical line on the *KN*,
3. Using equation (9) calculate the value of *HZ*.
4. In the fourth step, it is necessary to draw *HZ* on the drawing parallel to *KN* and place it so that it connects the symmetrical axis with the perpendicular to *KN*.

5. The *VCG*, the intersection of the symmetrical axis and *HZ* is the position of the center of gravity in height.

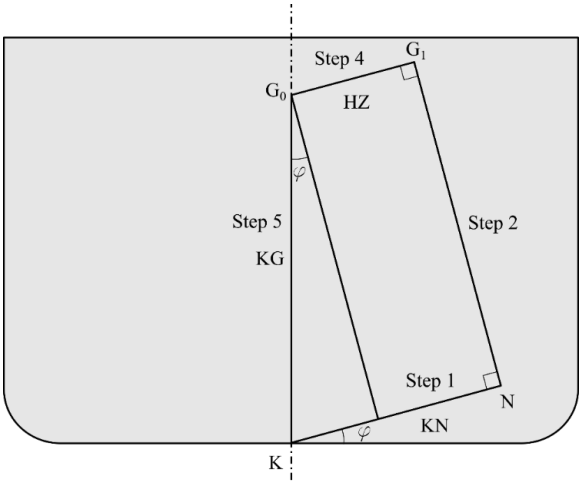

Figure 4. Graphical method display as in [6]

The final value of *KG* is obtained as the average value of all values obtained by the inclining experiment and is calculated by the equation:

$$VCG = \frac{\sum_{i=1}^{n} VCG_i}{n} \tag{14}$$

Also KG can be determined within the graphical method by calculation through trigonometric relations, when we know KN and the angle of inclination φ, KG is then determined using the equation:

$$VCG = \frac{KN - HZ}{\sin\varphi} \tag{15}$$

$$VCG\sin\varphi = KN - HZ \tag{16}$$

By comparing equation (16) of the graphic method with equation (13) of the general method, we can conclude that these are similar methods, but the graphical method does not take into account the position of the center of gravity over the breadth of the vessel. Therefore, the graphical method is accurate only for those vessels where the initial angle of inclination of the vessel is half a degree. For those vessels with a higher initial angle of inclination errors occur when calculating the value of the vertical center of gravity.

3.4. Polar method [7]

The polar method was the last of the three proposed methods. The method considers a line parallel to the metacentric radius, shifted up to the distance of heeling lever *HZ*, and this is shown in polar coordinates. The method is based on the fact that the position of the vertical and transverse center of gravity is in that direction in the initial position and remains constant in that position for each individual movement of weights during the experiment. That is, the starting position of the center of gravity lies constantly on the line while the total position of the center of gravity changes by the distance G_0G_i for each weight movement. The method is shown in Figure 5.

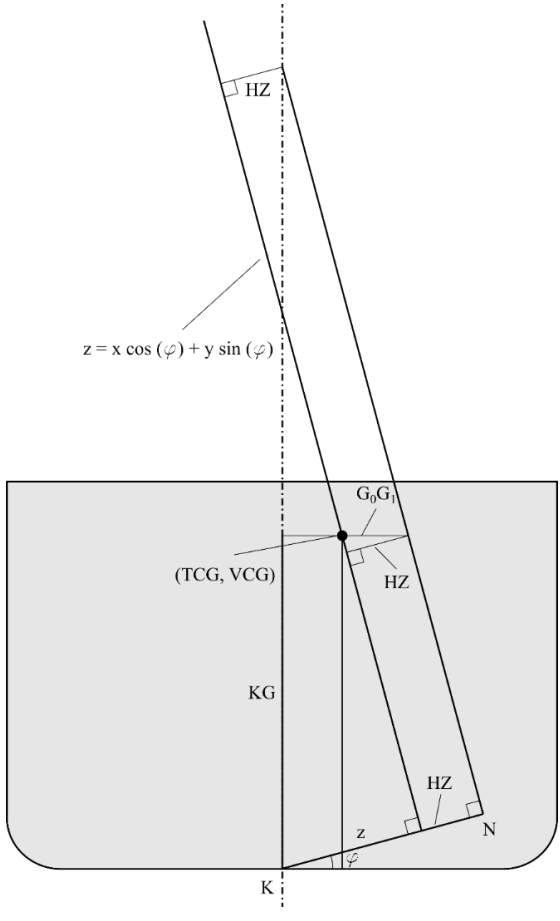

Figure 5. Polar method display as in [7]

The equation of line is given by the expression:

$$z = xcos\varphi + ysin\varphi \tag{17}$$

and knowing that the *x* coordinate is equal to the position of the transverse center of gravity and y vertical center of gravity at the following expression is obtained:

$$z = TCGcos\varphi + VCGsin\varphi \tag{18}$$

Also, *z* can be calculated using the following equation:

$$z = KN - HZ \tag{19}$$

that is, by including equation (18) in (19) we obtain:

$$KN - HZ = TCGcos\varphi + VCGsin\varphi \tag{20}$$

From known conditions:

$$TCG_0 = TCG_i \tag{21}$$

$$VCG_0 = VCG_i \tag{22}$$

The final equations can be established:

$$VCG = \frac{\left(KN_i - HZ_i\right)cos\varphi_0 - \left(KN_0 - HZ_0\right)cos\varphi_i}{cos\varphi_0 sin\varphi_i - sin\varphi_0 cos\varphi_i} \tag{23}$$

$$TCG = \frac{\left(KN_i - HZ_i\right)sin\varphi_0 - \left(KN_0 - HZ_0\right)sin\varphi_i}{cos\varphi_i sin\varphi_0 - sin\varphi_i cos\varphi_0} \tag{24}$$

If the vessel is symmetrical, i.e. the initial angle of inclination equals zero, the expressions are reduced to:

$$VCG = \frac{\left(KN_i - HZ_i\right)}{sin\varphi_i} \tag{25}$$

$$TCG = 0 \tag{26}$$

As with the previous methods, *KN* is calculated using a stability software model, i.e. actual 3D stability model and *HZ* using equation (9). The model should be free to

equilibrate in terms of trim when heeled. Values from a stability booklet originating from a stability 3D model may be used (interpolated values), but would introduce additional errors, and should be highlighted [7].

The polar method is general and applies to any initial inclination of the vessel.

4. Implementation of the methods

The calculation of the ship's center of gravity system is calculated according to the procedures and equations proposed in Section 3. The main particulars for the vessels chosen for testing of the calculation methods are presented in Table 2. The calculation is made for the following four ships:

Table 2. Ship characteristics

	LOA, m	*D,* m	*B,* m	*T,* m
Work vessel	42.0	2.0	8.0	0.78
Tugboat	54.8	3.85	16.2	2.8
Passenger ship	26.6	1.64	4.14	0.8
F41Container ship	163.0	18.6	32.0	11.8

Due to the extensive report for all those ships the results using each of the novel methods will be presented for container ship only. The container ship is chosen due to the design features, such as knuckles, larger flare angles, sharper chine lines and other nonconventional hull attributes. Additionally, the results will be presented for the work vessel using the generalized method, the tugboat with the graphical method and the passenger ship by implementing polar method.

For the real physical inclining experiment, the readings the *VCG* results are presented. With the influence on the stability margins whilst considering the error potential, the new corrected *VCG* values are included for each implemented method.

Table 3 shows the results of the calculation for the container ship by the general method. The value of *VCG* calculated by the generalized method for the container ship is 10,024 m.

Table 3. Calculation of the center of gravity of a container ship obtained by the generalized method

	tan φ	φ	Σ φ	φ	*HZ*	*KN*	sin φ	*VCG* sin φ
		°	°	rad	m	m		
0	0.000	0.000	0.032	0.001	0.072	-0.002	0.001	-0.002
1	-0.009	-0.521	-0.490	-0.009	-0.039	-0.110	-0.009	-0.081
2	-0.018	-1,003	-0.971	-0.017	-0.074	-0.239	-0.017	-0.171
3	0.009	0.493	0.525	0.009	0.037	0.135	0.009	0.088
4	0.002	0.091	0.123	0.002	0.000	0.200	0.018	0.186
5	0.008	0.464	0.496	0.009	0.034	0.123	0.009	0.084
6	0.018	1,020	1,052	0.018	0.074	0.275	0.018	0.187
7	-0.009	-0.498	-0.467	-0.008	-0.037	-0.126	-0.008	-0.078
8	0.000	0.000	0.032	-0.001	-0.072	-0.002	0.001	-0.002

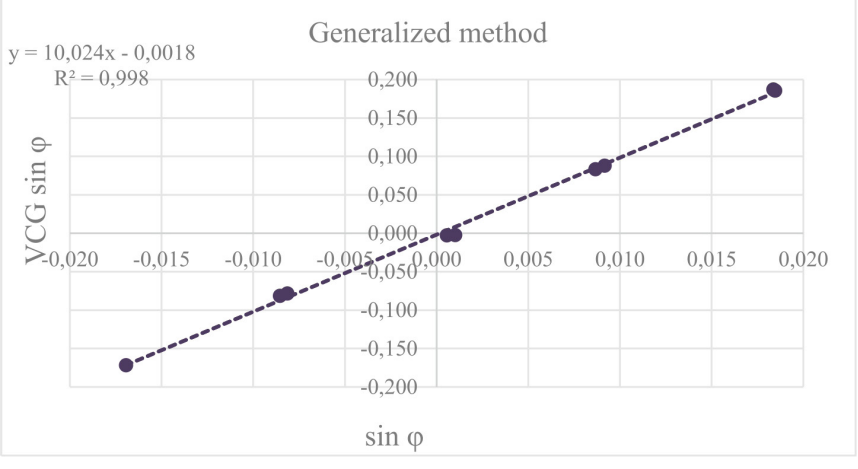

Figure 6. Diagram to determine the center of gravity of a container ship obtained by the generalised method

The graphical method, unlike the other two, uses averaged the *VCG* values from each shift governed by equation (14). A more suitable approach, as is stated in reference [7], would be to use least squares method which is applied here in order to maximize the capability of the graphical method. Strictly speaking, a proper way should be applying a

method in its original proposition for testing purposes, as intended by its authors. Table 4 shows the results of the calculation for the container ship by the graphical method. The value of *VCG* calculated by the graphical method for a container ship is 10,013 m.

Table 4. Calculation of the center of gravity of a container ship obtained by the graphical method

	tan φ	φ	Σ φ	φ	HZ	KN	sin φ	VCG sin φ
		°	°	rad	m	m		
0	0.000	0.000	0.042	0.001	0.000	-0.002	0.001	-0.002
1	-0.009	-0.521	-0.480	-0.009	-0.039	-0.110	-0.009	-0.085
2	-0.018	-1,003	-0.961	-0.017	-0.074	-0.239	-0.017	-0.171
3	0.009	0.493	0.535	0.009	0.037	0.135	0.009	0.082
4	0.002	0.115	0.157	0.018	0.000	0.200	0.018	0.181
5	0.008	0.464	0.506	0.009	0.034	0.123	0.009	0.087
6	0.018	1,020	1,062	0.018	0.074	0.275	0.018	0.189
7	-0.009	-0.498	-0.457	-0.008	-0.037	-0.126	-0.008	-0.080
8	-0.017	-0.980	-0.938	-0.017	-0.072	-0.002	-0.017	-0.168

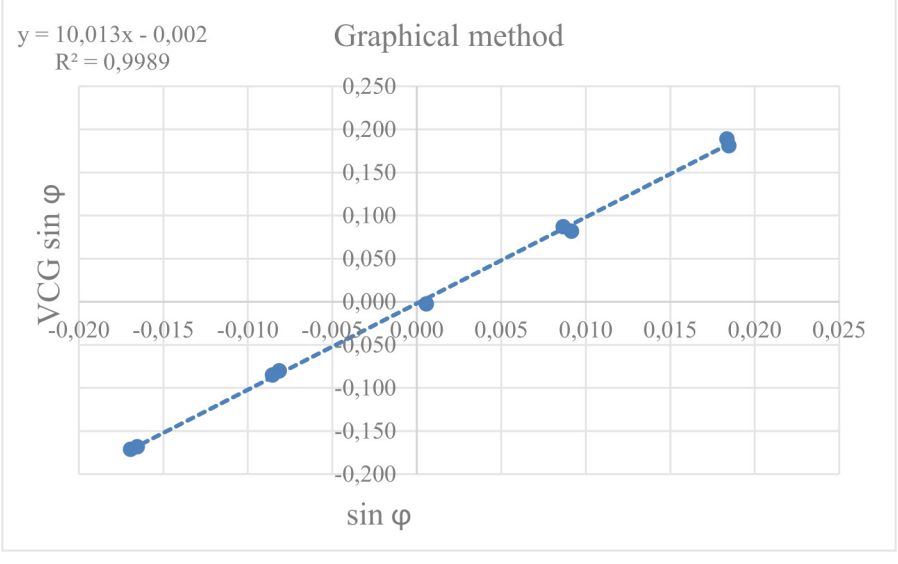

Figure 7. Diagram to determine the center of gravity of a container ship system by the graphical method

Table 5 shows the results of calculations for the container ship obtained by the polar method. The value of *VCG* calculated by the polar method for a container ship is 10,032 m.

Table 5. Calculation of the center of gravity of a container ship obtained by the polar method

	tan ϕ	ϕ	Σϕ	ϕ	HZ	KN	sin ϕ	sin (ϕ_i - ϕ_0)	VCG · sin(ϕ_i - ϕ_0)
		°	°	rad	m	m			
0	0.000	0.000	0.042	0.001	0.000	-0.002	0.001	0.000	-0.002
1	-0.009	-0.521	-0.479	-0.008	-0.039	-0.110	-0.008	-0.009	-0.091
2	-0.018	-1,003	-0.961	-0.017	-0.074	-0.239	-0.017	-0.018	-0.183
3	0.009	0.493	0.535	0.009	0.037	0.135	0.009	0.009	0.085
4	0.002	0.103	0.145	0.003	0.000	0.200	0.003	0.002	0.017
5	0.008	0.464	0.506	0.009	0.034	0.123	0.009	0.008	0.078
6	0.018	1,020	1,062	0.019	0.074	0.275	0.019	0.018	0.178
7	-0.009	-0.498	-0.456	-0.008	-0.037	-0.126	-0.008	-0.009	-0.078
8	0.000	0.000	0.042	0.001	-0.072	-0.002	0.001	0.000	-0.002

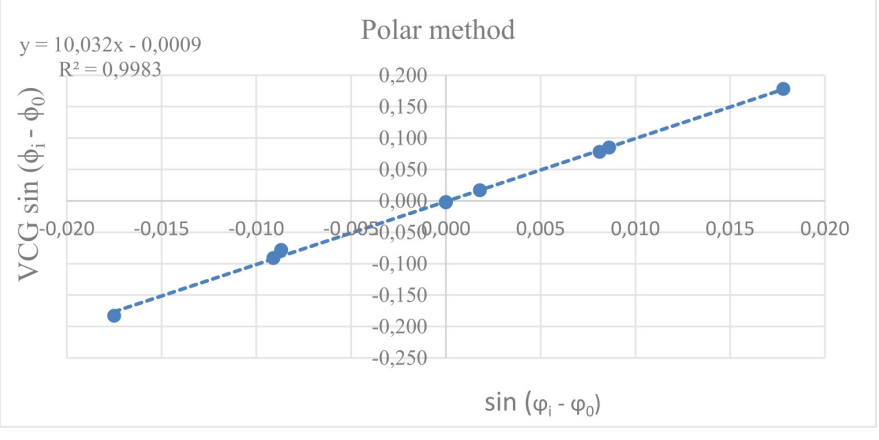

Figure 8. Diagram of the center of gravity of a container ship system obtained by the polar method

Table 6 shows the results of the calculation for the work vessel obtained by the general method. The value of *VC*G calculated by the general method for a work vessel is 2,015 m.

Table 6. Calculation of the center of gravity of the work vessel obtained by the generalized method

	tan φ	φ	Σ φ	φ	HZ	KN	sin φ	VCG sin φ
		°	°	rad	m	m		
0	0.000	0.000	0.000	0.000	0.000	0.000	0.000	0.000
1	-0.012	-0.688	-0.667	-0.012	-0.042	-0.059	-0.012	-0.024
2	-0.025	-1,410	-1,389	-0.024	-0.085	-0.113	-0.024	-0.049
3	0.013	0.745	0.766	0.013	0.044	0.065	0.013	0.026
4	0.001	0.057	0.078	0.001	0.000	0.002	0.001	0.005
5	0.012	0.705	0.726	0.013	0.041	0.053	0.013	0.025
6	0.026	1,467	1,488	0.026	0.085	0.112	0.026	0.052
7	-0.013	-0.745	-0.724	-0.013	-0.044	-0.065	-0.013	-0.026
8	0.000	0.000	0.000	0.000	0.000	0.000	0.000	0.000

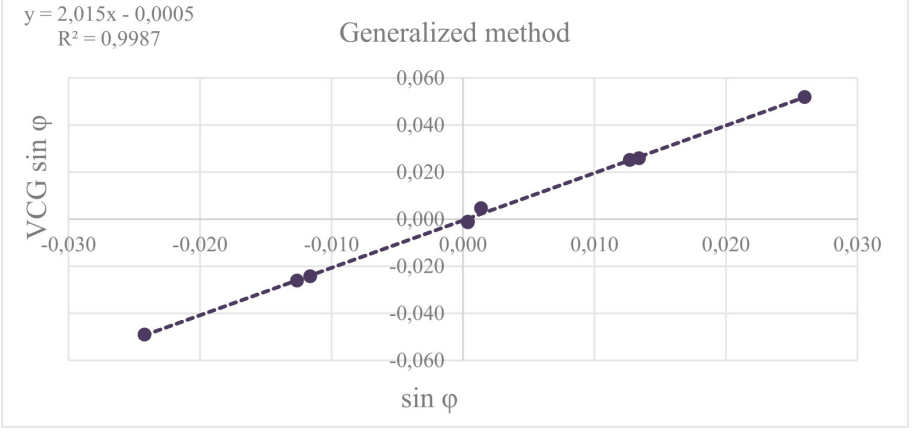

Figure 9. Diagram to determine the center of gravity of the workboat obtained by the generalized method

Table 7 shows the results of the calculation for the tugboat obtained by the graphical method. The value of *VCG* calculated by the graphical method for the tugboat is 3.185 m.

Table 7. Calculation of tugboat center of gravity obtained by the graphical method

	tan ϕ	ϕ	Σ ϕ	ϕ	HZ	KN	sin ϕ	VCG sin ϕ
		°	°	rad	m	m		
0	0.000	0.000	0.000	0.000	0.000	0.000	0.000	-0.001
1	-0.010	-0.544	-0.544	-0.010	-0.032	-0.063	-0.010	-0.031
2	-0.021	-1,175	-1,175	-0.021	-0.063	-0.131	-0.021	-0.068
3	0.010	0.584	0.584	0.010	0.031	0.062	0.010	0.031
4	0.000	0.000	0.000	0.000	0.000	0.000	0.000	0.000
5	0.010	0.544	0.544	0.010	0.033	0.065	0.010	0.032
6	0.023	1,318	1,318	0.023	0.063	0.133	0.023	0.070
7	-0.011	-0.630	-0.630	-0.011	-0.036	-0.072	-0.011	-0.036
8	0.000	0.000	0.000	0.000	0.000	0.000	0.000	0.000

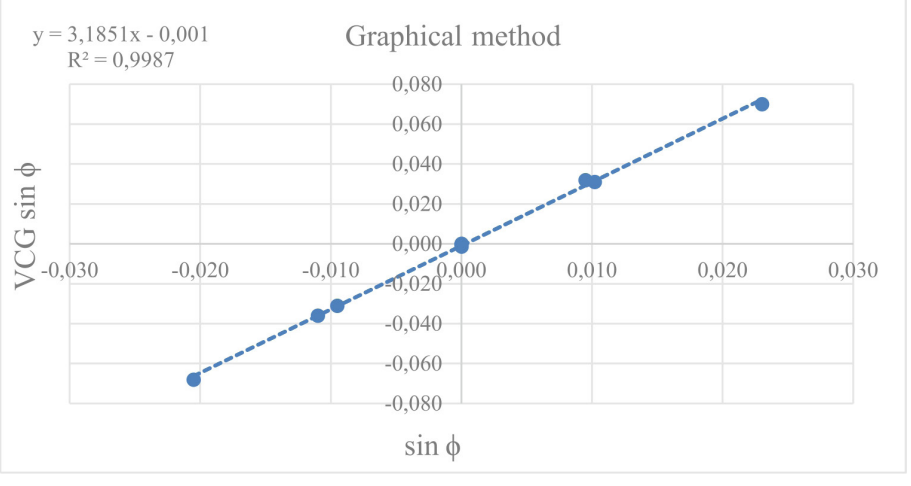

Figure 10. Diagram to determine the center of gravity of the tugboat obtained by the graphical method

Table 8 shows the results of the calculation for a passenger ship obtained by the polar method. The value of the *VCG* calculated by the polar method for a passenger ship is 0.83 m.

Table 8. Calculation of the center of gravity of a passenger ship obtained by the polar method

	tan ϕ	ϕ	Σ ϕ	ϕ	HZ	KN	sin ϕ	sin (ϕ_i - ϕ_0)	VCG · sin (ϕ_i - ϕ_0)
		°	°	rad	m				
0	0.000	0.000	0.000	0.000	0.000	0.000	0.000	0.000	0.000
1	-0.023	-1,331	-1,331	-0.023	-0.049	-0.068	-0.023	-0.023	-0.019
2	-0.046	-2,632	-2,632	-0.046	-0.092	-0.130	-0.046	-0.046	-0.038
3	0.022	1,272	1,272	0.022	0.048	0.067	0.022	0.022	0.019
4	0.002	0.115	0.115	0.002	0.000	0.000	0.002	0.002	0.000
5	0.022	1,238	1,238	0.022	0.049	0.068	0.022	0.022	0.019
6	0.046	2,637	2,637	0.046	0.092	0.130	0.046	0.046	0.038
7	-0.023	-1,318	-1,318	-0.023	-0.044	-0.063	-0.023	-0.023	-0.019
8	0.000	0.000	0.000	0.000	0.000	0.000	0.000	0.000	0.000

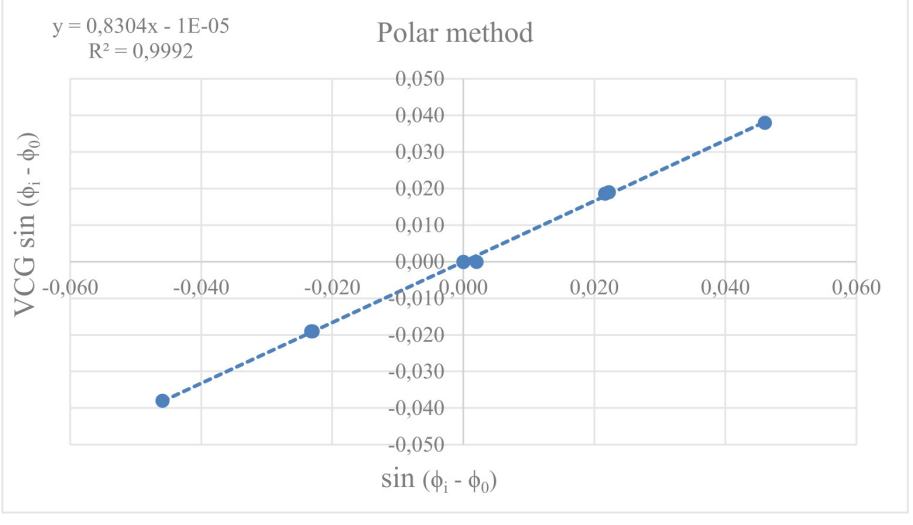

Figure 11. Diagram of the center of gravity of a passenger ship obtained by the polar method

5. Comparison of results

Table 9 shows the summary of the vertical center of gravity of the ships for each type of ship and for each method. The difference between the obtained position of the center of gravity by the classical method and alternative methods was calculated. The difference is shown graphically in Figure 12.

Table 9. Comparison of results

	Classical method	Generalized method			Graphical method			Polar method		
	VCG	VCG	Diff.	Diff.	VCG	Diff.	Diff.	VCG	Diff.	Diff.
Ship type	(m)	(m)	(mm)	%	(m)	(mm)	%	(m)	(mm)	%
Container ship	9,661	10,024	363	-3.75	10,013	352	-3.6	10,032	371	-3.8
Work vessel	2	2,014	14	-0.7	2,014	14	-0.7	2,014	14	-0.7
Passenger ship	0.805	0.83	25	-3.1	0.83	25	-3.1	0.83	25	-3.1
Tugboat	3.25	3.18	-70	2.1	3.18	-70	2.1	3.18	-70	2.1

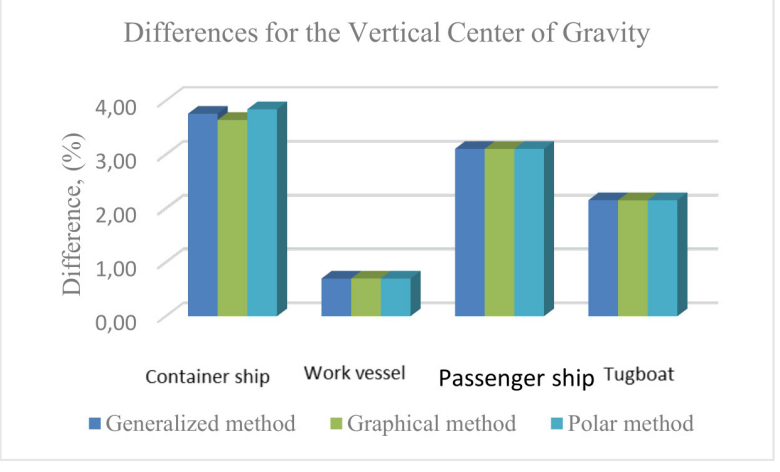

Figure 12. Comparison diagram for three novel methods

The results are presented by the absolute value of the percentage error, regardless of over or underestimation in order to compare the methods against each other.

By comparing the new methods, it can be deduced that all three methods yield virtually the same results for the the work vessel, passenger ship and tugboat. The difference is more subtle for the container ship. It comes as no surprise as one would expect that due to their more unconventional hull form with higher fore and aft flare and subsequent higher change in waterplane area.

All methods have been compared with results obtained from the classical method as shown in Figure 13.

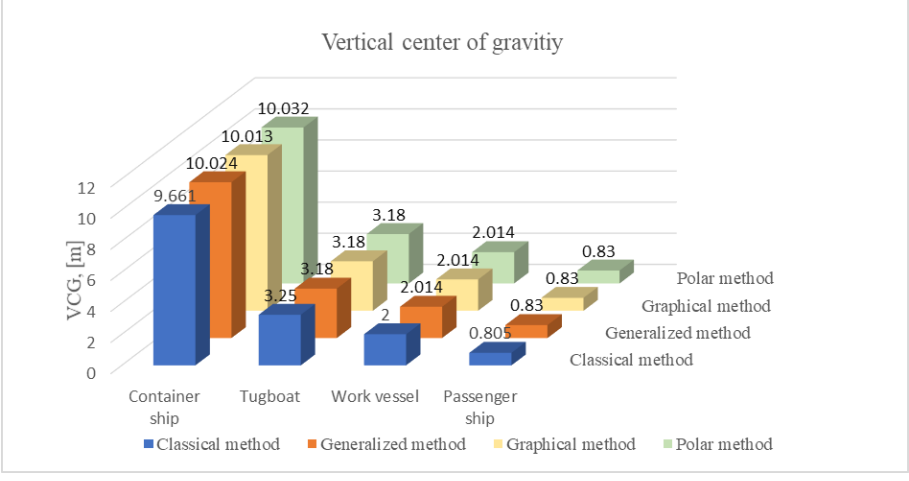

Figure 13. VCG values from all four methods

The difference between the vertical positions of the center of gravity for a container ship is 3.6% and this is the largest difference, while the lowest difference for the work vessel is less than 1%. The results demonstrate only the difference between methods, but not the methods difference from the actual VCG. Given that the results for three novel methods are similar if not the same, it certainly favours the statement that those three methods may replace the classical method as a convenient and more flexible alternative.

Furthermore, by not knowing the actual VCG it is difficult to use the results to conclude which method is more accurate or optimal than the others. In fact, based on the results in this paper, it is not possible to conclude that any calculation method is more accurate than the other, only their respective differences from each other, rather than the vessels' true *VCG*. However, in [10], it is proved that the polar method produces zero errors in a fully technical inclining experiment, and may, with correct assumptions, be used as the true *VCG* and baseline for the industry to know that there are other and more reliable alternatives to the classical method and this should be accounted for in the regulations and guidelines in use today.

6. Conclusion

In this paper, the results of the inclining experiment for four different ships are processed, where the calculation of the position of the center of gravity of the ship is determined by the classical method and three alternative methods.

The classical method is a simple, practical, and fast method based on the starting position of a metacenter. The location of the metacenter changes when the ship is heeled, but in the classical method this is neglected and the calculation of the position of the center of gravity of the system by height is inaccurate.

The calculation by alternative methods is not complicated, but it is more time-consuming because for each angle of inclination one needs to find the transverse position of the center of gravity, which prolongs the calculation process.

The general method is the first proposed one. It is a rather simple method, however precise because it takes into account the initial transverse position of the center of gravity. The graphical method is actually a general method converted into graphical form. The difference is that it does not take into account the initial transverse position of the center of gravity and therefore in ships with a transverse angle of more than half a degree it gives inaccurate results, which is not an improvement over the classical method. The polar method is the last proposed method that takes into account the initial transverse position of the center of gravity of the ship, the initial angle of inclination and the change of the transverse position of the center of gravity when moving cargo during the experiment, therefore the method is applicable to all angles.

The differences between the results of alternative methods are negligible. The differences between the positions of the center of gravity obtained by the classical method and the alternative methods are more profound.

Some additional research namely on the uncertainty and sensitivity analysis and certainly the reference studies should provide the International Maritime Organization an insight to consider alternative methods in its own regulations as relevant for determining the ship´s center of gravity.

7. References

1. Rules for the statutory certification of ships - Part 4: (2009) *Stability*, CRS
2. Dunworth, R. (2013) Up Against the Wall. *Proceedings of the Pacific international maritime conference,* Sydney, Australia.
3. Dunworth, R. (2014) Back Against the Wall. *RINA Transactions* (*International Journal of Small Craft Technology*), 156(B2): pp. 99-106.
4. Dunworth, R. (2015) Beyond the Wall. *International Conference on the Stability of Ships and Ocean Vehicles*.: Glasgow, UK.
5. Smith, A.C., Dunworth, R., & Helmore, P.J. (2015) Towards the Implementation of a Generalized Inclining Method for the Determination of the Center of Gravity. *Proceedings of the Pacific international maritime conference,* Sydney, Australia.
6. Kanifolskyi, O., & Konotopets, M. (2016) The Graphical Method for Analysis of the Inclining Test. *Mod. Inf. Technol. Sphere Security Defense* 3 (27), pp. 37–39.
7. Karolius, K., & Vassalos, D. (2018) Tearing down the wall- The inclining experiment. *Ocean Engineering*, 148, pp. 442-475.
8. Ozsaya, S., & Taylan, M. (2019) Another blow on the torn down wall-the inclining experiment. *Brodogradnja*, Volume 70 Number 2, pp. 135-153.
9. Djebli, M.A., Hamoudi, B., Imine, O., & Adjlout, L. (2015) The Application of a Smartphone in Ship Stability Experiment. *Journal of Marine Science and Application*, 14(04): pp. 406-412.
10. Karolius, K., & Vassalos, D. (2018) Second Generation Calculation Method for Use in the Inclining Experiment. *13th International Conference on the Stability of Ships and Ocean Vehicles*, Japan, 16-21 Sept.2018

Instructions for authors

Journal of Maritime & Transportation Sciences (JMTS) is a periodical which publishes research results in the domain of maritime affairs, transportation and traffic sciences. It primarily publishes scientific papers. However, other paper categories are allowed, such as professional papers, reviews, news, forum sections and conference reports.

1 Categories of scientific papers

Original scientific paper represents the unpublished, replicable research, both fundamental or applicable, where new scientific contributions are reported.

Preliminary communication is a paper containing new scientific elements, such as evidences, results and conclusions, although without sufficient details needed for replication or validation.

Review article is a comprehensive scientific overview of (exclusively) the latest state made in a respective research area, contributing with a new and unique approach of collection, analyses, synthesis and presentation of results.

2 Other contributions

Professional paper contains useful information obtained during research on a specific topic. The contribution is reflected in the theoretical and/or practical applicability of published results.

Expert revision/review refers to evaluation of other's scientific work, technological progress in a certain area or, in general, any actual topic significant to scientific and professional community in areas covered by JMTS. Examples of review topics are doctoral thesis, scientific books, textbooks, projects, patents, program tools and applications, technological products etc.

Forum is a written form of an expert's personal opinion regarding a certain topic,

often (but not exclusively) from a historical aspect. This section is subject to discussion among competent authors.

Categorization of scientific papers is made by the Editorial board based on positive reviews and reviewers' proposals. Once the paper is published, its category will be listed in the heading section and in the volume content.

3 The structure of the manuscript

The topic of the submitted manuscript should fit into the JMTS scope and covered areas. The submitted manuscript must, as much as possible, contain elements shown in the following table, and has to conform to the JMTS style.[1]

Heading section[1]	*Title of the paper*; *Name of Author(s)* (including e-mail and postal address); *Affiliation*; *Abstract;* and *Keywords*.
Research (main) section	*Introduction;* *Background*; *Methodology and resources*; *Research results*; *Discussion;* and *Conclusion*
Back section	*Supplements/ Annexes(if any);* *Acknowledgments(if any);* and *References.*

The text should be as concise as possible, but not at the cost of clarity. The paper title has to be short, informative and comprehensive, justifying all paper elements. Within the abstract, a short paper overview is presented containing all necessary information – research topic, its significance, author's main contributions and derived conclusions. Keywords represent main terms on which the paper resides. The abstract is written in one paragraph up to approximately 150 words.

The central part of the paper presents the author/s' contribution. It is strongly recommended that it contains elements needed for clear and concise presentation of course of study, research, results and conclusions:

- Within the introductory chapter it is necessary to place the research and the topic in broad context and to emphasize the importance of the conducted research. This is the place where the main objective of the paper is stated, as

[1] Author details are entered above the paper title. For additional explanation, refer to published issues.

well as derived conclusions and findings. It is desirable to indicate planned activities representing the continuation of the research;

- The background chapter refers to previous research in the area of the presented topic, including own contributions. Emphasis should be on the latest research and include the corresponding literature review. This chapter, either separately or as a part of the previous chapter, has to clearly and in detail introduce the reader to the main section;
- Methodology and resources have to be described distinctly, concisely and systematically in a way that the conducted research can be repeated. For usual scientific methods a short description is sufficient, while when employing new methods, particular emphasis should be given regarding their explanation;
- In the chapter on the results of the research it is necessary to provide a precise description of the results, and their objective interpretation and findings;
- Authors are encouraged to discuss their findings from the aspect of previous research and proposed hypothesis. Conclusions, findings and their eventual impact (implications) have to be discussed in as wide a context as possible, with a clear definition of their limitations and possible future development possibilities;
- The conclusion chapter summarizes the workflow of the paper, research results and findings. The reader should be familiar with any future planned activities and the possible continuation of the research.

The above elements do not have to be presented separately, but they can be placed in combination with other chapters (e.g. research results and discussion, introduction chapter and background etc.).

The back section contains acknowledgments (in case they exist), annexes which (if included) contain accompanying research documentation, and a mandatory list of references, listed alphabetically with numbers using Harvard style: bibliographic units, internet links, databases, software and programming tools etc. Throughout the text source numbers are used in square brackets and quoted before punctuation.

4 Referencing

1. (book, printed) Norris, A. (2001) ECDIS and Positioning. London, The Nautical Institute.
2. (e-book, electronic book) Sanz Subirana J., Juan Zornoza, J. M. & Hernandez-Pajares, M. (2013) GNSS Data Processing Book. Paris, European Space Agency. Available from: http://gage.upc.edu/gnss_book [Accessed 18th June 2017].
3. (book chapter) Hakkinen, J. M. & Posti, A. I. (2013) Overview of Maritime Accidents Involving Chemicals Worldwide and in the Baltic Sea. In: Weintrit, A. & Neumann, T. (eds.) Marine Navigation and Safety of Sea Transportation: Maritime Transport & Shipping. Boca Raton, CRC Press, pp. 15–26.
4. (scientific article, printed) Zhou, Y., Wang, W., Song, X. & Peng, Y. (2017) Container Shipping Network Optimisation Based on Steering Vector Search Pattern. Journal of Navigation. 70 (2), 395–410.

5. (scientific article, electronic) Lebedevas, S., Dailydka, S., Jastremskas, V. & Rapalis, P. (2017) Research of energy efficiency and reduction of environmental pollution in freight rail transportation. Transport. 32 (3), 291–301. Available from: http://www.tandfonline.com/doi/pdf/10.3846/16484142.2016.1230888 [Accessed 20th October 2017].
6. (article in the publishing process) Vilke, S., Brčić, D. & Kos, S. (2017) Northern and Southern European traffic flow land segment analysis as a part of the redirection justification. To be published in The International Journal on Marine Navigation and Safety of Sea Transportation.
7. (conference paper, published) Štern, A. & Bešter, J. (2012) Seamless Connectivity in a Networked Vehicle. In: Rijavec, R. & Anžek, M. (eds.) ISEP 2012: Linking people with ITS: Proceedings of the International Symposium on Electronics in Transport, ISEP 2012, 26–27 March 2012, Ljubljana, Slovenia. Ljubljana: Electrotechnical Association of Slovenia. pp. 132–137.
8. (standard) British Standards Institution (2005) BS EN 1993-1-2:2005. Eurocode 3. Design of steel structures. General rules. Structural fire design. London, BSI.
9. (report) Thomas, M. (2011) Global Navigation Space Systems: Reliance and vulnerabilities. The Royal Academy of Engineering. Report Number: 63.
10. (doctoral thesis) Kotcharat, P. (2016) A forecasting model for container throughput: empirical research for Laem Chabang Port, Thailand. Ph. D. Malmo World Maritime University.
11. (magazine article) Williams, A. I., Shaw, G. & Ward, N. (2015) ACCSEAS: The Innovative North Sea e-Navigation Demonstration. Coordinates. 11 (7) pp. 11–16.
12. (map, chart) British Geological Survey. (1998) South London. 270, 1:50 000. London, British Geological Survey.
13. (website) Marine Electronics & Communications. (2017) Thenamaris improves fleet communications and data flows. Available from: http://www.marinemec.com/technology/fleet-management.htm [Accessed 16th October 2017].
14. (official documents) International Maritime Organization. (2012) MSC.347(91): Recommendation for the protection of the AIS VHF data link. Resolution. London: IMO.
15. (online database) National Geodetic Survey. (2017) Continuously Operating Reference Station (CORS) Navigation messages in RINEX format. [Online]. Available at: https://www.ngs.noaa.gov/CORS/standard1.shtml [Accessed 20th October 2017].
16. (software) RTKLIB. (2013) Tokyo. Takasu, T.[2]

5 Checklist

It is strongly recommended that prior to the final manuscript submission author/s consider the following checkpoints:

- Originality of the paper, its significance and its contribution;
- Style of writing, intelligibility and clarity;
- Correct English language, grammar and appropriate vocabulary;
- Explanatory but concise paper title and abstract;
- Proper selection of keywords;
- Consistent and thorough literature review;
- Proper description of methodology, data and other resources used in the research;
- Careful and comprehensive interpretation of results and their critical discussion;
- Approach to presented topic, with relevant and exhaustive literature, emphasizing recent research in the area;

[2] For any unclassified reference type, authors are advised do contact editorial board.

- Adequate number and descriptive features of tabular and graphic presentations;
- The structure and contents of the conclusion chapter;
- General layout of the entire text.

6 Remaining guidelines

Acceptance of the paper for publishing is based on the review process from at least two reviewers. During this process the authenticity of the manuscript is determined as well and its originality is validated. The submission of the paper implies that it was not sent elsewhere for publishing consideration.

Manuscripts have to be submitted in Microsoft Word format, using Times New Roman font, size 12. Authors are kindly requested not to format the manuscript, both graphically and textually, except the general guidelines provided here together with the following:

- The text should be single spaced, without spaces between rows and paragraphs;
- Numbering of chapter and subchapter titles should be entered manually;
- Abbreviations, if used, should be explained when introduced;
- Footnotes are used as little as possible, preferably not at all;
- The SI measuring units system is allowed for use.

Tabular and graphical presentations should contain ordinal number, title and source (in case they are retrieved or adapted). The JMTS is printed in black and white, while online is published in color. Authors should consider this feature and customize all figures for the sake of clarity and understanding. For the same reason, within the presentations it is necessary to adjust the size of the text. Desirable image formats are TIF, JPG and PNG, with at least 300 dpi resolution.

Mathematical expressions should be numbered and written using appropriate MW Equation Editor.

The final size of the paper and its elements should not exceed 30 000 characters, being approximately 16 typewritten pages.

The JMTS official language is English. The paper title, abstract and keywords should be written both in English and in the corresponding author's native language. It is recommended that non-English authors prepare their manuscript and have it checked by a language expert or native English speaker.

The Editorial board reserves the right to adapt the manuscript to propositions of the Journal, as well as to comply with English and Croatian language standards.

Manuscript submissions are sent via email to the Association for Promotion and Development of Maritime Industries (*udruga.pomorstvo@gmail.com*). The same address should be used for any additional questions regarding submission, publishing of manuscripts or any other questionable detail.